Development of a Scanning Tunnelling Microscope for the Atomic-Level Characterization of Overlayers on Single Crystal Surfaces

Pong Wing Tat

St. John's College

Supervised by Dr. C. Durkan

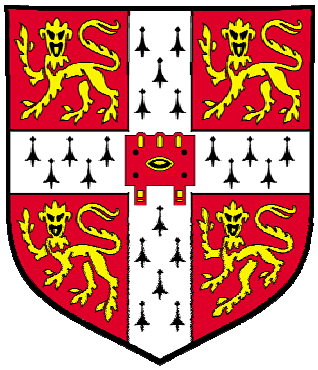

Nanoscience Centre, Department of Engineering
University of Cambridge

Thesis submitted for the degree of Doctor of Philosophy,

September 2005

Preface

This thesis describes the research carried out in the Department of Engineering, University of Cambridge, between October 2002 and October 2005. This dissertation is my own work and contains nothing which is the outcome of work done in collaboration with others, except as specified in the text and Acknowledgements. This thesis has not been submitted in whole or in part for a degree from any other University. This thesis contains not more than 65000 words and less than 150 figures, and it does therefore not exceed the limit set by the Degree Committee.

Abstract of thesis

Development of a scanning tunnelling microscope for the atomic-level characterization of overlayers on single crystal surfaces

by Wing – Tat PONG

(PhD candidate, Engineering Department, St. John's College)

The primary aim of this research project is to develop an ultrahigh vacuum scanning tunnelling microscope (UHVSTM) for the characterization of overlayers on single crystal surfaces, including free radical organic molecules on HOPG graphite and gold surfaces and iron silicides on silicon surfaces, with the future intention of conducting spin-polarized scanning tunnelling microscopy and single electron spin detection experiments on these overlayers.

In the course of this development, superlattice structures were observed on HOPG (graphite) surfaces with our STM. Such superlattices are worth investigating as their origins are not yet completely understood. The conventional belief is that they arise either from (a) the lattice mismatch of several atomic layers, or (b) a network of dislocations below the surface. In view of this, we expended considerable effort in investigating and analyzing the observed superlattices, together with the support of a simulation model, establishing a coherent and systematic understanding of the subject, and proposing a theory to unify the explanations of the previously unexplained phenomena.

Various means for depositing free radical organic molecules onto HOPG and gold, and iron silicides onto silicon reliably were explored, and their possibilities for single electron spin detection and spin-polarized STM experiments were discussed.

The organization of this thesis reflects the distribution of our research efforts: three of the chapters are about the development towards characterizing overlayers on single crystal surfaces at the atomic-scale, one chapter is concerned about the graphite superlattice structures, and the remaining chapter is the conclusion.

Acknowledgements

First and foremost, I would like to gratefully thank my supervisor, Dr. Colm Durkan, for his support, inspiration, encouragement, patience, guidance, and friendship over the past three years. From his exceptional research speciality, I have not only learned valuable scanning probe techniques, but also to be a respectable researcher and to live a fulfilling life. Endless gratitude is owed to him for he has taken me as his PhD student and he is a very nice supervisor, who has changed my life entirely. Many thanks go to Prof. Mark Welland for being my advisor, and giving me the opportunity to participate in the Nanotechnology Summer School in Japan.

I feel privileged to work in the Nanoscience Centre, where I have benefited a great deal from the research skills and established friendships with my fellow students and colleagues, in particular, Ghim Wei, Shu, and James. I owe a great debt of gratitude to Prof. Carl Sofield for his valuable advice, discussion, friendship, and help. His sense of humour is amazing, and it helped to integrate a lot of joy and pleasure into my research work in our STM laboratory.

Among all my friends in Cambridge, I would particularly like to thank Chris Golby, with whom I not only share tea time in the college common room, travel around Europe, have a pint of beer in the pub, feast fantastic meals in London China Town, but also interact with intellectually which leads me to think more broadly and deeply about life and science. Together with Kieren Hollingsworth, Tim Cooper, and Martin Worthington, college life in St. John's has always been good fun and joyful. I have to mention Ricky Chan, Zhao Ni, and Pei Chuan for sharing the ups and downs of being a foreigner in another country. These three years that I have spent in Cambridge will always be cherished and echoed in my life.

Several institutions have supported my research here. I would like to thank the Cambridge Overseas Trust and United Kingdom Government for scholarships, and the St. John's College and the European Union for financial assistance. Acknowledgement, with much appreciation, is extended to the Stephen Kam Chuen Cheong Memorial Scholarship which provided full scholarship support throughout my undergraduate study.

Although I have been in England for my PhD studies for three years, the friendship and contacts with my friends in Hong Kong never ceased. I still miss the good times I had with my classmates in University of Hong Kong, with whom I went through my undergraduate study. I would like to acknowledge and thank Dr. Alfred Wong, my undergraduate final year project supervisor, for inspiring and enlightening me into research field. Without him, I would not be writing these lines; his enthusiasm for teaching, patience with students, and outstanding research capability will always be the role model for my academic career. I would be remiss if I failed to mention my high school and primary school classmates. After all these years, despite the fact that we were not in touch as frequently as we used to be in schools, the flame of our friendship still burns. Among my best friends, I would like to present my best wishes to Cheng Cheung Hing. We are buddies since we were eight or ten, at the time we were intrigued by the elegance of mathematics and thought we would both be scientists in the future. My volunteer worker group “Starry Team” in YWCA Hong Kong has played a significant role in my life, which I will always treasure and remember. Particular thanks go to the group members – Sarah, Sa, Givens, Ivy, and Kin, for they have enabled me to understand different attitudes of life and made “Starry Team” a wonderful endeavour.

Of course, I am deeply indebted to my parents and brother for their constant love and support: to my father, for taking care of my family; to my mother, for her gorgeous cooking and never-ending care of all the bits and pieces of our family life; to my brother, for putting up with me and sharing the bunk bed with me over all these years.

To my parents

Research summary and organization of thesis

The primary aim of this research project is to develop an ultrahigh vacuum scanning tunnelling microscope (UHVSTM) which is specifically designed for characterizing overlayers on single crystal surfaces, with the future intention of performing single electron spin detection and spin-polarized STM experiments (SPSTM), which, in its own right, is a significant piece of scientific endeavour towards the ultimate resolution limit of detecting magnetic systems.

In the course of such development, we observed superlattice structures on HOPG graphite surfaces with our STM. A superlattice is worth studying because its origin is not yet completely understood, and the knowledge of it would certainly enrich our understanding of the principle of STM and expand the dimension of surface science to the regime which involves more than simply the surface layer as a superlattice is believed to arise from the lattice mismatch of several layers, and perhaps it is also induced by a network of dislocations deep in the crystal bulk appearing as a superperiodic hexagonal lattice by a mechanism which is still beyond our knowledge. In view of this, we expended considerable effort in investigating and analyzing the STM observed superlattices, together with a supporting simulation model, establishing a coherent and systematic understanding of the subject, and proposing a theory which can unify the explanations of the previous unexplained phenomena.

The organization of this thesis reflects the distribution of research efforts: three of the chapters concern the development towards atomic level characterization of overlayers on single crystal surfaces, one chapter is concerned with graphite superlattice structures, and the remaining chapter is the conclusion. The first chapter of this thesis gives an introduction to the STM as a technique which can probe surface properties at the atomic scale, and its application in electron spin detection and surface science. The second chapter describes the construction of the ultrahigh vacuum STM which is particularly designed for atomic level characterization of overlayers and is suitable for the future experiments of single electron spin detection and SPSTM. The novelties of our design are explained and the imaging performance of the system is tested. The third chapter consists of five sub-chapters. Chapter 3.1 is a comprehensive review of the reported research works on graphite superlattices with the STM. The purpose of this review is to collect together all the scattered research findings on the subject and present them in a coherent and structured manner so that other researchers can benefit from an overview of the subject. After that we discuss the experimental aspects, starting with the observation of the superlattice structures on graphite with our STM. In

chapter 3.2, we report the rippling fringes imaged on, and nearby, the superlattices on graphite which is indicative of the surface deformation by buckling. In addition, the corrugation conservation phenomenon observed on one of the superlattices is discussed. To support our argument, a simulation model of graphite layers is established and applied in our study of superlattices, as will be elaborated in chapter 3.3. There will be discussion on the origin and patterns of different kinds of superlattice boundaries appearing in STM images in chapter 3.4. Chapter 3.5 will give an outlook and conclusion to the research on graphite superlattices. Chapter 4, which is composed of two sub-chapters, is related to the STM characterization of overlayers on single crystal surfaces. Chapter 4.1 is dedicated to the deposition and characterization of free radical organic molecules. Chapter 4.2 is focused on iron deposited on silicon and its characterization. Finally, we will conclude our research project in chapter 5, summarize the major points, and suggest the future direction the research endeavours on graphite superlattices and STM characterization of overlayers on single crystal surfaces will go towards.

The works in chapters 2, 3, and 4 are published or under review as described at the beginning of the chapters.

Contents

Chapter 1

Introduction to STM and its applications in surface science

In this chapter, we will give an introduction to scanning tunnelling microscopy (STM), entailing its basic principles, operation modes, and the spin detection capability of the STM. Various spin detection techniques are reviewed, and spin-polarized STM and single electron spin detection STM are described. The applications of STM on surface science are discussed including the layered material – graphite, metal – gold, and semiconductor – silicon, on the basis of the STM images we obtained on these surfaces.

1.1 Scanning tunnelling microscopy (STM)

1.1.1 History and background

The principle of the scanning tunnelling microscope (STM) is based on a quantum mechanical phenomenon – electron tunnelling. Scientists started their exploration into the theory of electron tunnelling at the beginning of the twentieth century. Lilienfeld, Oppenheimer, Fowler and Nordheim, to name a few, were the pioneers in the field. In 1971, Young made an instrument named "topografiner". This instrument allowed electron tunnelling between tip and sample and it had two orthogonal (x and y directions) piezodrives, enabling raster scanning along the sample surface [1, 2]. It is a preliminary model of STM. However, the feedback control of the topografiner was not good enough to maintain a stable tunnelling current and moreover, the vibration isolation system was not sufficient and the vibration level eradicated any chance of atomic level scanning. Given these inadequacies, the topografiner could only achieve a vertical resolution perpendicular to the surface of around 30 Å and a lateral resolution in the plane of the sample surface of about 4000 Å which is far from atomic resolution. The combination of electron tunnelling and scanning capability was not successful until early 1980s. In 1981, Binnig, Rohrer, Gerber, and Weibel at the IBM Zurich laboratory invented STM [3, 4]. The STM allows imaging at unprecedented resolution. The birth of STM has initiated the commencement of the Nano unit scale or even Angstrom unit scale research. Nowadays, STM is an indispensable tool in every nanotechnology research institute.

1.1.2 Overview of STM

In STM, a bias voltage is applied between a sharp tip and a conducting sample to be investigated. By using piezoelectric drive, we can bring tip and sample within a distance of a few Angstroms. Due to the overlap of electron wavefunctions, a tunnelling current will flow across the gap, in the absence of mechanical point contact between tip and sample. The feedback electronics keeps the tunnelling current constant by adjusting the tip – sample separation. By scanning the tip over the sample surface and recording the vertical position of the tip, we can obtain a map of the local density of states of the surface. Lateral and vertical motions of the tip are enabled by piezoelectric drives. In addition to getting a surface topography, the feedback loop can be held and the tip is fixed at a point of the sample surface. The localized electrical properties of that point can be measured by scanning tunnelling spectroscopy (STS) [5-7].

1.1.3 Theory of STM

The theory of STM is based on a quantum mechanical phenomenon called "tunnelling". Tunnelling is a phenomenon that states there is a finite chance of finding a particle (an electron for STM tunnelling) at the other side of the barrier (vacuum gap between the tip and the sample for STM) even though the potential energy of the barrier is higher than that of the particle. Tunnelling is not possible in classical mechanics since the particle does not have enough energy to surmount the barrier. However, in quantum mechanics, the particle has a wave nature which allows tunnelling through the classically forbidden region.

In STM, the electrons tunnel from one electrode to another through the vacuum gap. Tunnelling can proceed from the tip to the sample and vice versa. Several mathematical models have been proposed to describe the tunnelling with different extents of accuracy and detail. The one-dimensional tunnelling model is the most well-known and easiest to understand, though it is far too simple to completely describe the tunnelling process of STM experiments.

One-dimensional potential barrier model

We can approximate the tunnelling situation in STM as a one-dimensional barrier model (Fig. 1.1). In this example, the electron with energy E (the Fermi energy of metals is typically ~5 eV) travels from the tip, penetrates through the barrier of height V (work function of metals is typically ~4 eV), and reaches the sample. Classically, the electron should be bounced back by the barrier and can never go through the barrier since the potential energy of the electron is lower than that of the barrier.

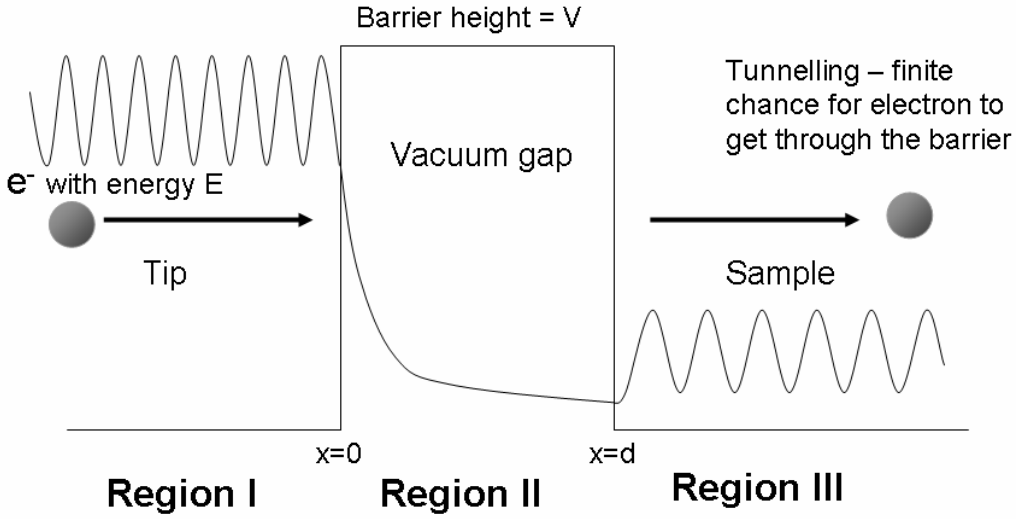

Fig. 1.1. One-dimensional tunnelling barrier.

In quantum mechanics, an electron is described by a wave function ψ that must satisfy the Schrödinger equation. The electron wave functions for the three regions are of these forms:

Region I : $\psi_I(x) = A_1 e^{ik_1 x} + B_1 e^{-ik_1 x}$ E - V > 0

Region II : $\psi_{II}(x) = A_2 e^{-k_2 x} + B_2 e^{k_2 x}$ E - V < 0

Region III : $\psi_{III}(x) = A_3 e^{ik_3 x} + B_3 e^{-ik_3 x}$ E - V > 0

$$k_1 = k_3 = \frac{\sqrt{2m_e E}}{\hbar} \qquad k_2 = \frac{\sqrt{2m_e (V-E)}}{\hbar}$$

m_e is electron mass, and $\hbar$ is Planck's constant

In region I and III, the wavefunctions are propagating waves while that in region II (inside the barrier) is an exponentially decaying wave. If the barrier is thin enough, there is a finite probability that electrons may penetrate through the barrier.

The probability for an electron to get through the barrier from x = 0 to x = d is:

$$\textbf{tunnelling probability} = \frac{\left|\psi_{II}(d)^* \psi_{II}(d)\right|}{\left|\psi_{II}(0)^* \psi_{II}(0)\right|} = \frac{A_2^{\,2} e^{-2k_2 d}}{A_2^{\,2}} = e^{-2k_2 d}$$

tunnelling current, $I_t \approx$ tunnelling probability

$$\Rightarrow I_t \approx e^{-2k_2 d}$$

There is an exponential relationship between the tunnelling current and the barrier width d. The current is very sensitive to the barrier width. 1 Å change of barrier width will bring about one order of magnitude change to the current. This explains the high resolution of STM and the need for vibration isolation.

Wentzel – Kramers – Brillouin (WKB) Approximation

In the ideal one-dimensional tunnelling model, the potential barrier is assumed to be a vertical step. However, this is physically impossible because abrupt changes in potential bring about infinite fields. To make the barrier assumption more reasonable, the potential should rise and fall smoothly without sharp turning points, which means the potential barrier will no longer be constant or linearly varying. As such, the barrier height is a function of position U(z), this complicates the Schrödinger equation and no straightforward solutions can be obtained. In this case, we will need the Wentzel – Kramers – Brillouin (WKB) method to approximate an arbitrarily shaped barrier to be uniform between its turning points. The turning points are the start and end points where the potential barrier rises above the energy of the electron (E), i.e. where E = U(z). Propagating and decaying wave functions are

determined, and they match with these turning points. In this light, the transmission probability can be found as

$$T \propto \exp\left(-\frac{2\sqrt{2m_e}}{\hbar}\int_{s_1}^{s_2}\sqrt{[U(z)-E]}dz \right), \quad (1.1)$$

and for low bias voltages, tunnelling is confined to energies near the Fermi level E_F, and according to the derivation of Simmons [8], eq. (1.1) can be simplified to

$$T \propto \exp\left(-\frac{2\sqrt{2m_e}}{\hbar}\Delta s\,\bar{\phi}^{1/2} \right), \quad (1.2)$$

where Δs is the width of the potential barrier above the Fermi level, and $\bar{\phi}$ is the average barrier height:

$$\Delta s = s_2 - s_1; \qquad \bar{\phi} = \frac{1}{\Delta s}\int_{s_1}^{s_2}\phi(z)dz \ .$$

Image potential

One explanation why the barrier does not have abrupt edges is the image potential. The image potential occurs when an electron is in close proximity to a metal surface, the other electrons in the metal will be repelled by the electrostatic force and thus the surface becomes polarized. This can be imagined as a "mirror image electron", i.e. an electron of opposite charge located inside the metal at the same distance from the surface. As such, the outside electron will be attracted to the polarized surface with a force, which is known as the image force P. Therefore, the potential of the electron at a distance z from the metal surface measured with respect to the vacuum level is

$$\begin{aligned} U_i(z) &= -\int_{\infty}^{z} P_i dz \\ &= -(1/4\pi\varepsilon)(e^2/4z), \end{aligned} \quad (1.3)$$

and the potential barrier will no longer be constant but instead a function of the distance z from the metal surface:

$$\begin{aligned} \phi_i &= \phi_0 + U_i(z) \\ &= \phi_0 - \frac{e^2}{16\pi\varepsilon z} \end{aligned} \quad (1.4)$$

This phenomenon is illustrated in Fig. 1.2. We can assume the image force will remain constant below a critical distance z_0. Although the correct value of z_0 is unknown, it is not essential in the WKB approximation since only the positions of the turning points are of interest, which are the points z, where $\phi_i(z) = E$.

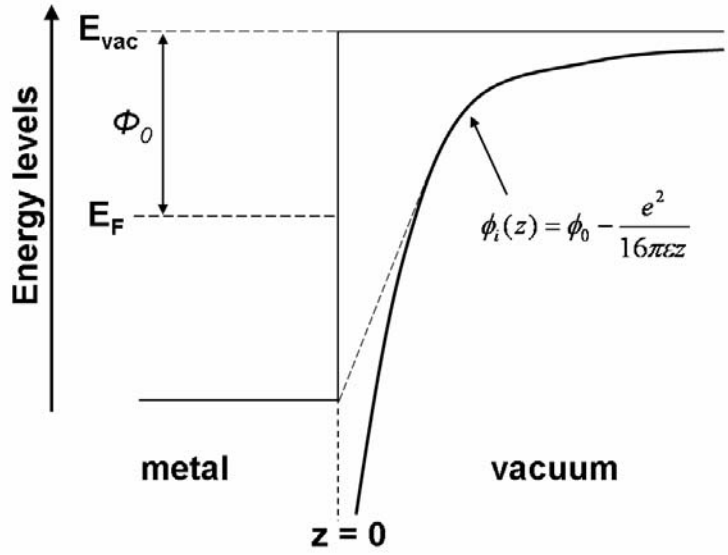

Fig. 1.2. Energy model of a metal – vacuum interface with a square barrier and the rounded barrier affected by the image potential.

Bardeen's Approach

In order to make the prediction for actual STM more accurate, we need to broaden the tunnelling theory to a three-dimensional case. Bardeen's approach, which is based on a perturbative treatment of tunnelling, is applicable for the three-dimensional situation and takes into account specific tip and sample surface properties, providing more insight into the physics of the tunnelling mechanism. In this approach, a time-dependent perturbation theory is applied and the two electrodes of the tunnelling junction are initially considered as two independent subsystems as shown in Fig. 1.3. The electronic state for each subsystem is determined by solving the stationary Schrödinger equations. The rate of transfer of an electron from one electrode to the other is calculated by making use of time-dependent perturbation theory. Bardeen [9] showed that the amplitude of electron transfer, or the tunnelling matrix element M, is dependent upon the overlap of the surface wave functions of the two subsystems at a separation surface. The position z_0 of the separation surface is chosen arbitrarily inside the tunnelling gap. We can then calculate the tunnelling matrix element M by a surface integral on this separation surface:

$$M = \frac{\hbar}{2m_e}\int_{z=z_0}\left(\psi_T^* \frac{\partial \psi_S}{\partial z} - \psi_S \frac{\partial \psi_T^*}{\partial z}\right) dS \ , \qquad (1.5)$$

where Ψ_T Ψ_S are the wave functions of the two electrodes (the tip and the sample respectively).

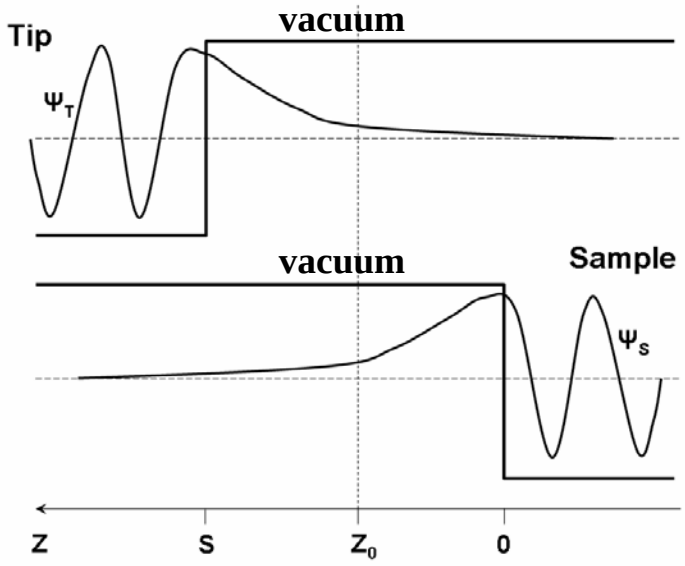

Fig. 1.3. Bardeen's Approach, the Schrödinger equations for the two wave functions of the tip and the sample are solved separately.

By Fermi's golden rule, the probability w of an electron in the state of Ψ_T at energy level E_T tunnelling into a state Ψ_S of energy level E_S can be determined by

$$w = \frac{2\pi}{\hbar}|M|^2 \delta(E_T - E_S), \qquad (1.6)$$

where the delta function ensures electrons only tunnel into states with the same energy level (i.e. energy is conserved). Adding up over all states, the tunnelling current is found to be

$$I = \frac{4\pi e}{\hbar}\int_{-\infty}^{\infty}[f(E_F - eV + \varepsilon) - f(E_F + \varepsilon)]p_S(E_F - eV + \varepsilon)p_T(E_F + \varepsilon)|M|^2 d\varepsilon, \qquad (1.7)$$

where $f(E) = 1/\{1+\exp[(E-E_F)/kT]\}$ is the Fermi distribution function, and $p_S(E)$ and $p_T(E)$ are the densities of states of the sample and the tip respectively (the two electrodes of the tunnelling junction). kT is the thermal broadening of the Fermi function, which is 25 meV at 300 K. Features in the density of states within kT of each other are not distinguishable. However, if kT is smaller than the energy resolution required in a measurement, we can approximate the Fermi function by a step function. As such, eq. (1.7) becomes

$$I = \frac{4\pi e}{\hbar}\int_0^{eV} p_S(E_F - eV + \varepsilon)p_T(E_F + \varepsilon)|M|^2 d\varepsilon, \qquad (1.8)$$

where V is the applied bias voltage. With the assumption that the magnitude of the matrix element M stays more or less constant in the interval of interest, the tunnelling current is the summation of the convolution of the densities of states of the tip and sample:

$$I \propto \int_0^{eV} p_S(E_F - eV + \varepsilon)p_T(E_F + \varepsilon)d\varepsilon. \qquad (1.9)$$

From eq. (1.9), we can see that the tunnelling current is basically the convolution of the

densities of states of the tip and the sample. If a tip with constant density of states is used, the tunnelling current is equal to the summation of the density of states of the sample within the energy range of eV. If we differentiate eq. (1.9) with respect to the bias voltage, then we obtain

$$\frac{dI}{dV} \propto p_S(E_F - eV), \qquad (1.10)$$

which shows that the density of states of the sample can be found from the dynamic tunnelling conductance if a tip with a constant density of states at the Fermi level is used for STM scanning.

However, the Bardeen's Approach did not take into account the influence of the image force. For small tip-sample distance, the image force will significantly lower the barrier height and an independent treatment of the two electrodes will no longer be applicable. In fact, since the image force is a long-range interaction, modification of the wavefunctions are important even at large tip-sample distances. A theoretical approach which considers such an effect is known as a Modified Bardeen Approach [10].

Tersoff and Hamann Theory

In order to get beyond qualitative properties of the tunnelling current, we have to approximate the tunnelling matrix elements more accurately. A common approximation in STM theory is the s-wave approximation for tip wave functions proposed by Tersoff and Hamann [11]. The tip is modelled with a locally spherical symmetry, and the tunnelling matrix element is evaluated for an s-type tip wave function, whereas contributions from tip wave functions with angular dependence (orbital quantum number $l \neq 0$) are neglected. Under this assumption and for a low bias and moderate temperature, we obtain the following expression for the tunnelling current:

$$\boldsymbol{I} \propto \sum_{E_S} |\psi_S(\boldsymbol{r}_0)|^2 \delta(\boldsymbol{E}_S - \boldsymbol{E}_F), \qquad (1.11)$$

where r_0 is the position of the centre of curvature of the tip as shown in Fig. 1.4.

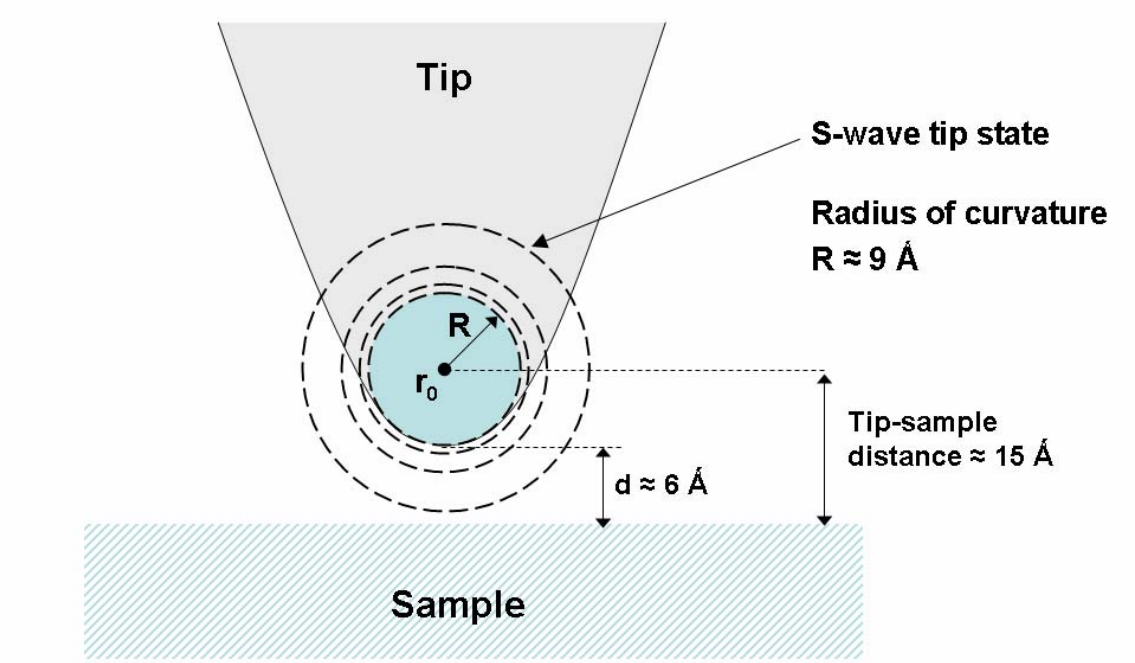

Fig. 1.4. In Tersoff and Hamann theory, the tip is modelled as a spherical potential well of radius R at position r_0 while the tip wavefunction is taken as s-wave.

Local density of states (LDOS) is the number of electrons per unit volume per unit energy. At a location z and energy E, the LDOS of the sample is defined as

$$p_s(z,E)=\frac{1}{\varepsilon}\sum_{E_n=E-\varepsilon}^{E}|\psi_n(z)|^2, \qquad (1.12)$$

for sufficiently small ε. Putting this LDOS definition into eq. (1.11), we obtain

$$I \propto eVp_s(r_0,E_F), \qquad (1.13)$$

which displays the relationship that the tunnelling current is directly proportional to the local density of states of the sample and depends linearly on the applied voltage. As such, with this s-wave tip model, a constant current STM image is a Fermi-level LDOS contour of the sample taken at the centre of curvature of the tip r_0.

Unfortunately, the simple interpretation of tunnelling current by Tersoff and Hamann is not applicable for high bias or for tip wavefunctions with angular dependence. Tungsten and platinum-iridium tips are most widely used in STM experiments, and the density of states at the Fermi level for these materials is dominated by d states rather than s states.

1.1.4 STM tips

Generally, STM tips are made from metal wires of tungsten (W), platinum-iridium (Pt-Ir), or gold (Au) by mechanical grinding, cutting with a wire cutter, or electrochemical etching. Most commonly tips are made from either a Pt-Ir alloy or tungsten wire [12-14]. Sodium hydroxide solution is used for preparing tungsten tips by etching. Sodium cyanide solution is used in electrochemical etching of platinum-iridium tips. The tips should then be thoroughly rinsed. The second way is by mechanical cutting. Firstly, the metal wire, the cutter, and the clamp are cleaned by solvents, for example, isopropyl alcohol. Then the cutter and the clamp are used to pull and cut the wire.

Tungsten tips are widely used for STM studies, especially, under UHV conditions, because tungsten is relatively hard and thus resistant against accidental or intentional contact with the sample surface during scanning. For STM measurements in air or under poor vacuum environments, tips made of noble metals like gold are favourable as they are inert materials. However, noble materials are relatively soft and thus vulnerable to damages due to accidental contact with the sample surface. Therefore, platinum-iridium alloys with increased hardness are commonly used for making tips for STM studies in air. Moreover, tungsten and platinum-iridium have relatively featureless densities of states. As we have learned from eq. (1.9), the tunnelling current is the convolution of the density of states of the tip and the sample. By using a tip made of tungsten or platinum-iridium, the resulting STM images and spectroscopy measurements will reflect the features of the density of states of the sample.

Obtaining an atomically sharp tip is one of the most intriguing parts of STM experiments. Atomic resolution images are certainly obtainable with STM tips made by etching or tearing a thin metal wire. Roland Wiesendanger gave a very insightful comment in his research group homepage [15]:

> *"Imagine pouring a bucket of sand on the floor. If you examine the resulting conic heap in most cases you will find a grain of sand that represents the outermost peak. Very seldomly you will have several grains exactly representing the peak together. Now take the heap of sand for the tip and remember the exponential decay of the tunnelling current. The tunnelling current is carried and the sample surface will be scanned only by this outermost grain of sand... sorry: atom."*

His analogy is a very concise elucidation on why it is possible to make atomically sharp tips with relatively simple methods.

1.1.5 Imaging mode

There are two modes of operation of STM for acquiring different information: constant current imaging (CCI) mode and constant height imaging (CHI) mode. These two modes are suitable for different topographical conditions and different scanning speeds.

Constant current imaging (CCI)

Constant current imaging (CCI) mode is the first and most widely used mode of STM operation as shown in Fig. 1.5. In CCI mode, the feedback loop is activated and it adjusts the tip vertical position during scanning by applying an appropriate voltage U_z to the z piezoelectric drive so that the tunnelling current is kept constant. The lateral tip position (x,y) is controlled by the computer. Depending on the local "topographical" property (actually the local electrical property), the applied voltage U_z can be different from different points on the surface. As the tip is scanned over the surface, the signal U_z is recorded by the computer. As the voltage – displacement sensitivities of the x, y, and z piezoelectric drives are known, the recorded signal, $U_z(U_x, U_y)$, can be interpreted into the topography z(x, y).

The main inconveniences of the CCI mode are the scanning speed and data acquisition time which are limited by the finite response time of the feedback loop. The CCI mode cannot image faster than the feedback can respond.

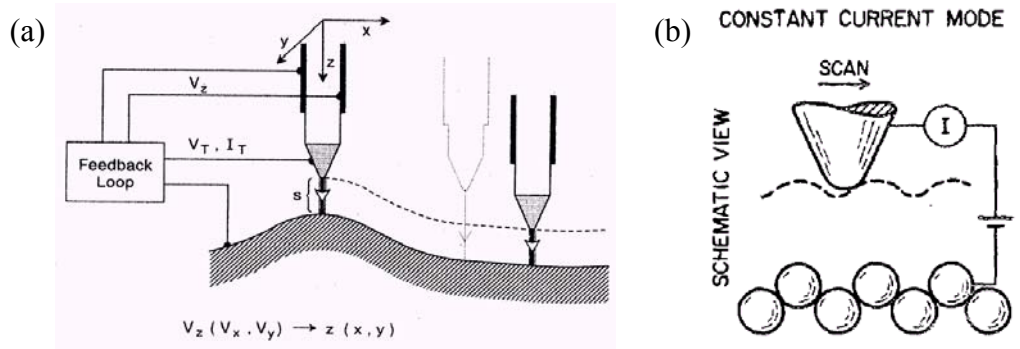

Fig. 1.5. Constant current imaging mode of the STM. Images reprinted from [16] and [17].

Constant height imaging (CHI)

To do fast scanning, constant height imaging (CHI) mode is employed (Fig. 1.6). In CHI mode, the feedback loop is switched off and the tip can scan over the sample surface

very quickly. Since there exists an exponential dependence of the tunnelling current on the tip-sample distance, so the modulation of the current due to the sample surface can be regarded as the atomic-scale "topography" provided that the response time of the tunnelling current preamplifier is fast enough to handle the scan speed.

The main advantage of CHI mode lies in the fact that it is possible to acquire STM images at real-time video rates. Moreover, STM is less susceptible to low frequency disturbances and noise in CHI mode.

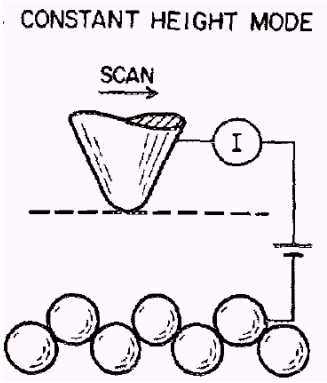

Fig. 1.6. Constant height imaging mode of the STM. Image reprinted from [17].

However, in CHI mode, the vertical height (z position) information is not directly available. Also, CHI mode is only applicable when the sample surface is atomically flat and the features' heights must be smaller than the tip-surface distance, otherwise, the tip will crash into the sample.

1.1.6 STM spin detection

Spin, as an intrinsic property of an electron, has long been the target of detection for various purposes and by a diversity of means. The ability to detect a single electron spin has applications in nanoscopic spin electronics, quantum information processing, and imaging of single free radical organic molecules, where individual spins are considered as carriers for quantum information. A variety of techniques are available for spin detection.

Electron spin resonance (ESR) is a branch of spectroscopy in which electromagnetic radiation (usually of microwave frequency) is absorbed by molecules, ions, or atoms possessing electrons with unpaired spins. ESR has been the conventional spin detection method for chemists for more than half a century with sensitivity of 10^{12} spins at room temperature, and 10^{7} spins as recently reported with more advanced imaging probe design incorporating advanced resonators and highly efficient gradient coils [18]. Another technique

is magnetic resonance imaging (MRI). First developed in 1973, MRI provides a non-invasive tool for three-dimensional imaging of subsurface structures, which relies on the principle that different nuclei have different relaxation rates for their spins and thus rendering contrast. The spatial resolution of this technique is limited by the smallest volume that contains sufficient nuclear or electronic spins (the current limit is 10^{12} nuclear spins [19]) to contribute a detectable signal.

In the respect of single electron spin detection, a single electron paramagnetic spin centre in the gate oxide of a silicon transistor was sensed by electrical means based on the principle that the spin orientation is converted to electric charge, which is measured as a change in the source/drain channel current [20]. In this way, the spin orientation, converted to electric charge, can be sensed by looking at the source/drain current in an FET transistor. Moreover, electrical single-shot measurement of the state of an individual electron spin was demonstrated in a semiconductor quantum dot [21]. The spin measurement is implemented with the initial spin-to-charge conversion, followed by charge measurement in a single-shot mode. A quantum point contact (QPC) in the tunnelling regime is located neighbouring the dot, and the current of the QPC is very sensitive to the electrostatic potential. Recording the changes in the current of the QPC thus reveals the original spin state of the charge. It was also demonstrated that single spin states can be detected by optical spectroscopy [22-24]. Magnetic resonance transitions for the spin state of a single molecule were optically detected [23, 24]. The spin state of a nitrogen-vacancy defect centre in diamond was also sensed by optical means [22]. Recently, the successful combination of the three-dimensional magnetic resonance imaging (MRI) with the excellent force sensitivity of atomic force microscopy (AFM) opens up the path towards the technique of scanned-probe MRI with much improved spatial resolution and sensitivity. Rugar *et al.* demonstrated the integration of MRI and AFM to achieve spin detection with sensitivity down to a single electron spin, a technique named magnetic resonance force microscopy (MRFM) [25].

In addition to imaging and spectroscopy measurements, the STM is capable for electron spin detection as well. Spin-polarized STM, making use of a magnetic tip, can map out the magnetic orientations on a sample surface at the atomic scale. Single electron spin detection STM is sensitive to the existence of a single electron spin by extracting the high frequency signal inherited in the tunnelling current which is the fingerprint of an electron spin.

1.1.6.1 Spin-polarized scanning tunnelling microscopy (SPSTM)

The rapid development of high-density magnetic data storage devices motivates scientists to establish a high-resolution magnetic imaging technique in order to image the magnetic structure of the sample with decreasing size. Spin-polarized STM (SPSTM) was developed to do magnetic imaging at the nm scale and below [26-28]. SPSTM is basically a normal STM but with a magnetic tip [29, 30]. The principle behind its operation is the detection of the local magnetization of the surface below the apex of an STM tip by utilizing spin-dependent tunnelling. Combining the high lateral resolution of STM with the magnetic sensitivity of the magnetic tip, SPSTM is successful in imaging surface magnetic domain structures of bulk material as well as thin films and nanostructured systems.

In normal STM, we only consider the tunnelling current dependence on the tip-sample distances, the local barrier height ϕ and the applied bias voltage V. In SPSTM, we also take the spin of the tunnelling electrons into account and consider the additional spin-dependence of the tunnelling current if magnetic electrodes are involved:

$$I = I(s, \phi, V, \uparrow) \qquad (1.14)$$

This spin-dependence property of tunnelling current can be applied in STM imaging to obtain magnetic contrast for different magnetic regions on sample surface. We need a highly efficient source or detector for spin-polarized electrons as the tip sensor. Ferromagnetic materials, for example, Fe, Ni and Co, or antiferromagnetic materials, such as Cr, are suitable tip materials for SPSTM. Ferromagnetic tips may perturb the magnetization of samples, so antiferromagnetic tips are better because they will not perturb sample magnetization while still provide spin-polarized current. SPSTM imaging can be carried out either with or without an applied external magnetic field.

Spin-polarized STM can operate in constant-current imaging mode and spectroscopy of the differential conductivity dI/dV mode. The potential of SPSTM was demonstrated on antiferromagnetic transition metals (Cr, Mn) [26-28], ferromagnetic transition metals (iron nanostripes, iron islands) [29, 30], and rare earth metals (Gd) [31]. The magnetic structure of the Cr(001) surface was resolved which shows the neighbouring terraces on the Cr(001) surface exhibiting a magnetization in opposite directions [27, 28]. Atomic spin-resolution on a two-dimensional antiferromagnet was accomplished with Mn on W(110) where adjacent Mn atoms at nearest-neighbour sites have magnetic moments with opposite directions on the non-magnetic W(110) substrate [26]. Iron on W(110) was studied and the orientations of different magnetic domains were exhibited on the iron nanostripes and iron islands [29, 30].

The rare earth metal, gadolinium (Gd), which is ferromagnetic, was deposited onto a W(110) substrate, and the magnetization of the Gd island was spatially resolved [31]. Tips play an important role in SPSTM measurements, as an appropriate orientation of tip magnetization can maximize the effect of spin tunnelling. Usually, an iron-coated probe tip has its magnetization axis in plane whereas a W tip coated with Gd is perpendicularly magnetized.

1.1.6.2 Single electron spin detection STM technique

When a dc magnetic field is applied in a STM system, the electrons in the spin centres (e.g. free radical organic molecules) acquire a torque and precess at the Larmor frequency (ν_L). The tunnelling current passing through the spin centre is modulated at radio-frequencies (RF) by the spin precession (the theory behind this is still not well developed). Such RF frequency is related to the sample's g-factor and the applied magnetic field B, in the way that $\nu_L = g\mu_B B/h$, where μ_B is the Bohr magneton, and h is the Planck constant. Only surfaces with single electron spins give such a signal. Therefore, by using a spectrum analyzer to detect this RF signal, we can locate single electron spins on sample surfaces, determine the coupling between spins and surfaces and obtain local spectroscopic information.

This STM technique, which exhibits the existence of an electron spin centre through the observation of high frequency modulation of the tunnelling current while the STM tip is tunnelling through an object with an unpaired electron, was first named as scanning tunnelling microscope – electron spin resonance (STM-ESR) technique, as it was believed to be physically related to the electron spin resonance phenomenon. However, the complete physical mechanism of this technique is still uncertain. Therefore we prefer to use "single electron spin detection STM" to denote such a technique, although in the literature it is more frequently recognized as "STM-ESR" or "ESR-STM".

Fig. 1.7 shows the experimental setup for doing STM-ESR experiments. It consists of an STM system incorporating some additional equipment for splitting the tunnelling current and detecting the RF signal.

1. To make the electron spin precess, an externally applied magnetic field is necessary. This field is provided by a magnet that is placed near the sample.
2. There is a current splitter (bias tee) to split the tunnelling current into two pathways: one goes to a 50 Ω impedance-matched RF amplifier which will amplify the signal for the spectrum analyzer, and the other goes to a high-gain current-voltage converter for the

STM system.

3. A spectrum analyzer with frequency range up to 3 GHz is used to detect the RF signal.
4. A hall probe is used to measure the magnetic field at a sample surface

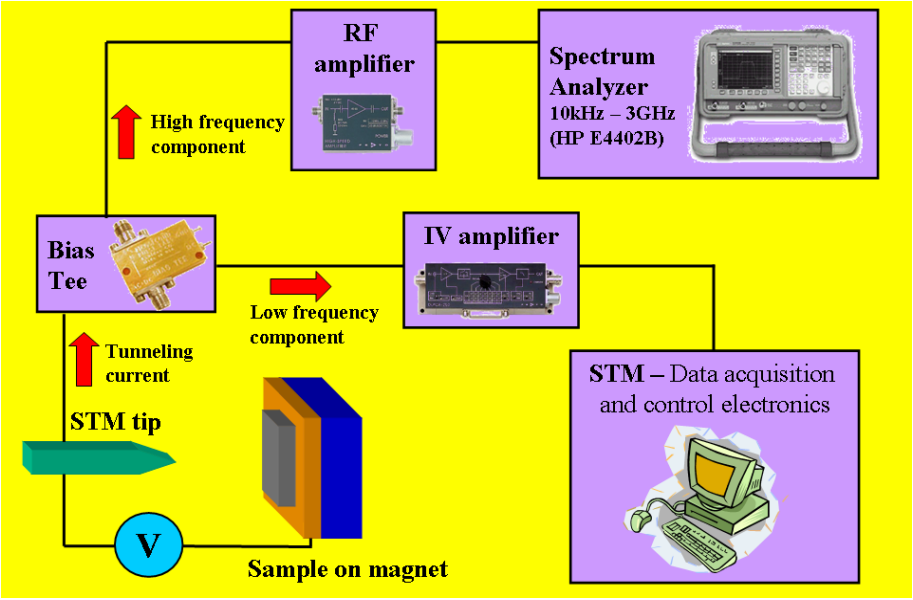

Fig. 1.7. Schematic of the STM-ESR system

1.2 Application of STM on surface science

1.2.1 Equipment

1. easyScan STM

At the initial stages of a research project concerning STM, some basic training on STM would enable a beginner in the field to understand and become familiar with the functionalities and limitations of a STM. To this end, the commercial easyScan STM (Fig. 1.8) by *Nanosurf* [32] is a sufficient teaching tool to learn the fundamentals of STM. The easyScan system is compact and easy to use. All the control electronics are packed into a single control box, and a vibration isolation system comes with the scan head set. The software for scanning is user-friendly and can carry out most of the functions of a normal STM. The easyScan system works in air and atomic resolution is possible with graphite. The maximum and minimum scan sizes of the easyScan STM are about 700 nm and 2 nm respectively.

2. Home-made STM

After sufficient practice with the easyScan system, another STM (Fig. 1.9) home-made by our research group for ultrahigh vacuum (UHV) experiments, which was the first prototype of our UHVSTM, was used for further practise. The scan range of this STM is wider and can cover about 2000 nm size, and it is equipped with a wobble stick as the manipulator. Graphite and gold (gold on mica purchased from SPI Supplies [33]) were scanned with this STM in air. Although the practise was carried out in the ambient conditions, the manipulator was used for loading samples and tips during the training to simulate the UHV working environment.

3. Omicron STM/AFM

This is an ultrahigh vacuum STM/AFM combined system by Omicron Nanotechnology GmbH. As it has both the functionalities of STM and AFM, this system is a versatile scanning probe microscope for many different types of samples, ranging from non-conducting to conducting, and from hard to delicate soft surfaces. It combines various STM and AFM measurement modes including contact mode AFM with simultaneous lateral force (friction) detection and non-contact mode AFM in a single instrument. In STM mode, it

provides a scan range (X x Y x Z) of around 4 x 4 x 1 μm^3. The vacuum level achievable is 10^{-11} mbar range. The system is equipped with in-situ heater, e-beam evaporator, and ion sputtering.

4. Tips

Chemically etched tips and mechanically cut tips were used in the scanning. The chemically etched tips were tungsten wire etched with sodium hydroxide solution, and the mechanically cut tips were cut with shear force by a cutter. Although chemically etched tips are more generally used, we found that the successful rate of mechanically cut tips is high, about 90% in our experience. It is convenient and economical time-wise to use mechanically cut tips, but they tend to be more likely to consist of multiple mini-tips. The chemically etched tips, due to their more uniformly shaped formation, have a more consistent shape and are less likely to have the multiple tip effect, though their successful rate is lower.

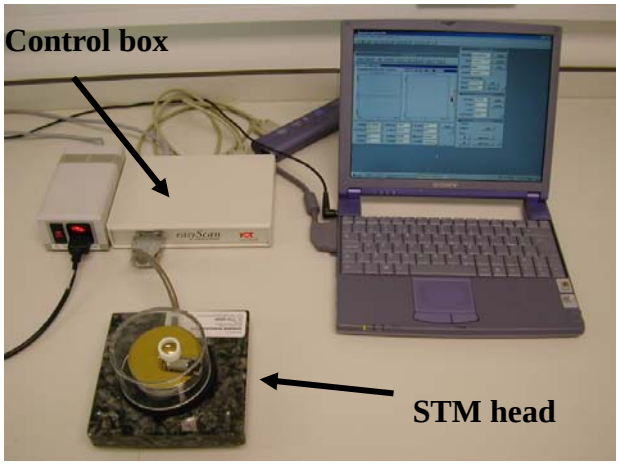

Fig. 1.8. easyScan STM system.

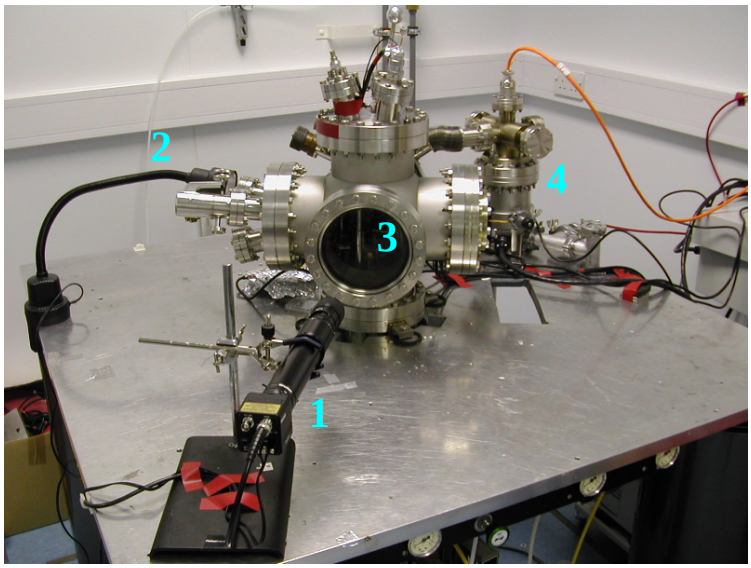

Fig. 1.9. Home-made STM system. (1) Telescope, (2) illuminator for visibility inside the chamber, (3) STM system, and (4) turbomolecular pump.

1.2.2 Application of STM on layered material – graphite (Figs. 1.10 – 1.22)

Layered materials contain many properties which make them exceptionally good for the application of scanning tunnelling microscopy. Since layered materials are composed of layers bound together by weak van der Waals forces, they can be easily cleaved to provide atomically flat terraces of up to several hundred nanometres which is ideal for atomic resolution STM imaging and serving as substrates for deposition of species for STM study. Moreover, dangling bonds are not created by cleavage on layered materials and thus a freshly cleaved surface may stay clean for a long time which enables atomic resolution imaging under ambient conditions. Layered materials are usually soft and this increases the influence of tip-sample interaction forces, leading to the observation of giant corrugation of the atomic lattice.

Graphite is the most extensively studied surface by STM. As atomic resolution imaging is possible in air on graphite, its atomic lattice acts as a standard testing tool for STM calibration. Graphite is made up of layers with a honeycomb structure of carbon atoms bonded together covalently. The nearest-neighbour distance is 1.42 Å, the in-plane lattice constant is 2.46 Å and the interlayer spacing is 3.35 Å. For hexagonal graphite, there is a relative shift between alternate layers, resulting ABAB… stacking sequence, and a C axis lattice constant of 6.7 Å perpendicular to the layers. As such, a graphite layer is actually composed of two sublattices: one sublattice (α-site) has its atoms located directly above an atom in the next layer, whereas the other sublattice (β-site) has its atoms located above the hollow site of the sixfold carbon ring in the second layer.

The preparation procedures for imaging in air and UHV conditions for graphite are the same. The sample surface is cleaved with a razor or adhesive tape. Depending on the quality of the graphite, the sample is stable from several minutes to days. Atomic resolution is usually possible for several hours. The HOPG graphite was purchased from Agar Scientific Limited [34].

1. Large scan size (100nm – 1000nm) on graphite (Figs. 1.10 – 1.15)

For this scan range, we can see a few steps on the graphite surface. Some of these steps are more than 1nm in height, and thus are multiple steps. In Fig. 1.11, the step edge is not very sharp in the image and it looks like there are two lines together. This is probably because of the artifact of double tip. Step edges are the most commonly observed surface features of graphite; occasionally, a superlattice structure, which has a superperiodic hexagonal lattice, can also be observed nearby steps or defects.

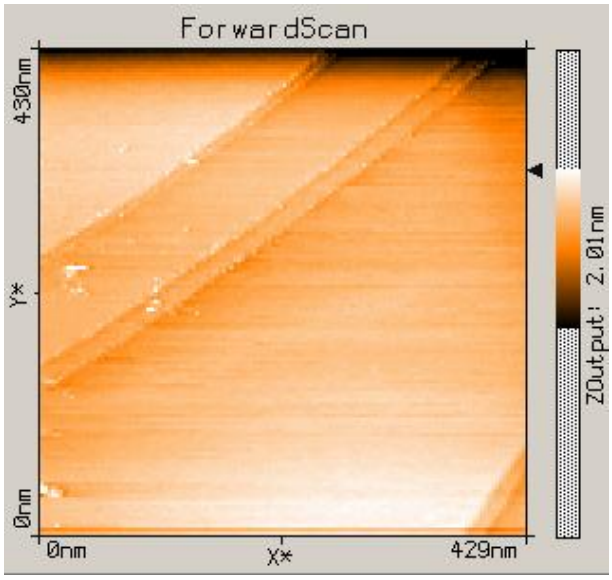

Fig. 1.10. Image size: 430nm x 430nm (I_t = 1.095nA, V_t = 0.065V, easyScan STM).

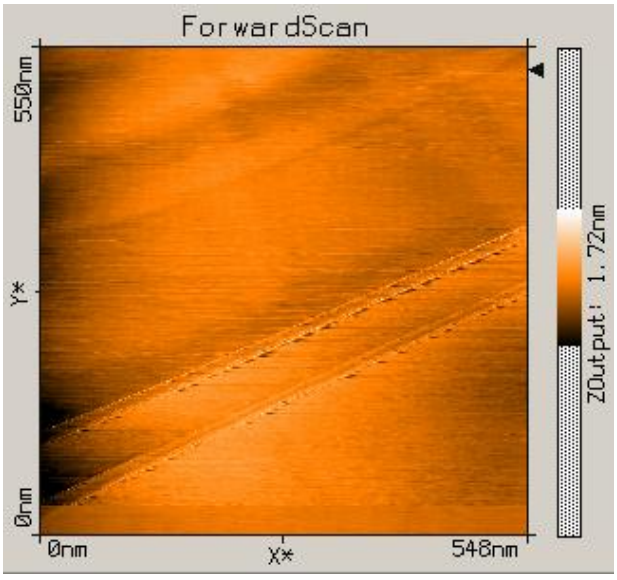

Fig. 1.11. Image size: 550nm x 550nm (I_t = 1.001nA, V_t = 0.050V, easyScan STM).

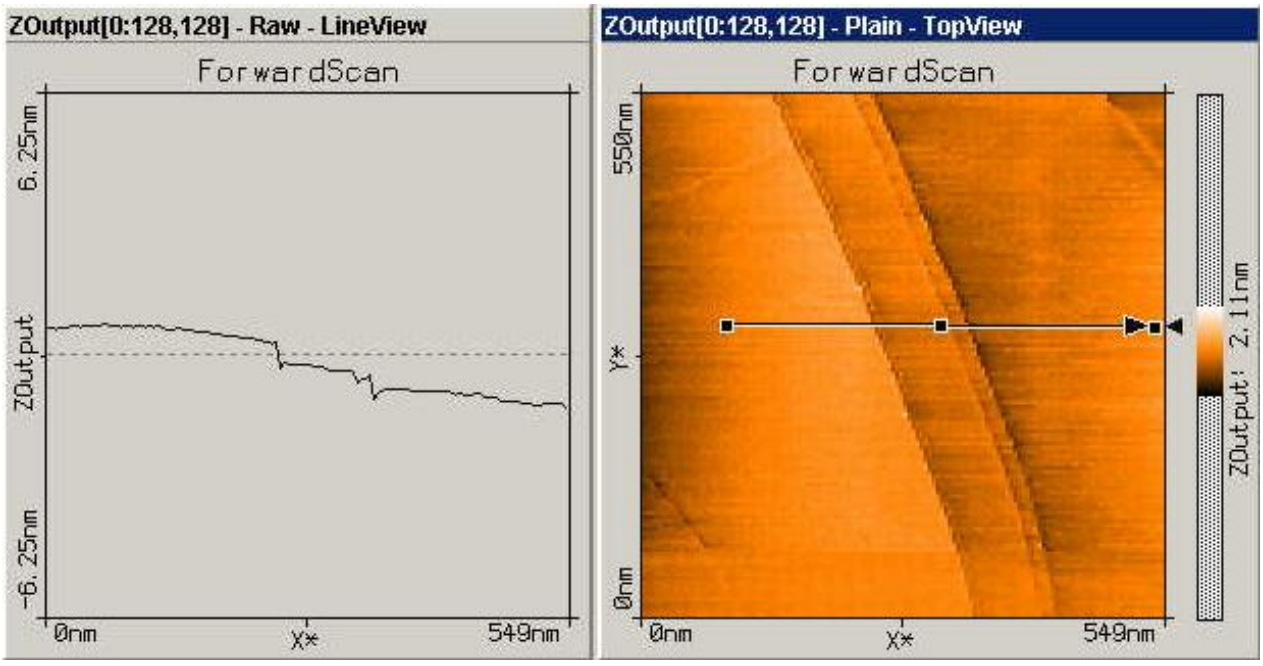

Fig. 1.12. Image size: 550nm x 550nm (I_t = 0.095nA, V_t = 0.065V, easyScan STM). The left graph shows the topographic cross-section of the black arrow in the image on the right.

Fig. 1.13. Image size: 500 nm x 500 nm (I_t = 0.5 nA, V_s = 206 mV, home-made STM). On the top right corner, a piece of graphite layer is peeled off and exposing the underlying layer on which a superlattice structure can be observed. Graphite superlattices will be discussed in detail in chapter 3.

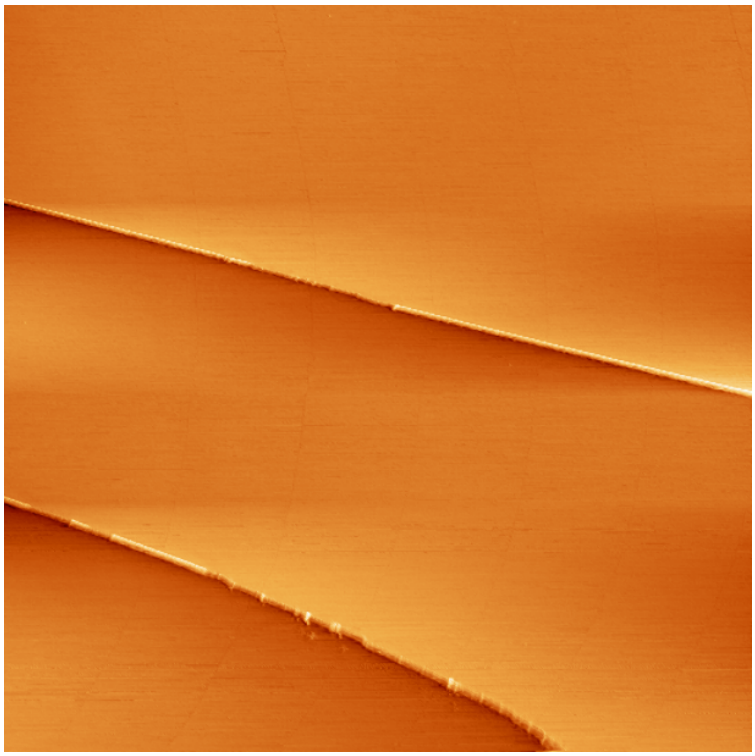

Fig. 1.14. Image size: 1000 nm x 1000 nm (I_t = 0.3 nA, V_s = 250 mV, home-made STM). Graphite step edges are visible.

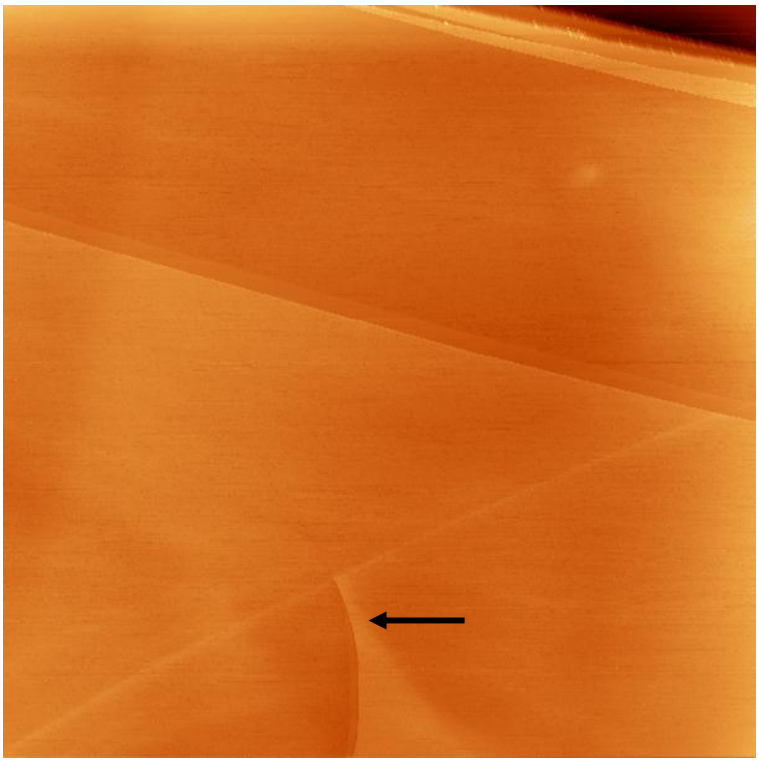

Fig. 1.15. Image size: 1000nm x 1000nm (I_t = 0.3 nA, V_s = 300 mV, home-made STM). Apart from step edges, a screw dislocation can be seen (indicated by the arrow).

2. Atomic scan size (less than 20nm) on graphite (Figs. 1.16 – 1.22)

STM images on graphite surface have displayed a triangular, rather than a honeycomb lattice with the distance between the maxima as observed in the images 2.46 Å, which suggests that only every other carbon atom is imaged by STM. Such an asymmetry reveals the importance of the electronic structure for understanding the observed image contrast in STM. It is well-known that the lattice constant of graphite as observed with the STM is 0.246 nm, instead of the actual physical atomic spacing of 0.142 nm, due to the overlapping of the electronic band at the Fermi level of the α-site atoms with the atoms directly underneath which leads to fewer electronic states at the Fermi level, and thus the STM can only see the β-site atoms which do not have atoms immediately below them. Figs. 1.16 to 1.22 are the STM images on the graphite atomic lattice. Some of the hexagonal lattices are slightly stretched because of thermal drift. Caution must be taken in distinguishing the atomic resolution from periodic noise waveform since they are both sinusoidal in nature in each z-position scan line. The way to determine the actual nature of the signal is by adjusting the scan speed to see if the features scale with the speed. For periodic noise, the periodicity will decrease as the scan speed increases, whereas for genuine lattices of atomic resolution, the image will not scale with the scan speed.

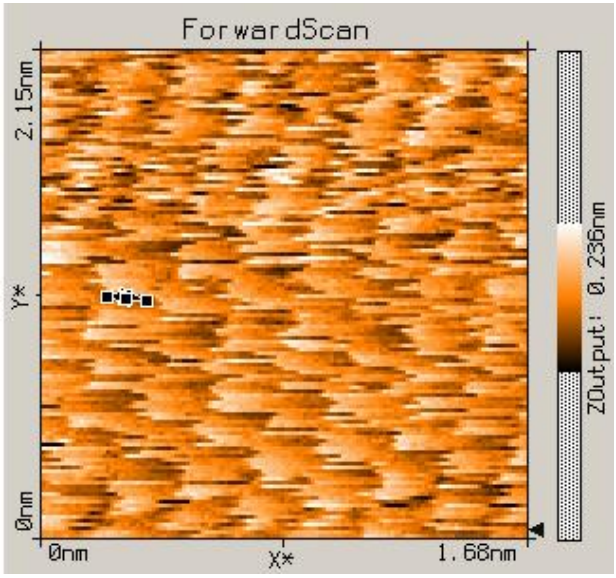

Fig. 1.16. Image size: 1.68nm x 1.68nm (I_t = 1.001 nA, V_t = 57 mV, easyScan STM).

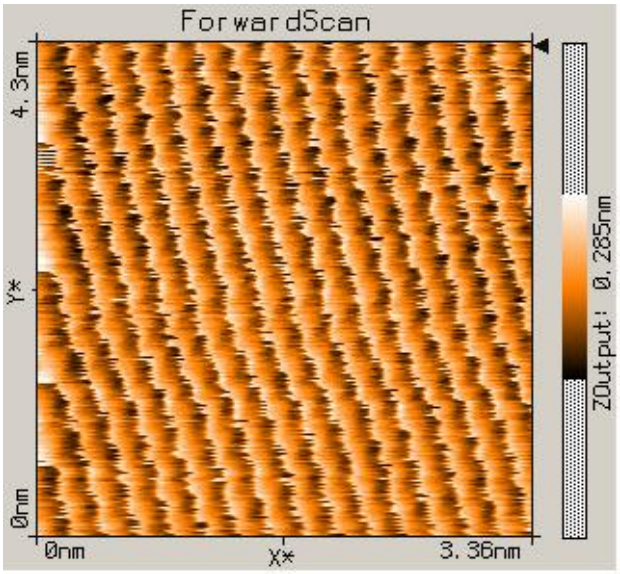

Fig. 1.17. Image size: 3.36nm x 3.36nm (I_t = 1.001 nA, V_t = 50 mV, easyScan STM).

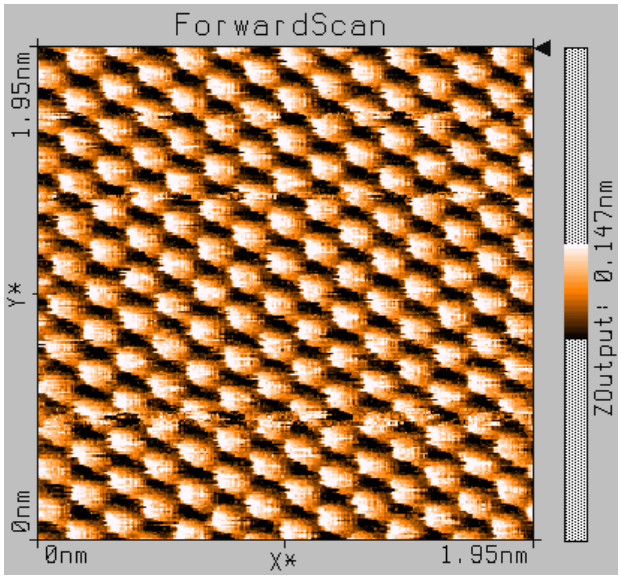

Fig. 1.18. Image size: 1.95nm x 1.95nm (I_t = 1.5 nA, V_t = 15.9 mV, easyScan STM).

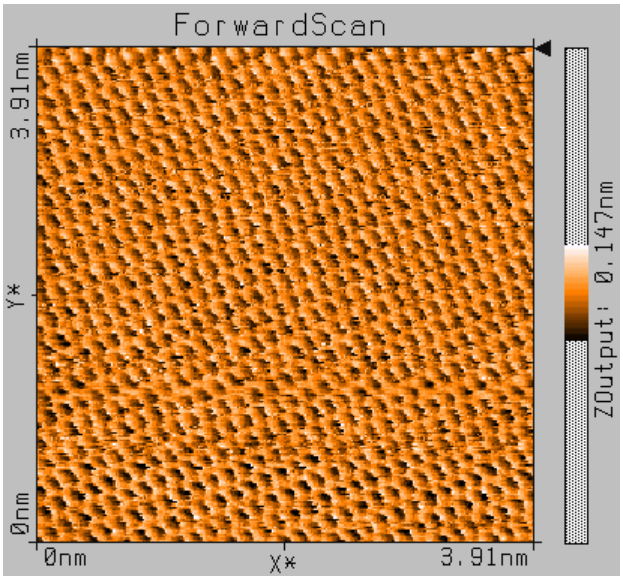

Fig. 1.19. Image size: 3.91nm x 3.91nm (I_t = 1.1nA, V_t = 145 mV, easyScan STM).

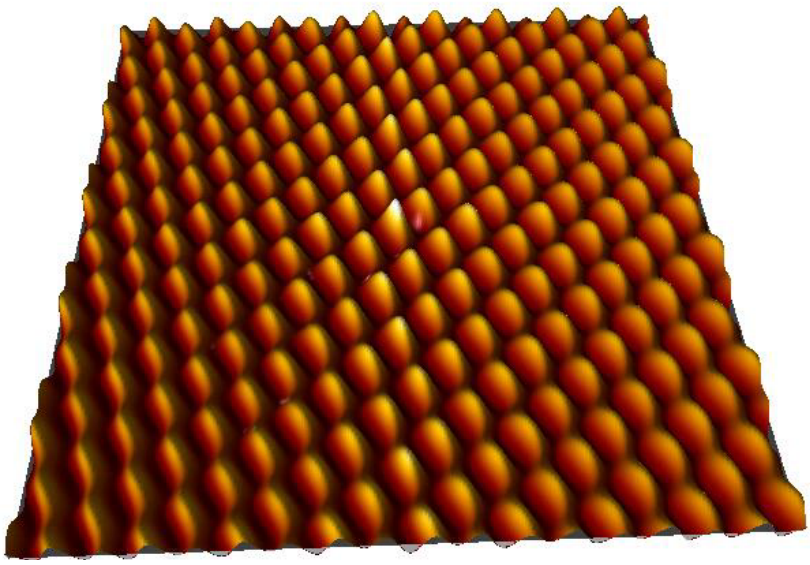

Fig. 1.20. Image size: 3.2 nm x 3.2 nm (I_t = 1.25 nA, V_s = 100 mV, home-made STM). Image processed by self-correlation[1].

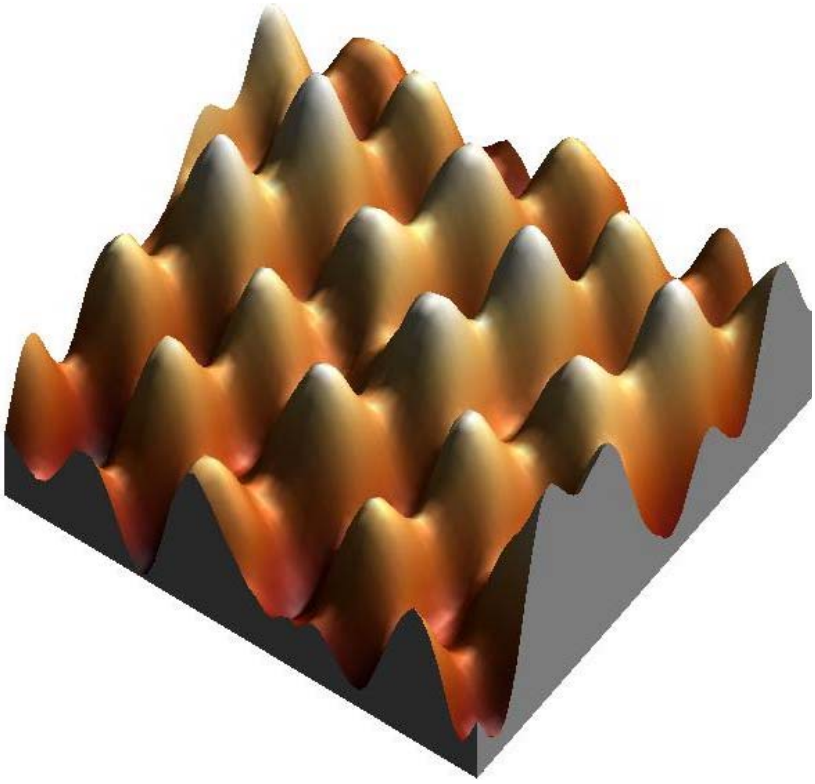

Fig. 1.21. Image size: 1 nm x 1 nm (I_t = 2.01 nA, V_s = 250 mV, home-made STM). Atomic resolution is shown with lattice spacing of 2.46 Å. Image low pass filtered.

[1]Self – correlation filter is defined as: $G(k_1,k_2)=\sum f(x,y)f(x+k_1,y+k_2)$ where f(x,y) is the image matrix. This equation correlates the image and the same image shifted a distance k_1 and k_2 in the X and Y axis with respect to the centre of the image, and the resulting image, $G(k_1, k_2)$, indicates how different the two images are. The more similar the image and the shifted image are, the higher the value of the self correlation. In self-correlation, the highest value is obtained at the centre of the image (where k_1 and k_2 are zero). Any periodicity in the original image will be shown as a periodic pattern in the self correlation.

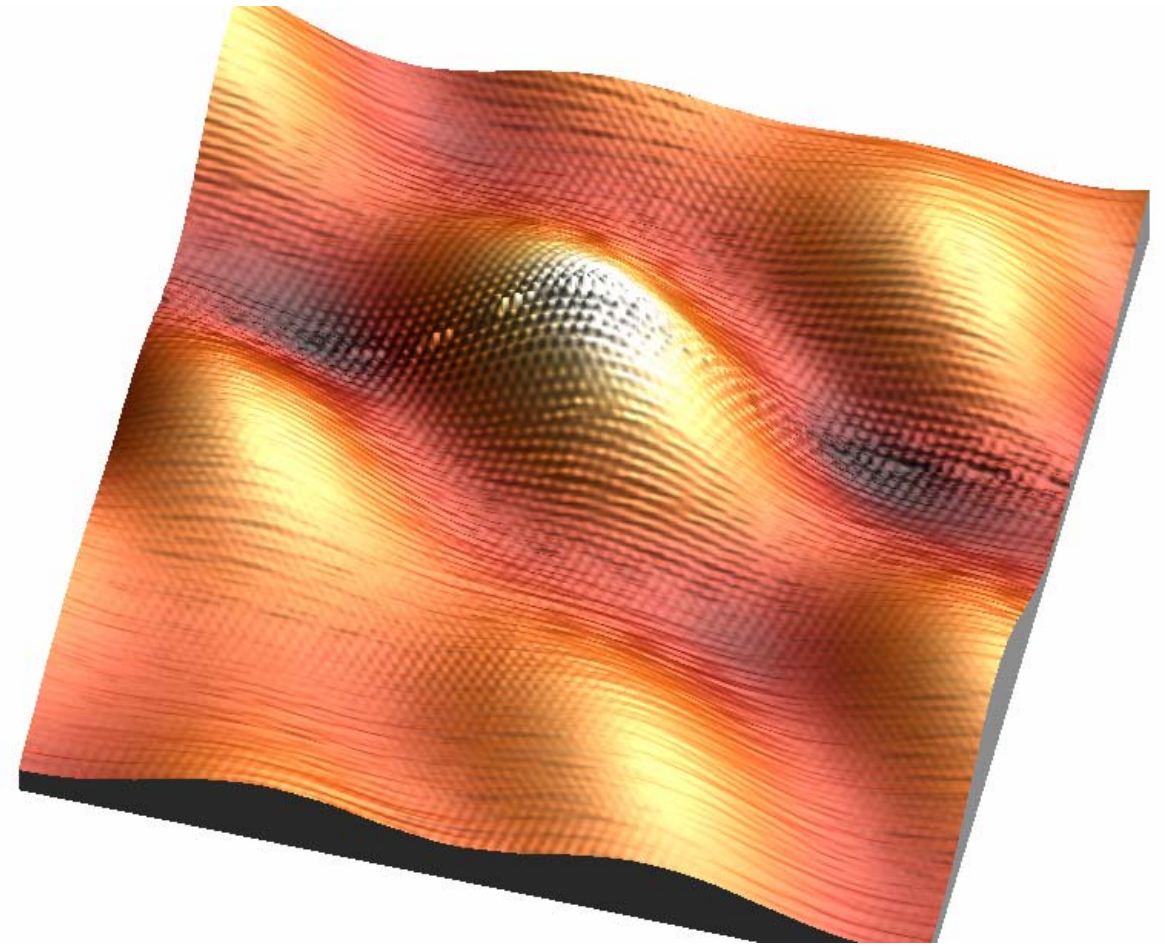

Fig. 1.22. STM image on graphite surface on which a superlattice (larger periodicity) superimposed with the atomic lattice (smaller periodicity) is visible. 15 nm x 15 nm, I_t = 0.36 nA, V_s = 450 mV, by home-made STM, image processed by self-correlation. More explanation on superlattices is given in chapter 3.

1.2.3 Application of STM on metal – gold (Figs. 1.23 – 1.28)

It is well-known that Au(111) surfaces consist of atomically flat terraces with step edges and pits, and the gold atoms on this plane are aligned at 60°. There exists a long-range superstructure (22 x √3 reconstruction) composed of a correlated periodic bending of the parallel corrugation lines by 120º, often known as "herringbone structure", which is caused by long-range elastic strain favoring an effective isotropic contraction on a larger scale against the locally favourable uniaxial contraction [35]. The measured atomic corrugation of the clean Au(111) surface in constant current STM images is typically of the order of 0.3 Å or below, depending upon the tip-sample distance and the sharpness of the STM tip [35]. The interatomic spacing of gold is 2.88 Å and the monolayer step is 2.5 Å in height. Atomic resolution of Au(111) is difficult to achieve under ambient conditions because of contamination on the surfaces. Pits, steps, terraces, and herringbone structures on Au(111) were observed here. Higher resolution images on herringbone reconstructions and atomic lattices of Au(111) were obtained later with our self – constructed UHVSTM as described in chapter 2.

An Au(111) single crystal surface can be cleaned by repeated cycles of ion sputtering and annealing under UHV conditions. Alternatively, an Au(111) film can be grown epitaxially on a suitable substrate, for example, mica. The gold samples that we used are commercially available gold on mica pieces produced by vacuum deposition. As they are clean and kept in nitrogen filled containers, there are no complicated cleaning procedures associated with them. Once these gold on mica samples are taken out from their containers, they are scanned immediately to minimize the contamination.

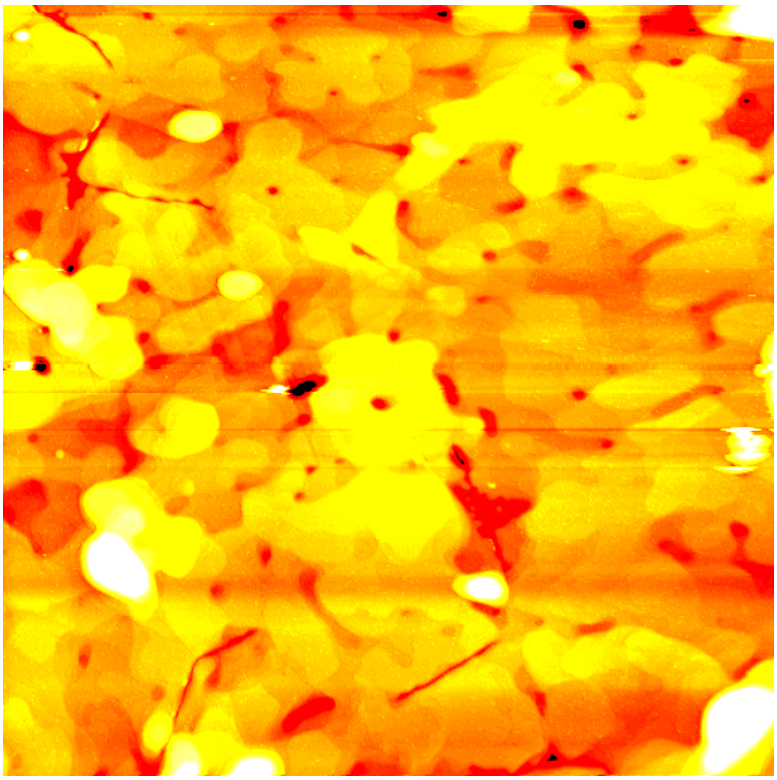

Fig. 1.23. Image on gold on mica, it shows typical Au(111) surface with many terraces. 2200 nm x 2200 nm, I_t = 0.06 nA, V_s = 850 mV, home-made STM. Terraces and steps are visible.

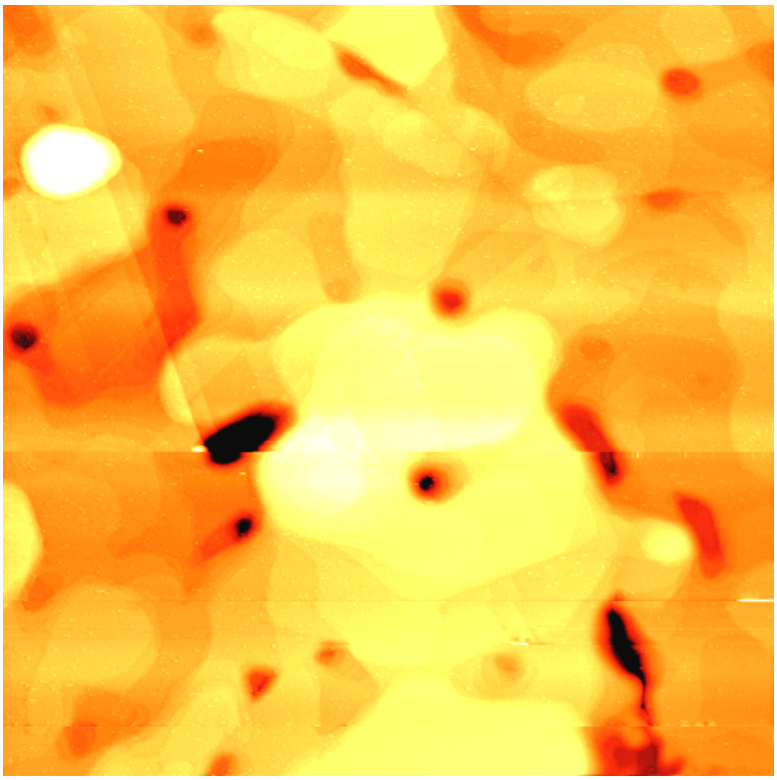

Fig. 1.24. A closer image on Au(111), 1000 nm x 1000 nm, I_t = 0.06 nA, V_s = 850 mV, home-made STM.

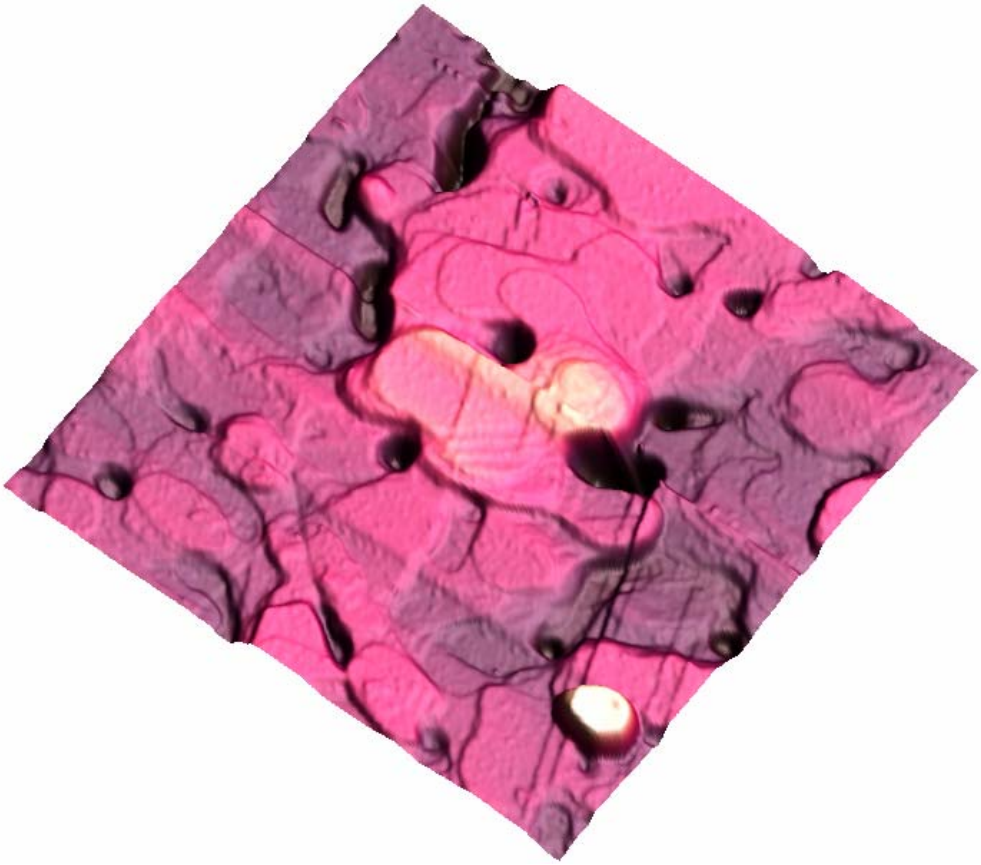

Fig. 1.25. 3D image on Au(111), 1000 nm x 1000 nm, I_t = 0.06 nA, V_s = 850 mV, home-made STM.

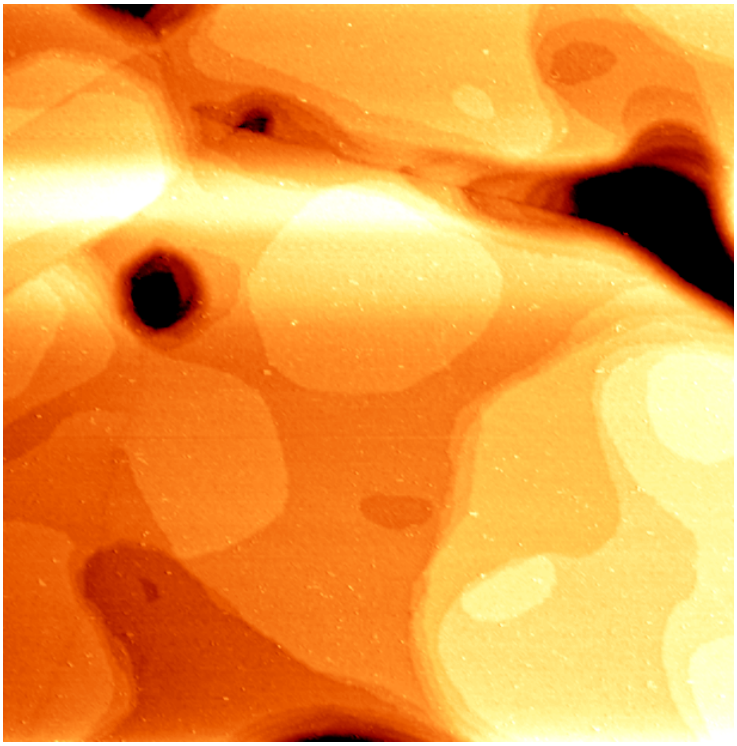

Fig. 1.26. We can see the terraces more clearly in this image. 353 nm x 353 nm, I_t = 0.06 nA, V_s = 850 mV, home-made STM.

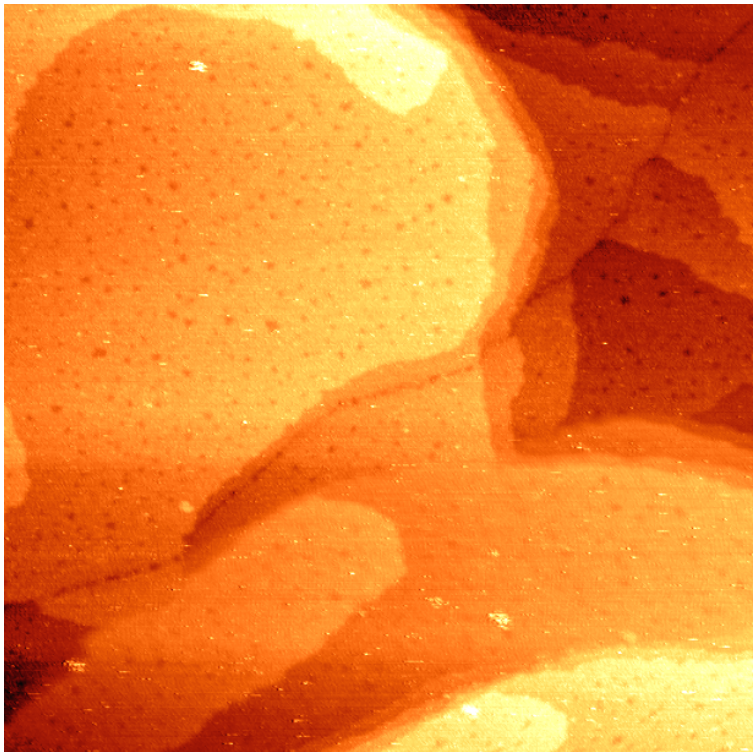

Fig. 1.27. The pits on the terraces are visible in this image. 200 nm x 200 nm, I_t = 0.06 nA, V_s = 850 mV, home-made STM. The height of the steps is about 2.3 Å. The pits are found to be effective in stopping deposited organic molecules diffusing around on the surface. This will be further discussed in chapter 4.1.

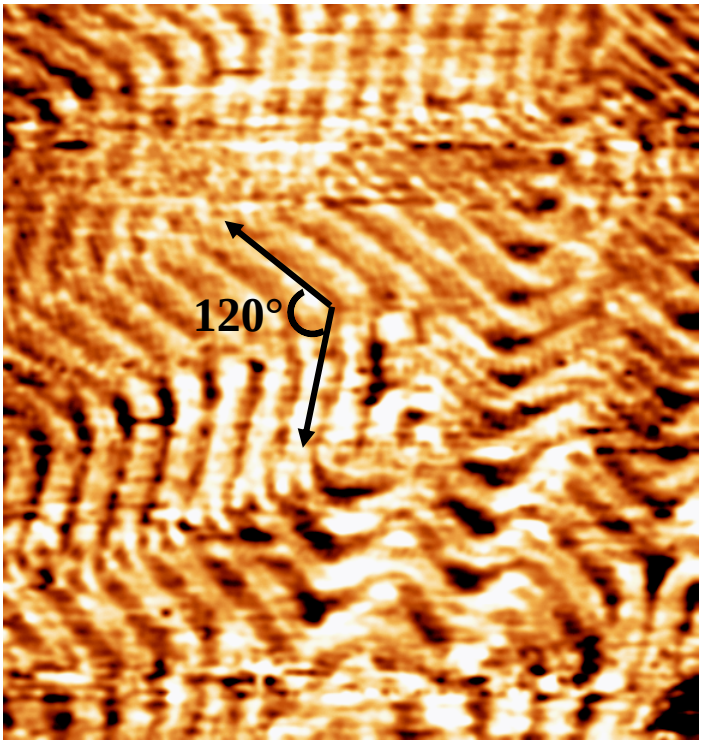

Fig. 1.28. Herringbone reconstruction on Au(111) surface. 113 nm x 120 nm, I_t = 0.7 nA, V_s = -500 mV, Omicron STM/AFM. The corrugations of the herringbone structure are measured as around 0.3 to 0.7 Å. The parallel corrugation lines show a periodic bending of 120°.

1.2.4 Application of STM on semiconductor – silicon (Figs. 1.29 – 1.33)

The STM study of semiconductor surfaces usually exhibits a pronounced bias voltage dependence of the observed images. The maxima in the STM images are generally associated with surface dangling bonds. Depending upon their energy, certain bonds are imaged at some particular sample bias voltage, but not at others. In fact, we can see all these characteristics by imaging on silicon.

The sample preparation procedure for silicon under UHV conditions is more complicated than that of graphite. The 7x7 reconstructed Si(111) surface is prepared by first degassing the sample at 600°C to 700°C. The oxide on the sample surface is then "flashed" off by heating to 1100°C in 1 to 5 seconds under UHV conditions in the 10^{-10} mbar range. The sample is then slowly cooled down at a rate of 10 to 50°C /min so that at about 860°C the high-temperature 1 x 1 surface structure is transformed into the energetically more stable 7 x 7 surface structure. The sample is usually stable for several hours, depending on the vacuum level. A more detailed description of 7 x 7 Si(111) surface preparation is given in chapter 4.2. The STM images on silicon were taken with the Omicron STM/AFM system.

Fig. 1.29 and Fig. 1.30 show the Si(111) 7 x 7 reconstructed surface, revealing 12 maxima of density of states per unit cell (the unit cell is outlined in Fig. 1.31). These maxima are due to the dangling bonds on the adatoms of the 7 x 7 surface structure. Each unit cell consists of 12 adatoms, and each adatom, due to the fourfold coordination of silicon, has three dangling bonds connected with the underlying atomic layer, and one dangling bond free. The dangling bonds on the adatoms are partially filled and therefore contribute to both empty and filled states. The polarity of STM bias voltage does not affect the positions of the observed maxima, which means the maxima of the empty and filled states are spatially coincident. In this light, STM images can directly provide geometric information about the surface atom positions. The missing of an adatom as shown in Fig. 1.30 can thus be interpreted as a point defect on the silicon surface. Although STM images of the Si(111) 7 x 7 surface show directly the adatom positions, STM images obtained with positive sample bias voltage (Fig. 1.29 and Fig. 1.30) are different from images with negative sample bias voltage (Fig. 1.31, Fig. 1.32, and Fig. 1.33). In the images obtained with negative sample bias voltage, there are also 12 adatoms in each unit cell (as outlined in Fig. 1.31); however, the adatoms in the faulted half of the unit cell are higher than those in the unfaulted half. Such a contrast between two halves can be seen in Fig. 1.32, and is clearly visible in Fig. 1.33 after accentuating the image contrast.

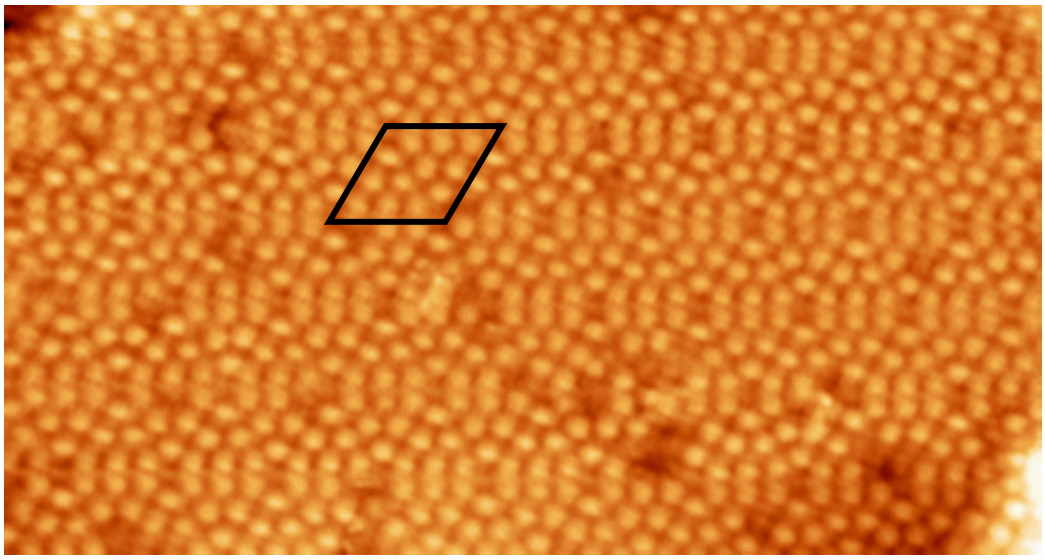

Fig. 1.29. 23 nm x 12 nm image of silicon. I_t = 0.8 nA, V_s = 2000 mV. The 7 x 7 surface reconstruction of silicon is clearly visible. The 7 x 7 unit cell is outlined and the 12 adatoms are observed.

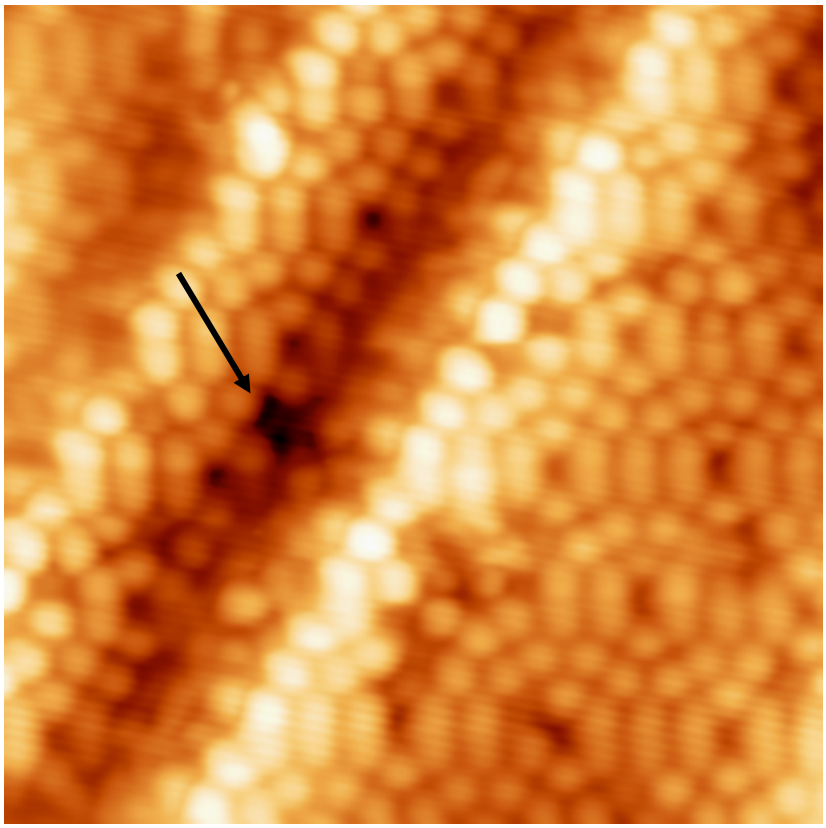

Fig. 1.30. 11.6 nm x 11.6 nm image of silicon. I_t = 1.0 nA, V_s = 2000 mV. The 7 x 7 surface reconstruction of silicon can be seen. There are some defects on the surface, one of them is indicated by an arrow where there is a missing adatom.

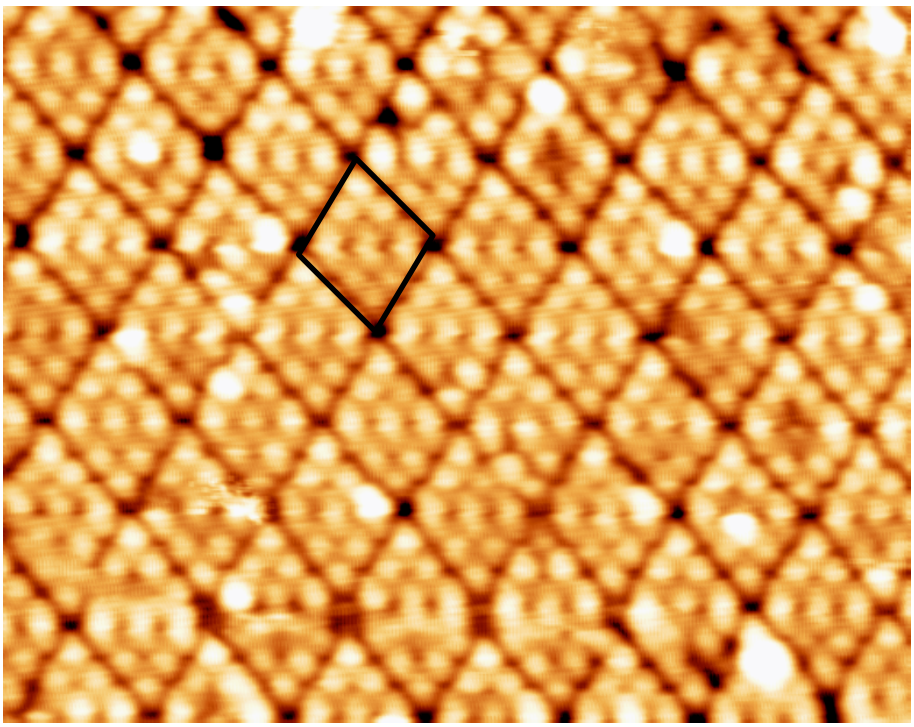

Fig. 1.31. 15.6 nm x 12.3 nm image of silicon. I_t = 1.0 nA, V_s = -2000 mV. The 7 x 7 unit cell is outlined and the 12 adatoms are observed.

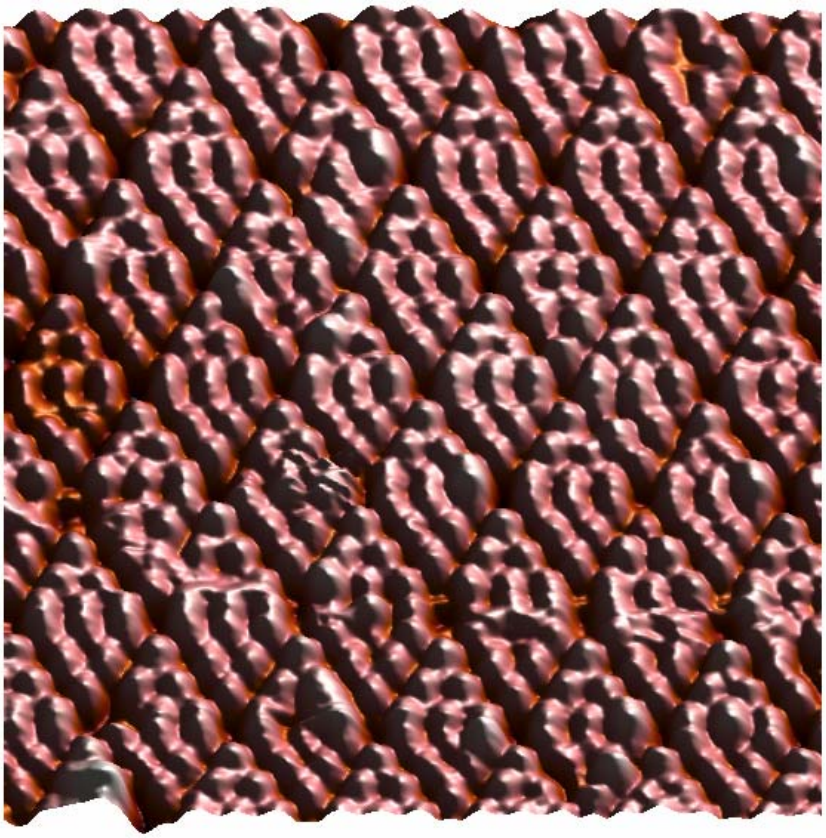

Fig. 1.32. 13.4 nm x 13.4 nm image of silicon. I_t = 1.0 nA, V_s = -2000 mV. The 7 x 7 unit cell is visible, and the fault and unfaulted parts of the silicon surface can be distinguished.

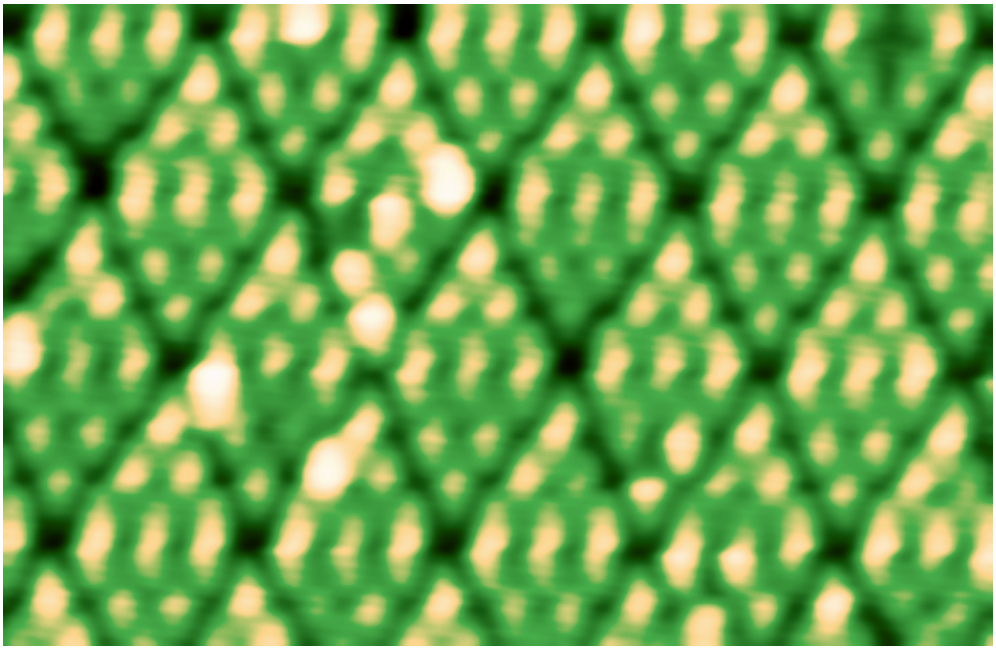

Fig. 1.33. 11.8 nm x 7.7 nm image of silicon. I_t = 1.0 nA, V_s = -2000 mV. This image shows the faulted and unfaulted halves more clearly with the image contrast accentuated. The faulted half of the unit cell appear “higher” than the unfaulted half.

1.3 Conclusion

In this chapter, we have carried out a brief introduction to the STM. Various spin detection techniques are reviewed and compared. We have carried out discussion on the applications of STM on surface science. STM was utilized to study the surfaces of a layered material – graphite, metal – gold, and semiconductor – silicon, and the images obtained were displayed. This chapter gives us a foundation to the following parts of the thesis. In the next chapter, the construction of our ultrahigh vacuum scanning tunnelling microscope (UHVSTM) for overlayers characterization will be described in detail.

Chapter 2

Construction of an ultrahigh vacuum scanning tunnelling microscope (UHVSTM) for overlayers characterization

An ultrahigh vacuum scanning tunnelling microscope (UHVSTM) operating at room temperature has been developed for the purpose of characterizing overlayers on single crystal surfaces at the atomic-level. This system is potentially applicable for future experiments of single electron spin detection via measurement of tunnelling noise at microwave frequencies and spin-polarized STM experiments. The design and construction of this UHVSTM are described in this chapter. Based on a conventional STM, a bias tee, RF amplifier, and spectrum analyzer are integrated into the system for detecting the presence of electron spins. A novel slip-stick mechanism ("walker") which positions the sample and magnet relative to the tip is described. A high-frequency coaxial cable is used to carry the tunnelling current in order to preserve the strength and quality of the spin signal. The supporting frame of the STM provides not only rigidity but also extra shielding for the cabling. We have conducted measurements under both ambient and UHV conditions. The work of this chapter is published in the Conference Proceedings of the 5th International Conference of the European Society for Precision Engineering and Nanotechnology 2005, vol.1, p. 241 – 244.

2.1 Introduction

2.1.1 Motivation

Since its invention in 1982 [3], the STM has been used to study surfaces with atomic spatial resolution, and it is now an indispensable tool in the Nanotechnologist's toolbox. It has opened the pathway to probe surface electrical properties such as the local density of states and conductivity of surfaces with atomic spatial resolution. To take further advantage of this high spatial resolution of the STM, scientists have been exploring the possibilities of extending the territory of STM from measuring electrical properties to the characterization of magnetic systems. The inventions of spin-polarized STM by Wiesendanger [28] and single electron spin detection technique by Manassen [36] have together proved the STM's sensitivity to magnetic properties with ultimate resolution down to single electron spin. Both of these magnetic system characterization techniques with STM involve overlayers on single crystal surfaces, for example, free radical organic molecules were deposited on graphite surfaces to provide spin signal for single electron spin detection, and tungsten crystal surfaces covered by ferromagnetic iron forming a binary magnetic system were studied by SPSTM. In this light, it is very important to be able to characterize overlayers on single crystal surfaces under a clean environment. Such is the motivation of building this UHVSTM which can deposit and characterize overlayers in-situ. The design of this system also enables future experiments of single electron spin detection with STM and SPSTM.

2.1.2 Uniqueness of this UHVSTM

In addition to its functionality as a UHVSTM for characterizing overlayers on single crystal surfaces, this system is constructed in such a way that future magnetic characterization experiments can be conducted on overlayers by SPSTM and single electron spin detection with STM. As such, it is necessary to split the tunnelling current into its DC and microwave components, which implies a conventional STM (i.e. one without microwave-compatible cables) would not fit this purpose; so it was necessary to build a STM with the desired characteristics. The use of a high-frequency coaxial cable to carry the tunnelling current is one of the unique elements of this UHVSTM, the slip-stick walker which carries a sample and enables lateral and rotary movements is the other.

2.2 Construction of UHVSTM

2.2.1 Overall design

The whole UHVSTM system is shown in Fig. 2.1. There are three levels of vibration isolation. The whole STM is situated on an aluminium table supported by four air legs which in turn are placed on a foundation which is separate from the rest of the building. Internally, the STM is suspended by springs with eddy current damping as shown in Fig. 2.2.

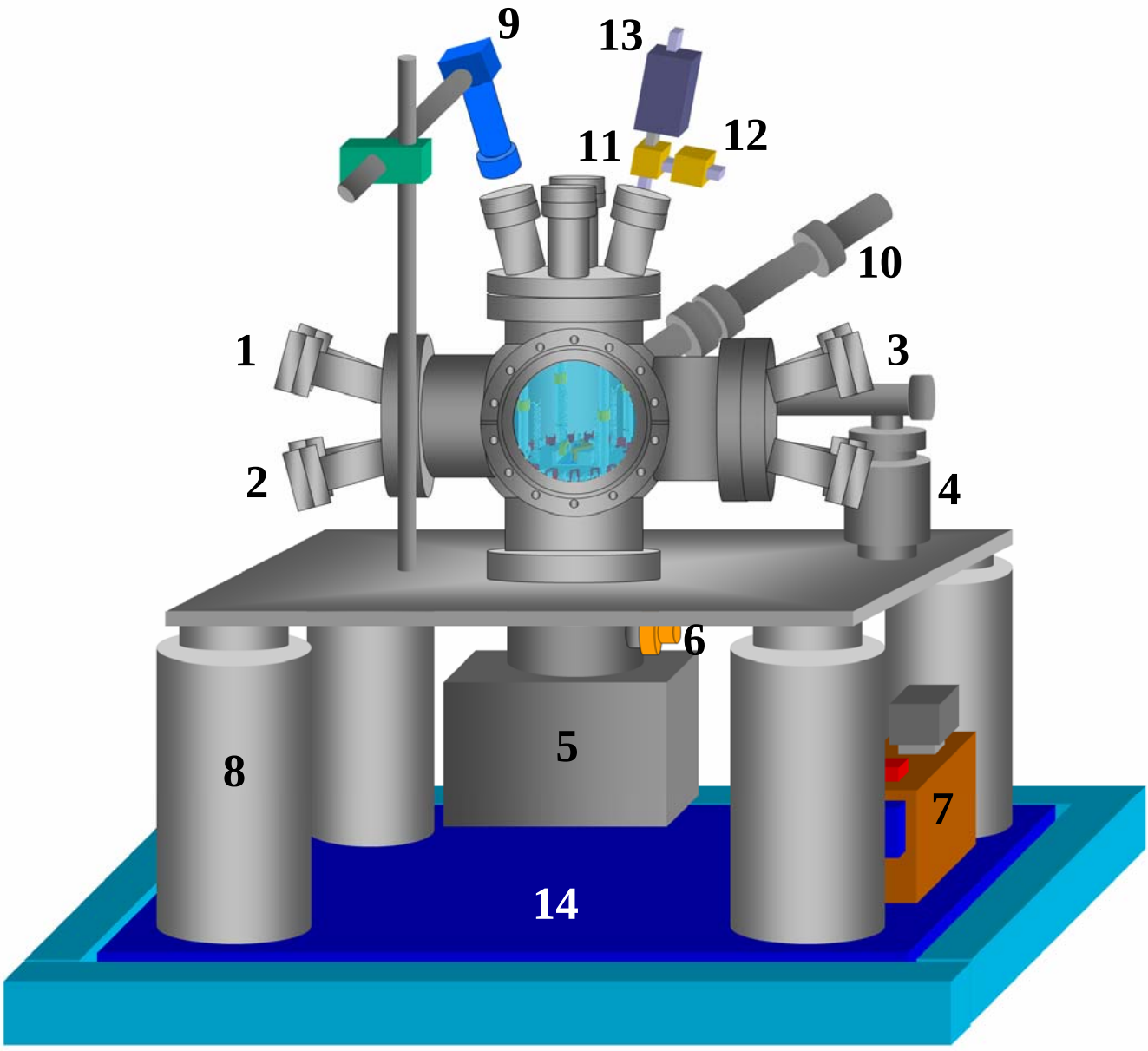

Fig. 2.1. The schematic of the whole UHVSTM system. (1) ion gun, (2) K-cell, e-beam evaporator, (3) quartz crystal microbalance for measuring deposited film thickness, (4) turbo pump, (5) ion pump, (6) titanium sublimation pump, (7) rotary pump, (8) air legs, (9) CCD camera, (10) load lock with magnetic linear rotary drive, (11) bias tee, (12) RF amplifier, (13) IV amplifier, and (14) the whole system is sitting on a separate foundation.

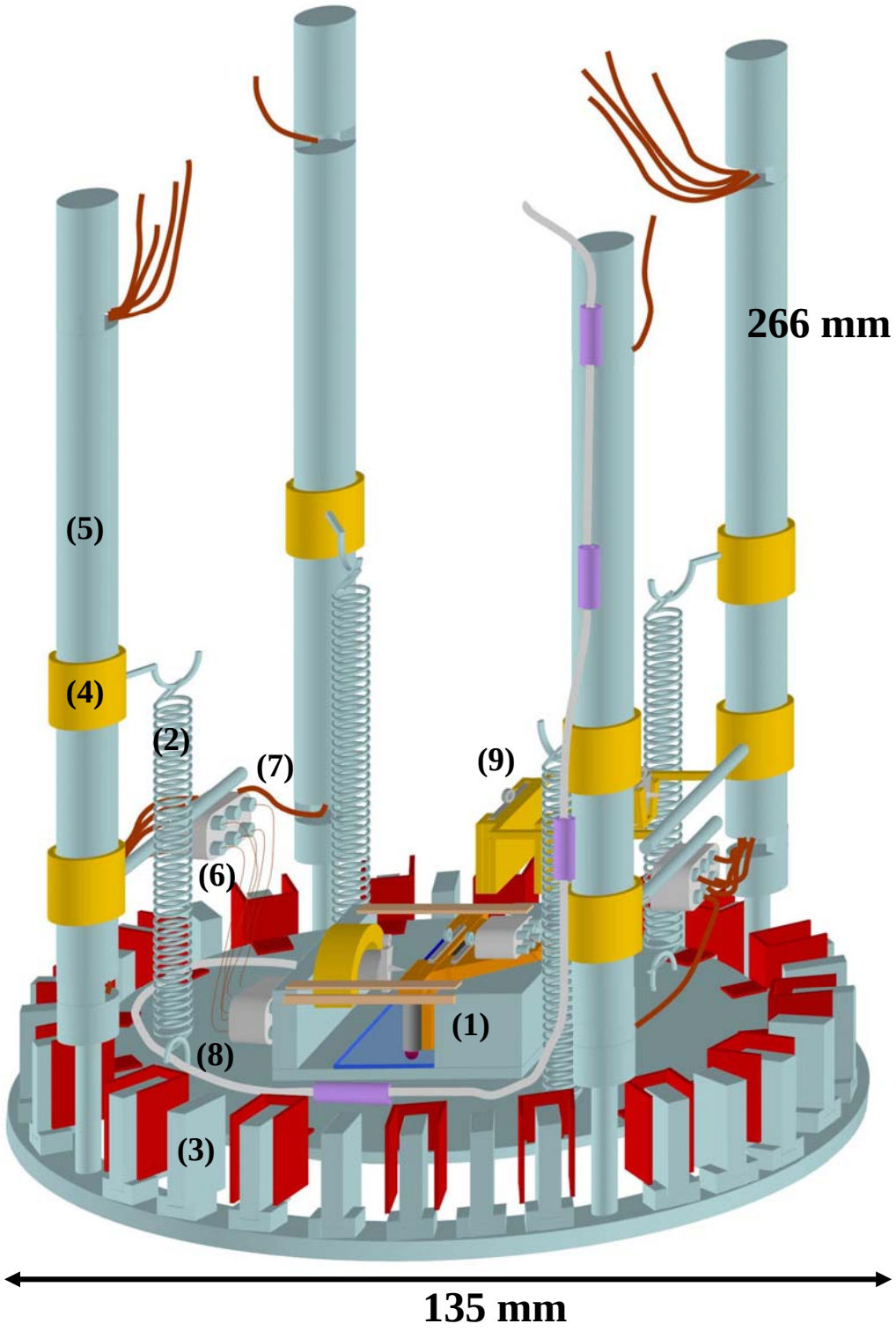

Fig. 2.2. Inner and outer stages of the STM. The STM scanning head (1) is situated on top of the inner stage. The inner stage is suspended by four springs (2) with eddy current damping (3). The levels of the collar rings (4) on each of the supporting rods are adjustable. The supporting rods (5) are hollow inside with slit openings near the top and bottom for the wires to pass through, offering extra electrical shielding. The electrical connections between inner and outer stages are established with 30 μm wires (6) for vibration isolation, whereas the connections from the outer stage to the electrical feedthroughs are done by 0.213 mm wires (7). The high-frequency coaxial cable (8) is used for carrying the tunnelling current. The storage rack (9) which can hold two samples and two tips is attached to the supporting rod.

In addition to a STM, the system is equipped with: an ion gun for sputtering; a K-cell (WA Technology, United Kingdom) for in-situ deposition of molecules onto substrates; an e-beam evaporator for in-situ deposition of materials onto tips and substrates; a bias tee and a radio frequency (RF) amplifier for splitting the tunnelling current into its low frequency and high frequency components, the latter of which is amplified, and can indicate the presence of a spin centre in the future single electron spin detection experiments. The tunnelling current is carried by a high-frequency coaxial cable (Filotex, USA) with maximum operating frequency of 3 GHz and impedance of 50 Ω in order to preserve the high frequency electron spin signal inherited in this current which is important for future single electron spin detection.

2.2.2 System design (1) - vibration isolation

2.2.2.1 Design consideration

Vibration isolation is one of the most important issues for STM imaging. Vibration from the building or acoustic noise can rule out atomic resolution imaging [37]. For example, if high-resolution is desired, a vertical resolution of 0.1 Å is necessary. This means the stability of the tip-sample distance should be maintained at a level of better than 1 pm. This is about six orders of magnitude smaller than typical floor vibration amplitudes (0.1 – 1 μm). Such high requirement of stability can be accomplished by a combination of an effective vibration isolation system and rigid STM instrument design.

Most STM instruments are equipped with a vibration damping system. A damping system with a low resonance frequency is required. At frequencies at or below the resonance frequency of a STM, the system will amplify perturbations instead of diminishing them. On the other hand, the low frequency vibration left by the external damping system will disturb the stability of the tip-sample distance. To reduce this effect, the first resonance frequency of the STM should be as high as possible. Therefore the tunnel unit has to be very rigid and small in size.

Common damping systems for vibration isolation include:

1. Viscoelastic materials, e.g. rubber or Viton – these effectively eliminate large-amplitude shock and high-frequency vibration.
2. Metal springs combined with a damping system – metal springs provide little damping and they are usually used together with an eddy-current damping system consisting of copper elements and permanent magnets (e.g. SmCo).

3. Pneumatic feet – These feet have resonance frequency of 2 Hz or less.
4. Magnetic levitation on a superconducting bowl – This design was used in the IBM 1981 design. It is very effective but relatively expensive.

For further information regarding the theory and design of vibration isolation, readers are referred to the paper by M. Okano titled "Vibration isolation for scanning tunnelling microscopy" [37].

2.2.2.2 Simulations of single-stage vibration isolation system

The vibration isolation system is critical to the success of STM experiments. The STM must have a good vibration isolation system to have a steady environment in order to achieve atomic resolution.

Simple computer modelling for a single-stage vibration isolation system gives us the knowledge of how the STM vibration isolation system responds and how to optimize it. This simulation work gives an insight to the design of a STM system. The mathematical software program "MATLAB" was used to simulate the vibration response. The codes for the MATLAB simulation programs are included in the Appendix A.

Single-stage vibration isolation system

A MATLAB program was written for simulating a single-stage vibration isolation system with spring suspension and magnetic damping. Simulations were implemented in order to understand how to optimize the system via adjusting various system parameters (i.e. mass, spring constant and damping coefficient), and the vibration response of the system.

1. Optimization via adjusting system parameters

Fig. 2.3 shows the frequency response with different masses (w is the vibration angular frequency and wo is the natural angular frequency of the system):

With a smaller mass, the gain of the system reduces and the oscillation is attenuated. A lighter system tends to have better stability, and thus the STM stage should be as light as possible.

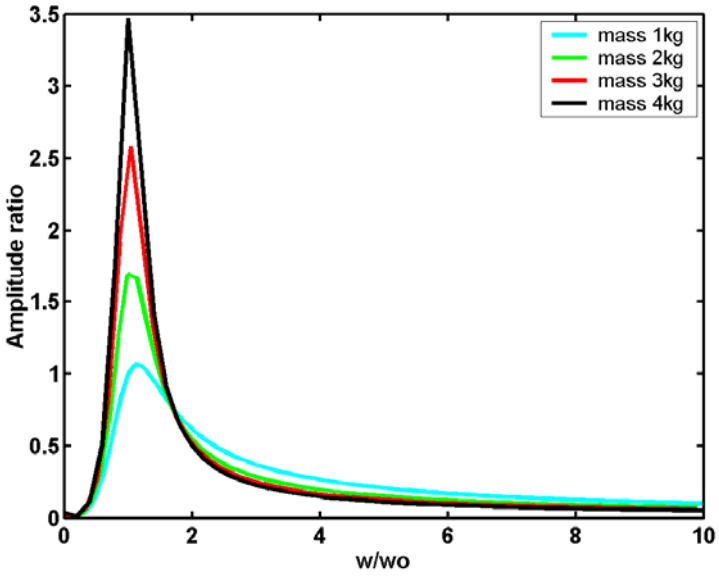

Fig. 2.3. The frequency response of the simulated STM system with different masses.

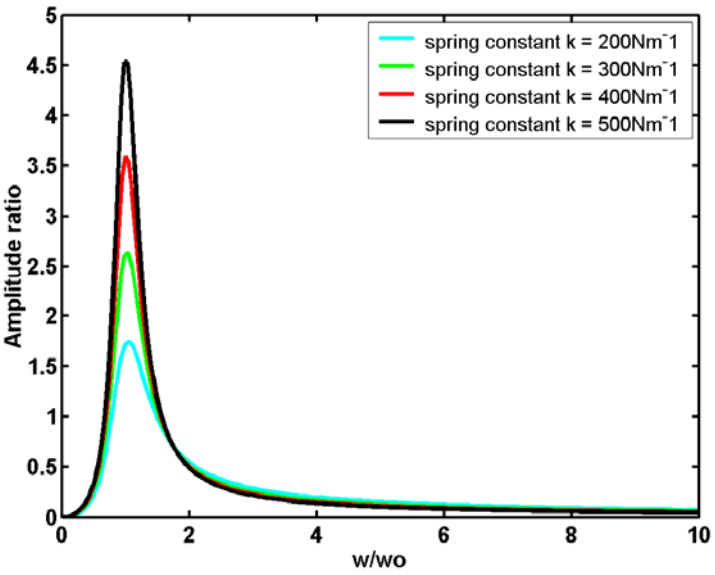

Fig. 2.4. The frequency response of the simulated STM system with different spring constants.

Fig. 2.4 shows the frequency response with different spring constants. It is observed that a smaller spring constant gives a better frequency response. Therefore springs with lower stiffness should be used for the vibration isolation system.

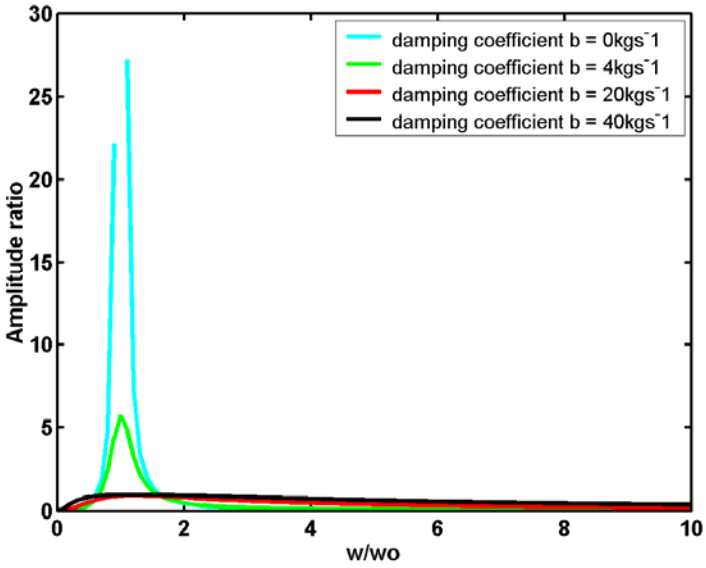

Fig. 2.5. The frequency response of the simulated STM system with different damping coefficients.

Fig. 2.5 shows the frequency response with different damping coefficients. By comparing the blue curve with the green curve, it is found that the system oscillation is reduced considerably with damping. The damping can make the system much more stable and resistant to vibration. However, after increasing the damping to a certain level, the extra stability comes with extra damping is less pronounced as we can see from the red curve and the black curve. The damping coefficient of the black curve is larger than the red curve by 20 kgs^{-1} but their frequency responses are more or less the same. Moreover, excessive damping will weaken the system's capability of attenuating noise as shown in Fig. 2.5 that the vibration response of the green curve (4 kgs^{-1}) is more stable than that of the red (20 kgs^{-1}) or the black (40 kgs^{-1}) curves.

To conclude, in order to have good vibration isolation, the STM stage should be light, the spring constant should be small and moderate damping should be used. Metal springs themselves provide only little damping and therefore in our STM design, we combined the spring system with the eddy-current damping (magnetic damping) for its reliability and thermal stability [38, 39].

2. Vibration response of the system

The above simulation result indicates that a light STM stage with damping would help to eliminate vibration. The vibration performance of our STM system can be optimized with approximately the following parameters: mass of 0.8 kg, spring constant of 200 Nm^{-1}, damping coefficient of 8 kgs^{-1}.

The frequency and time responses of the system to vibration were then investigated. Fig. 2.6 shows the simulated frequency response of the system:

The system is sensitive to vibration at the resonant frequency. The resonant frequency wo/2π is about 2.52 Hz. This means low frequency noise at about 2.52 Hz should be avoided. Fig. 2.7 shows the simulated time response of the system:

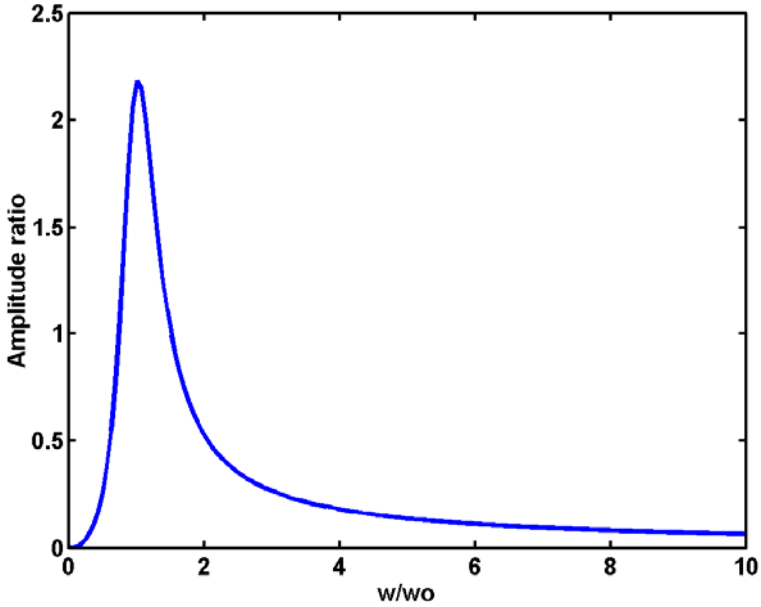

Fig. 2.6. The frequency response of the simulated STM system.

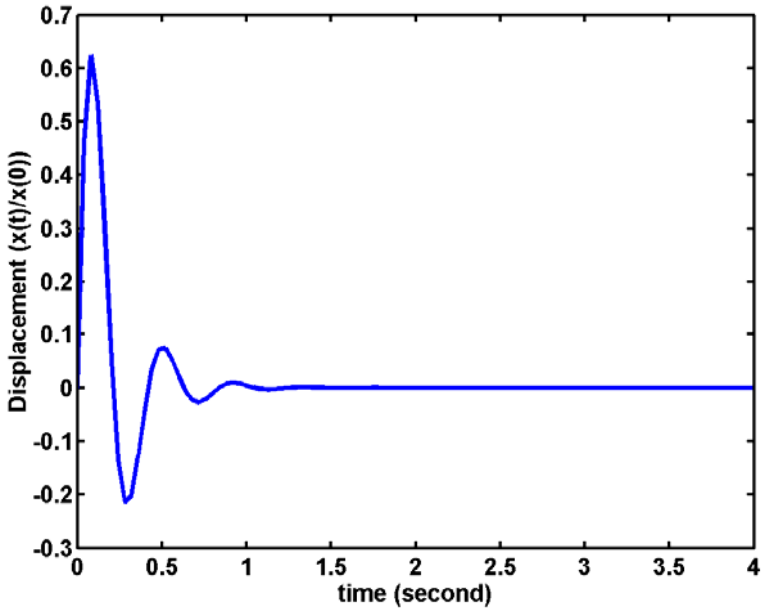

Fig. 2.7. The time response of the simulated STM system.

The oscillation of the system dies down quite quickly. After one or two periods of oscillation (about one second), the system becomes stable again.

In conclusion, with a light STM stage and magnetic damping, the STM system performs well in response to vibration. It can resume stability in about one second. However, external vibration with frequency of about 2-3Hz should be avoided as much as possible because the amplitude of such vibration will be amplified by the system. These results act as the general guidelines for designing a STM and they are applied in the construction of our system.

2.2.2.3 System vibration isolation

Three levels of vibration isolation are included in our UHVSTM. Externally, the entire UHV system is mounted on four active damping air-legs (Melles Griot, USA), which are in turn mounted on a separate foundation stack (1.2 m x 1.2 m). We have found this combination of damping schemes to be highly effective. Internally, the STM is mounted on a single-stage spring suspension platform with eddy current damping as shown in Fig. 2.2. The internal damping utilizes 4 stainless steel springs of stiffness k = 200 N/m with free length 32.5 mm. There are 28 magnets arranged symmetrically around the STM outer stage. On the inner stage, there are 16 OFHC copper plates which, together with the magnets, provide effective eddy-current damping. The magnets are made of SmCo 25 mm x 10 mm x 5 mm with remanent magnetization of 0.85 T (Magnet Sales & Services Ltd, United Kingdom); they have a maximum working temperature of 250°C which is compatible with the bakeout process. The details of the magnetic damping system are shown in its design drawing attached in section B.1 of Appendix B which contains the designs for the inner and outer stages entailing the positions of the hooks attaching to the springs, and the magnets and copper plates (Design 1.1 – 1.4), the magnetic mountings that holds each magnet in place (Design 1.5), and the copper plates in the "U" shape (Design 1.6). The structures of the outer and inner stages are shown in Fig. 2.2. On the outer stage there are four stainless steel supporting rods which mechanically connect the whole STM system to the top flange of the chamber. The brass collars with hooks can slide up and down the rods which allow us to adjust the level of the inner stage which is suspended by the four springs. There are brass collars with extension arms to provide mechanical support to the wire connector and the tip/sample storage rack. The design details are included in the section B.2 of Appendix B with Design 2.1 for the supporting rods on the outer stage, Design 2.2a and 2.2b for the internal structures of the supporting rods, and Design 2.3 for the brass collars with the extension arms. The design of the vibration isolation system is guided by the simulation result in the section 2.2.2.2; a relatively light inner stage with 451.2 g and spring system with

magnetic damping are used in the STM system, and its observed vibration response agrees well with that predicted by the simulation. The imaging capability of the STM system is shown in section 2.3.

2.2.3 System design (2) – scanning head

2.2.3.1 Scanning head and walker

The scanning head is rectangular in shape measuring 50 x 38 x 25 mm^3 (Fig. 2.8) including the slip-stick walker and the piezoelectric tube. The piezoelectric tube is protected with a brass semi-cylindrical block at the top. The slip-stick walker is wedge-shaped with the aim that it will reach the same starting position as it retreats all the way back. The slot behind the sample on the walker is for mounting a magnet such that a magnetic field is established directly behind the sample for electron spin detection measurements. Two trailing rails are

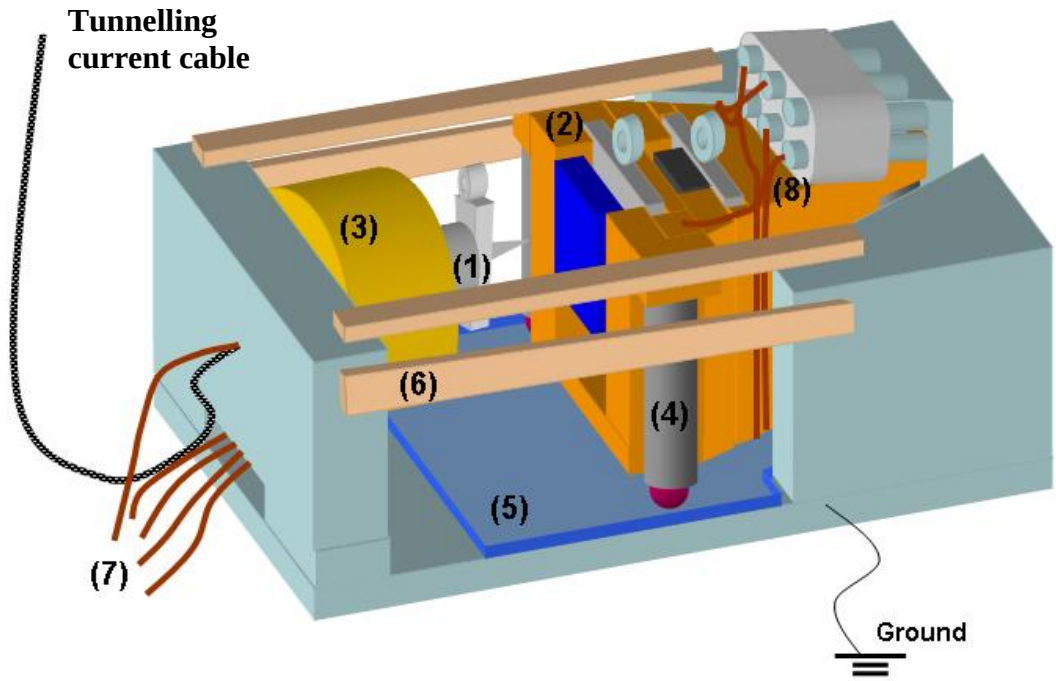

Fig. 2.8. The scanning head with the piezoelectric tube (1) and the slip-stick walker (2). There are two slots on the walker, the one at the front is for a sample while the one at the back is for a permanent magnet. The piezoelectric tube is protected at the top by the semi-cylindrical block (3). The walker is actuated by three piezoelectric legs with ruby spheres (4) and can move around on a layer of sapphire crystal (5). The trailing rails (6) are for keeping the walker in place during sample transfer and preventing the walker falling off the scanning head. The wires (7) to +X, -X, +Y, -Y, and Z electrodes of the piezoelectric tube are 0.213 mm in diameter. The piezoelectric legs and the walker itself are connected with wires (8) for controlling the sideways, back/forth, and rotation movement and sample bias.

established on each side of the scanning head in order to avoid the slip-stick walker falling off the scanning head. Two additional rails at the top are used to keep the slip-stick walker in place during sample transfer. The design drawings (Design 3.1a and 3.1b) for the scanning head are included in section B.3 of Appendix B.

Approaching mechanism of the slip-stick walker

The structure and wiring of the slip-stick walker are shown in Fig. 2.9(a) and Fig. 2.9(b) respectively. The walker is an inertial slider. Its movement is carried by the three piezoelectric legs as shown in Fig. 2.8 and Fig. 2.9 (two at the front and one at the rear). In order to realize the movement of the walker, a series of voltage pulses (Fig. 2.10) are sent to the piezoelectric legs via one of the contact plates [Fig. 2.9(b)] which activate the motion of back/forth, sideways, or rotation. The voltage pulses are in cycles consisting of a slope and a sudden drop in voltage. The mechanism is illustrated in Fig. 2.11. As the voltage increases along the slope, the piezoelectric legs have their outer electrodes excited and thus bent towards the directions according to the wiring connections as shown in Fig. 2.9(b). Since the voltage increases relatively slowly (slope A is 15.2 Vms^{-1}), there is no relative movement between the ruby spheres of the piezoelectric legs and the sapphire crystal surface as the static friction effected at the interfaces is large enough to resist the bending action of the piezoelectric legs. As such, the ruby spheres of the piezoelectric legs act as a pivot and the

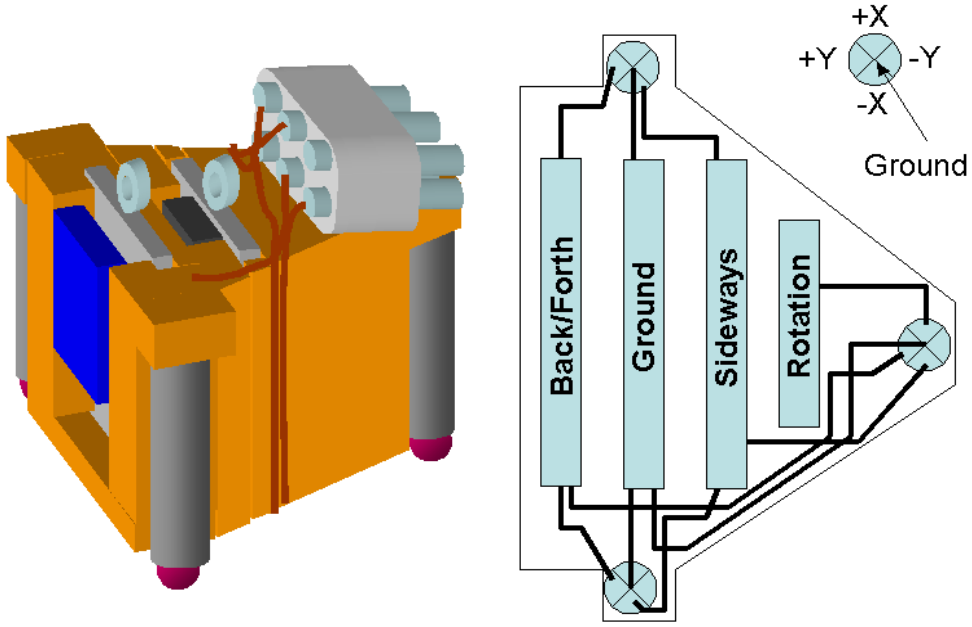

Fig. 2.9(a). Schematic drawing of the walker. Fig. 2.9(b). Bottom view of the walker and the wiring diagram. The circles represent the piezoelectric legs while the rectangular boxes represent the contact plates.

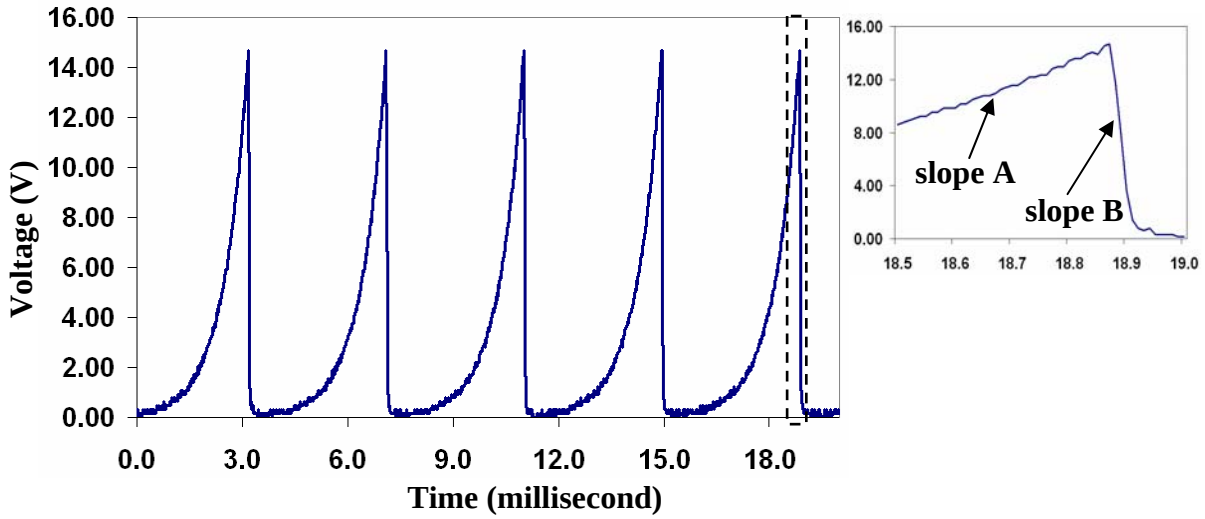

Fig. 2.10. Voltage pulses sent to the piezoelectric legs to actuate the motion of the walker. The voltage pulses are in cycles of an upward slope and a sudden drop in voltage. The amplitude and the frequency of these voltage pulses can be manually controlled. The framed pulse is shown more clearly in the inset where slope A is found to be approximately 15.2 Vms^{-1} and slope B is about -273 Vms^{-1}. Slope B is around 18 times stiffer than slope A, and thus the voltage drops much more quickly than the rise of voltage.

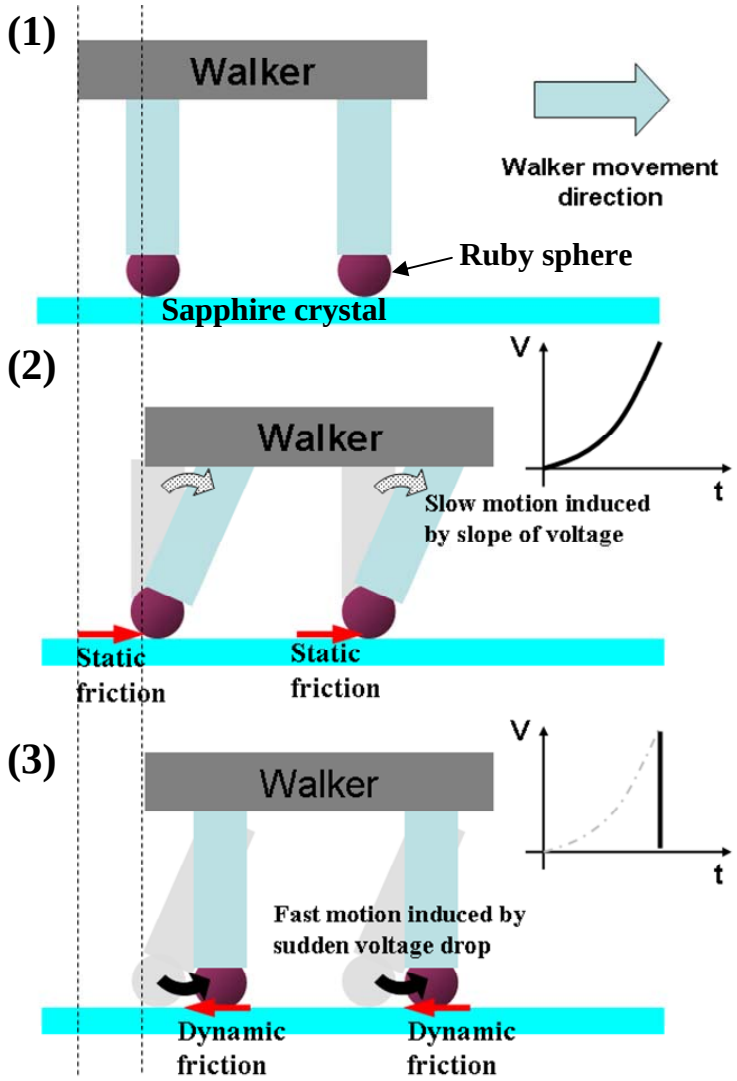

Fig. 2.11. Illustration showing the mechanism of the walker movement activated by the piezoelectric legs. The voltage pulses sent to the legs excite their bending motions with different speeds and directions. The alternation of the type of friction at the interface of the ruby spheres and the sapphire crystal surface is essential for the movement mechanism.

bending actions move the walker forward. After that, there is a sudden drop in voltage (slope B is -273 Vms^{-1}) which leads to the bending of the piezoelectric legs in the opposite directions. The voltage drop is very fast (about 18 times faster than the rise of the voltage), thus the original static friction becomes dynamic friction at the interfaces. Since the coefficient of dynamic friction is smaller than the coefficient of static friction, the friction force cannot sustain the bending actions of the piezoelectric legs and there are relative motions between the ruby spheres and the sapphire crystal surface. In this way, the piezoelectric legs change back to their original shapes while the walker stays at its new position without being moved back. This cycle of motions is repeated by the series of voltage pulses and the walker is thus carried along by the piezoelectric legs. The amplitude and frequency of the voltage pulses can be adjusted manually in the range of around 40 V to 140 V and up to 2 kHz, which will affect the speed and the direction of the walker movement. In our STM measurements, configuration of around 50 V and 400 Hz is generally used for approaching which corresponds to a step size of around 170 nm.

The three piezoelectric legs are wired up in such a way that the walker can move back and forth, sideways and rotate [Fig. 2.9(b)]. The three legs work together to mobilize the walker back and forth and sideways. For rotation, the front legs halt with the driving force coming from the back leg. Since the walker movement depends on the concerted coordination of the three piezoelectric legs, it is of paramount importance to have the three legs exactly the same size.

The control electronics [40] allow us to select the desired mode of walker motion with positive or negative polarity (i.e. different directions) under feedback control during automatic approach. For example, if we want to move to an area which is neighbouring the present scan area, the sideways motion can be selected with automatic approach, and since the step size of the walker is smaller than the scan size, there will be recognizable overlapping regions between these two scan areas; if there is a tilting between the sample and the tip, rotation movement can be chosen during automatic approach in order to rectify the tilting.

2.2.3.2 Piezoelectric tube

Design consideration

The scanning mechanism relies on three-dimensional movement of the sensor tip. The movement of the tip is achieved by using piezoelectric drives which can be bars, tubes or bimorphs. Nowadays, most STMs use the tube geometry for its relatively high piezo

constants, high resonance frequency, and it is simpler than both the tripod and bimorph – based scanners.

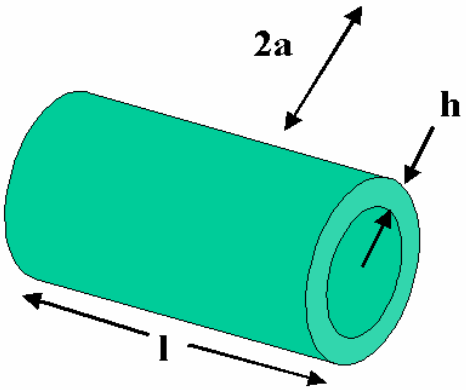

Fig. 2.12. Piezoelectric tube.

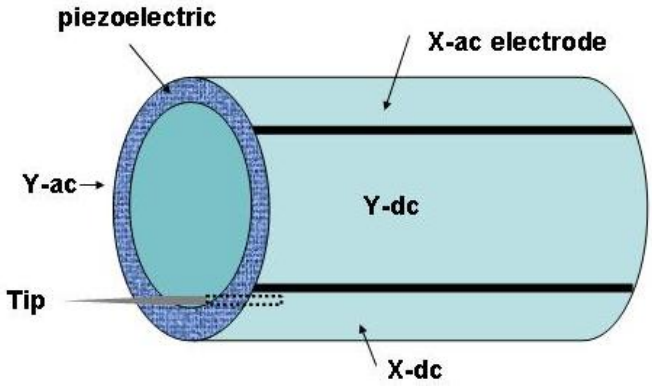

Fig. 2.13. Tube scanner with the outside electrode sectioned into four equal areas parallel to the axis of the tube.

If a voltage U_p is applied between the inner and outer electrodes of a piezoelectric tube of length l and wall thickness h (Fig. 2.12), the resulting length change Δl is given by:

$$\Delta l = d_{31}\frac{l}{h}U_p \qquad (2.1)$$

where d_{31} is the relevant piezoelectric coefficient.

A single-tube scanner with its outer electrode divided into four segments is useful for providing three-dimensional movement to the tip (Fig. 2.13). If we excite the pairs of opposite outer electrode segments by a voltage, the tube will bend in one direction and thereby allow for x-y movement. By applying the same voltage to all outer electrode segments and the opposite voltage to inner electrode, the tube will expand or contract along the tube axis and so z movement is feasible [41]. Careful design of the piezoelectric tube is necessary in order to guarantee the subsequent satisfactory piezoelectric drive movement. When designing the piezoelectric scanning unit, the following issues should be considered:

1. High resonance frequency and high scan speed – High resonance frequency ensures stable STM operation and thereby allows faster scanning.
2. Low cross-talk between x, y, and z piezodrives – Cross talk between the three orthogonal directions of movement can become significant for large scan area and this distorts the imaging.
3. Low non-linearities, hysteresis and creep – Nonlinearities are the result of an increased scanner sensitivity with increased scan size. Hysteresis means the tube does not go back to its original position after expansion and contraction. In addition, piezoelectric elements

exhibit a slow logarithmic creep after a fast voltage change. All of these can cause image distortions, so should be avoided.

4. Low thermal drifts – Temperature variations and the difference between the thermal expansion coefficients of the different materials can result in thermal drift in STM. That is why, even when scanning the same area, the images always differ slightly. Thus materials with similar thermal expansion coefficients as the piezoelectric ceramic should be used if the materials are going to have contact with the piezoelectric tube.

System design

The piezoelectric tube (PTYY-0186, PI Ceramic) of our system has a dimension of 6.09 x 6.36 x 5.39 mm (Length x Outer diameter x Inner diameter) with d_{31} of 180 x 10^{-12} mV^{-1}. We can use eqs. (2.2) and (2.3) to calculate the vertical and lateral scan ranges:

$$\Delta Z = \frac{d_{31} V L_1}{h} \tag{2.2}$$

$$\Delta X, Y = \frac{2\sqrt{2} d_{31} V L_1^2}{\pi D h}(1 + 2\frac{L_2}{L_1}) \tag{2.3}$$

where V is the voltage span which is 300 V for X and Y, 150 V for Z; L_1 is the length of the tube; h is the thickness of the tube wall; D is the mean diameter; L_2 is the extension from the tube end to the tip end (in our design the tip is on the piezoelectric tube, see Fig. 2.8 and Fig. 2.14), which includes the thickness of the washer, insulating ceramic, and tip holder, and the length of the tip. L_2 is typically about 6 mm. The vertical and lateral scan ranges are predicted to be 0.339 μm and 1.880 μm respectively, which agree well with the actual values of 0.302 μm (vertical) and 1.65 μm (lateral).

The wires connected to the electrodes of the piezoelectric tube are Kapton-coated copper wires (SWG 35, 0.213 mm diameter, Bicalex Cable United Kingdom). Silver glue was used to connect the wires to the tube and then Torr Seal (Varian USA), which is a low vapour pressure resin for high vacuum applications, was used to further strengthen the contacts.

2.2.3.3 High-frequency coaxial cable for tunnelling current

The tunnelling current from the tip is carried by a high-frequency coaxial cable [(8) in Fig. 2.2]. This cable (RG 178 ST) is manufactured by Filotex, with maximum operating frequency of 3 GHz and impedance of 50 Ω, and it is electrically protected by a layer of

single braid silver plated copper. Its signal attenuation at 900 MHz is 1.5 dB/m, and since only 50 cm of the cable is needed, the actual attenuation is around 0.5 dB. It has an operating temperature range from -90°C to 200°C. The cable, with a length of 50 cm, contains capacitance of 47.5 pF. This high-frequency coaxial cable can preserve the high frequency modulation of the tunnelling current which is the corresponding signature to the electron spin signal. All the connections from the inner stage to the outer stage, except the tunnelling current cable, are established with 30 μm diameter wires (Scientific Wire Co., United Kingdom) [(6) in Fig. 2.2]; after that, Kapton-coated copper wires (SWG 35, 0.213mm diameter) [(7) in Fig. 2.2], which go through the central hollow supporting rods providing further electrical shielding, are used for connections between the outer stage and the electrical feedthroughs.

Whilst the high-frequency coaxial tunnelling cable can sufficiently preserve the electron spin signal, it comes with the disadvantage that the high-frequency coaxial cable is 3 mm in diameter and is relatively rigid, which in terms of vibration isolation is problematic as

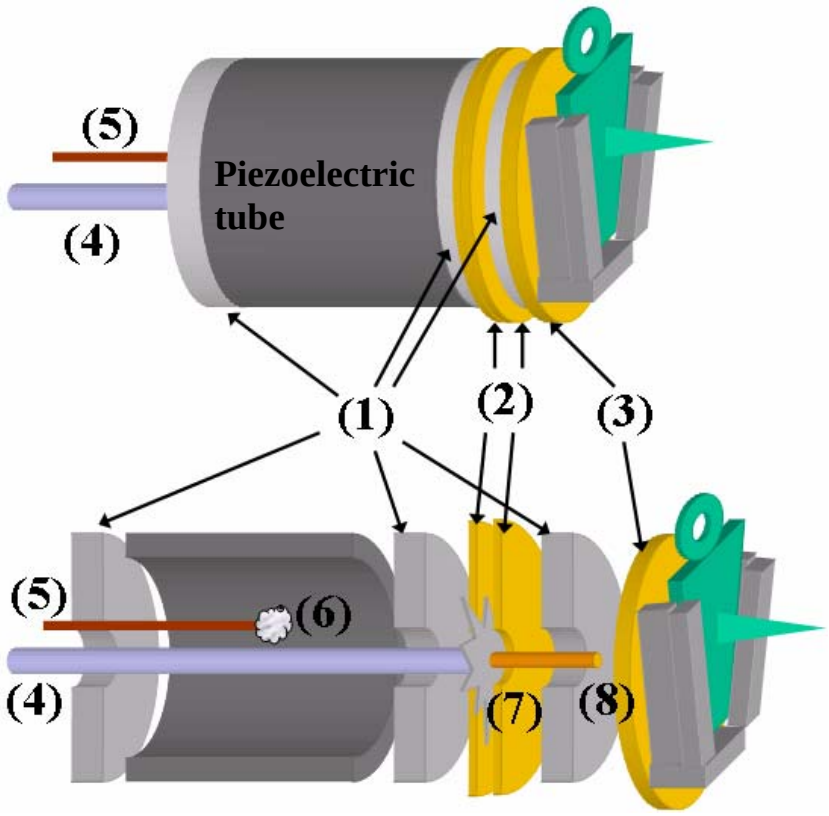

Fig. 2.14. The structure of the scanning tube assembly with a cross-section at the bottom. (1) ceramic disks for electrical insulation, (2) brass plates clamping the grounded shielding of the cable for electrical protection to the front end, (3) brass plate with the tip holder, (4) high-frequency coaxial cable for carrying tunnelling current, (5) Kapton-coated copper wire (0.213 mm diameter) for the Z-electrode, (6) contact is made by silver glue and strengthened with Torr Seal (Varian USA), (7) electrical shielding of the high-frequency coaxial cable, (8) central conductive core of the cable electrically connected to the tip holder. All the components are glued together by Torr Seal.

it mechanically couples the STM to the external environment. Due to the stringent control requirements of the tip-sample separation for STM (must be controlled to better than 10^{-11} m) to prevent building vibrations (which are typically in the frequency range 1-100 Hz, at amplitudes of up to a few microns), STMs must be mechanically decoupled from the environment. Moreover, due to the fact that the bias tee is not UHV compatible, the tunnelling cable has to be as long as 50 cm in order to connect to the nearest electrical feedthrough. A multi-pronged approach was taken to tackle this engineering challenge as to the rigidity and length of the tunnelling current cable. First of all, the scanning tube was designed in such a way that the stiffness of the cable is considered. The cable goes through the piezoelectric tube as shown in Fig. 2.14. This design delivers the advantage that as the cable is parallel to the tube axis, its stiffness will not hinder the scanning motion whereas if the cable was connected sideways to the tip holder, the rigidity of the cable would apply a lot of stress onto the tube which could greatly hamper the scanning movement. That is the reason why route 1 in Fig. 2.15 is not selected. The lower part of Fig. 2.14 displays the bisection of the scanning tube. The tunnelling current cable and the Z-electrode wire go together into the inside of the tube. The Z-electrode wire is connected to the inner wall of the tube, whilst the cable goes further and has its electrical protective shielding, which is grounded, half peeled off and clamped with two brass plates in order to provide electrical protection to the tip, the origin of the tunnelling current. The central conductive core of the cable is connected with another brass plate, where the tip is located for carrying the tunnelling current. Secondly, given its stiffness, we need to carefully consider how the cable is placed. Route 2 and 3 for the cable in Fig. 2.15 are not adequate because, although they are shorter than route 4, the turning angle is too sharp so the cable would be subject to too much stress. Route 4 is a longer route but it does not have such a sharp turning point and thus the cable can sit more

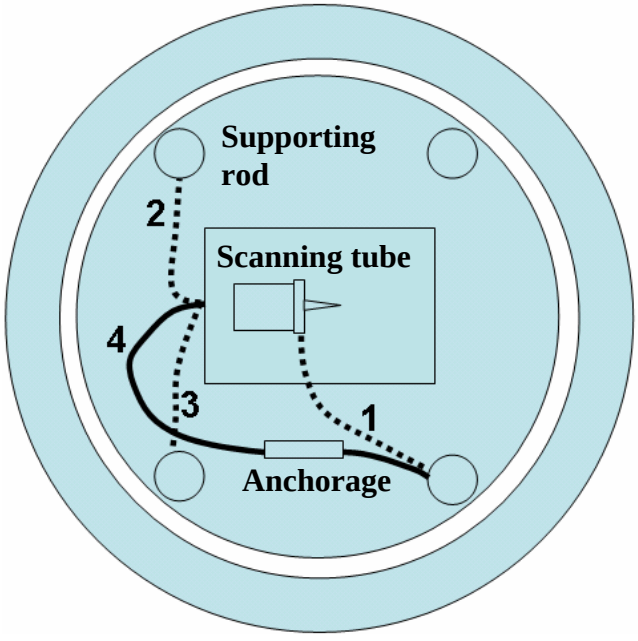

Fig. 2.15. Plan view of the inner stage of the STM

naturally without too much tension. In addition, the cable has to be constantly anchored at the interval of around 7 cm as shown in Fig. 2.2 and Fig. 2.15 so as to break down its vibration mode. This method can effectively attenuate the vibration coupled by the cable. The cable does not go inside the supporting rod but along the outside because of the sharp turning point at the slit openings, and the protective shielding of the cable itself can offer sufficient electrical protection.

2.2.4 System design (3) – modules for handling tunnelling current

Unlike conventional STM, the tunnelling current in this UHVSTM is first passed into a bias tee (ZFBT-4R2GW, Mini-Circuits, USA) for splitting the high frequency and low frequency components before going into a current-voltage (IV) amplifier. The bias tee has a frequency range from 0.1 MHz to 4.2 GHz. Since the bias tee is not vacuum compatible, it is installed directly at the top of the chamber to minimize the length of the tunnelling cable.

The low frequency component of the tunnelling current passes into an IV amplifier (DLPCA-200, FEMTO, Germany) which has bandwidth of 200 kHz for a gain of 10^8 and 1.2 kHz for a gain of 10^{11}. With a high gain of 10^{11}, it is possible to perform low current imaging at as low as 500 fA. The limiting factor for the tunnelling current is the inherent system noise rather than the inadequacy of the IV amplifier. It is essential for our experiments of overlayers characterization to have low-current imaging capability as overlayers, for instance organic molecules, may not be very conductive. On the other hand, the high frequency component is passed into a Radio Frequency (RF) amplifier (HSA-X-1-40, FEMTO, Germany). The RF amplifier has a frequency range from 0.01 MHz to 2 GHz and a gain of 40 dB. A RF amplifier is used instead of a conventional IV amplifier because a larger bandwidth is needed to preserve the high frequency signal quality. After amplification, the current will reach the spectrum analyser (HP E4402B, Hewlett Packard Agilent, USA) with a sensitivity of -166 dBm and a frequency range from 9 kHz to 3 GHz for detection of high frequency modulation in the tunnelling current.

2.2.5 System design (4) – materials

The scanning head is made of brass because brass degases relatively quickly, and its high thermal conductivity means the system becomes thermally stable more quickly. The inner stage is made of aluminium in an effort to reduce the mass, which is vital to the eddy current damping and provides better vibration response as shown by the simulation result in section 2.2.2.2. It would have been preferable to make the scanning head with aluminium

since aluminium is lighter than brass; however, aluminium does not have as good thermal conductivity as brass. The supporting rods and outer stage are made of steel for rigidity, and since they are not involved in the scanning or damping, their mass is not a matter of concern. The springs, magnet holders, outer stage, and supporting rods are all made of non-magnetic stainless steel so that they will not interfere with the magnetic damping.

2.2.6 UHV system

The STM is situated in a stainless-steel six-way cross vacuum chamber with a small load lock [Fig. 2.16(a)]. A turbo pump (Leybold Vacuum, Germany) is connected to the load lock with a rotary pump as backup. There is a gate valve between the load lock and the chamber. The main chamber is pumped with an ion pump (Leybold Vacuum, Germany) and titanium sublimation pump (Caburn, West Sussex, United Kingdom). The pressure is monitored by the ion gauge with a pressure gauge controller (PGC2D, Caburn, United Kingdom). A heat tent, ion pump heater, bakeout fan unit (Caburn, United Kingdom) and heating tapes are used for bakeout.

Samples and tips are introduced through the load lock which can be pumped to 10^{-7} mbar in about 30 minutes. A magnetic coupled transfer arm (VF 169, Huntington, USA) with a linear travelling distance of 18 inches conveys the sample and tip from the load lock into the main chamber. The structure of the sample holding plate of the transfer arm is shown in Fig. 2.17. Two tips and one sample can be loaded at any one time. There is a storage rack which is attached to one of the supporting rods [(9) in Fig. 2.2] for holding two tips and two samples inside the chamber (Fig. 2.18). With appropriate arrangement, two tips and one sample can be taken away, and one tip and one sample can be loaded into the STM. There is a window on the main chamber, through which the movement of the sample transfer arm and the heater and the situation of the STM head can be seen. A wobble stick from the top of the chamber is used for tip or sample transfer from the STM head.

Efficient usage of space allows us to have a relatively compact chamber. A heater with direct and resistive heating functionalities, ion gun, and evaporator are all accommodated within the spherical chamber (DN160CF, Caburn, United Kingdom) space of 16 cm in diameter. In order to achieve this, the appropriate and accurate orientation of each component is designed as shown in Fig. 2.16(a) and Fig. 2.16(b). The ion gun, K cell and e-beam evaporator are facing towards the centre of the chamber where a sample can be positioned by the wobblestick which allows 3 inches of motion (ZWS075, universal wobble stick, Vacuum Generators, United Kingdom). The heater, mobilized by a linear feedthrough

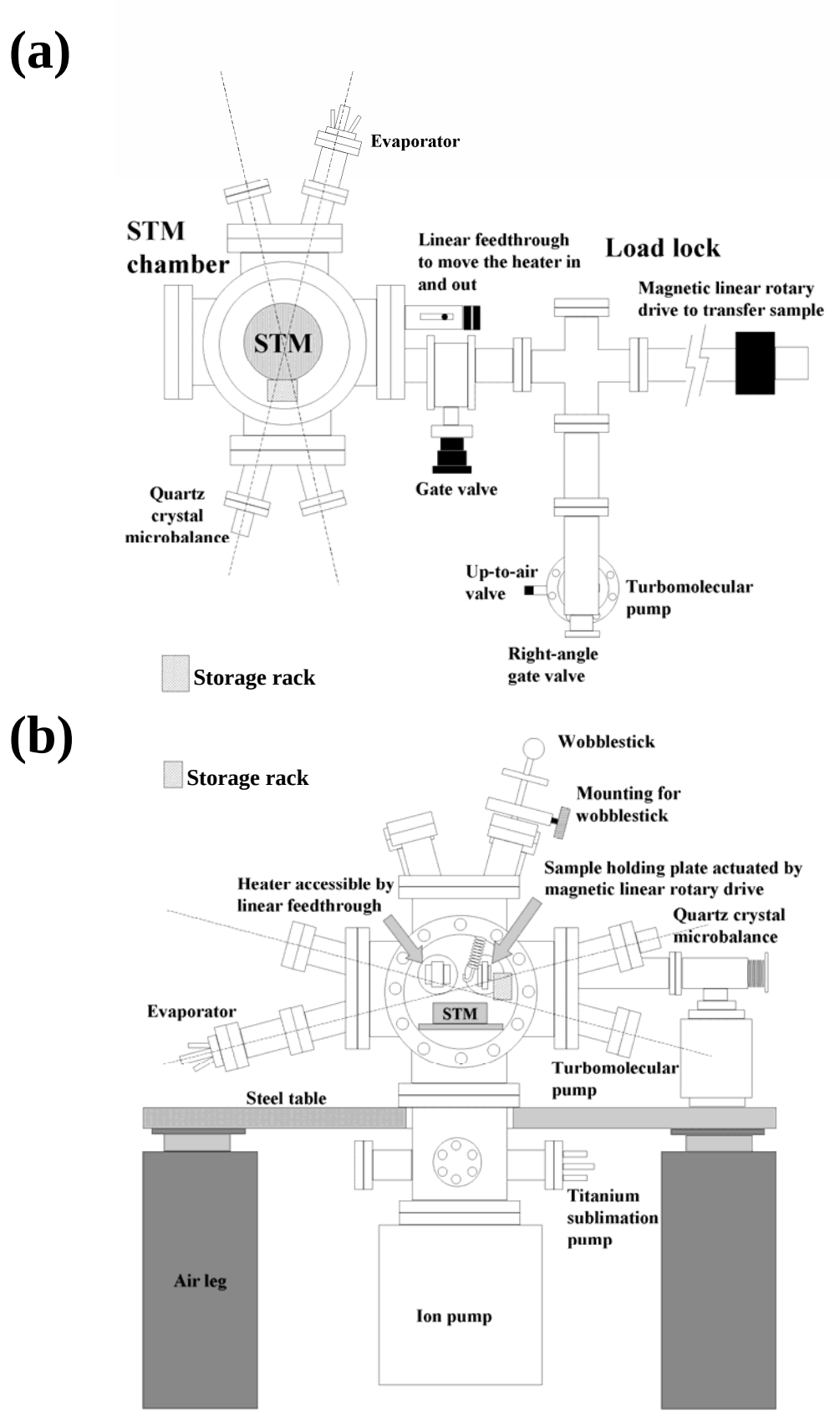

Fig. 2.16(a). Plan view of the STM system. Fig. 2.16(b). Side view of the STM system.

(Kurt. J. Lesker, USA), can be extended into the chamber for direct or resistive heating, and it can also be retreated in order for the usage of the evaporator.

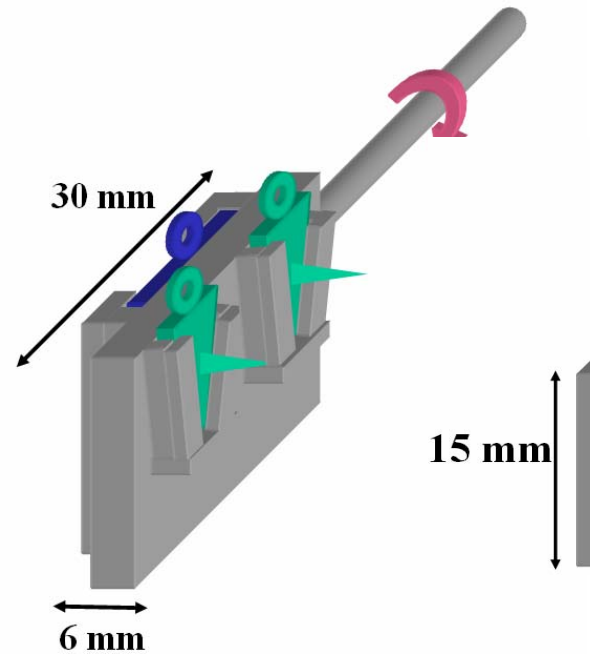

Fig. 2.17. Sample holding plate of the transfer arm. There are two slots for tips (green) and one for a sample (blue). The transfer arm can be rotated, facilitating the transfer of sample and tips.

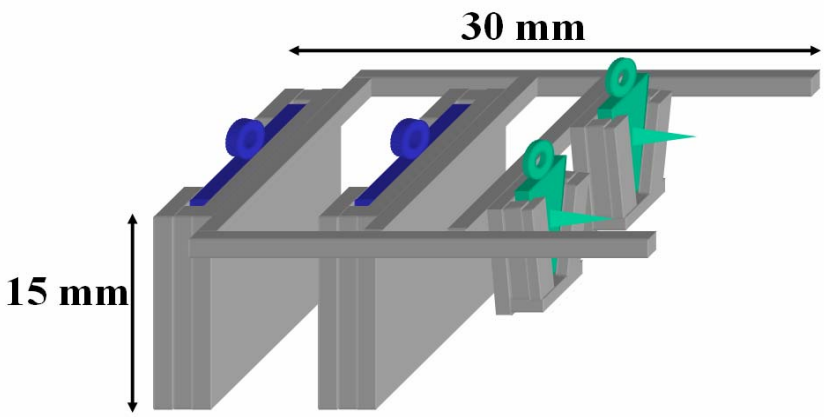

Fig. 2.18. The storage rack is made of brass and it can carry two samples (blue) and two tips (green).

2.2.7 Electronics and control

The STM electronics play a major role in the imaging process. A block diagram showing our STM electronics system is shown in Fig. 2.19.

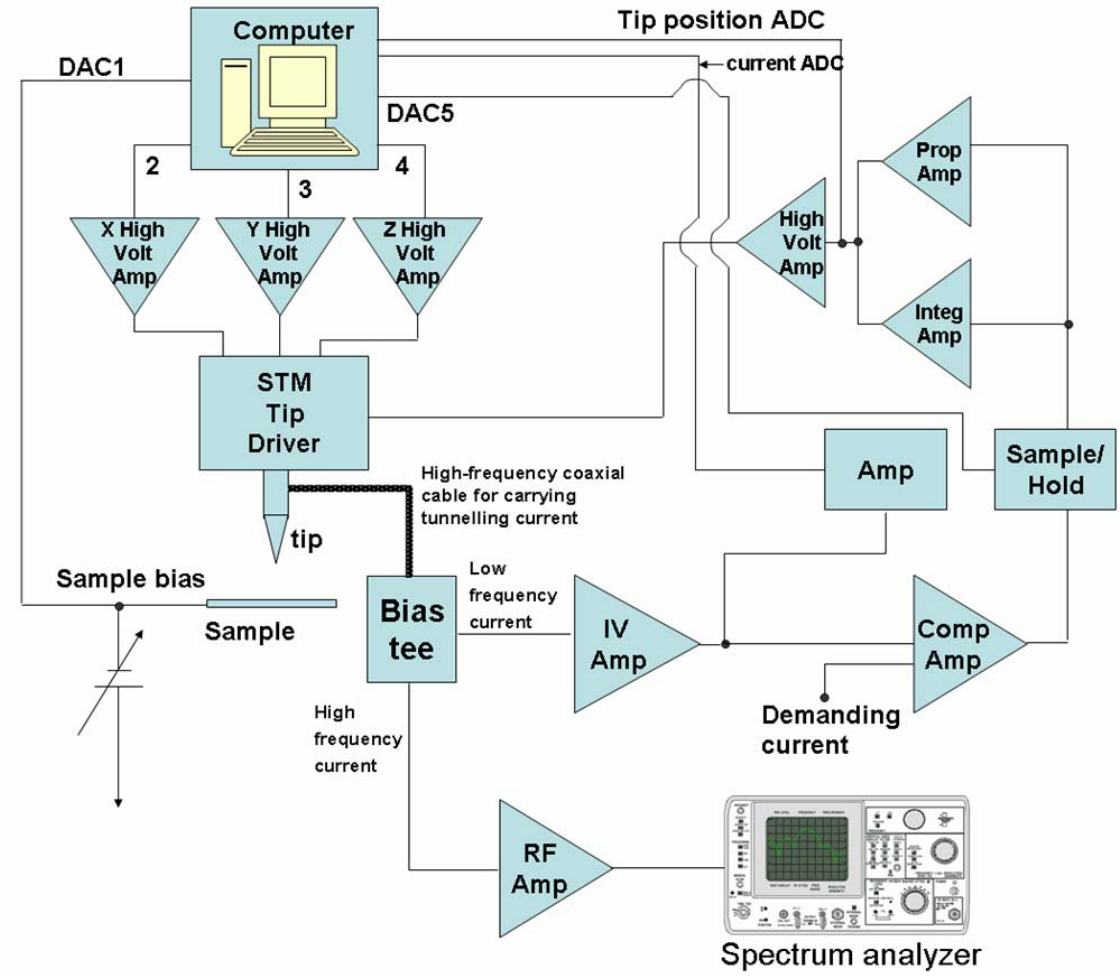

Fig. 2.19. Block diagram of the STM electronics system.

1. The sample bias voltage (typically between 1 mV and 10 V) is supplied by a computer-controlled digital-to-analog converter (DAC) (DAC1 in Fig. 2.19).
2. After regulating, the tunnelling current is amplified by a current amplifier with a gain of $10^3 – 10^{11}$ VA^{-1}.
3. The tunnelling current is carried from the tip by a high-frequency coaxial cable to preserve its high frequency signal.
4. The bias tee splits the tunnelling current into its low frequency component and high frequency component. The low frequency component is then, like conventional STM, passed to the IV amplifier, whereas the high frequency component is passed to the RF (radio frequency) amplifier to amplify the high frequency signal.

5. After the IV amplifier, the low frequency current goes to the feedback control which consists of a proportional (P) amplifier and an analog integrator (I) whereas the high frequency current goes into the spectrum analyzer to look for any high frequency modulation.
6. The control signal from the feedback control is then sent to a high voltage amplifier and then an amplified voltage signal is supplied to the z piezoelectric drive.
7. Computer-controlled DACs provide signals to other high voltage amplifiers to control tip movement in the x-y plane.
8. A sample-and-hold amplifier is installed so that we can hold the tip position for acquiring I/V, dI/dV spectroscopic information.

For further details of the electronics of STM, see Kuk and Silverman [42].

Our STM operates with the software program "DSP-Scan version 6.0" provided by ECS Ltd. DSP-Scan is a control and data acquisition program for scanning probe microscopes. It uses programmable digital electronic hardware to provide a flexible, high speed control and data acquisition system for a wide variety of microscopies including STM and atomic force microscopy (AFM).

2.3 System specification and performance

The STM operates in UHV conditions, and facilities are equipped for in-situ sample and tip preparations. Table 2.1 shows the specification of the UHVSTM system.

Table 2.1. The specification of the UHVSTM system

Base pressure	$<10^{-10}$ mbar
STM scan area	x, y ≈ 1.9 μm z ≈ 0.34 μm
Sample size	up to 1 cm x 1 cm x 5 mm
Tips	Pt/Ir or W
Tunnelling current	~0.5 pA - 10 nA
Tunnelling junction voltage	1 mV- 10 V
Sample preparation	resistive heater for metal samples, direct heating for semiconductors, ion gun for sputtering, K-cell and e-beam evaporator for deposition
Tip preparation	field emission, argon-ion sputtering

The STM has been tested under ambient and UHV conditions. Graphite was used for imaging in air as it is easy to clean and atomic resolution is readily available under ambient conditions. Fig. 2.20 shows some graphite step edges with atomically flat terraces where atomic resolution is obtained as shown in Fig. 2.21 and Fig. 2.22. The hexagonal atomic structure with periodicity of 2.46 Å is shown. The superlattice structure in Fig. 2.23 has been imaged which is only occasionally observed on graphite surfaces. The superlattice structure is due to the mismatch of graphite layers. Its periodicity is 5.5 nm, which is much bigger than that of graphite atomic structure. Some peculiarities on this superlattice were found using this STM and they are discussed in chapter 3. Gold on mica is used for testing the STM in UHV. In Fig. 2.24 terraces and pits which are typical features on Au(111) surface are seen. The step height is 2.4 Å, which is a monoatomic step. The herringbone reconstruction of Au(111) surface is imaged in Fig. 2.25 and Fig. 2.26. Atomic resolution image on Au(111) is shown in Fig. 2.27. The background of Fig. 2.27 is not plane because of the herringbone reconstruction and also the image filtering process by self-correlation. It shows the gold atomic lattice with triangular symmetry and lattice constant of 2.9 Å. The atomic structure is shown in 3-dimensional view in Fig. 2.28. These images showing atomic structures (Fig. 2.25 – Fig. 2.28) are the tunnelling current images. The atomic structures are not as clearly shown in their corresponding topography images as the corrugation of gold atoms is extremely small, on the order of 0.1 Å. Similar to graphite, the terraces are atomically flat, making gold on mica a suitable candidate for depositing free radical organic molecules. BDPA molecules, which have unpaired single electrons and thus are the typical sample for electron spin resonance (ESR) measurement, are deposited in-situ onto the Au(111) by evaporation and ESR results show that the spin signals of BDPA molecules remain after the deposition, which is discussed in detail in chapter 4.1. As is seen in Fig. 2.29, the molecules tend to form islands and aggregate together. These islands scatter quite evenly on the Au(111) surface, probably because the pits on the gold surface have some influence on the interaction between the surface and the molecules. A relatively low current of 20 pA was used for imaging as free radical organic molecules are not very conductive. Details of the sample preparation for the overlayers of BDPA molecules are described in chapter 4.1.

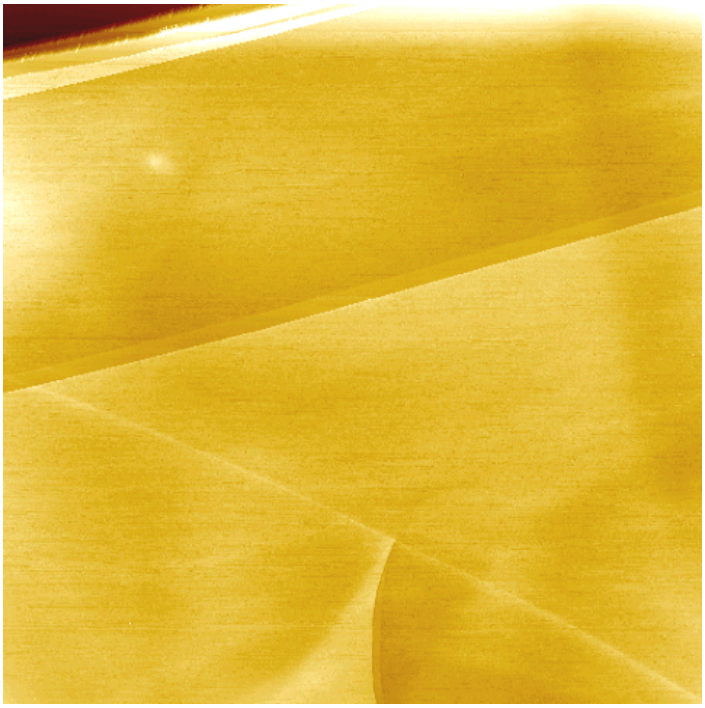

Fig. 2.20. 1000 nm x 1000 nm area on graphite, I_t = 0.3 nA, V_s = 300 mV. Step edges and flat terraces can be observed.

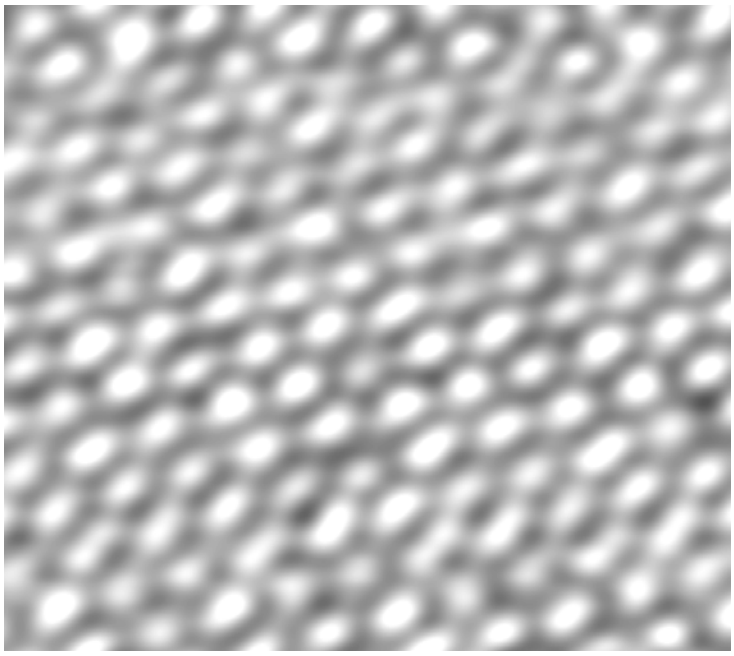

Fig. 2.21. 3.2 nm x 3.2 nm image on graphite with atomic resolution, I_t = 1.25 nA, V_s = 100 mV. Image low pass filtered.

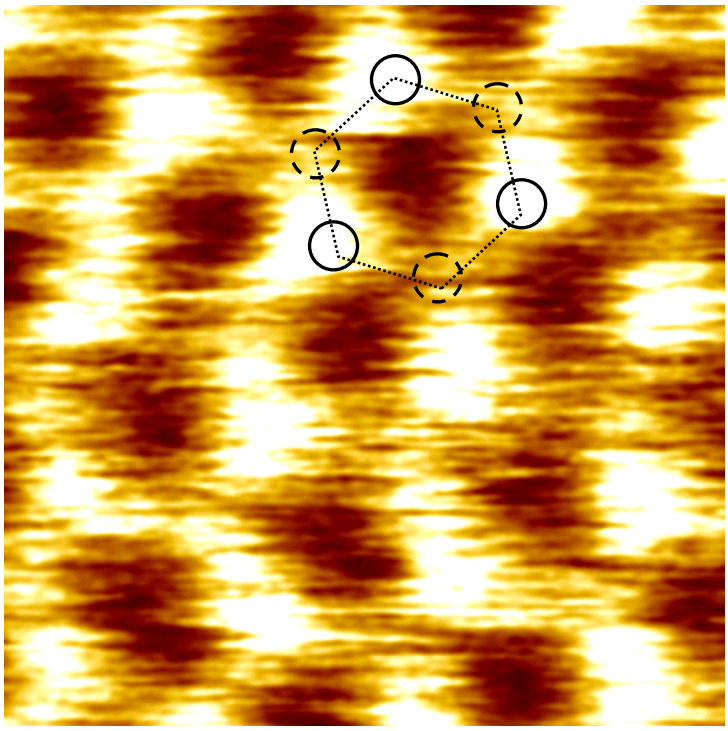

Fig. 2.22. 0.86 nm x 0.86 nm, I_t = 2 nA, V_s = 100 mV, STM image showing atomic resolution on graphite in air. The relatively dimmer α-sites (dashed circles) of the carbon rings (dashed hexagon) can also be observed. The brightest spots are the β-sites (solid circles).

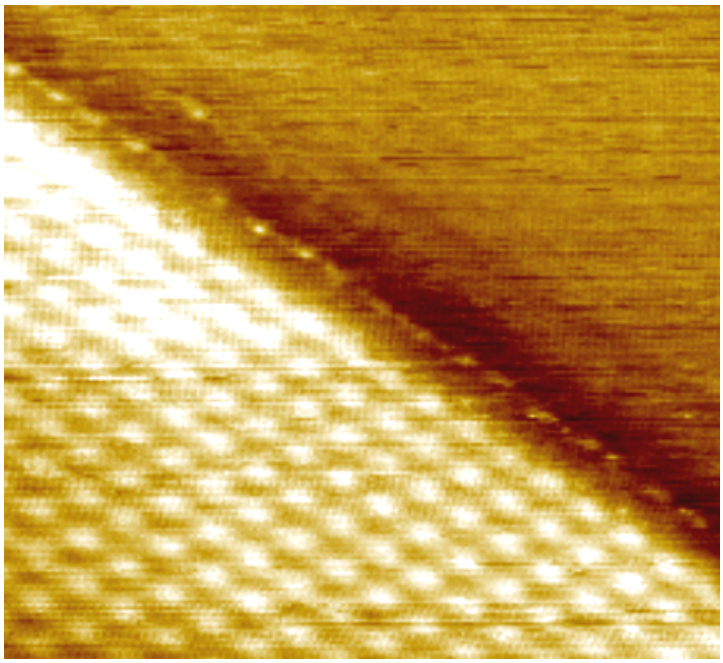

Fig. 2.23. 102 nm x 112 nm area on graphite (I_t = 0.5 nA, V_s = 206 mV). The hexagonal lattice structure on the lower left half of the image is the superlattice structure whose periodicity is 5.5 nm, much larger than atomic lattice periodicity.

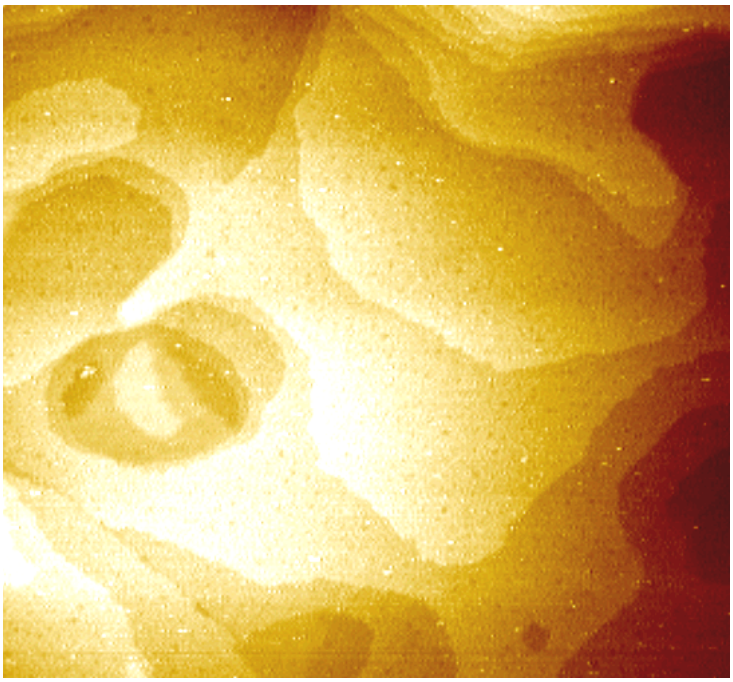

Fig. 2.24. Pits and terraces can be observed on the gold surface (240 nm x 260 nm, I_t = 0.06 nA, V_s = 850 mV).

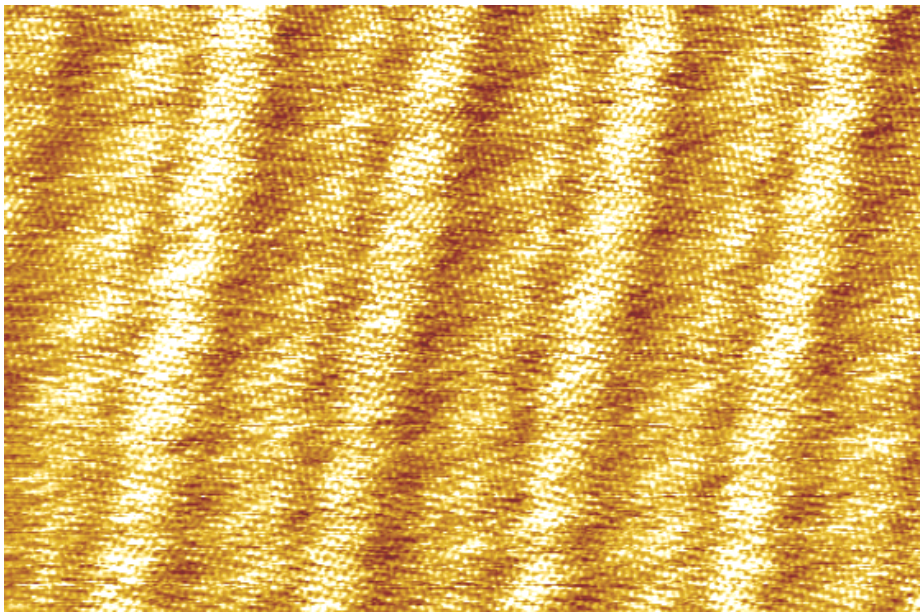

Fig. 2.25. The herringbone reconstruction of Au(111) surface with atomic resolution. 30 nm x 20 nm area, I_t = 1.51 nA, V_s = 50mV. (Tunnelling current image)

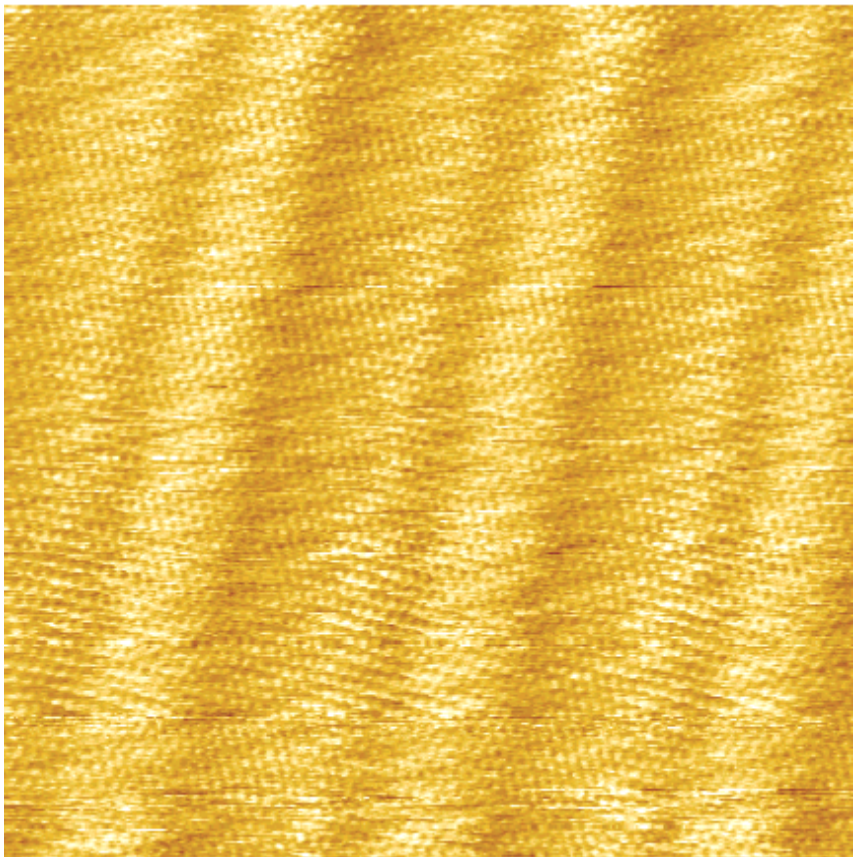

Fig. 2.26. 18 nm x 18 nm, I_t = 1.5 nA, V_s = 50 mV. Herringbone structure with atomic resolution on Au(111) surface under UHV conditions. (Tunnelling current image)

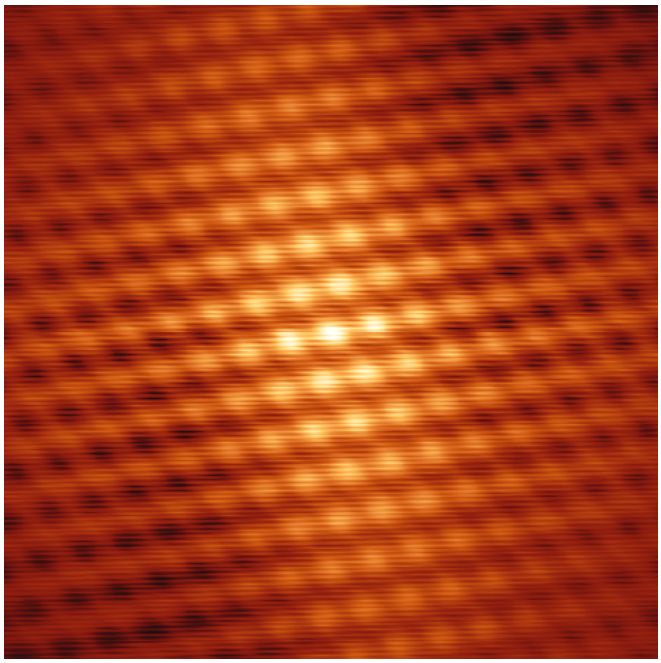

Fig. 2.27. 4 nm x 4nm STM tunnelling current image (I_t = 1.5 nA, V_s = 50 mV) on Au(111) surface showing atomic lattice with triangular symmetry and lattice constant of 2.9 Å. The background of the image is not plane because of the herringbone reconstruction and the image is processed by self-correlation. The mechanism of self-correlation is explained in the footnote on P. 24.

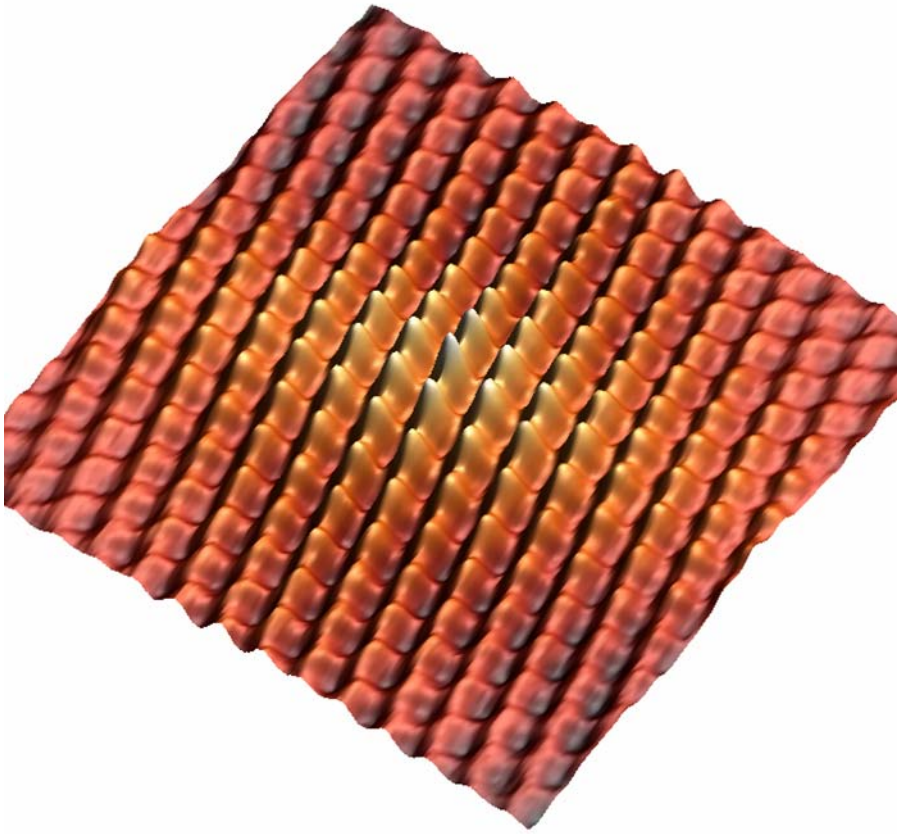

Fig. 2.28. 4 nm x 4nm STM tunnelling current image (I_t = 1.5 nA, V_s = 50 mV) on Au(111) surface in 3-dimensional view; the image is processed by self-correlation. It shows the atomic lattice with triangular symmetry and lattice constant of approximately 2.9 Å.

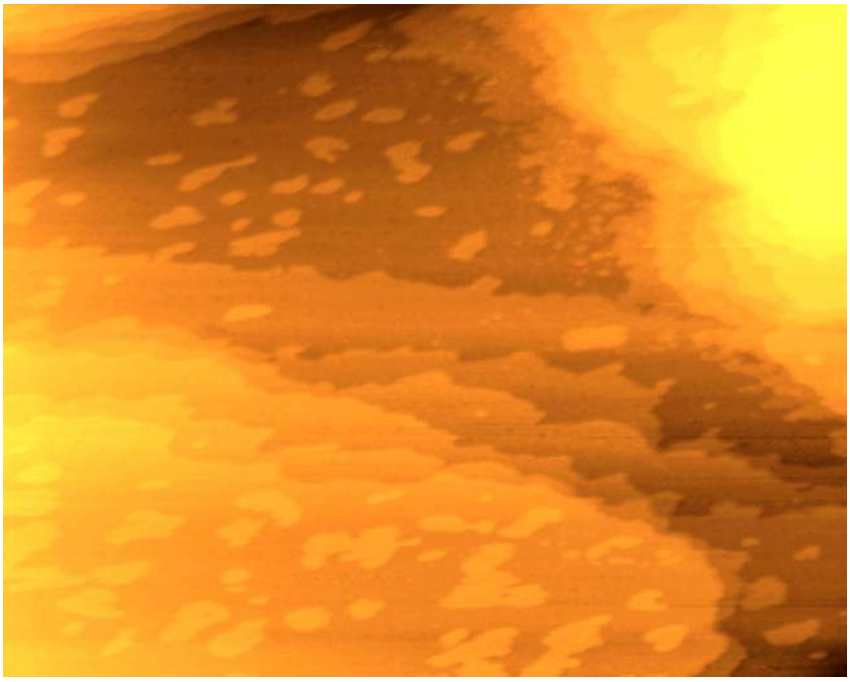

Fig. 2.29. 300 nm x 300 nm area with BDPA molecules on gold, I_t = 20 pA, V_s = -850 mV. A low current of 20 pA is necessary for scanning free radical organic molecules as they are not very conductive. The scattering of the BDPA molecules is quite even on the gold surface. They tend to aggregate together and form small islands.

2.4 Conclusion

A UHVSTM was constructed for characterizing overlayers on single crystal surfaces at the atomic scale with the future intention of performing single electron spin detection experiments and SPSTM. In addition to its function as a standard UHVSTM, the novelties of the design include the use of a high-frequency coaxial cable for carrying the tunnelling current and the versatile movement of the slip-stick walker under regulation. The STM performance is proved by imaging graphite in air and Au(111) under UHV. The novel design of the slip-stick walker grants extra territory for the scanning range, which is beneficial for characterizing overlayers on single crystal surfaces which sometimes involve scattered molecules or atoms. The high frequency signal extracting and analysing capability along with the high-frequency coaxial cable saving the spin signal quality are essential for single electron spin measurement. The work in this chapter is published in the Conference Proceedings of the 5th International Conference of the European Society for Precision Engineering and Nanotechnology 2005 [43].

A number of designs and prototypes were developed before the final establishment of the UHVSTM system. A few iterations of design, construction, and testing were gone through until the imaging capability of the STM was improved to satisfaction as presented in this chapter. The designs and developments of the system occupied a significant amount of time in this PhD research project.

After constructing this UHVSTM, some graphite superlattice structures, which were caused by rotated topmost graphite layers forming moiré rotation patterns on top of the graphite crystals, were observed which deserved investigation. The next chapter is about graphite superlattices and our research on it.

Chapter 3

Observation of graphite superlattices by scanning tunnelling microscopy

This work is mainly motivated by the fact that graphite superlattices observed with STM have not been fully understood and all the relevant research results are not well catalogued. Most of the reports so far were made on superlattices formed by chance during cleaving, however not many follow-up works were done to systematically investigate this intriguing phenomenon, mostly as there is no repeatable means to prepare a superlattice. This technical difficulty is an obstacle to carrying out thorough studies on superlattices. Over recent years, experimental and modelling techniques have been developed to study this anomalous regime of STM; however, there lacks a systematic classification of these scattered information. Therefore, in this chapter, firstly, we organize all of these results so as to enable a more comprehensive understanding of this phenomenon prior to analysis of our own data on graphite superlattices in the later parts of this chapter. We then report our research efforts on the observation of large-scale features on graphite, simulation study of graphite superlattices and the study on graphite superlattice boundaries. Finally, an outlook is made to envision the future experimental and theoretical research possibilities to unveil the mystery of this anomaly of STM, and applications of graphite superlattices are also proposed. The review and outlook work in chapters 3.1 and 3.5 are accepted for publication as a review article, while the analysis results in chapters 3.2 and 3.3 are published and the results in chapter 3.4 are under review for publication.

Chapter 3.1 Introduction to graphite superlattices

Summary

Since its invention in 1981, scanning tunnelling microscopy is well-known for its supreme imaging resolution enabling one to observe atomic-scale structures, which has lead to the flourishing of nanoscience. As successful as it is, there still remain phenomena which are observed with STM but are beyond our understanding. Graphite is one of the surfaces which have been most extensively studied with STM. However, there are a number of unusual properties of the graphite surface. First reported in the 1980s, superlattices on graphite have since been observed many times and by many groups, but as yet our understanding of this phenomenon is quite limited. Most of the observed superlattice phenomena are widely believed to be the result of a Moiré rotation pattern, arising from the misorientation between two graphite layers as verified experimentally. A Moiré pattern is a lattice with larger periodicity resulting from the overlap of two lattices with smaller periodicities. As graphite layers are composed of hexagonal lattices with periodicity of 0.246 nm as observed with STM, when there are misoriented graphite layers overlapping with each other, a Moiré pattern with larger periodicity depending on the misorientation angle will occur and appear as a superperiodic hexagonal structure on top of the graphite atomic lattice of the topmost surface layer. It is important to study graphite superlattices because firstly, knowledge of this phenomenon will enable us to properly interpret STM images; secondly, it helps us to understand the correlation between electronic structures and atomic-structure rearrangement of graphite which is of tremendous aid for engineering material properties; thirdly, and perhaps most importantly, the observation of the phenomenon exhibits the imaging capability of STM on the nature of internal defects which are below the surface.

3.1.1 Graphite as a common substrate for STM

Graphite is one of the most commonly used substrates in scanning tunnelling microscopy (STM). Being a Bernal-type structure with $\boldsymbol{D_{6h}^4}$ symmetry, graphite consists of layers of sp^2 bonded carbon atoms [44], the layers being bound together by Van der Waals forces with ABAB stacking along the c axis. Upon cleavage, the surface comprises atomically flat terraces ranging in size from a few hundred nanometres to tens of microns, and graphite surfaces are relatively chemically inert. Moreover, graphite can provide atomic resolution in STM even under ambient conditions, thus is the standard benchmark for STM

performance. It has been extensively used as a substrate for deposition of chemical and biological species [45-58].

3.1.2 Graphite superlattices

Graphite superlattices have been observed by many groups over the last two decades (e.g.[59-67]). The subject of study here is superperiodic hexagonal structures on a graphite surface whose formation is due to intrinsic defects of the substrate crystal. They arise because dislocations occur during crystal growth or cleavage. Broadly speaking, there are four situations in which superperiodic structures can be observed. Firstly, it is well known that graphite forms intercalation compounds, for example with alkali-metals or electrolytic solutions, which show large-scale periodic superstructures, such as 2 x 2 and √3 x √3 superstructures. Secondly, there is a superlattice with the size of √3 times the graphite lattice constant observed by STM, e.g. √3 x √3 R30° superstructure [68-76]. Its cause is the perturbation of charge density by steps, point defects, and grain boundaries. This structure is not a surface reconstruction where atoms are rearranged or removed from the surface. It is effectively similar to the Friedel oscillations in the charge density around an impurity, and moving away from the impurity will decrease the amplitude of the density modulation, and consequently this kind of √3 x √3 R30° superstructure is usually confined within a relatively small area of a few nanometres neighbouring to a defect. Thirdly, superstructures can be due to adsorbed species on the graphite surface. Fourthly, superlattices may be observed if there is a misorientation of one or more of the graphite layers on or near the surface. In this chapter, we will concentrate on the latter kind of superlattice.

3.1.3 Significance of studying graphite superlattices

An STM image represents the electronic structure (local density of states) of a surface, which generally closely correlates with the geometric surface topography. However, in some cases, the STM image does not show the actual atomic arrangement at the surface. One typical example is on graphite, where the STM can only observe every second atom, i.e. the carbon atoms (β sites) on a graphite surface which do not have atoms directly below them. The origin of this is that the other carbon atoms (α sites) have their electronic density of states at the Fermi level reduced by the atoms directly below them. Another example is the charge density waves observed on some low dimensional materials, such as TaS_2 and $NbSe_3$, resulting from the atomic displacement of a few tenths of an angstrom which induces

patterns superimposed onto the atomic lattice in the STM images [77-79]. It is important to understand how to interpret STM images, therefore superlattices observed on graphite surfaces is an important subject to study as it is believed that a superlattice is a direct consequence of the interlayer electronic interaction of the topmost surface with the bulk, rather than an actual topographical feature. Such an electronic interference exhibits a potential problem for imaging deposited species on graphite, particularly, if the deposited molecules form periodic structures on the graphite surface. Graphite is commonly used for deposition of various kinds of molecules or biological samples in STM experiments. In order to properly distinguish the presence of deposited materials on the graphite surface from the apparent modification in the atomic corrugation of graphite induced by the electronic interaction of the surface layer with the layers which are a few layers underneath, it is of paramount importance to understand the origin of the formation of graphite superlattices and the relationship between the superlattice pattern and the interlayer interaction.

Another reason for studying graphite superlattices is their interesting electrical properties. The electronic properties of graphite are changed with the modification or intercalation of the basic AB-stacked Bernal structure, and as a consequence the electrical properties can be varied from insulator to superconductor [80]. As a superlattice involves the rotation of a graphite layer and modifies the graphite Bernal structure to include simple hexagonal and rhombohedral graphite structures, studies of superlattices will help us to understand the correlation between electronic structures and atomic-structure rearrangement of graphite which is of tremendous aid for engineering material properties. In this respect, STM studies on superlattices can provide information on the LDOS and atomic images to reveal such a correlation.

Perhaps the most intriguing and potentially useful aspect of graphite superlattices stems from the fact that the observation of a superlattice structure on graphite surface indicates that the STM, in addition to its imaging capability on the topmost surface, can potentially investigate the nature of internal defects which are in the bulk of the sample. This imaging capability of STM is not well studied. Our knowledge on superlattices will enable us to understand this respect of STM functionality better.

3.1.4 Observation of graphite superlattice under STM

3.1.4.1 Large-scale features observed on graphite under STM

Graphite has been commonly used as a substrate in STM experiments since the invention of STM, as it offers many advantages for surface science research. However it does not come without drawbacks. Since 1990, there has been growing concern about various kinds of surface features associated with graphite. Although images illustrating the capability of the STM to resolve the helicity of DNA were presented [46, 81-83], Clemmer and Beebe discussed the ambiguities of graphite as a substrate for biological studies and reported the observation of regular periodicity from features that appear to meander across a freshly cleaved blank graphite surface [84]. Chang and Bard completed a comprehensive study on various kinds of surface features which are frequently observed upon cleavage of graphite [85]. Here we present a brief review of graphite surface defects as they are closely related to the occurrence of superlattices; indeed, most superlattices are observed next to defects.

First of all, the common types of crystal dislocations are reviewed. Edge dislocations and screw dislocations are the basic types of dislocations, while mixed dislocations are mixture of both. Edge dislocations and screw dislocations are commonly observed on graphite by STM.

Edge dislocation

An edge dislocation is caused by the insertion of an extra half-plane of atoms. The position of the dislocation is shown in Fig. 3.1.1(a) where there is a termination of an extra vertical half-plane of atoms. This kind of dislocation is mobile because of the mechanism described in Fig. 3.1.1(b). When there is an applied stress, the lattice at first strains elastically and the bonds in the dislocation region are distorted even more. Eventually, the stretched bonds in the dislocation region break, then new bonds form between these atoms and others that are at or near the correct distance apart for an unstrained lattice. In this way, part of the crystal slips one interatomic distance with respect to the other part. This process is repeated. The bonds usually break and reform one at a time, so that the amount of strain energy stored in the crystal at any one time is small. Once the dislocation has passed completely through the crystal in this way, the lattice is left internally strain-free (the half plane has moved to the outer edge of the crystal), although the crystal itself has undergone a permanent, plastic deformation. Movement of dislocations in this way is called dislocation glide or slip.

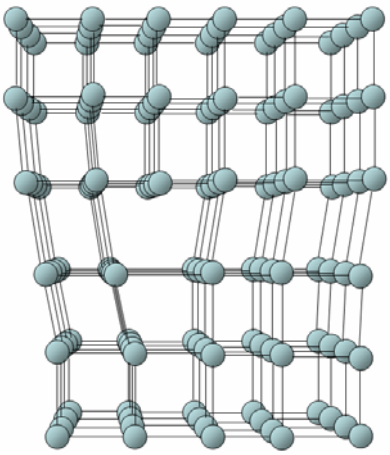

Fig. 3.1.1(a). Structure of an edge dislocation. The dislocation is caused by the occurrence of an extra plane of atoms on the upper half of the crystal lattice. The spacing between the atoms in the upper half are compressed by the extra plane whereas those in the lower

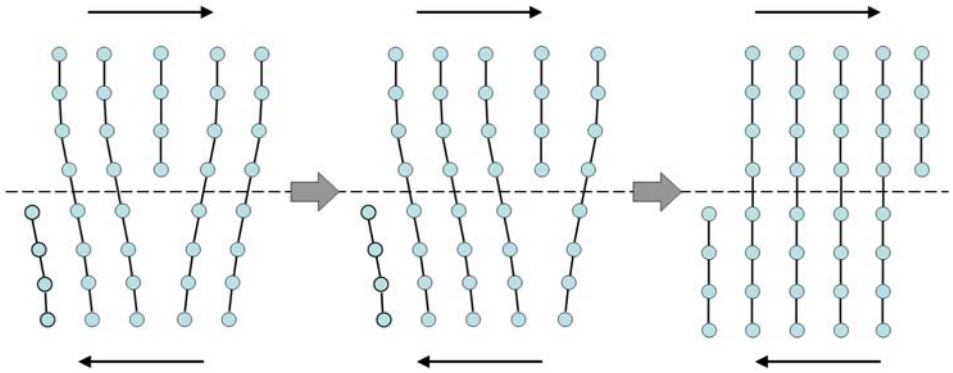

Fig. 3.1.1(b). Shifting of an edge dislocation under stress moves the upper half of the structure to one direction whereas the lower half to the other. As such, the dislocation is moved from the inside of a crystal to its outer edge.

Screw dislocation

Another simple kind of dislocation is the screw dislocation, sketched in Fig. 3.1.2(a) and 3.1.2(b). The formation of a screw dislocation can be imagined as a plane terminating at the dislocation line, above which the crystal is displaced by a lattice vector of one atomic spacing in a direction in parallel with the dislocation line, instead of lying perpendicular to it as for the edge dislocation. A screw dislocation transforms successive atomic planes into the surface of a helix; this is the origin of the name of the dislocation.

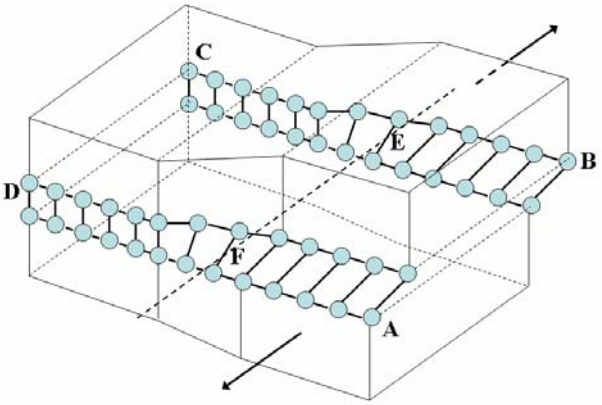

Fig. 3.1.2(a). Structure of a screw dislocation. A part of the crystal ABEF has slipped in the direction parallel to the dislocation line EF.

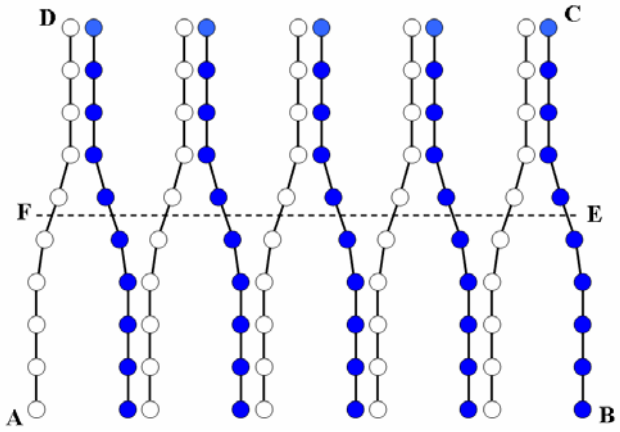

Fig. 3.1.2(b). Plan view of a screw dislocation. A screw dislocation can be viewed as a helical arrangement of lattice planes. The plane is changed as we go completely around the dislocation line.

Mixed dislocation

A mixed dislocation is a combination of an edge dislocation and a screw dislocation as illustrated in Fig. 3.1.3. In practice, most of the dislocation systems are mixed dislocations.

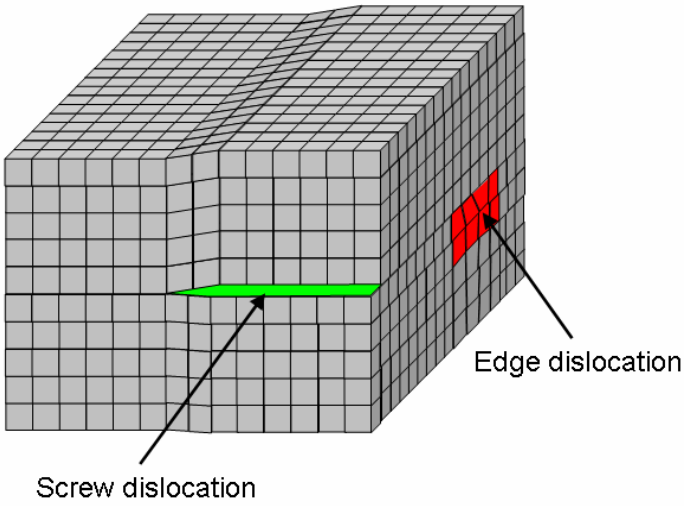

Fig. 3.1.3. A mixed dislocation is a combination of an edge dislocation (red) and a screw dislocation (green).

Since dislocations cannot end within a crystal, they must either form dislocation loops or reach the surface. That is where we can see them by STM. For an edge dislocation, if its dislocation line is perpendicular to the surface and leads into the crystal bulk, we will only see its end in the STM images as illustrated by the atomic arrangement in Fig. 3.1.4. If an edge dislocation is moved entirely through the crystal and its dislocation line is in plane with the surface, we will see the dislocation in form of a step edge in the STM images as shown

schematically in Fig. 3.1.5. For a screw dislocation, it will look like a step edge starting at the dislocation core (dislocation line) in STM images as we can see in Fig. 3.1.6.

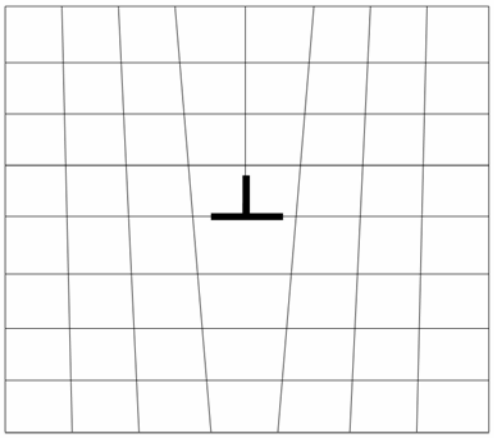

Fig. 3.1.4. The dislocation line of the edge dislocation is perpendicular to the surface and leads into the crystal bulk. Therefore we cannot see the edge dislocation in STM images. STM images will show the atomic arrangement around the dislocation indicated by the ⊥ symbol. The dislocation line is pointing into the paper from the ⊥ symbol.

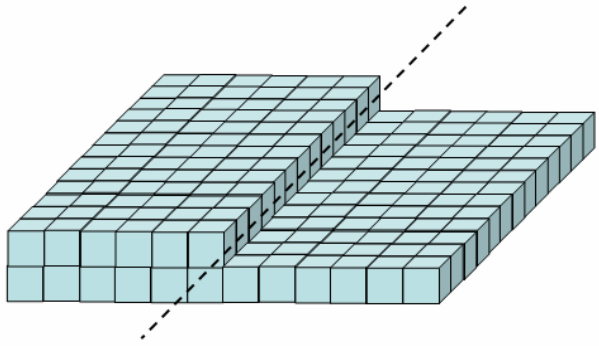

Fig. 3.1.5. The dislocation line (dashed line) of the edge dislocation is in plane with the surface, and thus we can see the edge dislocation in the STM images. The edge dislocation manifests itself as a monoatomic step edge.

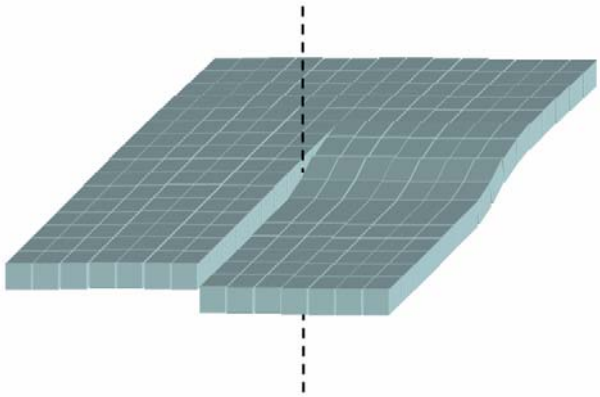

Fig. 3.1.6. In STM images, a screw dislocation is observed as a step edge emerging from its dislocation line (dashed line).

Fig. 3.1.7 shows the summary of the types of large-scale features often observed on graphite surfaces. The classification was conducted by Chang and Bard in 1991 [85]. Such a classification is not exhaustive as structures have been observed that cannot be classified into any of these categories. There are seven categories in total: 1) Cleavage steps [Fig. 3.1.7(a)]. They can either be perfect steps [left of Fig. 3.1.7(a)] or distorted steps [right of Fig.

3.1.7(a)]; (2) Ridges [Fig. 3.1.7(b)]; (3) Graphite strands [Fig. 3.1.7(c)], which are often irregular in shape; (4) Graphite fibres and fibre clusters [Fig. 3.1.7(d)]; (5) Folded-over flakes [Fig. 3.1.7(e)], pieces of graphite attaching to the cleavage steps where they are originated. Superlattice structures due to Moiré rotation can often be observed on these folded-over flakes as there is usually a misorientation angle between the flake and the substrate. The folding over of graphite layers can be made use of in the preparation of a superlattice which will be discussed in section 3.1.4.6.(VI); (6) Broken pieces [Fig. 3.1.7(f)], graphite pieces completely detached from the substrate and are often in the form of a sheet; (7) Ultrasmall carbon particles [Fig. 3.1.7(g)], broken carbon pieces with size of one to a small number of carbon atoms.

In our STM measurements, another large-scale feature on graphite, related to superlattices was imaged. They are 1-D fringes with periodicities of 20 nm and 30 nm and corrugations of 0.1 nm and 0.15 nm observed on a superlattice. It is believed that these fringes are reflecting the actual surface topography of graphite accompanied by the superlattices underlying and nearby. This feature on graphite superlattices was not reported before, we will give our interpretation and analysis on it in chapter 3.2.

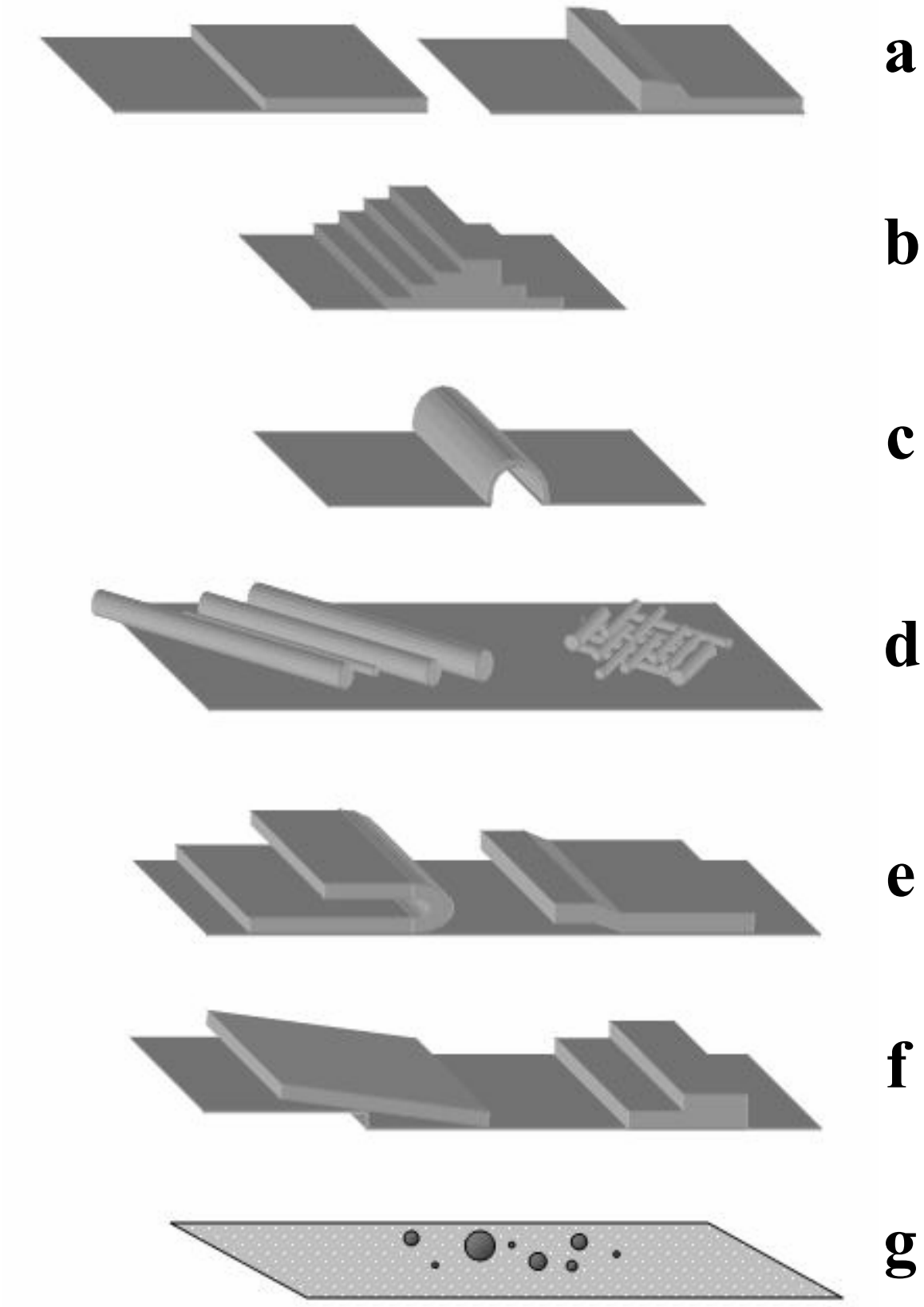

Fig. 3.1.7. Schematic illustration of various kinds of surface defects observed on cleaved HOPG graphite. Categorization here follows the classification scheme proposed in [85]. (a) cleavage steps; (b) ridges; (c) graphite strands; (d) fibres and fibre clusters; (e) folded-over flake and piece; (f) broken graphite pieces; (g) broken carbon particles.

3.1.4.2 Experimental procedures and results

Most of the literature on graphite superlattices reports observations of freshly cleaved HOPG surfaces. As pointed out by Chang and Bard [85], HOPG surfaces cleaved by adhesive tape contain a larger coverage of defects than those cleaved by a razor blade. Since the occurrence of a superlattice is closely related to defects, graphite surfaces cleaved with adhesive tape are more likely to exhibit superlattice structures. Mechanically cut Pt/Ir tips were commonly used in experiments, although there were a few exceptions of using etched gold tips [86], etched tungsten tips [74, 86-90], etched Pt/Ir tips [64, 91, 92], heteropolyacid (HPA) – functionalized Pt/Ir tips [93], and silicon tips [67]. Apparently the tip material does not affect the observed superlattice structures. The experiments were mostly conducted under ambient conditions, although some were under ultrahigh vacuum conditions [65, 90, 91, 94], Oden *et al*. [92] imaged graphite under triply distilled 18MΩ water. Except for achieving atomic resolution on the underlying graphite atomic lattice, constant current mode was generally used to image superlattices (except [87, 95] where constant height mode was used). Various tunnelling conditions have been used, with bias voltages ranging from 10 mV to 650 mV, and tunnelling current from 0.09 nA to 5.6 nA. The periodicity of observed superlattice structures ranges from 1.7 nm to 44 nm, with corrugation from 0.5 Å to 20 Å. Table 3.1.I is a list of the reported tunnelling conditions and the corresponding observed superlattices' periodicities and corrugations.

Fig. 3.1.8(a) and Fig. 3.1.8(b) show typical superlattices observed on graphite with the STM. In Fig. 3.1.8(a), the region to the right of the sharp boundary with a straight array of bright beads exhibits a hexagonal giant lattice with periodicity of 3.8 nm, a superlattice. The superlattice extends over an area of 500 nm x 500 nm. Superlattices generally measure a few hundred nanometres up to a micrometre across [87]. A zoom-in of Fig. 3.1.8(a) is displayed in Fig. 3.1.8(c) where the hexagon shows a unit cell of the superlattice. Superlattices have three-fold symmetry similar to the graphite atomic lattice, and in a superlattice unit cell, there are three brightest spots, three medium bright spots, and one dark hole. Various kinds of notations are used to denote these different sites of a superlattice unit cell, for instance: white spots, grey areas, dark areas [67]; peaks, valleys [63, 80]; g-β-site, g-α-site, g-h-site [67]. Despite such a variety, basically, in a superlattice unit cell, there are three levels of electron density of states, with three spots being the highest, three being the medium, and one being the lowest, which in fact is analogous to the graphite atomic lattice where a unit cell consists of three brightest β sites, three medium bright α sites, and one dark hole site. The three-fold symmetry of superlattices will be discussed in section 3.1.4.5. Fig. 3.1.8(b) is another closer

view of the superlattice where the atomic resolution is shown. The orientation between the giant and atomic lattices is ~28º, which agrees with the prediction by Moiré pattern assumption for a superlattice with periodicity of 3.8 nm. The relationship between the periodicity of a superlattice and its rotation angle and orientation will be delineated in section 3.1.4.5.

STM images of superlattices have been reported to be stable over a period of more than 30 hours [63]. Also, superlattice structures have been observed to be independent of the variations of scan size (10 to 396 nm), scan rate (3.13 to 78.13 Hz), and image modes in the same experiment [64].

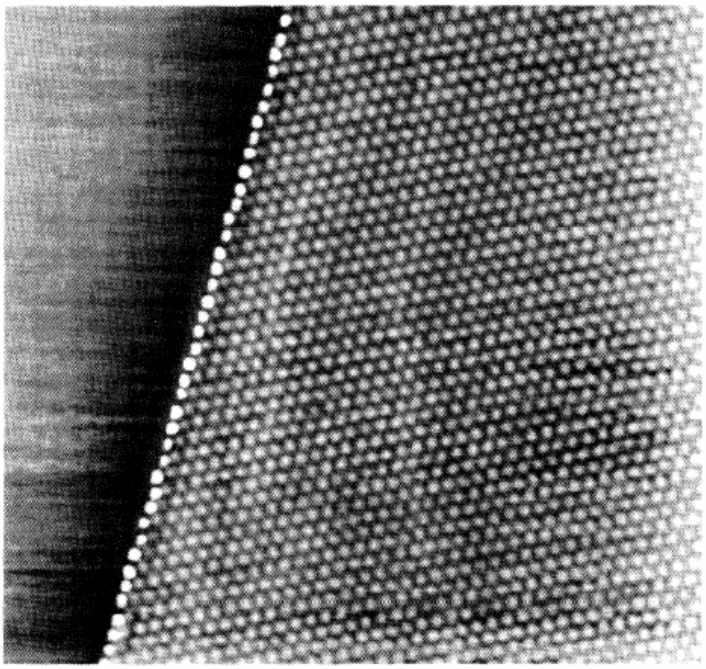

Fig. 3.1.8(a). 160 nm x 160 nm. On the left of the image, there is a sharp boundary separating the superlattice from normal graphite. The superlattice on the right has a hexagonal symmetry with periodicity of 3.8 nm. Image reprinted from [67].

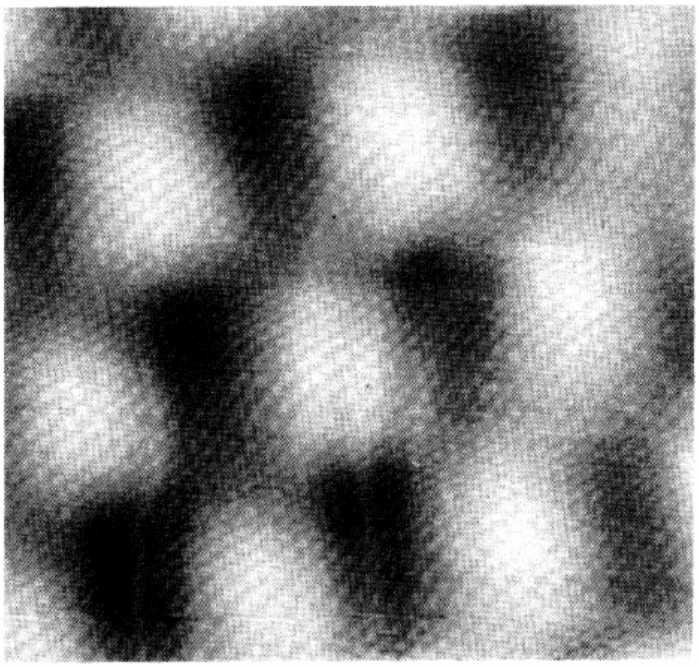

Fig. 3.1.8(b). 10 nm x 10 nm image which shows the superlattice and atomic lattice simultaneously. Image reprinted from [67].

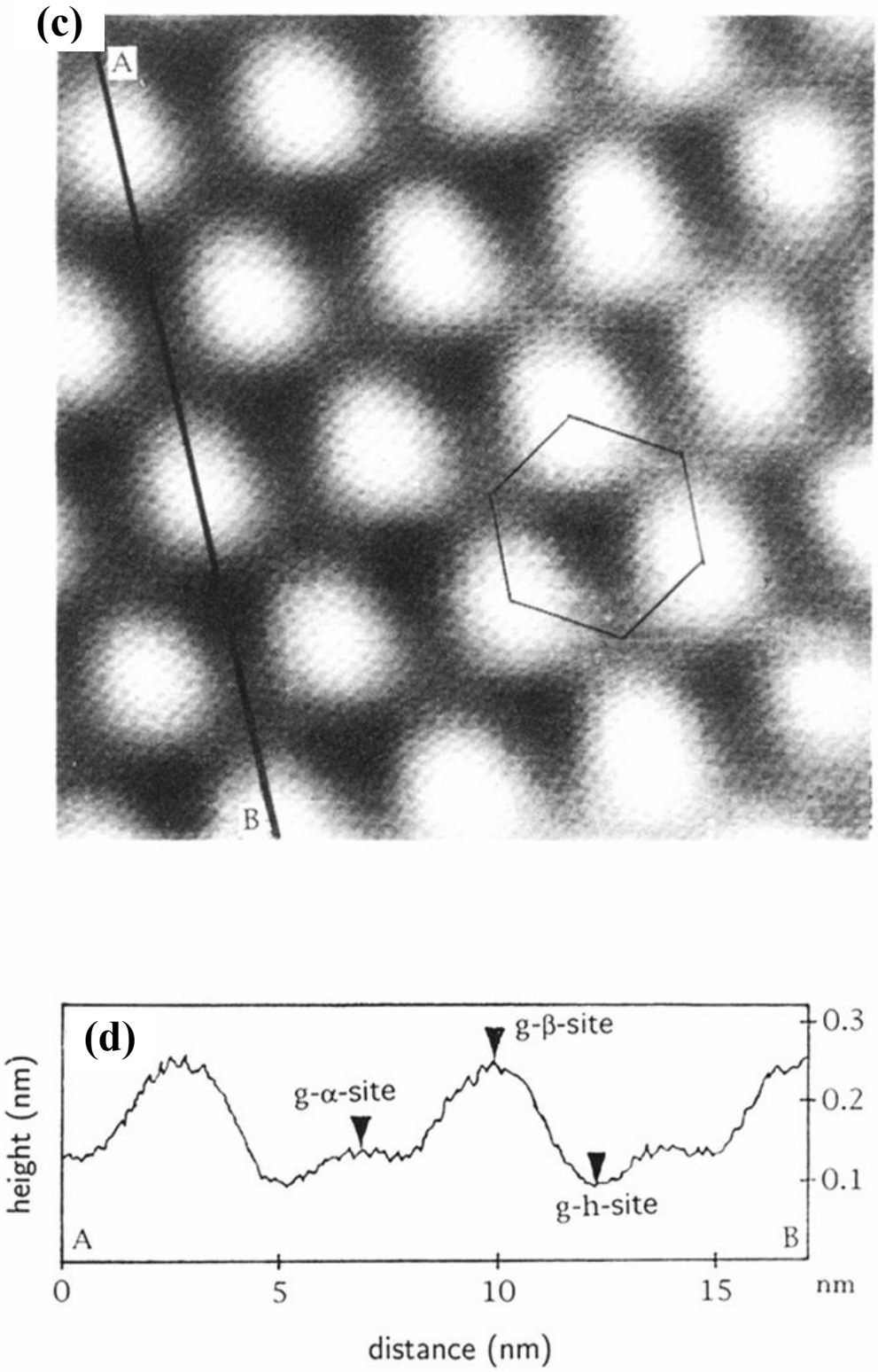

Fig. 3.1.8(c). A STM image (17 nm x 17 nm) on a graphite superlattice with periodicity of 3.8 nm. The hexagon shows a unit cell of the superlattice. Similar to graphite atomic lattice, there are three different sites with different heights (compared to the hole sites) in a superlattice unit cell. Image reprinted from [67].

Fig. 3.1.8(d). A line profile along the line AB in Fig. 3.1.8(c). We can see that the g-β-site, g-α-site and g-h-site are of different heights with the g-β-site being the brightest in the STM image. Image reprinted from [67].

Table 3.1.I. The tunnelling conditions for imaging superlattices with STM reported in the literature with the corresponding observed superlattices' periodicities and corrugations.

Source of data	Bias voltage (V) mV	Tunnelling current (I_t) nA	Superlattice periodicity (D) Å	Superlattice corrugation (ΔZ_s) Å	Atomic corrugation (ΔZ_a) Å
[65]	100	2	82	0.85±0.15	1.2
[60]	500 – 650	0.8 – 3.5	35±5	3±0.4	-
[89]	150	-	50±2	0.5	-
[96]	-	-	110	20	-
[97]	0.01	3	15	2	-
[98]	230	0.5	-	-	-
[98]	450	0.36	-	-	-
[98]	206	0.5	-	-	-
[99]	-	-	70.3	-	-
[100]	-	-	35	-	-
[100]	-	-	85	-	-
[86]	20	0.8	300	15	-
[86]	50	1	300	-	-
[86]	20	0.8	24	-	-
[86]	20	1.5	42	-	-
[62]	100	1	35	-	-
[66]	490	2.3	66	-	-
[66]	535	5	66	1*	0.4
[66]	72	5	66	2.6	0.6
[67]	-500 to +200	4.5	38^{ϕ}	12 – 14	2 – 3
[67]	-500 to +200	4.5	150^{ϕ}	1	-
[87]	33	0.4	60	-	-
[87]	30	0.26	117 – 124	-	-
[87]	43	0.19	117 – 124	-	-
[87]	50	1.2	117 – 124	-	-
[87]	80	0.35	117 – 124	-	-
[87]	4.9	0.4	96*	-	-
[91]	100	0.8	180 – 720	-	-
[63]	75	1	77±2	10 – 15	-
[63]	102	1	77±2	-	2±1
[80]	125	1	36	$0.6^{\#}$	0.35
[80]	15	0.8	36	1.7	-
[80]	72	5.6	66	2.3	-
[80]	180	0.9	36	0.4*	-
[80]	20	0.8	36	1*	-
[90]	100	1	80	3.8	-
[90]	100	1	80	$1.6^{\#}$	-
[88]	150	1.1	105±5	2.6±0.1	0.36±0.04
[94]	480	0.6	40±1	-	-
[94]	210	0.6	40±1	-	-
[94]	60	0.6	60 – 100	2 – 4*	-
[92]	100	1	148	2.1	-
[92]	100	1	105	2	-
[92]	100	1	50	5	-
[92]	100	1	440	5	-

[64]	20.1	2	44±2	3.8±0.2	-
[64]	178	2.4	44±2	-	0.8
[101]	93	0.09	54±1	1.4±0.5	-
[61]	100	2	39±4	-	-
[59]	-	-	17.6	-	-
[59]	-	-	21.7	-	-
[95]	20	1.9	17.1	-	-
[95]	30	0.7	91	-	-
[102]	-50 to +100	0.5 – 5	31	-	-
[102]	-50 to +100	0.5 – 5	77	-	-
[102]	-50 to +100	0.5 – 5	59.5	-	-
[102]	-50 to +100	0.5 – 5	10.6	-	-
[102]	-50 to +100	0.5 – 5	12	-	-
[71]	-	-	√3 x 2.46	-	-
[74]	-	2	√3 x 2.46	-	-
[76]	3 – 160	1.5 – 14	1.5 x 2.46	-	-
[70]	48	3.2	√3 x 2.46	-	-
[68]	-300 to +300	0.1 – 0.5	√3 x 2.46	-	-
[69]	100	1	√3 x 2.46	-	-
[73]	100	1	√3 x 2.46	-	-
[75]	100	1	√3 x 2.46	-	-
[103]	50	1	101 – 760	-	-
[103]	150	1	60±1	-	-
[103]	20.1	1	52±2	-	-
[104]	-500 to +500	1	7.5	-	-
[105]	-	-	70 x 2.46	-	-
[106]	-	-	√3 x 2.46	-	-
[107]	1200	-	81	0.75	-
[107]	1200	-	81	0.35[#]	-
[107]	222	-	8.7	-	-
[107]	700	-	192[ϕ]	-	-
[107]	700	-	32.5[ϕ]	-	-
[107]	703	-	71	-	-
[107]	698	-	48	-	-
[107]	703	-	81	1.5	-
[107]	703	-	24	0.5	-
[107]	689	-	76	3	-
[107]	689	-	76	0.55	-
[107]	770	-	44	-	-
[108]	20	0.02	88	-	-
[108]	20	0.02	125	-	-
[109]	84	-	35	-	-
[110]	30	2	22	-	-
[93]	100	1.5	70.4	-	-
[93]	100	1.5	14.97	-	-

*values measured from the figures, as they are not provided in the text
[#]corrugation covered with one overlayer
[ϕ]superlattices superimpose with each other

3.1.4.3 Proposed explanations on origin of superlattice

Superlattices on graphite is an intriguing phenomenon in the STM, and some proposals have been made to explain its origin of formation. The origin of superlattices is attributed to a network of dislocations, physical surface deformation, multiple tip effect, adsorption of impurities, bond shortening, Moiré rotation pattern, and nanoscale defects in the subsurface. The Moiré rotation pattern assumption, supported by experimental evidence as discussed in section 3.1.4.4, is the most widely accepted explanation to superlattices on graphite.

3.1.4.3.(I) Twist subboundary by a network of dislocations

Garbarz *et al*. [62] interpreted the superlattice as the twist boundaries in the basal plane of graphite. They stated that the superlattice consists of a twist boundary which is formed by a "honeycomb" network of dislocations, located in a basal plane a few Angstroms underneath the surface. A model was proposed for this theory as shown in Fig. 3.1.9 which schematically shows the atomic displacement in a basal plane just above such a boundary. The dislocation splitting is not considered in this model. The dislocation segments of the honeycomb network have the Burgers vectors of the lattice constant (**b** = 0.246 nm) and have a screw orientation. The translation vectors **d** and the dislocation segments are perpendicular to each other in the dislocation network. The misorientation angle of the twist boundary can be found by $\theta \approx b/d$. Bernhardt *et al*. [94] also attributed the appearance of the superlattice with non-constant periodicity observed on the stressed graphite islands to the presence of a network of dislocations.

The evidence to support this explanation is their observation of a kink along the atomic row each time the row traverses across from one bright superlattice spot (higher local density of states) to another, which agrees with their model of the honeycomb network of dislocations [62]. However, such a kink can also be explained by the odd-even transition theory proposed by Osing *et al*. on a superlattice, based on the Moiré rotation assumption [65]. The theory states that when the Moiré rotation-pattern induced superlattice is formed by one graphite monolayer, an atomic row should be wavy in pattern as it goes from one bright superlattice spot to another, and this theory is further supported by the simulation work which will be described in chapter 3.3. The odd-even transition theory will be further discussed in section 3.1.4.6.(VII).

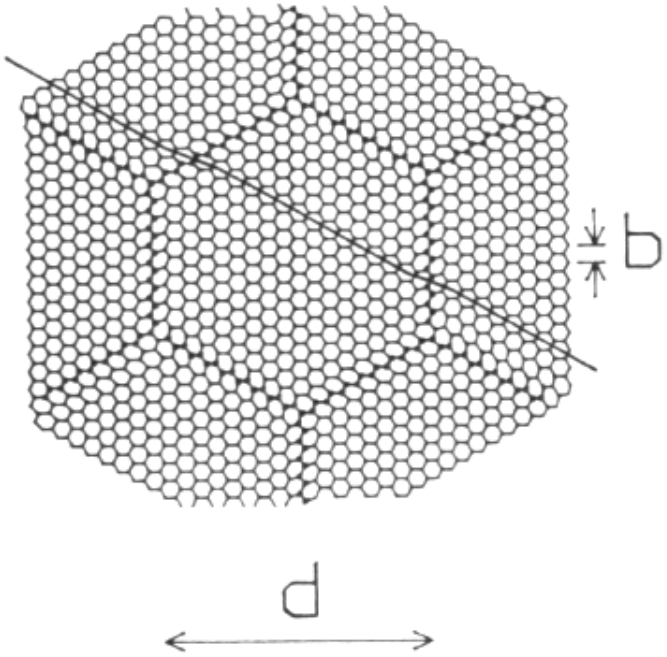

Fig. 3.1.9. The honeycomb network of dislocation. The atomic displacement in a graphite layer close to a twist boundary is shown. The small hexagonal rings are the atomic lattice of graphite. The line traverses across the lattice indicates a kinked atomic row. **b** is a translation of the lattice and **d** is a translation of the dislocation network. Image reprinted from [62].

3.1.4.3.(II) Physical buckling of surface

It is intuitive to interpret STM superlattice structures as the corrugation reflecting a physical buckling of the top graphite layer. A simple rigid-sphere intuition of graphite atoms inclines us to think that the interlayer spacing of AA-stacked graphite would be larger than that of AB-stacked graphite, because it is appealing to perceive that the AA stacking of graphite would be repulsive as each atom on the first layer has another atom directly underneath it. Rong *et al*. [66] have shown that this proposal does not fit. First of all, according to the *ab initio* calculation by Charlier *et al*. [111], hypothetical graphite with AA stacking has essentially the same interlayer spacing as AB stacked graphite. The diffraction study of CAB-stacked orthorhombic graphite by Lipson *et al*. [112] also shows the same interlayer spacing. In addition, although rolling up a stiff sheet like graphite or paper does not require much energy, physically buckling a surface where the sheet is alternately expanded and compressed needs much more energy. In view of these, the corrugation of a superlattice is unlikely to represent the real atomic arrangement.

The first-principle calculation by Charlier *et al*. [111] found the compressibility of bulk AAA graphite along the c axis to be six times lower than that of AB stacked graphite. Thus a difference in the deformability of the different stacking structures can possibly explain superlattice structures. Nevertheless, the experimental result of Rong *et al*. [66] disproved this possibility as the superlattice they observed had a corrugation of 2.6 Å and it was formed by a rotated graphite monolayer located 3.3 Å (very close to the ideal interlayer spacing 3.35

Å, which means the deformation, if there is any, must be very small) above a common substrate and deformability effect was much smaller than the superlattice corrugation.

3.1.4.3.(III) Multiple tip effect

When the graphite superlattice was first observed in 1987, its cause was attributed to a multiple tip effect [59]. It was suggested that because of the microscopic roughness of the tip, two or more minitips may exist at the end of the tip, and when these minitips are very close or in contact with the surface, the repulsive forces arising from this contact will maintain these minitips at equal heights, thereby the relative contribution of the tunnelling current from these minitips can be approximately the same. As such, the resulting STM image would be the superposition of the images from each minitip. If the multiple tips lie in more than one grain domains with different orientations of the atomic lattices simultaneously, the Moiré pattern would arise and result in the superlattice structure as observed on the graphite surface under the STM.

However, the images having two domains showing both normal atomic resolution and long-range periodicities along the grain boundaries is beyond the explanation by using the multiple tip effect model (Fig. 2(a) in [103]). It is rather improbable that two minitips resolving atomic lattice contribute the same amount to the tunnelling current. In addition, this model fails to explain why such superlattice structures are not observed on other surfaces that contain grain boundaries.

3.1.4.3.(IV) Adsorption of impurities

In most cases the graphite samples were cleaved in air and the STM images were taken under ambient conditions, so it is intuitive to conceive that some gas or liquid could be adsorbed onto the graphite surfaces, producing the superlattice structures. In the work of Kuwabara *et al*. [63], both superlattice structure and underlying atomic lattice were imaged simultaneously, and this excluded the possibility that the superlattice they observed was due to adsorbed species. Also, superlattices have been observed under UHV conditions.

3.1.4.3.(V) Dangling bonds at step edges leading to bond shortening

Buckley *et al*. [87] suggested that the breakage of carbon-carbon bonds at step edges creates dangling bonds, where the valence electrons pair up and increase the double bond character of the surrounding carbon bonds. Since the double bond electrons are delocalized in

graphite due to its conjugated structure, the increase in double bond character can spread over a large area and give rise to shortening of carbon-carbon bonds. In this way, some regions of the topmost layer could become reduced in size compared with the bulk graphite. This change in size can induce the Moiré pattern without rotational misorientation between graphite layers. Even a few percent reductions in bond lengths could bring about large-scale periodicity as seen under the STM. However, not much experimental evidence or theoretical work has followed to support this hypothesis.

3.1.4.3.(VI) Moiré rotation pattern assumption

Later Kuwabara *et al*. and Liu *et al*. proposed another explanation that the observed superperiodic structure is a rotational Moiré pattern resulting from the overlap between a misoriented layer of graphite and the graphite crystal underneath [63, 64]. The interlayer rotation is possibly caused by the cleavage step with a shear force or an epitaxial rotation in the growing process of graphite. The Moiré pattern [113, 114] assumption provides a good explanation for the observed periodicities of the superlattices in terms of the rotation angle between the graphite layers.

Moiré patterns, which are well-known from optics, are interference patterns resulting from rotation between two layers of any regular lattice (see [115] for a detailed description of Moiré patterns). When the two layers of lattice are rotated with respect to each other, interference occurs and it creates a superperiodic structure which shares the same symmetry as the original lattice on the two layers. This superperiodic structure is what is known as a superlattice. The periodicity of this superlattice is dependent upon the rotation angle between the two original lattices. Fig. 3.1.10 visualizes a Moiré pattern formed by overlapping two lattices with identical hexagonal patterns and rotating them with respect to each other. The periodicity D of the resulting Moiré superperiodic hexagonal structure is related to the rotation angle θ between the two layers of hexagonal lattice by

$$D = d/[2\sin(\theta/2)], \quad (3.1.1)$$

with d being the lattice constant of the smaller hexagonal lattice. The orientation of the Moiré pattern ϕ with respect to the atomic orientation of the top layer is related to the rotation angle θ by

$$\phi = 30^\circ - \theta/2. \quad (3.1.2)$$

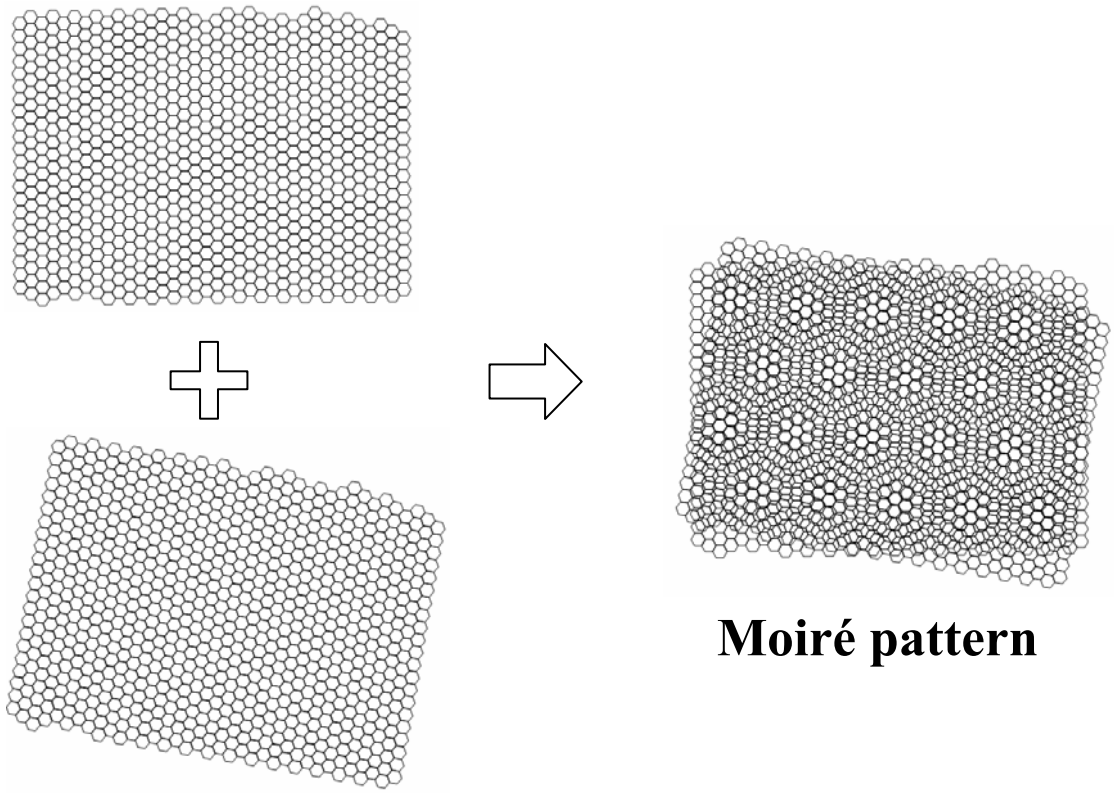

Fig. 3.1.10. Visualization of Moiré pattern. There are two sets of hexagonal lattices with a misorientation angle of ten degree between them, when they are overlapped together, another hexagonal lattice with larger periodicity appears, which is the resulting Moiré pattern.

3.1.4.3.(VII) Nanoscale defects a few layers underneath the surface

Demonstrated by numerical calculations, Kobayashi proposed that, on the basis of three-dimensional tunnelling of STM, nanoscale electronic waves can propagate through many layers without decay due to the typical value of Fermi energies, which means nanoscale structures can be observed in STM even if they are buried a few layers underneath the surface [116]. With this in mind, it is possible that a network of nanoscale defects in the subsurfaces can manifest itself on the topmost surface and modify the density of states, leading to the formation of a superlattice. No direct experimental proof was reported in this respect so far. The corrugation conservation phenomenon to be reported in chapter 3.2, which cannot be explained by Moiré rotation pattern, may be an example of the nanoscale waves propagating many layers without decay. Kobayashi also demonstrated numerically that when the tip-sample distance is short, only the atomic structure of the topmost layer is seen in STM images, and as the distance increases, the Moiré pattern becomes distinct. This simulated result is opposite to the experimental result of Osing *et al*. [65] that they observed the

superlattice when the tip was close to the surface, while only graphite atomic lattice was imaged when the tip-sample distance was increased. This experimental result of Osing *et al*. will be discussed again in section 3.1.4.6.(IV).

3.1.4.4 Experimental results verifying the Moiré rotation pattern hypothesis

Kuwabara *et al*. [63] worked out the relative orientation ϕ between the atomic lattice and the superimposed superlattice, and the periodicity D of the superlattice from STM images. By eq. (3.1.1) the rotation angle for a Moiré pattern to produce a superlattice with the periodicity D was calculated (with **d** being the graphite atomic lattice constant 0.246 nm), which matches with the rotation angle found by eq. (3.1.2) considering the relative orientation of the Moiré superlattice ϕ. This is consistent with the Moiré rotation pattern assumption.

Rong *et al*. [66] did a similar experiment as Kuwabara. Rong *et al*. looked at the rotation of the atomic corrugation in the superlattice region with respect to the exposed second layer and the normal graphite region next to the superlattice by imaging the surfaces with atomic resolution. This rotation angle was found to match with the result calculated by substituting the periodicity of the superlattice, which can be measured from the STM image, and the already known graphite atomic lattice into the Moiré pattern equation [eq. (3.1.1)]. Moreover, the superlattice was found to be rotated about 30 degrees with respect to the atomic lattice orientation, which agrees with the predicted orientation for a Moiré pattern by eq. (3.1.2).

In Beyer's experiment [60] a graphite topmost monolayer was torn apart during the sample cleaving, and this layer folded back onto the substrate. By simultaneously imaging the part of the graphite covered by the rotated layer and the part not covered by such a layer, Beyer *et al*. investigated whether the Moiré rotation pattern assumption is the correct explanation for a superlattice. Their results unambiguously show that only the overlapping area with a rotation angle between the two successive layers exhibited the superlattice structure whereas the area not covered by the rotated layer just showed the normal graphite lattice structure. The rotation angle θ between the two neighbouring layers was measured from the STM image and, knowing the atomic lattice constant d of graphite, the superlattice periodicity D was calculated and found to agree with that observed in the STM image. Gan *et al*. [61] did a similar experiment but they used the tip to tear off the graphite layer and fold it back onto the substrate. The misorientation angle between this folded-back graphite layer

and the substrate graphite crystal induced a superlattice with the periodicity as predicted by the Moiré rotation pattern assumption, again confirming the validity of the Moiré hypothesis.

These experimental results indicate that the Moiré rotation pattern assumption can successfully explain the origin of many of the superlattices observed on graphite.

3.1.4.5 Symmetry of superlattices (from the perspective of Moiré patterns)

Graphite superlattices have hexagonal symmetry, similar to the graphite atomic lattice in the sense that in a superlattice unit cell there are also three different sites; Xhie *et al*. have provided elucidation on this [67]. Xhie *et al*. used g-h-site, g-α-site, and g-β-site as notations for the "hole site" (darkest in STM superlattice images), "α site" (second brightest), and "β site" (brightest) in a superlattice respectively to avoid confusion with those in the atomic lattice [Fig. 3.1.8(d)].

The symmetry of the superlattice can be explained by considering the layered structure of graphite [67]. Graphite is normally made of ABAB… stacking where each alternate layer is laterally shifted by one nearest-neighbour distance, and carbon atoms in each layer are in the form of a honeycomb structure. The three-dimensional schematic drawing of the first three graphite layers is shown in Fig. 3.1.11(a). The shifting between alternate layers can be more easily seen from the plan view in Fig. 3.1.11(b). Every alternate atom on the top layer has an atom directly below and these atoms on the top layer are notated as α sites while the other atoms which do not have atoms directly underneath them are β sites. The graphite surface is composed of two hexagonal lattices: an α sublattice consisting of α sites; and a β sublattice consisting of β sites. Looking along the direction of the arrow in Fig. 3.1.11(b) will give out the side view shown in Fig. 3.1.11(c). When a twist boundary occurs and the top layer is rotated, the original normal ABAB… stacking of graphite is distorted to CABAB…, where C is the notation for the rotated top layer. The misorientation between the top layer with stacking C and the second layer with stacking A induces a Moiré pattern which appears as the superlattice structure under the STM. By looking at the vertical alignment of the top layer atoms with the second layer atoms, we can categorise the atoms on the top layer into three groups. The model in [67] illustrates this categorization. Fig. 3.1.11(d) shows the top C-layer rotated 3.5° with respect to the underlying A-layer. The large solid circles and the large dashed circles are of different kinds of regions with different atomic arrangements. In the large solid circles, each α atom in the A layer has an atom in the C layer directly or partially above it whereas in the large dashed circles, each β atom has an atom in the C layer directly or partially above it. In this way, the sublattice contributed by the large

solid circles and another sublattice established by the large dashed circles form the two hexagonal lattices, composing the large honeycomb structure of the Moiré pattern, which is similar to graphite atomic structure where the structure is composed of the hexagonal lattice of α sites and the hexagonal lattice of β sites. The giant honeycomb in Fig. 3.1.11(d) is a unit cell of the Moiré pattern. The following notations for the honeycomb structure are used: "M-α-sites" for the centres of the large dashed circles; "M-β-sites" for the centres of the large solid circles; and "M-h-sites" for the centre of the giant honeycomb. This is the reason for the Moiré pattern to display a hexagonal symmetry with three different sites in a unit cell. This symmetry comes from the difference between α and β sites of the second layer, and this explains the similarity between the atomic structure and the superlattice structure of graphite.

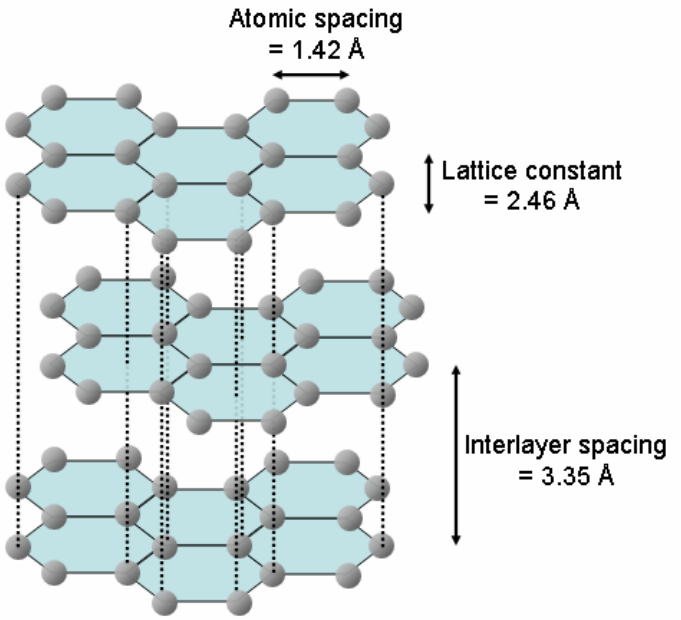

Fig. 3.1.11(a). A schematic drawing for three layers of graphite

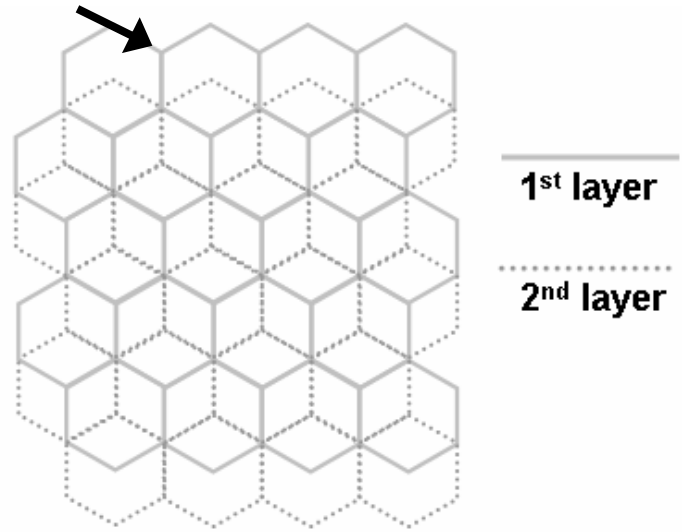

Fig. 3.1.11(b). The plan view of the two neighbouring layers of graphite

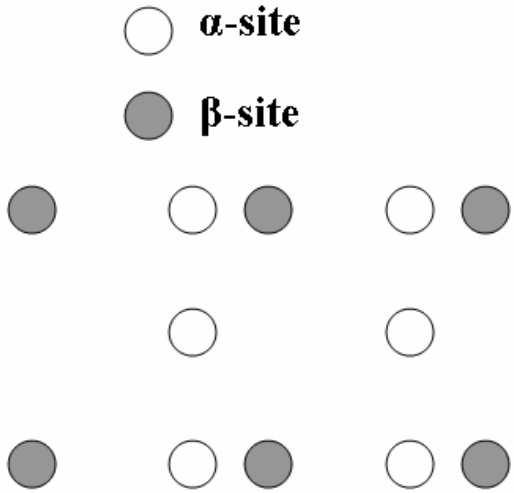

Fig. 3.1.11(c). The side view of the layered structure of graphite along the arrow in Fig. 3.1.11(b).

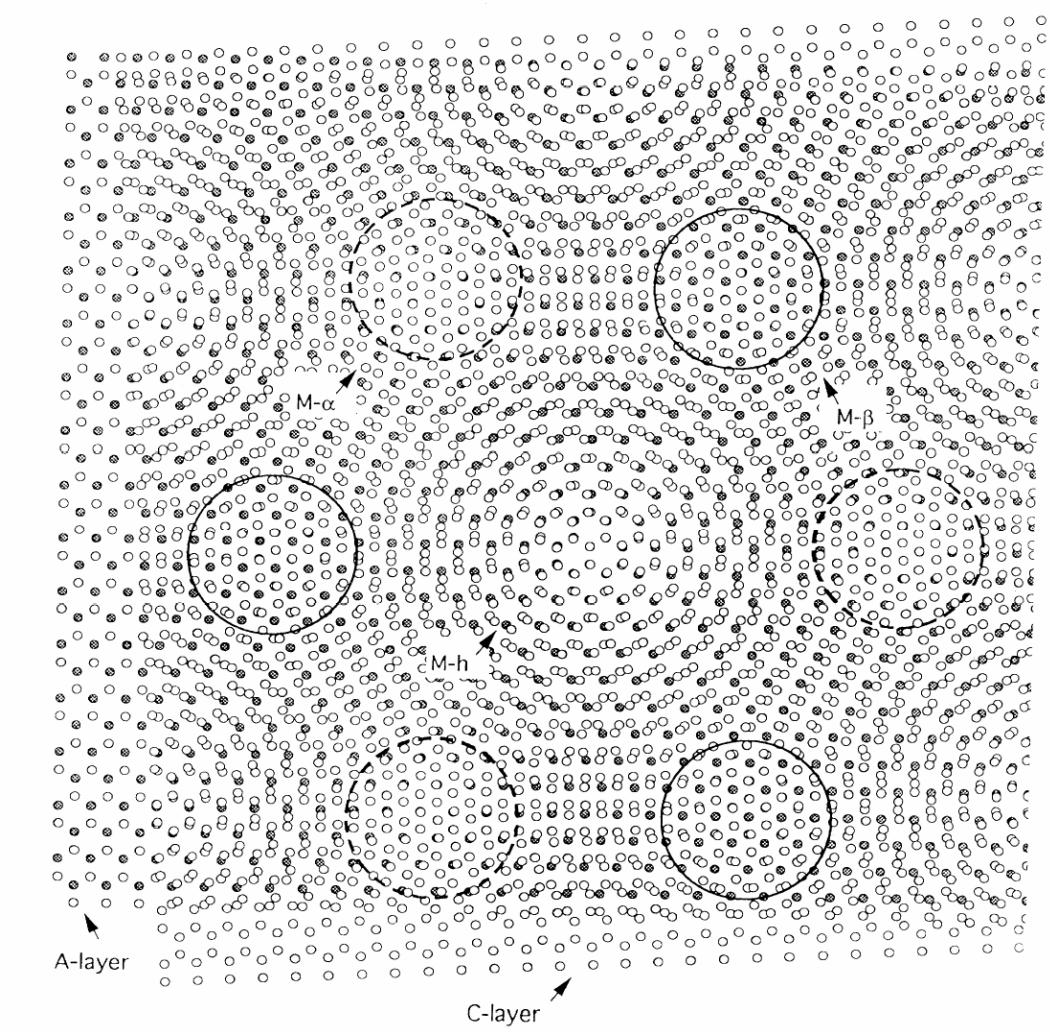

Fig. 3.1.11(d). The model of Moiré pattern proposed by Xhie *et al*. [67]. Two layers of hexagonal atomic lattice are overlapped together with a misorientation angle of 3.5º. Image reprinted from [67].

Xhie *et al*. also suggested an explanation for the coexistence of the atomic lattice and the superlattice. Despite the fact that every atom on a graphite surface is essentially identical, the atoms (β sites) which sit above the holes in the second layer appear at a higher intensity in STM images than the atoms (α sites) which sit above the atoms in the second layer. Therefore, the atomic spacing for graphite under the STM is 0.246 nm rather than the actual 0.142 nm as the STM is imaging every other atom, and therefore the six-fold symmetry of the carbon rings appears as three-fold symmetry under the STM. Such an asymmetry arises because of the ABAB… stacking of the graphite layers which lead to the distinction between the α sites and β sites. The electronic interlayer interaction creates a band overlap and moves the wave functions of the α atoms away from the Fermi energy. Since the STM is imaging at the small energy range around the Fermi level, the β atoms are much more noticeable in the STM images. This is the situation for normal graphite ABAB stacking. The atomic arrangement becomes more complex when the top layer is rotated, that is the stacking changed from ABAB… to CABAB… An atom in the top layer can be above any site in the second layer, it can be above an α site, a β site, a hole site, or anywhere in between these locations. Although not proven by theoretical calculation, by using the similar reason as in the intensity difference between the α atoms and β atoms for normal ABAB… stacking, Xhie *et al.* proposed that an atom in the top rotated layer above a hole site in the second layer would show maximum intensity in the STM images just like β atoms in a normal graphite lattice with normal stacking. Likewise an atom above an α atom in the second layer would show less intensity and an atom above a β atom would show the minimum intensity. With that assumption in mind, we then look at the atomic arrangement inside "M-α-sites", "M-β-sites", and "M-h-sites". In a M-h-site, atoms in the top layer are either covering an α site or β site in the second layer, and those above the α sites would be brighter in the STM images and constitute a hexagonal lattice. In a M-α-site (M-β-site), atoms in the top layer are either above hole sites in the second layer or above β sites (α sites), and the atoms above the hole sites would be brighter in the STM images and appear as a hexagonal lattice. In this way, the hexagonal atomic lattice is maintained throughout the surface even in the presence of the Moiré induced superlattice structure. The M-β-sites of the Moiré pattern should appear the brightest as the atoms of the M-β-sites are above either the hole sites or α sites in the second layer, which will render the atoms of the M-β-sites a higher electronic density of states. Likewise the M-α-sites are expected to be the second brightest while the M-h-sites are the darkest in the STM images. Following this analysis, M-β (g-β) -sites should be the peaks of

the superlattice; M-α (g-α)-sites should be the valleys of the superlattice; M-h (g-h)-sites should be the holes of the superlattice. The model proposed by Xhie *et al*. can explain the three sites with different brightness in a superlattice and the coexistence of the superlattice and the atomic lattice; however, theoretical calculation would be necessary to further confirm its validity. The above analysis is based on the model in Fig. 3.1.11(d) whose misorientation angle is 3.5º; models with other misorientation angles should also be tried out in order to verify the above analysis.

The model by Xhie *et al*. is based on the surface-atom location relative to normal AB stacked graphite crystal underneath: atoms above hole sites give the highest density of states, atoms above α sites give the second-highest density, and atoms above β sites give the lowest. However, Rong *et al*. [66] performed the assignment of local stacking by considering the local crystal structure of the topmost layers from the perspective of the band-structure calculation by Charlier *et al*. [117]. The difference between Xhie's and Rong's models will be further discussed in section 3.1.4.7.(III).

3.1.4.6 Other properties of superlattices

3.1.4.6.(I) Transition by high bias and tip-sample interaction

Since graphite layers are held together by weak Van der Waals forces, it is relatively easy to induce transitions of dislocation structures on a graphite surface by varying the bias voltage of the STM. Also the superlattice structure can be damaged by scanning with a high bias. Buckley *et al*. demonstrated that by scanning with a bias of 3 V in constant height mode, a 20 x 60 nm superlattice area was completely disrupted, and repeated scanning at 50 mV produced extensive damage with a stripe of graphite layer removed [87]. Feddes *et al*. managed to change the top graphite layer shift near the twist boundary [91]. They applied a voltage pulse of a few volts to the superlattice region around a screw dislocation site, which initiated the relaxation of the top layer, increasing the superlattice periodicity, and eliminating the screw dislocation. By applying a 5 V, 200 ns short voltage pulse, Wei *et al*. [118] induced the transition of the occurrence of a superlattice on the HOPG graphite surface from one place to a neighbouring locality.

The disruption brought about by the tip can be ascribed to the tip-sample interaction. Snyder *et al*. [119] demonstrated that a small variation in the tip-to-substrate voltage bias (0.1 V – 0.24 V – 0.1V, tunnelling current constant at 2.4 nA) gives rise to a reversible transition between dislocation network (star-shaped network – triangular shaped network – star-shaped

network) (see Fig. 4 in [119]). This reversible transition was reported to be reproducible during continuous imaging over a period of two days without degradation of the network structures. It is believed that the mechanism for the transition between network geometries involves the concerted motion of dislocations within the network, for which the shear stresses resulting from interactions between the tip and graphite surface are held responsible. Snyder *et al*. proposed an explanation that when the bias voltage is low (0.1 V), the tip is close to the surface and thus the tip-sample interaction generates shear forces which distort the dislocation network and initiate the transition. This transition is reversed as the bias voltage is raised (0.24 V) because the tip is lifted up and thus the shear forces are cancelled, the restoring forces that result from a local distortion of the network compel the dislocation network back to its previous shape. The shear forces resulting from the STM tip onto the graphite surface is estimated to be around 200 MPa, comparable to 500 MPa estimated by Gilman [120] for dislocation motion to be achieved at room temperature, larger than 0.6 MPa that Soule and Nezbeda [121] found for the macroscopic average critically resolved shear stress for the basal plane of annealed HOPG graphite. Ouseph *et al*. [88] observed a tip-induced slow correction of rotational misalignment, and a transformation of the superlattice into triangular dislocations, with the tunnelling condition of tip bias voltage 150 mV and 1 nA tunnelling current. The tip-surface interaction slowly and continuously reduced the misorientation angle of the Moiré pattern over several scans, the superlattice periodicity and the triangle size increased with each scan, and finally the misorientation was corrected uniformly over the whole area of the superlattice. In addition, Ouseph [89], by repeated scanning with a tip bias voltage of 0.15 V, induced the area with normal graphite structure between closely spaced dislocation ribbons to change into a superlattice with the same superlattice periodicity as those of the original ribbons. Such a transformation was ascribed to the tip-sample interaction as well.

On the basis of these findings, it is not surprising that by varying the bias voltage and thus the tip-sample distance, the STM tip can induce shear forces sufficient enough to move or rotate a graphite layer which will affect a Moiré superlattice pattern.

3.1.4.6.(II) α-β-site asymmetry

It is well known that the graphite atomic lattice exhibits asymmetry under the STM due to the interlayer electronic interaction which divides the carbon atoms on the surface into either α sites or β sites, and β sites appear to be brighter (higher local density of states) in the STM images. Such asymmetry can also be observed on the graphite atomic lattice which is

superimposed by a superlattice. Rong *et al*. [66] quantified the α-β-site asymmetry in the superlattice by this equation;

$$A = (z_\beta - z_\alpha)/(z_\beta + z_\alpha) , \qquad (3.1.3)$$

where A is an arbitrary unit for asymmetry quantification, z_β is the corrugation amplitude for a β site, and z_α is the corrugation amplitude for an α site. It is found that the α-β-site asymmetry is maintained throughout the whole superlattice, and in the regions which correspond to g-α-sites in the notation of Xhie *et al*. [67] (i.e. the grey regions in the image), the asymmetry is ~0.56 while in the white regions, corresponding to g-β-sites, it is ~0.17, which indicates the asymmetry is more pronounced in the greyish regions then in the white regions. Such a difference in α-β-site asymmetry can be explained by the theory of Xhie *et al*. [67] described earlier in section 3.1.4.5. In g-α-sites, an atom is either above a hole site in the second layer or a β site, and thus the asymmetry is large because in the second layer, the electronic density of states of a β site is much larger than a hole site which leads to a larger difference in density of states on the top layer, whereas in g-β-sites, an atom either above a hole site in the second layer or an α site and thus the asymmetry is smaller because the difference in electronic density of states is smaller.

3.1.4.6.(III) Superlattice boundary

Although to date not much discussion has been focussed on superlattice boundaries in the literature, a superlattice boundary is an intriguing subject on its own due to the fact that the boundary is the region where the transition from normal graphite to a superlattice occurs. Understanding of the nature of these boundaries will help us to understand the origin of the superlattices. As superlattices tend to occur near or along lattice dislocations and defects, steps in particular, most of the time a superlattice is terminated by a step edge. In chapter 3.4, we report on scanning tunnelling microscopy (STM) observations of several different kinds of superlattice boundaries on highly-oriented pyrolytic graphite (HOPG) including an array of bead-like structures, a thin wall-like boundary, a monolayer deep trench, a zig-zag shaped termination, a plain boundary without features, and a low-angle grain boundary with a varying tilt angle.

3.1.4.6.(IV) Dependence of superlattice corrugation amplitude on tunnelling condition

Rong *et al*. [66] performed an experiment to study the influence of the bias voltage on the superlattice, and it is found that as the bias voltage changed from 72 mV to 535 mV, the

superlattice corrugation was reduced by a factor of 3, and the greyish regions (g-α-sites) disappeared (Fig. 3.1.12). The decrease of superlattice corrugation amplitude with the increasing bias voltage can be explained by the fact that the local density of states on the top layer are only affected by the stacking faults of the underneath layers at the immediate vicinity of the Fermi level, and these densities should be more or less the same when it is far from the Fermi level because they are all mostly dominated by the two-dimensional in-plane interactions [117].

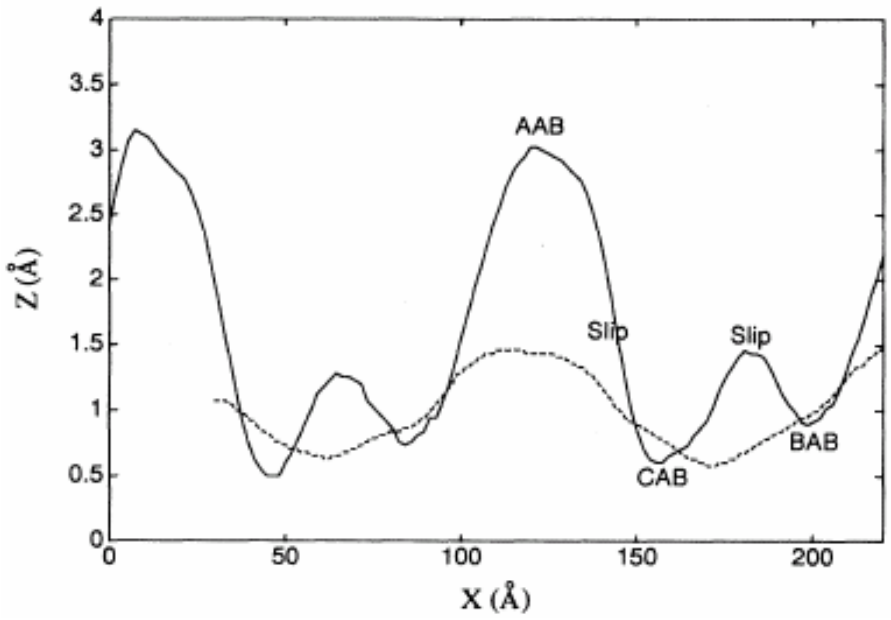

Fig. 3.1.12. The cross-sections along the maxima and minima of the superlattice. Solid curve: tip bias 72 mV; Dashed curve: tip bias 535 mV. Image reprinted from [66].

Tunnelling with the same bias voltage but different tunnelling current may provide completely different image of superlattices. Osing and Shvets imaged a superlattice with bias voltage of 100 mV and tunnelling current of 2 nA [65]. However, after the tunnelling current was set to 0.1 nA, only the surface topography without the superlattice was observed (compare the Fig. 2a with the Fig. 2b in [65]). Osing and Shvets concluded that there is close correlation between the appearance of the superlattice structures in STM images and the tip-sample distance, and the fact that the superperiodic features are observed with high current indicates that for graphite, the variation of the electron density of states associated with the nanoscale features decays much faster in the direction from the surface to the vacuum than the variation of the electron density associated with the atomic lattice. Such a conclusion is different from the proposal of Kobayashi [116] that a superlattice should not be as obvious when the tip-sample distance is short.

Combining the experimental results of Rong *et al*. and Osing *et al*., apparently the effect of superlattices decays with higher bias voltage and lower tunnelling current, both will lead to larger tip-sample distance, thus attenuating superlattice corrugations electronically. However, we cannot interpret superlattice corrugations purely from the electrical point of view. The tip-sample mechanical interaction, which is also tip-sample distance (and thus tunnelling condition) dependent, is believed to play a significant role as will be discussed in section 3.1.4.8.(II). We need to consider both electronic and mechanical effects in order to interpret superlattice corrugation properly.

The interrelation among superlattices, bias voltage, tunnelling current, and tip-sample distance is an important subject to look at (please see the section of "*Possible experiments to do"* in chapter 3.5 for more details).

3.1.4.6.(V) Attenuation of superlattice corrugation by overlayers

It was observed that when a superlattice is covered by an overlayer, its corrugation will be attenuated [64, 80, 90] by a factor, named the attenuation factor, which is the ratio between the corrugations of a direct Moiré pattern and a Moiré pattern covered by an overlayer. In our graphite superlattice images, we have observed two different situations, in one where this attenuation effect occurred with an overlayer, whereas in the other superlattice corrugations were preserved (corrugation conservation phenomenon) even in the presence of an overlayer. In chapter 3.2, these two situations will be discussed and the attenuation factor will be elucidated further.

3.1.4.6.(VI) Preparation of a superlattice

A graphite superlattice is caused by dislocations which occur during the growth of the crystal or from the cleavage process, upon which we have little control. Therefore, a graphite superlattice is perceived to be a natural structure which cannot be prepared in a controlled manner. However, efforts have been made to artificially produce graphite superlattices.

Beyer *et al*. [60] cleaved a graphite surface with a shear force, tearing apart a graphite monolayer which folded back onto the graphite substrate with a small rotation. A superlattice was formed on the rotated layer and ended sharply at the borders of this layer. Beyer *et al*. [60] suggested a few advantages about the method of producing a superlattice on graphite by cleaving the surface with a shear force: 1) The part of the layer which is folded back and rotated will have a hole associated with it, that is an indication that the folded layer was

originally part of the topmost layer; 2) The misorientation angle between the graphite substrate and the folded part can be determined from the STM image; 3) From the surface topography shown in the STM image, we can know that there is a relative rotation of two adjacent layers; 4) Comparison is available to check whether the superlattice is confined within the folded layer or it also occurs in other areas.

Gan *et al*. [61] created a superlattice structure by scanning for several times against a step of graphite in constant current mode and tearing off a part of the graphite layer which folded back onto the graphite substrate and formed the superlattice. The experiment is illustrated in Fig. 3.1.13. This provides a means to prepare a superlattice on graphite. However, there is not much control on the exact position and the periodicity of the superlattice to be generated as we cannot precisely manipulate the location and the angle of the tearing of a graphite layer.

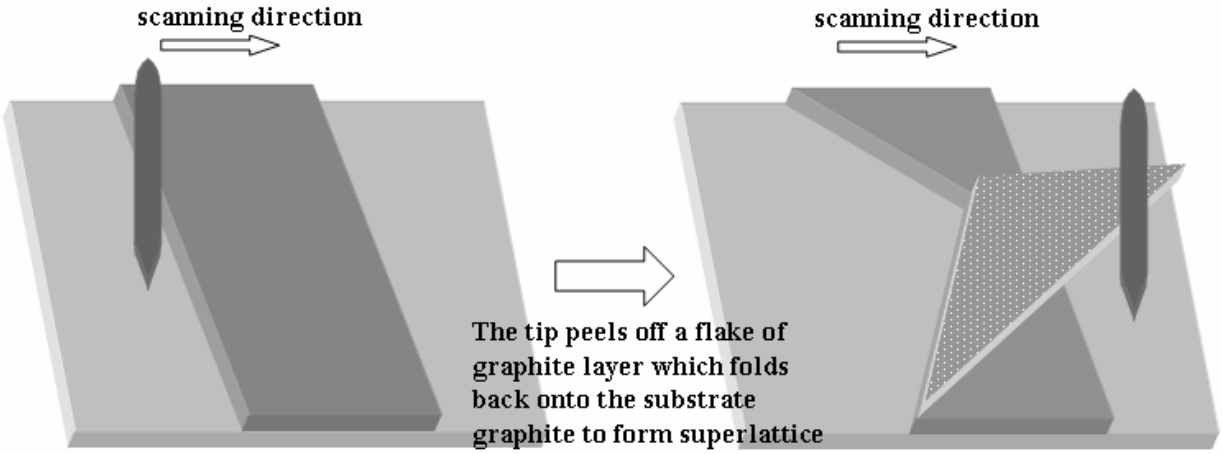

Fig. 3.1.13. Explanation of Gan's method by using the STM tip to fold over a graphite monolayer to form a superlattice.

Similar to Gan's experiment above, Bernhardt *et al*. [94] managed to manipulate nanometre sized graphite sheets consisting of only one or a few graphite monolayers with the STM tip to create a superlattice with varying periodicity. This provides a promising means to artificially produce graphite superlattices. In the first step, they located the tip over some stepped and structured regions on the graphite surface and looked for appropriate graphite flakes, while the tunnelling voltage was held at about 800 – 1000 mV (tunnelling current, 1 nA) so as to minimize tip-sample interaction. The tip-sample interaction on graphite increases dramatically as the tunnelling voltage is set below 500 mV (tunnelling current, 1 nA) [122-124]. Therefore in the second step they made use of this effect and scanned over weakly

bound graphite sheets with decreased tunnelling voltage (370 mV, 1 nA), i.e. small tip-sample distance, and managed to fold back the graphite sheets with height from one to three monolayers. During the whole procedure the feedback system was not interrupted, and the folding direction can be controlled to a certain extent by variation of the scanning direction.

Exposing graphite to chloroform was demonstrated to produce a high concentration of superlattices [107], which can be another means to artificially producing graphite superlattice structures. The graphite samples were cleaved by adhesive tape. The clean surfaces were then exposed to chloroform through drop-wise deposition or submersion. The samples left to soak in chloroform for several weeks showed a very high concentration of various kinds of defects, including hexagonal superlattices, glide defects, and many types of hole. Even in samples exposed to only modest amounts of chloroform (through drop-wise deposition), graphite superlattice structures could still be observed after cleaving off several layers of graphene. The effect of the chloroform is believed to extend well into the crystal bulk, generating several kinds of defect including Moiré superlattices.

3.1.4.6.(VII) Odd-even transition

The theory of Moiré rotation pattern originally did not illustrate the whole picture of a superlattice superimposed on the atomic lattice because it could not explain the fact that in some occasions (Fig. 2a in [66], Fig. 3 in [67], Fig. 11 in [102]), a wavy behaviour of the atomic rows were seen with the presence of the superlattice. In light of that inadequacy, Osing and Shvets completed the story by proposing the odd-even transition phenomenon to explain the wavy appearance of the atomic rows [65]. The idea of the odd-even transition theory is elucidated by the model in Fig. 3.1.14 from [65]. In the model there are two graphite layers rotated with respect to each other, rearranging the stacking sequence which in turn modifies locally the density of states. Such modification brings about two different groups of atomic lattice with different stacking and thus different density of states. In region 1, the layers are of AA-stacking, an atom of a layer is on top of the atom of another, whereas in region 2, the layers are of normal AB-stacking. The atomic corrugation in region 1 is smaller because all atoms are in α sites and thus have similar density of states. On the other hand, in region 2, the atomic corrugation is more obvious as α-β-asymmetry applies here which gives rise to the usual atomic graphite lattice (highlighted as a centred hexagon in Fig. 3.1.14). Saadaoui *et al*. [125] have shown that the β sites in a region of type 2 become the α sites in the neighbouring region 2. Nysten *et al*. [102] clarified this point further by stating

that if the hexagon atoms are denoted from 1 to 6, those being the β sites will be, for example, the 1-3-5 atoms in one area and will be the 2-4-6 atoms in the neighbouring one. By observing on the schematic model, we can see there is a shift between the atomic rows of two adjacent regions of type 2 (indicated by the thick solid line in the schematic). This shifting of atomic rows is the origin of the wavy appearance in some STM images of the atomic lattice on the superlattice, yielding the odd-even transition phenomenon. Osing and Shvets concluded that for a Moiré superlattice pattern superimposed onto the atomic graphite lattice, there must be at least two layers in the AB-stacking sequence on the surface to constitute the normal hexagonal lattice without wavy appearance in a STM image. We have proven this theory with our simulation model, which will be described in detail in chapter 3.3.

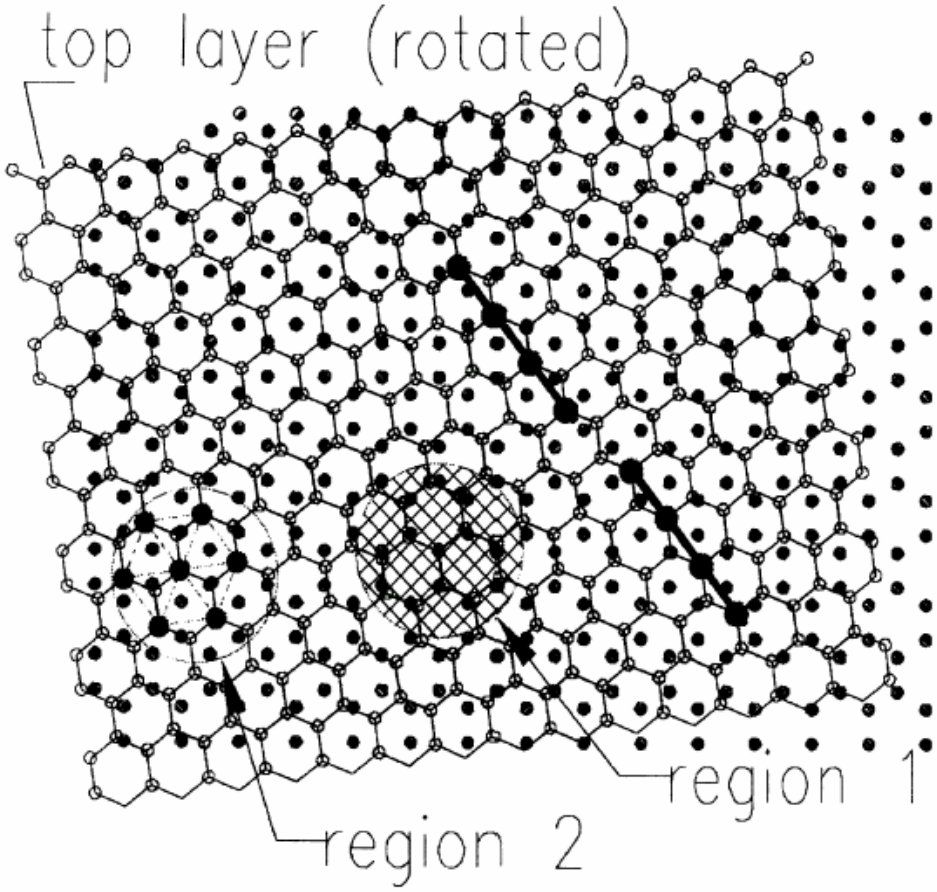

Fig. 3.1.14. Schematic illustration of the odd-even transition phenomenon. The two graphite layers with a rotation angle between them produce a Moiré superlattice pattern. There are two types of regions: region 1 with the AA stacking sequence which leads to an α-site character for every atom; region 2 with the usual AB stacking which gives rise to normal α-β-asymmetry, producing the usual graphite atomic lattice in STM images. There is a shift between the atomic rows of two adjacent regions of type 2 indicated by the thick solid line. Image reprinted from [65].

3.1.4.6.(VIII) Adsorption sites for particles

As a superlattice periodicity is comparable to particles, it is interesting to see the influence of the superlattice structure on the deposition of the particles on the surface. Xhie *et al*. deposited some cobalt particles with size of 1 – 5 nm onto a graphite superlattice with periodicity of around 3.8 nm, the cobalt particles settled on top of the peaks of the superlattice [67]. Previous experiments showed that single atoms and atomic dimers of noble metals prefer β sites of the graphite atomic lattice because of the higher local density of states at the Fermi level than the other sites [126, 127]. The size of cobalt particles is too large compared to the graphite atomic lattice to adsorb to any atomic sites. The periodicity and symmetry of the superlattice makes it possible for the cobalt particles to position themselves on the g-β-sites whose local density of states at the Fermi level is larger than the other sites. The dependence of the adsorption sites on graphite for atoms and clusters on the local density of states at the Fermi level is potentially a way to manipulate the deposition of the particles onto the surface which makes a superlattice a useful template for patterning particles on a surface. Such a potential application is further discussed in chapter 3.5.

3.1.4.7 Controversies on graphite superlattice

Although the Moiré rotation pattern assumption is widely accepted as the primary cause of graphite superlattices, some experimental and simulation works were reported which contradict the Moiré pattern explanation.

3.1.4.7.(I) Formation of superlattice without rotation of graphite layer

Patrick *et al*. observed a superlattice structure in an experiment involving the liquid crystal 4-octyl-4'-cyanobiphenyl (8CB) and monolayer-deep etch pits on graphite with the STM [101]. A terrace on the graphite showed a superlattice with periodicity of 54±1Å, corrugation amplitude of 1.4±0.5Å, having a hexagonal symmetry. This superlattice is superimposed onto the underlying atomic graphite lattice with both the superlattice structure and atomic lattice visible in the STM images. In the middle of the terrace was a 325Å diameter etch pit where a normal graphite atomic lattice was imaged without any superlattice structure, which inclines us to expect that the graphite layer at the bottom of the pit should have a different orientation from the top terrace layer as only the top terrace layer exhibits the superlattice. However, by comparing the atomic resolution images obtained from the bottom of the pit and the terrace with the superlattice, the atomic lattice in these two layers are

aligned with each other without misorientation. Patrick *et al*. believed that a simple Moiré rotation pattern assumption cannot explain this contradiction and some other mechanism must be involved in the formation of the superlattice in this case.

However, there are two points worth further consideration. First, the depth of the pit is not a monolayer but 4.8±1 Å instead, which is around 43% larger than the interlayer spacing of graphite (3.35 Å). Such a difference was ascribed to the presence of the superlattice. Nevertheless, it could be possible that during the etching or the deposition of the liquid crystal molecules, some species went underneath the bottom of the pit and thus lifted the layer by about one and a half angstrom. Moreover the heating process whereby the graphite was heated in air to above 550°C might have disrupted the normal graphite layered structure at the top few layers. Since this particular piece of graphite was prepared in a more complicated way rather than simple cleaving and similar experimental results on graphite superlattices have not been reported elsewhere, we may regard this non-Moiré pattern induced superlattice as an exception where the etching and deposition of a liquid crystal produced such a peculiar superlattice.

3.1.4.7.(II) Corrugation conservation phenomenon

It is reported in the literature that when a superlattice traverses across a graphite step, its corrugation will be attenuated by the overlayer by a factor of around 2. However, in our STM images, a superlattice which stretches across a step was observed without any detectable attenuation in its corrugation amplitude. Such a controversial phenomenon is discussed in chapter 3.2.

3.1.4.7.(III) Correlation between local stacking and density of states

Rong *et al*. [66] categorized local stackings of graphite superlattices in a different way to Xhie [67]. Xhie *et al*. categorized all the surface-atom sites into M-α, M-β, and M-h sites, on the basis of the surface-atom location relative to the AB stacked substrate graphite crystal [Fig. 3.1.11(d)], whereas Rong *et al*. did the categorization of surface atoms according to the local stacking of the topmost three graphite layers and formed four groups: AAB, slip-AB, AB (normal stacking), and CAB stacking (Fig. 3.1.15). There are four groups of surface-atom sites for Rong's model but there are only three for Xhie's because Rong *et al*. distinguished two types of valleys with different intensities in STM superlattice images while Xhie *et al*. regarded all the valleys as the same type.

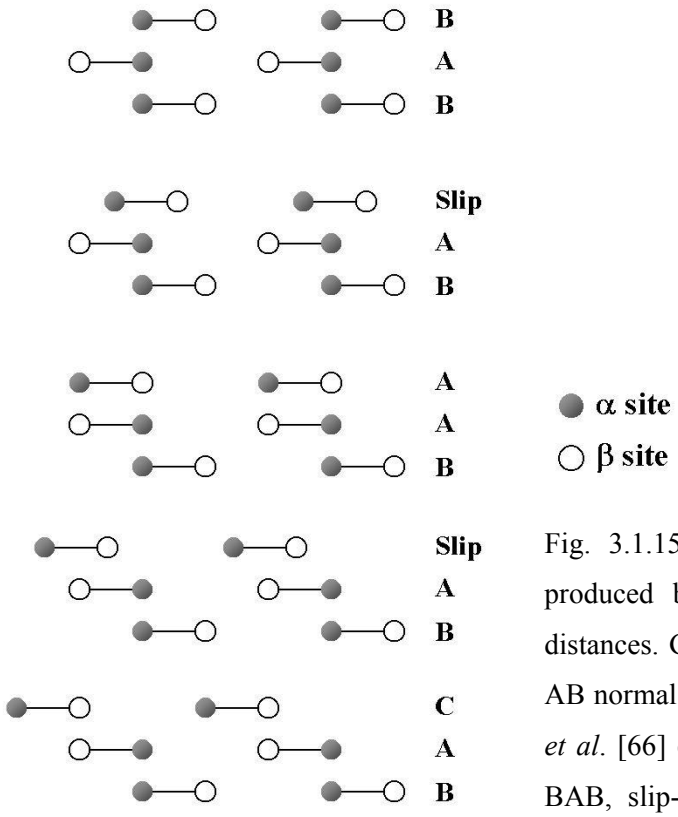

Fig. 3.1.15. Different stacking structures of graphite are produced by sliding the top graphite layer by different distances. Grey circles and white circles are α and β sites of AB normal stacking respectively. Based on this model, Rong *et al*. [66] categorized the atomic sites in a superlattice into BAB, slip-AB, AAB, and CAB, and assigned them with different intensities in STM images according to the band-structure calculation of Charlier *et al*. [117]

The band-structure calculation using a tight-binding description of the electronic structure [117] indicates that AA-stacked graphite has a density of states at the Fermi level of 0.0085 states/eV, which is three times larger than that of AB or CAB stacked graphite, contrary to the expectation from an analogy to α sites (the analogy that Xhie *et al*. used in their model). The density of states at the Fermi level for normal AB stacked graphite is 0.0033 states/eV (0.0056 states/eV for β sites and 0.0011 for α sites, which average to 0.0033 states/eV), and it is 0.0021 states/eV for CAB stacked graphite. As such, Rong *et al*. assigned the brightest peaks of a superlattice in STM images to AAB stacking, the second deepest valleys to normal AB stacking, and the deepest valleys to CAB stacking (Fig. 3.1.12). The remaining slip-AB stacking is assigned to be the second brightest peaks of a superlattice.

If we translate Xhie's model into Rong's model, M-β-sites (brightest superlattice spots in Xhie model) correspond to AB normal stacking which are the second deepest valleys in Rong's model, M-α-sites (medium brightest superlattice spots) correspond to CAB stacking which are the darkest valleys, and similarly, M-h-sites (darkest holes) are AAB stacking which are the superlattice peaks in the other model. Rong's model appears to be

more convincing as it is supported by first principles calculation while Xhie's model is only based on the deduction that the interlayer electronic interaction for the top rotated layer from the substrate should be the same as the interaction for normal AB stacked graphite: atoms above hole sites are the brightest in the STM images, atoms above α sites are the second brightest, and atoms above β sites are the darkest. Whilst Rong *et al*. referred to the work of Charlier [117] as the foundation of their model, the calculation by Charlier was based on the models that the AAA, AB or CAB stacking is maintained throughout the whole graphite crystal rather than just the top three layers with substrate as normal AB stacked graphite. In other words, for a real superlattice, the actual stackings are ABABAB…, CABABAB…, and AABABAB… but the calculation by Charlier is about ABABAB…, CABCAB…, and AAAAAA… Although they look similar for the first three layers, the structures of the bulks of the crystal models are completely different. Such a difference may render Rong's model questionable, and definitely further rigorous theoretical calculation is needed for justification.

3.1.4.7.(IV) Unusual aspects of superlattice structures on HOPG from Cee *et al.*

Cee *et al*. reported a few unusual aspects of superlattice structures which cannot be explained by the generally accepted Moiré rotation pattern hypothesis [128]. They used the simulation model to generate a superlattice with the contribution of each graphite layer decreases in weight with its depth from the surface (W_2 = 0.5 and W_3 = 0.125, normal weighting). The resulting simulated pattern is a superstructure of hexagonal symmetry, unlike the three-fold symmetry on the experimentally observed superlattices where three of the six maxima are more intense in STM images. Then they carried out another simulation with an exaggerated difference in the relative contributions of the second and third layers (W_2 = 0.125 and W_3 = 0.25, exaggerated weighting), which does not agree with the idea that the electronic influence from a lower layer should be less as the interlayer electronic interaction decays with distance. Surprisingly, this superlattice simulated with counterintuitive weightings appears to exhibit three-fold symmetry as observed with the STM. Consequently, this simulation result brings out the contradiction that Moiré rotation pattern assumption cannot be true unless the electronic contribution from the third layer is larger than the second layer which is obviously non-physical.

In the STM images on etched graphite, Cee *et al*. observed two superlattices in contact on the same layer, each with a different periodicity, separated by a well-defined boundary (Fig. 5 in [128]). Without apparent topographic defects in the area, for instance, buckling, cracking, or grain boundary of the graphite layer, a change in the rotation angle of

the graphite layer is unlikely. The observation is thus beyond the explanation of Moiré rotation assumption. On another surface of graphite deposited with the liquid crystal molecule 4'-octyl-4-carbonitrile (8CB), Cee *et al*. also imaged a transient superlattice in the middle of a thin strip of graphite with two defects confining the superlattice and causing stretching at the edges (Fig. 6 in [128]). They then applied a voltage pulse from –0.4 to –4 V several times at the middle of the superlattice. This action made the defect marking the left boundary of the superlattice and the superlattice itself vanish. However, the vanishing did not come with the change in the orientation of the strip of terrace where the superlattice was, which is not compatible with the expectation of the Moiré pattern hypothesis that the vanishing of the superlattice should have come with the change of the orientation of the strip of terrace. In addition, on a graphite sample which was etched by heating to 650ºC in air, on which much of the topmost layer was etched away with several isolated islands of graphite layer remaining, a superlattice existed on one of the islands while another island nearby on the same graphite layer did not contain any superlattice (Fig. 7 in [128]). Cee *et al*. stated that Moiré rotation could not be the cause of the superlattice because the whole layer, thus both islands, would otherwise be expected to contain a superlattice, and secondly the possibility of a grain boundary was excluded because of the mode of etching of the uppermost layer.

The experimental and simulation results presented by Cee *et al*. were arguments against the Moiré rotation pattern assumption, which suggests we should rethink the origin of graphite superlattices. Nevertheless there are different accounts of their results. We have carried out simulation modelling and obtained different results to that of Cee *et al*. Our work thus affirms the validity of the Moiré rotation pattern assumption. This will be discussed in chapter 3.3 (section 3.3.3.3) where we talk about a simulation model of graphite superlattice and its applications in the investigations of superlattices.

3.1.4.7.(V) Superlattice with square symmetry

Apart from hexagonal superlattices, cubic superlattices were observed on graphite. Oden *et al*. [92] obtained the images of the square lattice under triply distilled 18 MΩ water, with the $Pt_{0.7}Ir_{0.3}$ tunnelling tips coated with Apiezon wax up until the tip apex, and Faradaic leakage current limited at 10 pA; the bias voltage between the tip and substrate was 0.1 V. Around 1% or less of the graphite surface was covered with square superperiodic features with observed periodicities ranging from approximately 45 to 440 Å with corrugation amplitudes distributed from 2 to 5 Å. In terms of periodicity and corrugation amplitude, the square arranged superlattices are similar to normal superlattices, apart from the fact that these

square superlattices are not composed of hexagonal symmetry, and thus cannot be explained by the Moiré rotation pattern assumption.

However, atomic resolution images were not obtained on the square lattices, thus one cannot rule out the likelihood that the square superlattices are due to adsorbed species from the solution. Another possibility is the solution molecules go into the graphite interlayer space and cause surface deformation which gives rise to this kind of square superlattice.

3.1.4.8 Unexplained phenomena

There are some phenomena concerning graphite superlattices which, while not contradicting the Moiré rotation pattern assumption, still remain unexplained.

3.1.4.8.(I) More metallic nature of the superlattice than normal graphite

In their experiment, Kuwabara, Clarke and Smith performed current-voltage spectroscopy measurements on both the superlattice region and the adjacent normal graphite region, and the measurements indicate that the superlattice region is more metallic than normal graphite while there is no appreciable difference between the peaks and valleys of the superlattice [63]. Rong *et al*. [66] demonstrated that the Moiré induced superlattice pattern changes its shape with the variation of the bias voltage, which indicates that different stacking configurations of graphite layers have different I-V characteristics. This can possibly explain the more metallic nature of a superlattice as the stacking configuration of a superlattice is different from normal graphite.

3.1.4.8.(II) Superlattice large corrugation amplitude

The origin of the anomalously large corrugation amplitude in some superlattices is not well understood. While the observed corrugation of the graphite atomic lattice is around a few Angstroms (amplified by the tip-surface interaction), the corrugation of a superlattice can be several nanometres. This is not understandable simply by considering surface morphology and density of states, rather, it is believed to be associated with tip-induced mechanical deformation of the surface [63]. According to the Moiré rotation hypothesis, the formation of a superlattice is due to a thin layer of graphite misoriented with respect to the bulk crystal. It is reasonable to expect that, if the corrugation of graphite atomic lattice can be attributed to the STM tip induced surface deformation, the tip would bring about even larger surface deformation on a superlattice region. Indeed, superlattice corrugations and atomic

corrugations of graphite exhibit similar dependence on the bias voltage; both corrugations decrease in amplitude as the bias voltage is increased [62, 66, 88], which can be supportive of the argument that large superlattice corrugation has the same origin as the giant corrugation of the atomic lattice which has been routinely observed on a graphite surface with the STM. Garbarz *et al*. [62] showed that there exist interatomic forces between tip and surface and such forces vary rapidly as the tip-to-surface distance varies. As such the vertical displacement of the tip will be amplified and induce a large elastic deformation. Deformation is particularly pronounced at dislocation sites since the softness of the crystal is increased locally by the mobility of a dislocation. Beyer *et al*. attributed the giant corrugation of the superlattice to the effect of elastic tip-sample interaction as well [60]. The tip-sample interaction is dependent on tip-sample distance; when the distance is larger (smaller), the interaction is weaker (stronger), and thus the superlattice corrugation becomes smaller (larger). As discussed in section 3.1.4.6.(IV), electronic effects depending on the tunnelling conditions are a factor in the apparent superlattice corrugation; together with the tip-sample interaction, they give a more comprehensive idea about the origin of superlattice corrugations.

3.1.4.8.(III) Coexisting superlattice

In most of the cases reported, only one superlattice exists in an area at a time. However, it has been reported that two superlattices with different periodicities were seen to coexist on the same area of graphite. Xhie *et al*. observed that on top of the superlattice (giant lattice) with a periodicity of 3.8 nm, there is another superlattice (supergiant lattice) with slightly distorted hexagonal pattern with a periodicity of approximately 15 nm (see Fig. 3.3.7 in chapter 3.3). The corrugation of the supergiant lattice is around 0.1 nm, which is 1/10 of the corrugation of the giant lattice. Xhie *et al*. attributed this phenomenon to the strain produced by the small rotation of the top layer [67]. It is also possible that the top two graphite layers are rotated with different angles with respect to the third layer, resulting in two overlapping Moiré patterns while the slight distortion of the hexagonal pattern of the supergiant lattice may be caused by the strain due to the misorientation of the graphite layers. Ball *et al*. [107] observed a similar phenomenon comprising two overlaid hexagonal superlattices of different periodicities of 3.25 nm (corrugation 0.1 nm) and 19.2 nm (corrugation 0.2 nm) (see Fig. 3.3.8 in chapter 3.3). They also attributed it to the two rotated graphene planes with different rotation angles. Such an effect can be studied with a simulation model which is described in chapter 3.3.

3.1.5 Conclusion

In this chapter, we have reviewed and introduced the anomaly of scanning tunnelling microscopy – superlattices on graphite, now we are more familiar with it. This enables us to move on to chapters 3.2, 3.3, and 3.4 to analyze our own STM data on the graphite superlattices. The next chapter is to report our observation of some large-scale rippling fringes on graphite superlattices, corrugation conservation phenomenon on a superlattice covered by an overlayer, and a proposed equation relating the attenuation factor to the number of overlayers.

The reorganization and categorization of documented information concerning graphite superlattices in this chapter, together with some analysis in chapters 3.2, 3.3, and 3.4, and the outlook in chapter 3.5, is accepted for publication as a review article in the Journal of Physics D: Applied Physics [129].

Chapter 3.2 Observation of large-scale features on graphite by scanning tunnelling microscopy

Summary

Superlattice structures and rippling fringes were imaged on two separate pieces of graphite (HOPG) by scanning tunnelling microscopy (STM). We observed the corrugation conservation phenomenon on one of the superlattice structures where an overlayer does not attenuate the corrugation amplitude of the superlattice. Such a phenomenon may illustrate an implication that nanoscale defects a few layers underneath the surface may propagate through many layers without decay and form the superlattice structure on the topmost surface. Some rippling fringes with periodicities of 20 nm and 30 nm and corrugations of 0.1 nm and 0.15 nm were observed in the superlattice area and in nearby regions. Such fringes are believed to be due to physical buckling of the surface. The stress required to generate such structures is estimated, and a possible cause is discussed. An equation relating the attenuation factor to the number of overlayers is proposed, and we have reviewed the attenuation factors reported in the literature. The work of this chapter is published in the Japanese Journal of Applied Physics, vol. 44, no. 7B., p.5443-5446 [98].

3.2.1 Introduction

Graphite is one of the most commonly used substrates for scanning probe microscopy experiments because of its chemical inertness, commercial availability, and atomically flat terraces, as well as being easy to cleave to provide a fresh surface. However, it has been reported that graphite has various kinds of defects on its surface [84, 85], and one has to be careful in distinguishing those defects from the features of the deposited materials. Therefore it is of paramount importance to have a detailed understanding of the surface features of graphite.

Amongst the intrinsic defects of graphite, a superperiodic structure named a superlattice has been reported by many groups [63, 64, 66, 67, 80, 90, 92]. A superlattice is a lattice structure of hexagonal shape with triangular symmetry, its periodicity is usually several to tens of nanometres and its corrugation is around several angstroms to a nanometre. An explanation as to the origin of such superlattices is the Moiré rotation pattern assumption which states that a superlattice is the consequence of the relative rotation between adjacent

graphite layers. The rotation angle θ can be related to the periodicity *D* by eq. (3.1.1) which we have mentioned in chapter 3.1 previously

$$D = \frac{d}{2\sin(\theta/2)}, \qquad \text{[eq. (3.1.1) from chapter 3.1]}$$

where *d* is the atomic lattice constant. By measuring the periodicity of the superlattice from STM images, its corresponding rotation angle can be obtained. Kobayashi [116] has proposed a three-dimensional tunnelling theory to describe superlattices. Moreover, he has suggested that nanoscale features are visible even if they are buried a few layers deep as nanoscale waves may propagate through many layers without decay. This implies that the corrugation amplitude of a superlattice may not be attenuated by the overlayers in some circumstances. In this chapter we report the observation of the corrugation conservation phenomenon in which the corrugation amplitude is conserved even with an overlayer, and also the case where the overlayer attenuates the superlattice corrugation.

Our observed rippling fringes are some fringe structures with periodicities of around 20 nm and 30 nm and corrugations of around 0.1 nm and 0.15 nm. The fringes occur in one of the superlattice regions and the area nearby, and they extend over a few hundred nanometres. These fringe distortions seem to indicate a physical deformation which extends and contracts the layer simultaneously. In this chapter, a simple calculation is performed to estimate the magnitude of stress required to generate those rippling fringes, and a possible origin of those fringes is suggested in order to provide an overall picture of the graphite surface condition.

3.2.2 Experiment

Experiments were performed on two pieces of highly oriented pyrolytic graphite (HOPG). The samples were cleaved by adhesive tape for a few times before scanning. The home-made STM described in chapter 2 and a Nanosurf STM [32] were operated in constant current mode to carry out the experiments under ambient conditions. Mechanically cut Pt/Ir tips were used for imaging.

3.2.3 Results and discussion

3.2.3.1 Corrugation conservation phenomenon

The first image in Fig. 3.2.1(a) shows a superlattice structure extending across a monoatomic step edge and covering an area of around 200 nm x 200 nm. The superlattice has boundaries on the left and right, and the step edge at the middle separates the superlattice into two areas which are labelled region A and region B in the figure. Fig. 3.2.1(b) shows the cross-sections of both regions. As we can see from the cross-sections, the corrugations in region A and B are more or less the same. However, it is reported in the literature [80, 90] that the corrugation of a superlattice stretching across a monoatomic step edge will be attenuated by the overlayer by a factor of around 2. In our case, there is no detectable attenuation in corrugations from region A into region B. This corrugation conservation phenomenon may exhibit an implication that nanoscale features can propagate through many layers without decay and form the superlattice on the surface.

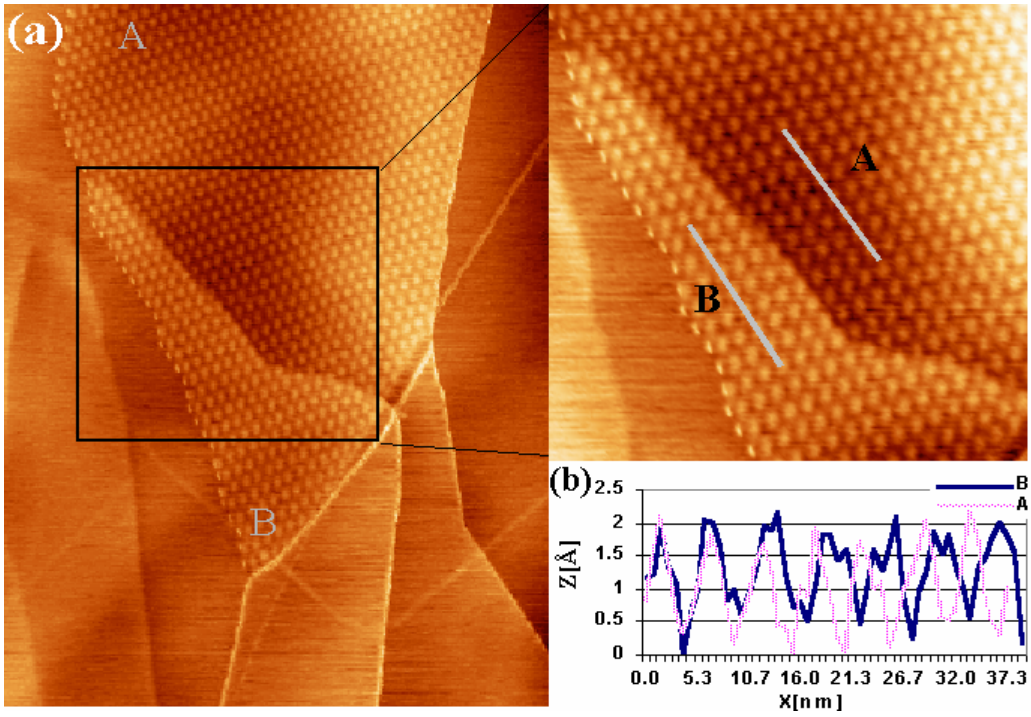

Fig. 3.2.1(a). 319 nm x 300 nm image (I_t = 0.5 nA, V_t = 230 mV) on graphite with the superlattice structure covering about 200 nm^2 area. The zoom-in on the right shows the superlattice in region A and B more clearly. The superlattice extends across the monoatomic step edge without much attenuation as we can observe in the cross-section in Fig. 3.2.1(b). Fig. 3.2.1(b) shows the cross-sections in region A and B.

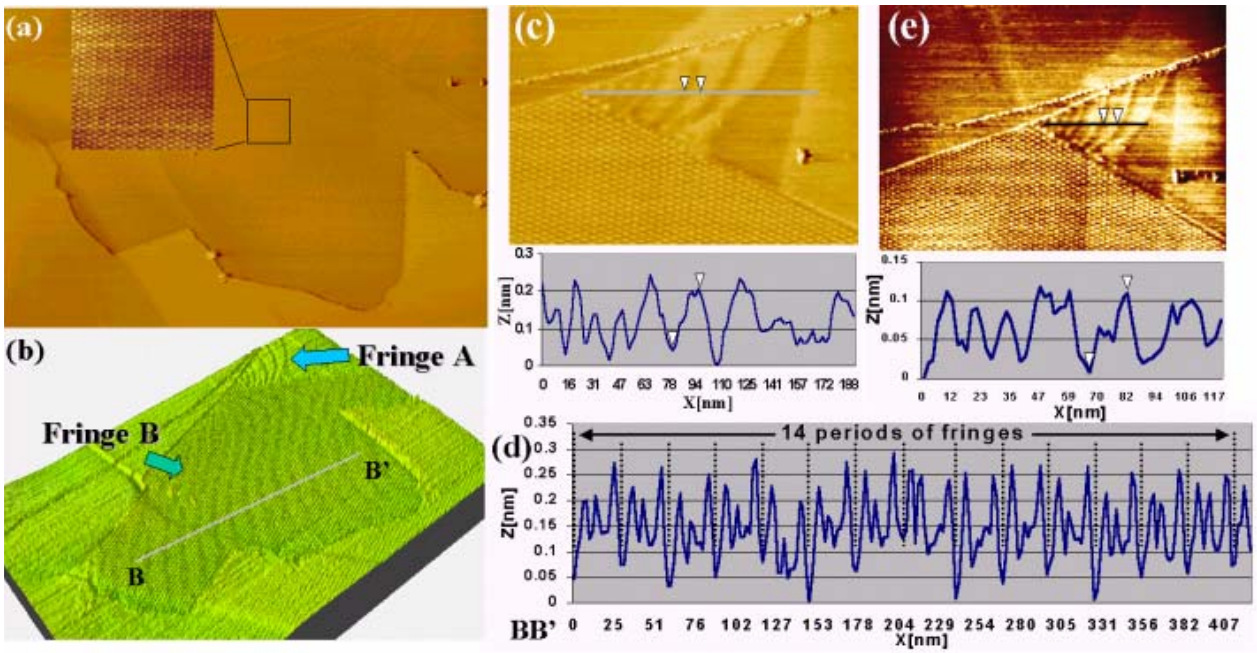

Fig. 3.2.2. The rippling fringes on the graphite. (a) 700 nm x 500 nm image (I_t = 0.36 nA, V_s = 450 mV) on graphite with the central part being the superlattice as shown by the inset. (b) 3D image of Fig. 3.2.2(a) with the contrast enhanced. The fringes at the corner and in the central part are labeled as Fringe A and Fringe B respectively. The line profile BB' is shown in Fig. 3.2.2(d). (c) 290 nm x 200 nm image (I_t = 0.5 nA, V_s = 206 mV) of Fringe A in Fig. 3.2.2(b) with its cross-section. (d) Cross-section of Fringe B along BB' in Fig. 3.2.2(b). There are 14 periodicities of the rippling fringes shown in Fig. 3.2.2(b). The fringes are buried in the superlattice, so the contrast has to be enhanced in order to display the rippling fringes in Fig. 3.2.2(b). (e) 400 nm x 350 nm image (I_t = 0.36 nA, V_s = 450 mV) of Fringe A in Fig. 3.2.2(b) with its cross-section.

3.2.3.2 Observation of rippling fringes

The superlattice on another piece of graphite is displayed in Fig. 3.2.2(a). Due to the lack of contrast, we cannot see many features apart from the superlattice itself from the image. The contrast of the image is enhanced by changing the colour scheme, and it is displayed in 3-dimensional form in Fig. 3.2.2(b). From Fig. 3.2.2(b), we can observe rippling fringes at the corner (Fringe A) and in the centre (Fringe B). Figures 3.2.2(c) and 3.2.2(d) are the line profiles of Fringe A and B respectively. Fringe A has a periodicity of around 20 nm with corrugation of about 0.1 nm while the periodicity and corrugation of Fringe B are around 30 nm and 0.15 nm respectively. Fringe A was imaged under two different tunnelling conditions, and the fringe structure can be observed in both Figs. 3.2.2(c) and 3.2.2(e). Moreover, the electronic wavelength on a planar graphite sheet is calculated to be 2.51 nm from eq. (3.2.1)

$$\lambda = \frac{h}{m_e v_f}, \qquad (3.2.1)$$

where h is the Planck's constant, m_e is the electron mass, and v_f is the Fermi velocity on planar graphite; from the gradient of the energy-band structure of a graphite sheet at the Fermi surface, we find that the Fermi velocity is 2.9 x 10^5 ms^{-1}. The electronic wavelength is smaller than those periodicities of Fringe A and B by an order of magnitude, and therefore those fringes are unlikely to be an electronic standing wave on the surface. The fact that the fringe structures were observed under different tunnelling conditions and they are not an electronic wave inclines us to think that those rippling fringes are related to the actual surface topography of graphite, and they are not just an electronic effect. Some rippling fringes were imaged in the nearby regions as well. Similar fringes can be observed in the central part of Fig. 3.2.3(b) which is a 3-dimensional image of Fig. 3.2.3(a) with enhanced contrast. In addition, to the bottom left corner of Figs. 3.2.3(b) and 3.2.3(a), there is a pit of monolayer depth associated with some rippling fringes [see Fig. 3.2.3(c)] which stretch from the pit, along around 700 nm, to the step edge at the upper part of the image. Rippling fringes were observed across a number of different areas and were not confined to one particular region.

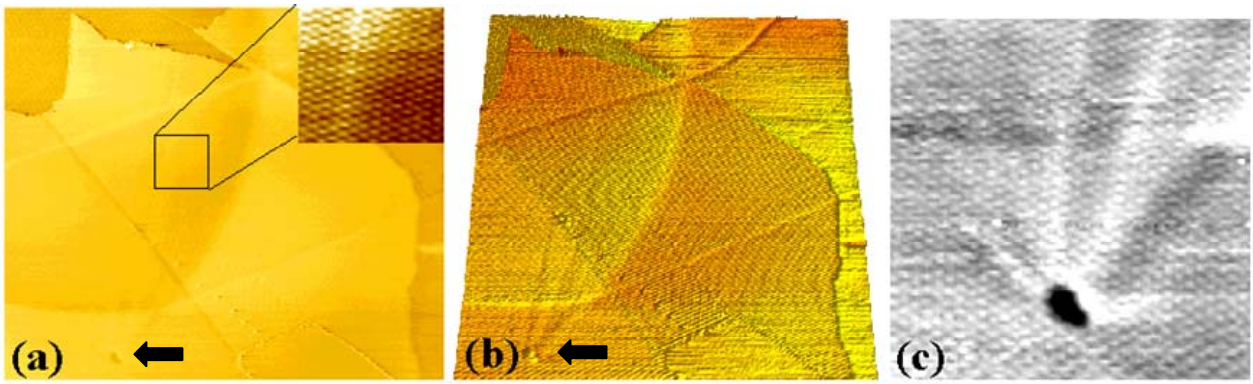

Fig. 3.2.3. Another area with rippling fringes. (a) 800 nm x 750 nm image (I_t = 0.5 nA, V_s = 206 mV) with most of the area being superlattice as shown by the inset. (b) The 3D and contrast-enhanced image of Fig. 3.2.3(a), from where we can observe the rippling fringes again localized in the central part of the image. (c) The pit of monolayer deep associated with some long-ranged fringes which is positioned at the bottom left hand corner of Fig. 3.2.3(a) and Fig. 3.2.3(b) indicated by the arrows.

A simple model is established for these rippling fringes, and an estimation of the stress required to generate those fringes is made. A graphite layer under zero applied force will be flat and has a corresponding length, L. When a lateral force is applied to the layer, it buckles and the atomic spacing becomes smaller in order to provide resistive force to act against and balance the applied force. Its horizontal length decreases by ΔL to L' (Fig. 3.2.4).

When the surface is buckled, since the atomic spacing is now smaller, the Young's modulus will be larger. However, we do not know how much smaller the atomic spacing becomes and thus do not know the actual Young's modulus. In this case, we can only use the normal Young's modulus of graphite for calculation. The surface buckling is modelled as a sinusoidal wave, and the normal Young's modulus of graphite, E (121.9 x 10^9 Nm^{-2}), is obtained from [94]. Using L' = 400 nm which is approximately the length of the rippling region of Fringe B and working through eq. (3.2.2) – (3.2.4), the stress is found to be 170 MPa which is a lower bound value for the actual stress because the Young's modulus used in this calculation is smaller than the actual one.

$$\Delta L = L - L' \qquad (3.2.2)$$

$$L = \int_0^{L'} \sqrt{1 + (A/2)^2 \cos^2(2\pi \frac{x}{T})}\,dx \qquad (3.2.3)$$

$$E = stress / strain \qquad (3.2.4)$$

where A is the corrugation amplitude (0.15 nm) and T is the periodicity of fringe (30 nm).

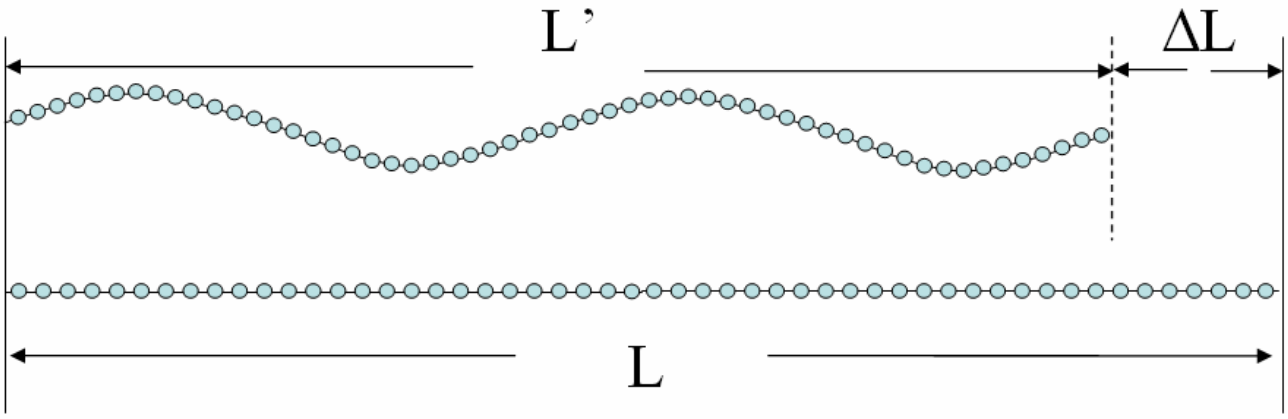

Fig. 3.2.4. When there is no applied force, the graphite layer is flat and its length is L. As force is applied, the layer becomes buckled and its horizontal length decreases by ΔL and becomes L'.

Simulations of the superlattice based on the assumption of Moiré rotation pattern were performed and rippling fringes were not observed in the simulation results. This confirms our experimental finding that those rippling fringes are not related to the superlattice itself and their formation is due to something else. Details of the simulation can be found in section 3.3.3.2 of chapter 3.3. Analysis on Fig. 3.2.3(b) may give us some hints about the possible cause of the rippling fringes. Figure 3.2.5 is about the same area as in Fig. 3.2.3(b) but with the image divided into domains. From Table 3.2.I, we can observe that there is quite a wide

range of values for periodicities of the superlattices in the image of Fig. 3.2.5. However, if we focus within each domain, the variation is actually not too broad, and therefore a representative periodicity is selected for each domain. According to the Moiré rotation pattern assumption, the change of a superlattice periodicity is related to the change of a rotation angle. The fact that the periodicity is changing from one domain to another, especially among domains E – K, means that each domain has a different rotation angle and thus the domains are rotating against each other. In this way, a lot of intralayer stress is generated, and we think it is the possible cause of the physical buckling of the surface which appeared as those rippling fringes under the STM.

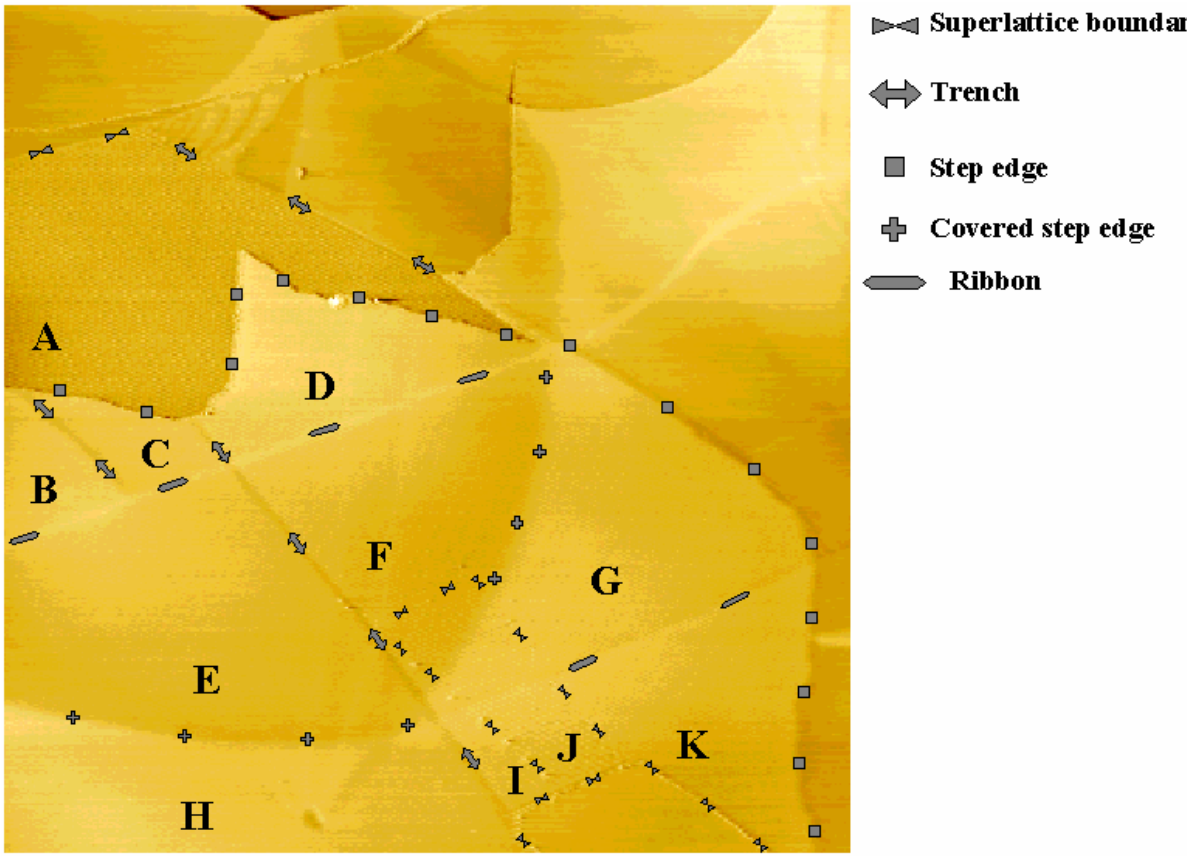

Fig. 3.2.5. 1000 nm x 1000 nm (I_t = 0.5 nA, V_s = 206 mV) image which is about the same area as in Fig. 3.2.3(a) and Fig. 3.2.3(b). Different kinds of superlattice domain boundaries are marked with different labels.

Table 3.2.I. The periodicities and rotation angle for each domain shown in Fig. 3.2.5.

Domain	Periodicities within domain (Å)	Representative periodicity for each domain (Å)	Representative rotation angle for each domain (degree)
A	49.8, 50.3, 50.8, 48.7, 50.5, 48.3, 5.09, 51.4, 50.3	50±2	2.82
B	53.5, 54.3	54±1	2.61
C	53.9, 54.6, 54.2	54±1	2.61
D	52.9, 51.5, 52.1	52±1	2.71
E	57.7, 57.5, 55.1, 57.1, 57.8	57±2	2.47
F	56.2, 56.2, 53.0, 55.0, 55.2	54±2	2.61
G	52.6, 54.8, 54.2, 54.2, 55.8	54±2	2.61
H	63.3, 63.1, 65.3, 66.6, 64.9	65±2	2.17
I	63.3, 64.8	63±1	2.24
J	62.0, 66.3, 72.1, 76.8	70±8	2.01
K	58.1, 58.0, 59.1, 60.4	59±1	2.39

3.2.3.3 Attenuation factor by overlayers

It was observed that when a superlattice is covered by an overlayer, its corrugation will be attenuated [64, 80, 90] by a factor, named the attenuation factor, which is the ratio between the corrugations of a direct Moiré pattern and a Moiré pattern covered by an overlayer. The attenuation factors (AF) reported in the literature are listed in Table. 3.2.II, where we can see the attenuation factor for one layer is about 2.6 while for two layers it is around 5.

The superlattice in Fig. 3.2.6 extends across a monoatomic step, and this time the overlayer attenuates the superlattice corrugation with the attenuation factor (AF) of 2.3. Liu *et al.* have reported an AF of 5 for two overlayers [64]. Putting this data into eq. (3.2.5), which we propose for relating an AF_n to its corresponding number of overlayers n, we can work out K_1 to be 1 and K_2, which we name the "attenuation coefficient", to be 0.81.

$$\boldsymbol{AF_n = K_1 e^{K_2 n}} \qquad (3.2.5)$$

This equation predicts the AF_3 for three overlayers to be 11.4. The attenuation of the corrugation of this superlattice is in stark contrast to the corrugation conservation observed in Fig. 3.2.1(a). The superlattice in Fig. 3.2.6 is due to the Moiré rotation pattern and thus shows attenuation in the presence of overlayers. The superlattice in Fig. 3.2.1(a) is more complex to understand, as within our measurement limits, the corrugation amplitude is identical on both sides of the atomic step. According to our eq. (3.2.5), the ratio of the amplitudes of the corrugation on both sides of the step should be $\exp(K_2)$. To fit our data in this case then, K_2 would have to be extremely small, of the order 0.03 or less. This is obviously significantly smaller than the value we have just found of 0.81. We can only speculate that this discrepancy suggests that in this particular case, the superlattice is not entirely due to a Moiré rotation, but may in fact be due to a network of nanoscale defects below the surface.

Fig. 3.2.7 (solid line) shows the plotting of the attenuation factor (AF) against the number of overlayers (n) with eq. (3.2.5), and it predicts the attenuation factor for three overlayers to be 11.4. Dalidchik *et al*. [100] also suggested an equation to describe the superlattice corrugation covered by n number of layers:

$$\boldsymbol{H_n = H_0 \times \alpha^n} \qquad (3.2.6)$$

where α is found to be around 0.5 from their own experimental data. If we interpret eq. (3.2.6) in terms of attenuation factor, i.e. $AF = H_0/H_n$:

$$AF_n = 2^n \quad (3.2.7)$$

Fig. 3.2.7 (dashed line) shows the plotting of the attenuation factor (AF) against the number of overlayers (n) by eq. (3.2.7), and it calculates AF_1=2, AF_2=4. The attenuation factor for three overlayers is predicted to be 8, smaller than the one by eq. (3.2.5). Both eq. (3.2.5) and eq. (3.2.7) exhibit an exponential relationship between attenuation factor and number of overlayers, which is not surprising as the electronic influence from a subsurface layer is expected to decay exponentially with its depth. Considering the attenuation factor for four overlayers to be approximately 20.8 [the average from eqs. (3.2.5) and (3.2.7)], a superlattice covered by four overlayers would be very difficult to observe as its corrugation amplitude is likely to be less than 0.5 Å, which is even smaller than graphite atomic lattice corrugation.

Although the corrugation of a direct Moiré rotation induced superlattice (without overlayer) is voltage dependent, the voltage dependence of a covered Moiré induced superlattice is rather weak [80]. As a consequence the attenuation factor is subject to the change of the bias voltage, which is reflected by Table 3.2.II wherein we can see, even for the same number of overlayers, the attenuation factor changes slightly according to the tunnelling conditions.

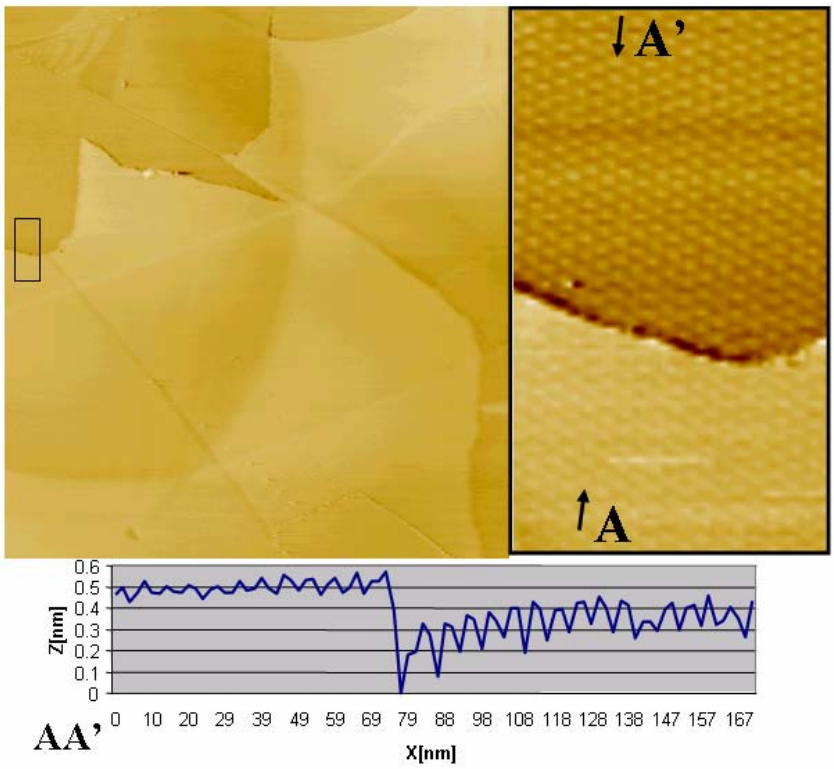

Fig. 3.2.6. 935 nm x 853 nm image (I_t = 0.5 nA, V_s = 206 mV) which is about the same area as in Fig. 3.2.3(a). The black squared area on the left is zoomed in and displayed on the right where we can observe a superlattice being attenuated by an overlayer. The cross-section along AA' is shown at the bottom.

Table 3.2.II. The reported experimental values of an attenuation factor in the literature.

Source of data	Tunnelling condition	Number of overlayer	Attenuation factor
[80]	V_t = 20 mV, I_t = 0.8 nA	1	2.6
[80]	V_t = 180 mV, I_t = 0.9 nA	1	2.3
[80]	V_t = 15 mV, I_t = 0.8 nA	1	2.6
[80]	V_t = 180 mV, I_t = 0.9 nA	1	1.6*
[100]	(not provided)	1	2#
[100]	(not provided)	2	4#
[98]	V_s = 206 mV, I_t = 0.5 nA	1	2.3
[64]	V_t = 178 mV, I_t = 2.4 nA	2	5
[90]	V_s = 100 mV, I_t = 1.0 nA	1	2.4
[89]	V_t = 150 mV	1	1.59
[107]	V_s = 1200mV	1	2.15

*This is the attenuation factor for the bead-like boundary of the superlattice covered by one overlayer

#The authors of [100] observed the superlattices covered by one and two graphite sheets, and from these data, they proposed eq. (3.2.6); however, without mentioning explicitly the attenuation factors that they observed experimentally for one and two overlayers. The values in Table 3.2.II are calculated from eq. (3.2.6).

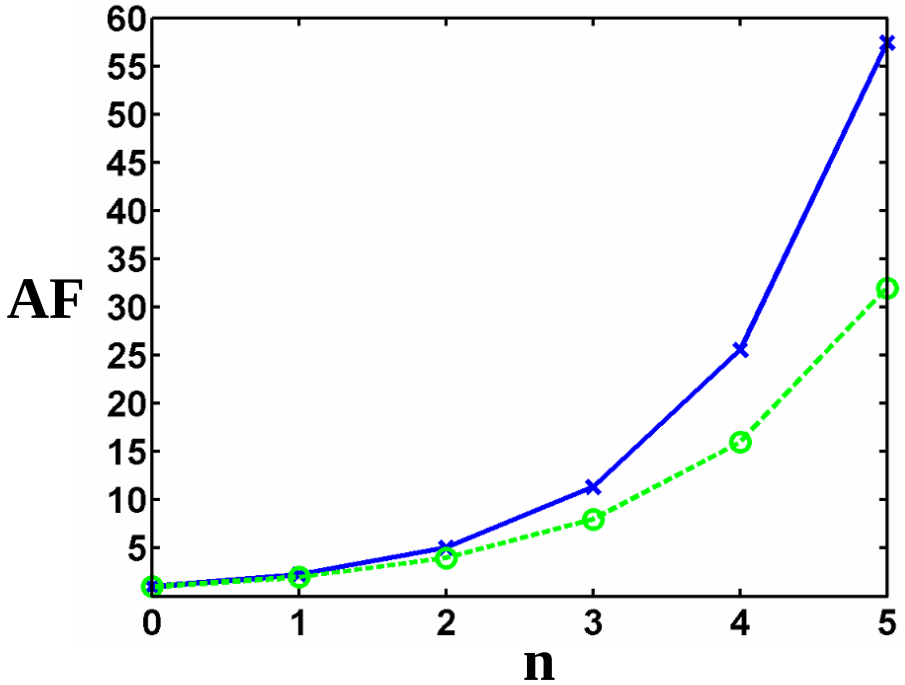

Number of layers (n)		0	1	2	3	4	5
Attenuation factor (AF)	Eq. (3.2.5) $AF_n = e^{0.81n}$	1	2.25	5.05	11.4	25.5	57.4
	Eq. (3.2.7) $AF_n = 2^n$	1	2	4	8	16	32

Fig. 3.2.7. Plotting of attenuation factor (AF) against the number of overlayers (n) by eq. (3.2.5) [solid line] and eq. (3.2.7) [dashed line]. The values of each data point are shown in the table below the graph.

3.2.4 Conclusion

The corrugation conservation phenomenon was observed on a graphite superlattice and this may exhibit an implication that nanoscale defects a few layers underneath the surface propagating through many layers without decay can also be the cause of a superlattice; however, its origin is still unclear and worth further investigation. Some rippling fringes were imaged on the superlattice areas and nearby regions, whose cause may be due to the physical buckling of the surface under intralayer stress, appearing as rippling fringes under the STM. The intralayer stress is explained in terms of different periodicities and thus different rotation angles of the superlattice domains. An equation is proposed to relate the attenuation factor to the number of overlayers, and it predicts the attenuation factor for three overlayers to be 11.4. We have reviewed the attenuation factors reported in the literature and conducted comparison between the equation proposed by us and the equation by Dalidchik *et al*. The attenuation factor for four overlayers is predicted to be approximately 20.8, thus a superlattice covered by four overlayers would be very difficult to observe.

In the next chapter, we will move on to introduce the simulation model of graphite superlattices, and how we apply it in the study of the superlattice phenomenon.

Chapter 3.3 Simulation study of graphite superlattices

Summary

A model of graphite which is easy to comprehend and simple to implement for the simulation of scanning tunnelling microscopy (STM) images is introduced in this chapter. This model simulates the atomic density of graphite layers, which in turn correlates with the local density of states. The mechanism and construction of such a model is explained with all the necessary details which have not been explicitly reported before. This model is applied to the investigation of rippling fringes which have been experimentally observed on a superlattice as described in the previous chapter, and it is found that the rippling fringes are not related to the superlattice itself. A superlattice with abnormal topmost layers interaction is simulated, and the result affirms the validity of the Moiré rotation pattern assumption. The "odd-even" transition along the atomic rows of a superlattice is simulated, and the simulation result shows that when there is more than one rotated layer at the top, the "odd-even" transition will not be manifest. The coexisting superlattices phenomenon which we have mentioned in chapter 3.1 is also studied with this model. Moreover, we will mention the related simulation works by other workers. The work of this chapter is published in the Japanese Journal of Applied Physics, vol. 44, no. 7B, p.5365-5369 [130].

3.3.1 Introduction

Scanning probe microscopy investigations have extensively used graphite as a substrate due to its chemical inertness and ease of cleaving. The atomically flat surface of graphite has provided an ideal platform for surface scientists to deposit various kinds of materials of interest for imaging and examining. The natural graphite surface is worthy of further understanding as it contains a variety of defects [84], among which superlattice structures have been observed a number of times, whose origin is not yet completely understood [67].

Kuwabara *et al.* have proposed the Moiré rotation pattern assumption to explain the origin of superlattices, and eq. (3.1.1) in chapter 3.1 relates the periodicity D of a superlattice to its rotation angle θ between two graphite layers

$$D = \frac{d}{2\sin(\theta/2)}, \qquad \text{[eq. (3.1.1) from chapter 3.1]}$$

where *d* is the atomic lattice constant [63]. Kobayashi has suggested another mechanism that nanoscale features a few layers underneath the surface can propagate through many layers without decay to explain superlattice formation [116]. Although there is still no clear conclusion on the origin of superlattices, the Moiré rotation pattern should have a role in the formation of superlattices since Rong *et al.*[66] and Xhie *et al.*[67] have shown that the Moiré pattern equation [eq. (3.1.1)] can properly describe the experimental results of the periodicity of the superlattice and the rotation angle by directly imaging the related atomic lattice vectors with the STM. Therefore, it is of paramount importance to investigate the origin of superlattices from the Moiré rotation pattern assumption point of view.

In order to achieve this, a simulation model of a Moiré rotation-induced superlattice would be indispensable since a superlattice cannot be experimentally prepared beforehand, as it happens randomly. Without a simulation model, it would be difficult to amass data for analysis. Having been applied first in molecular dynamic simulations [131], this model has been used to study superlattices a number of times [90, 91, 128].

3.3.2 Simulation model

The model is based on a formula which describes a continuous hexagonal lattice similar to the atomic lattice of graphite [128, 131]. This formula has appeared in [90, 128, 131]; however, explanation and description on its formation was not reported before. Here we describe all the necessary details of the mechanism and construction of this model and the way we simulate the relative shift between the alternating layers. The atomic density of a layer n, Φ_n, at a position (x, y) is:

$$\Phi_n = 1 - \frac{2}{9}\left[\cos\left[\left(\frac{2\pi}{2.46}\right)\left(x'' + \frac{y''}{\sqrt{3}}\right)\right] + \cos\left[\left(\frac{2\pi}{2.46}\right)\left(x'' - \frac{y''}{\sqrt{3}}\right)\right] + \cos\left[\left(\frac{4\pi}{2.46}\right)\left(\frac{y''}{\sqrt{3}}\right)\right] + \frac{3}{2}\right] \quad (3.3.1)$$

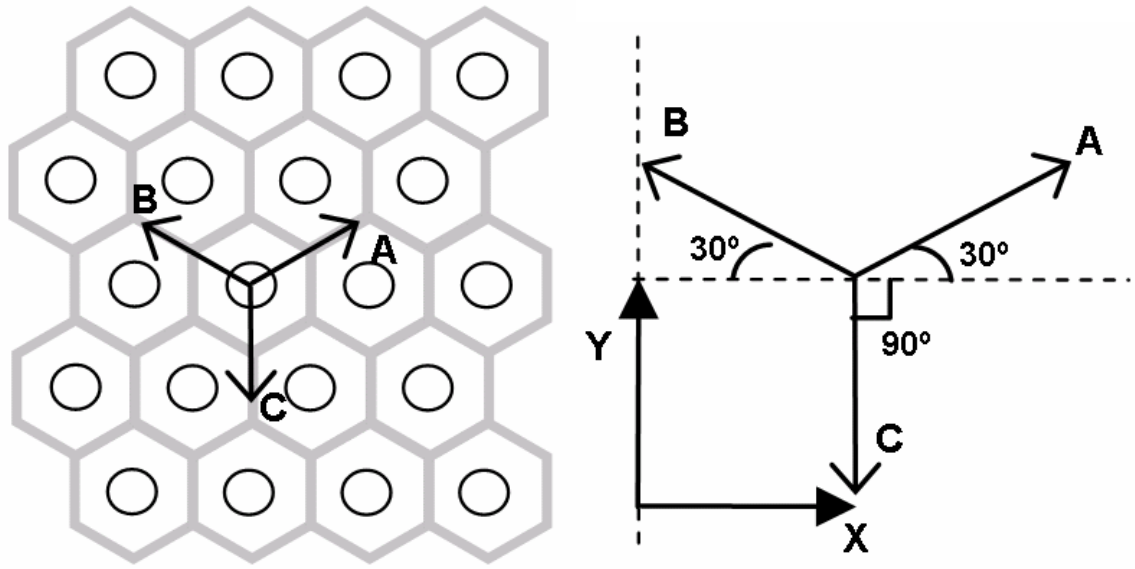

Fig. 3.3.1. Vectors ***A***, ***B***, ***C*** represent the directions of the three key cosine components in eq. (3.3.1). They point to three different directions which are 120º separated from each other, and their functions describe the hexagonal lattice. Vectors ***X, Y*** are the unit vectors, with which the vectors ***A***, ***B***, ***C*** can be formed as in eqs. (3.3.2) – (3.3.4). The atomic density variation along directions ***A***, ***B***, ***C*** is approximately sinusoidal, which can be simulated by the cosine functions in eq. (3.3.1).

In eq. (3.3.1), there are three key cosine components with their directions described by the vectors ***A***, ***B***, and ***C*** in Fig. 3.3.1, and they correspond to the three vectors describing the hexagonal lattice and pointing to three different directions which are 120º separated from each other. Vectors ***X*** and ***Y*** (see Fig. 3.3.1) are unit vectors directed to the X and Y directions, and they are the component vectors for vectors ***A***, ***B***, and ***C*** [eqs. (3.3.2) – (3.3.4)].

$$\vec{A} = \vec{X} + \tan 30° \bullet \vec{Y} = \vec{X} + \frac{\vec{Y}}{\sqrt{3}} \qquad (3.3.2)$$

$$\vec{B} = -\vec{X} + \tan 30° \bullet \vec{Y} = -\vec{X} + \frac{\vec{Y}}{\sqrt{3}} \qquad (3.3.3)$$

$$\vec{C} = -\sqrt{1^2 + \left(\frac{1}{\sqrt{3}}\right)^2} \bullet \vec{Y} = \frac{2}{\sqrt{3}}\vec{Y} \qquad (3.3.4)$$

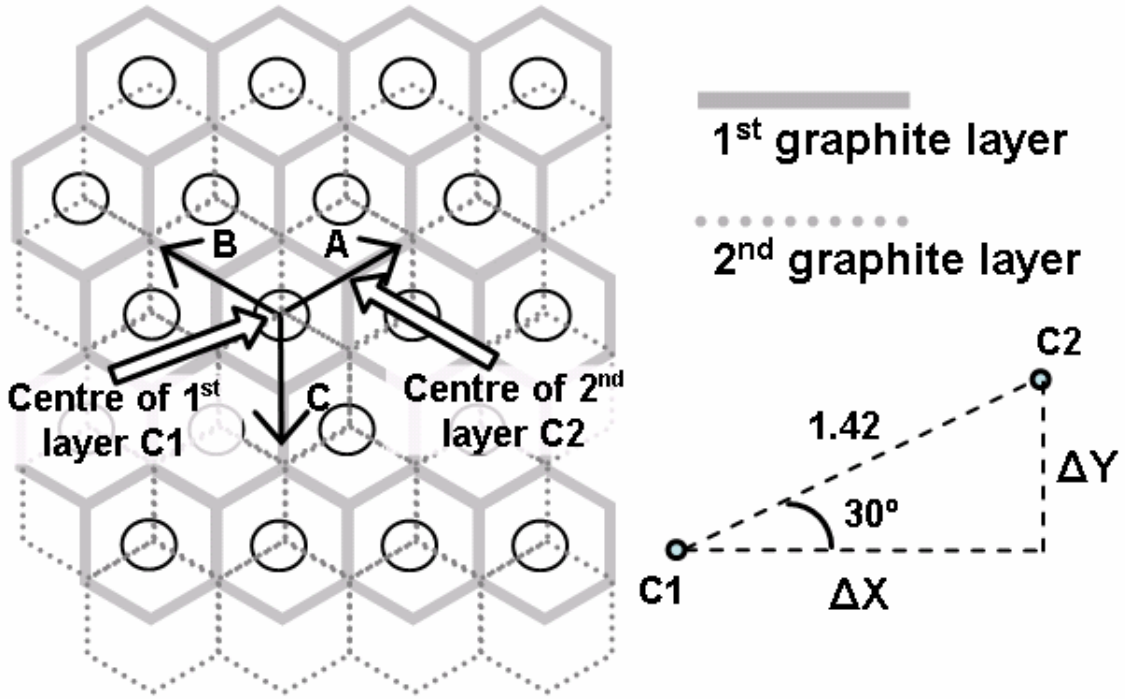

Fig. 3.3.2. The relative shift between alternating graphite layers is as shown. The centre of the 2nd layer C2 is displaced from the centre of the 1st layer C1 by a distance of 1.42 Å with the displacement of Δx along X direction and Δy along Y direction. The angle 30º is found by simple geometry from the hexagonal lattice structure. With the x and y coordinates modified by Δx and Δy as in eqs. (3.3.5) – (3.3.6), the shift can be integrated into the model.

Starting from the beginning of the vectors and propagating along the vector directions, the varying atomic density can be approximately simulated by a cosine function with a period of 2.46 Å. The offset of 3/2 at the end inside the bracket is to shift the whole function above zero value while the 2/9 at the front of the square bracket is for normalizing the bracket function. The operation of "1-" at the very front is to make such a function in phase with the actual atomic density variation. To build up a layered structure of graphite, more than one layer needs to be modelled. However, bear in mind that there is a relative shift between the alternating layers (see Fig. 3.3.2). This can be taken care of by modifying x, y in eqs. (3.3.5) and (3.3.6) so that the centre is shifted from C1 to C2. With regard to the rotation of graphite layers which will happen in a superlattice, eqs. (3.3.7) and (3.3.8) integrate the rotation angle into the model by rotating the coordinates with an angle θ.

$$x' = x + \Delta x = x + 1.42 \times \cos 30^\circ \qquad (3.3.5)$$

$$y' = y + \Delta y = y + 1.42 \times \sin 30^\circ \qquad (3.3.6)$$

$$x'' = x' \cos\theta - y' \sin\theta \qquad (3.3.7)$$

$$y'' = x' \sin\theta + y' \cos\theta \qquad (3.3.8)$$

3.3.3 Applications to superlattices

A superlattice structure on graphite can be simulated with this model for various kinds of investigations. First of all, we show that by using this model, the atomic lattice and superlattice structures of graphite can be simulated as observed under the STM. Then, we apply it to the investigations of the rippling fringes of the superlattice which we observed on graphite. One of the unusual aspects of superperiodic features on graphite proposed by Cee *et al.* [128] is compared with our corresponding simulation results. The "odd-even" transition along the atomic rows of the graphite atomic lattice on which a superlattice is superimposed, is simulated and investigated to observe how this transition phenomenon evolves as the periodicity of the superlattice changes [65]. The coexisting superlattices phenomenon is simulated with this model as well.

3.3.3.1 Modelling of superlattice structure

A superlattice can be modelled as two graphite layers with a rotation angle between them. Simulations of STM images generally entail including the effect of a third layer underneath the first two. There is a different weighting for each layer depending on the contribution of each layer to the overall structure. In normal cases, 1, 0.5, and 0.125 (normal weightings) are used for the 1st, 2nd, and 3rd layers respectively to reflect the assumption that the influence of a layer should decay with its depth from the surface [90]. By adding the atomic density contribution of each layer together, an STM image can be simulated with the intensity, I, at a point (x, y) as:

$$I(x,y) = \Phi_1(x,y) - W_2\Phi_2(x,y) + W_3\Phi_3(x,y), \qquad (3.3.9)$$

where Φ_n is the atomic density of layer n, and W_2 and W_3 are the weightings representing the relative contribution of the 2nd and 3rd layers. Figures 3.3.3(a) and 3.3.3(b) are the 20 nm x 20 nm superlattice area simulated with a rotation angle of 1st layer of 2.5 º, $W_2 = 0.5$ and $W_3 = 0.125$. The three-fold symmetry of a superlattice is shown as observed under the STM.

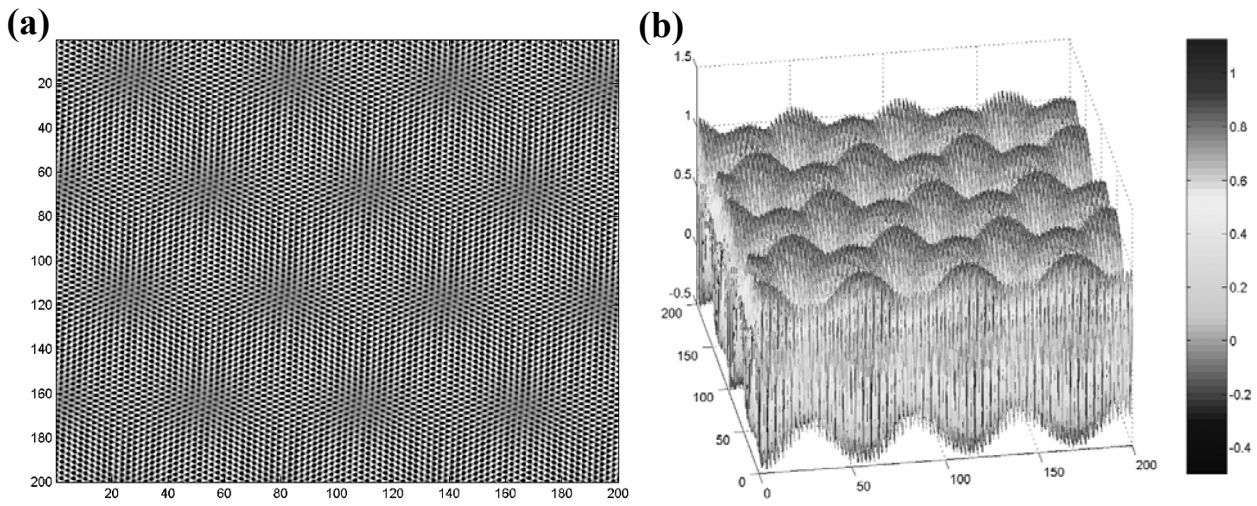

Fig. 3.3.3(a). The 2-dimensional image of the 20 nm x 20 nm superlattice with a rotation angle of 2.5° (periodicity 5.64 nm) is simulated with $W_2 = 0.5$ and $W_3 = 0.125$. The bright area is higher than the dark area. Fig. 3.3.3(b). 3D image of the 20 nm x 20 nm superlattice in Fig. 3.3.3(a). The three-fold symmetry is obvious in Fig. 3.3.3(b) where the height difference between alternating peaks is discernible.

3.3.3.2 Rippling fringes on superlattice

We have observed rippling fringes on a HOPG superlattice in our STM experiments. Those rippling fringes in the central part of Fig. 3.3.4(a) on the superlattice are of periodicity around 30 nm and corrugation 0.15 nm. In order to study whether the rippling fringes are related to the superlattice, a 400 nm x 400 nm superlattice area, which resembles the one in Fig. 3.3.4(a) where the rippling fringes appear, is simulated with the normal weightings and with a rotation angle of 2.56º [Fig. 3.3.4(b)]. The simulated area is flat with the superlattice structure but without any large-scale features which can be associated with those rippling fringes in Fig. 3.3.4(a). We have performed the simulations with translational dislocations, and still we cannot observe any kind of fringes existing in the simulation result. Therefore the rippling fringes on the graphite are not due to an electronic effect of the superlattice and they are not part of the superlattice itself. One possible explanation for those rippling fringes is the physical buckling of the surface due to the intralayer strain. We believe this arises because the graphene sheet is bounded on three sides (laterally) by graphene sheets at different orientations, and also this sheet is rotated with respect to the substrate. This large degree of mismatch causes strain which can be relieved in the layer by buckling.

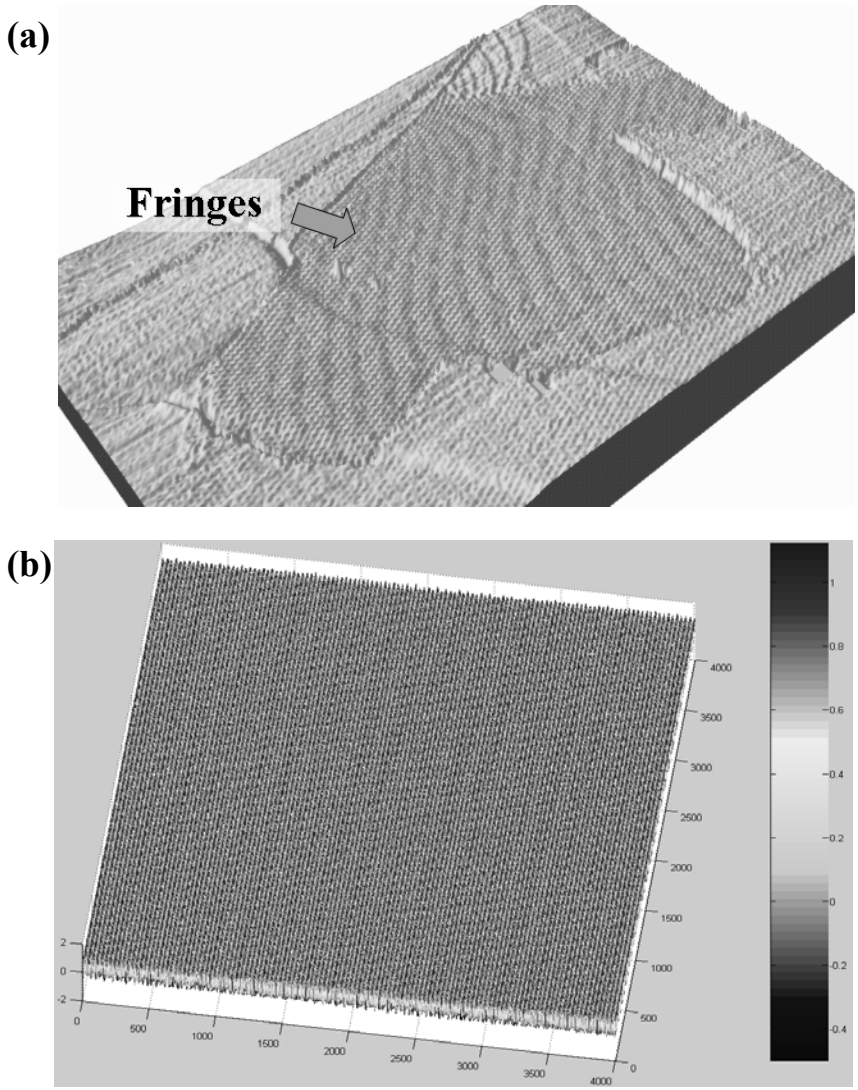

Fig. 3.3.4. Simulation of the rippling fringes on the superlattice of graphite. (a) The STM image of 700 nm x 500 nm (I_t = 0.36 nA, V_s = 450 mV) on graphite wherein we can observe the rippling fringes with periodicity of around 30 nm and corrugation 0.15 nm on the superlattice with a rotation angle of around 2.56° (periodicity 5.51 nm). (b) A superlattice with similar size and rotation angle is simulated with the normal weightings. However, there are no comparable rippling fringes in the simulation result.

3.3.3.3 Study on the unusual aspect of superlattice proposed by Cee *et al.* [128]

Cee *et al.* have simulated a superlattice, and reported that by using the exaggerated weightings of W_2 = 0.125 and W_3 = 0.25 which are counterintuitive in the respect of the Moiré rotation pattern, a better contrast and three-fold symmetry can be obtained on the simulated superlattice. We have performed the same simulation with these weightings and the same rotation angle of 5º but we obtain different results. The difference in contrast in the simulated

superlattice between using the normal weightings (W_2 = 0.5 and W_3 = 0.125) [Fig. 3.3.5(c)] and the exaggerated weightings (W_2 = 0.125 and W_3 = 0.25) [Fig. 3.3.5(d)] is not very significant. Cee *et al.* did not specify in their paper how they simulated the relative shift between alternating graphite layers which may be the reason for the difference between their results and ours. That is why we make the details of the simulation model explicit in section 3.3.2 which were not clearly explained in the literature before, so that other workers can compare their results with ours. Also the difference in contrast would be more appropriately shown when the simulation results are displayed in 3D with the same absolute vertical scale. We found that the atomic lattice of the superlattice generated with the exaggerated weightings [Fig. 3.3.5(b)] does not have as obvious three-fold symmetry as that generated with the normal weightings [Fig. 3.3.5(a)], and indeed, it is difficult to observe the three-fold symmetry in Fig. 3.3.5(b). This is expected because the three-fold symmetry of the atomic lattice arises from the α and β sites on a graphite surface which in turn are due to the subtraction of the electronic density of states of the second graphite layer from the first; by using the exaggerated weightings of W_2 = 0.125 (instead of 0.5 for normal weightings), the effect of the subtraction is significantly diminished. Therefore, our simulation results show that the normal weightings which are consistent with the Moiré rotation pattern assumption can generate a more physically realistic graphite atomic lattice and superlattice structures. The validity of the Moiré rotation pattern assumption is asserted by our simulation model in this case.

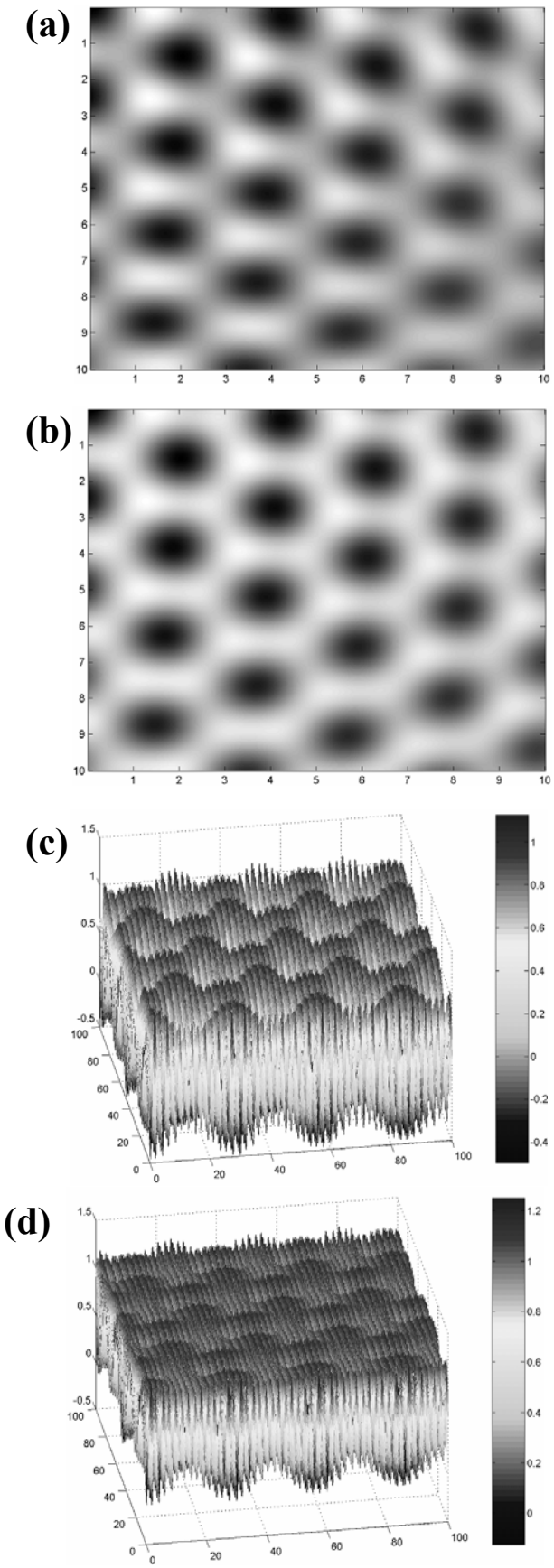

Fig. 3.3.5. Comparisons between the normal weightings and exaggerated weightings. (a) 1 nm^2 superlattice area simulated with the normal weightings. (b) 1 nm^2 superlattice area simulated with the exaggerated weightings. (c) 10 nm^2 superlattice area simulated with the normal weightings. (d) 10 nm^2 superlattice area simulated with the exaggerated weightings. All rotation angles are 5° (periodicity 2.82 nm). The three-fold symmetry of the atomic lattice is more distinct in Fig. 3.3.5(a) than in Fig. 3.3.5(b). The contrast in height is higher in Fig. 3.3.5(c) than in Fig. 3.3.5(d).

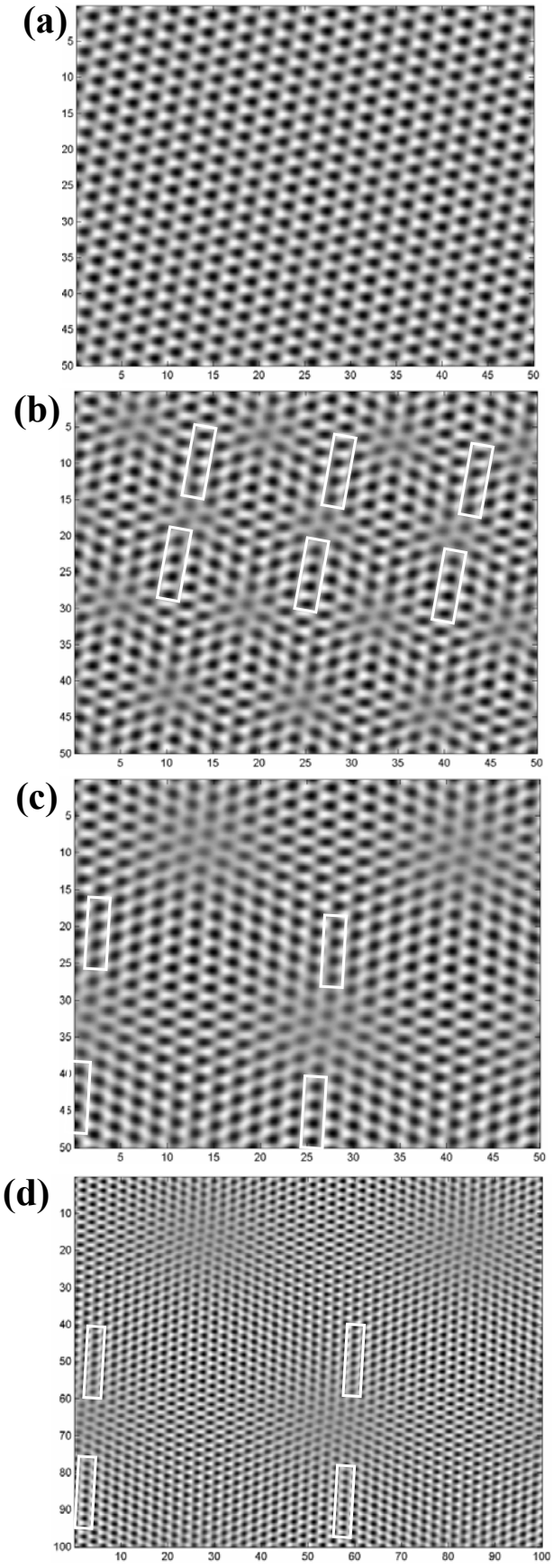

Fig. 3.3.6. "Odd-even" transition phenomenon on superlattice. (a) 5 nm^2 superlattice area with 1st and 2nd layers rotated by 10º relative to 3rd layer and periodicity of 1.41 nm. (b) 5 nm^2 superlattice area with 1st layer rotated by 10º relative to 2nd and 3rd layers and periodicity of 1.41 nm. (c) 5 nm^2 superlattice area with 1st layer rotated by 5º relative to 2nd and 3rd layers and periodicity of 2.82 nm. (d) 10 nm^2 superlattice area with 1st layer rotated by 2.5º relative to 2nd and 3rd layer and periodicity of 5.64 nm. All images are simulated with the normal weightings of $W_2 = 0.5$ and $W_3 = 0.125$. Osing's proposal of the "odd-even" transition is proven by the simulation results shown in Fig. 3.3.6(a) and Fig. 3.3.6(b) where only Fig. 3.3.6(b) shows the transition. As the periodicity increases from Fig. 3.3.6(b) to Fig. 3.3.6(d), the transition phenomenon gets smeared out over distance.

3.3.3.4 "Odd-even" transition along atomic rows

It has been observed that when a superlattice structure is superimposed onto the underlying atomic lattice, the "odd-even" transition, which is a shift along an atomic row, will be manifested on the graphite surface (Fig. 12 in [102]). Osing *et al.* have proposed that such a transition will only occur if there is only one single layer rotated, thus it can be used as a criterion for determining whether the number of rotated layers is more than one [65]. Osing's proposal has been proved by our simulation results [Fig. 3.3.6(a)] which show that when there are two rotated layers, the "odd-even" transition will not be manifested, whereas the transition phenomenon will be obvious if there is only one rotated layer [Fig. 3.3.6(b)].

We have investigated the influence of the periodicity of a superlattice on its "odd-even" transition phenomenon. From our simulation results, it is found that as the periodicity of the superlattice increases, the transition will be less significant due to the fact that the transition occurs over a longer distance and thus gets smeared out [see Figs. 3.3.6(b) – 3.3.6(d)]. In the STM scanning, as the scanning size increases, the effect of thermal drift is likely to have a role in the images, and therefore, it would be difficult to decide, if the transition exists, whether it is due to the single layer rotation or thermal drift, especially, when the scan size is more than, for example, 10 nm.

3.3.3.5 Coexisting superlattices

In most of the cases reported, only one superlattice exists in an area at a time. However, Xhie *et al*. [67] and Ball *et al*. [107] have reported coexisting graphite superlattices – a superlattice with a larger periodicity on top of another coexisting superlattice. In the image from Xhie *et al*. (Fig. 3.3.7), on top of a superlattice, there is another superlattice with a larger periodicity but having a slightly distorted hexagonal shape, while in the image from Ball *et al*. (Fig. 3.3.8), the two superlattices with different periodicities having hexagonal symmetry coexist in the same area. Such a phenomenon is ascribed to two rotated graphene layers with different rotation angles. It is possible to verify this explanation by simulating a superlattice with the top two layers rotated with different angles.

A superlattice can be simulated with the top two layers rotated with different angles with respect to the third layer. In this way, we will be able to see whether two superlattices can coexist in the same area by Moiré rotation. We have carried out a simulation to model the coexisting superlattice (Fig. 3.3.8) observed by Ball *et al*. The simulated area is 67 nm x 67 nm, similar to the 63 nm x 63 nm image of the coexisting superlattice (Fig. 3.3.8). The first

graphite layer is simulated with a rotation angle of 4.3°, while the second graphite layer is simulated with 0.73°, both with respect to the third layer. Normal weightings of $W_2 = 0.5$ and $W_1 = 0.125$ are used and the simulation result is shown in Fig. 3.3.9. The simulated results show coexisting superlattices with periodicities and hexagonal symmetries similar to the observation of Ball *et al*.

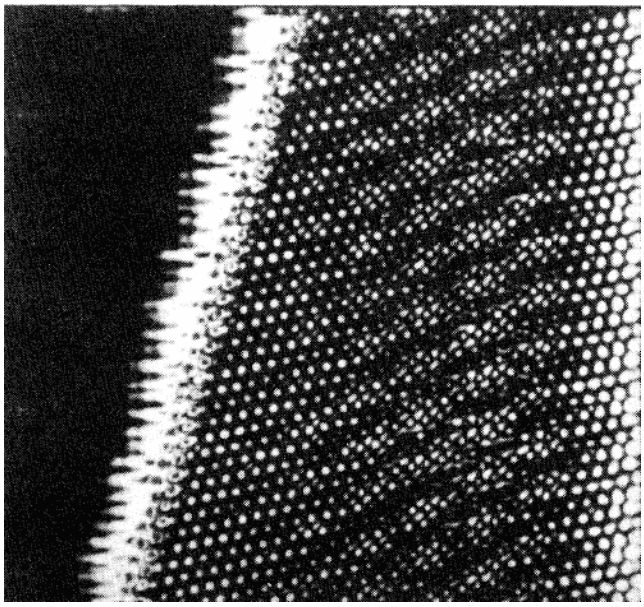

Fig. 3.3.7. STM image of 160 nm x 160 nm. The region on the right-hand side of the boundary shows a superlattice superimposed by another superlattice with a larger periodicity (supergiant lattice). The corrugation of the supergiant lattice is around 1/10 of the superlattice. Image reprinted from [67].

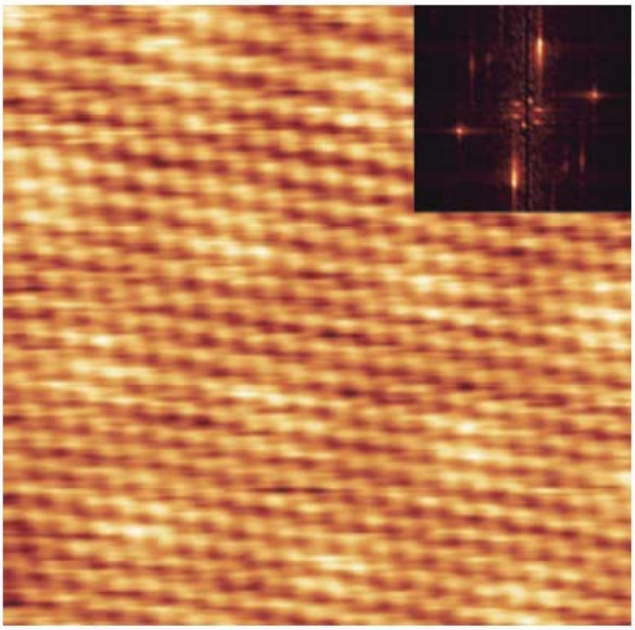

Fig. 3.3.8. 63 nm x 63 nm, $V_s = +700$ mV. Coexisting superlattices with periodicities of 19.2 nm and 3.25 nm observed by Ball *et al*. The inset shows the corresponding FFT spectrum. Image from "Observation of solvent-induced superlattices at graphite surfaces" 2005, in preparation, authored by S. J. Ball, J. M. MacLeod, and A. B. McLean [107].

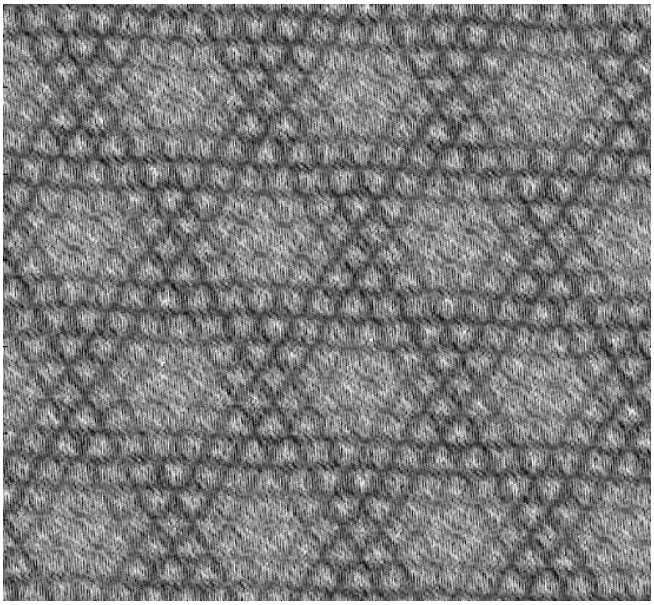

Fig. 3.3.9. A superlattice with area of 67 nm x 67 nm simulated with the top layer rotated 4.3° and the second layer rotated 0.73° with respect to the third layer respectively. The simulation result is similar to the STM image in Fig. 3.3.8.

3.3.3.6 Superlattice with screw dislocation

Superlattices generally have constant periodicities and their patterns remain the same over the whole region. However, Feddes *et al*. [91] observed a superlattice with its periodicity varying around a screw dislocation [Fig. 3.3.10(a)]. The periodicity of the superlattice varies from 18 nm to 72 nm around the screw dislocation. Feddes *et al*.used a different model which is based on the similar idea as eq. (3.3.1) but it is slightly different in the way that the model has two conditions to rule out non-physical phenomena: first, the atomic density is not allowed to increase as a result of interlayer interactions; second, the simulated density cannot become smaller than the minimum value of the first layer. These are achieved by adjusting a cut-off parameter of the second layer and a scaling parameter for controlling the subtraction of the second layer atomic density from the first layer. In Feddes model, the simulated atomic density of a layer at any point (x, y) is:

$$p(x,y) = \delta(x,y) + \delta(x,y-1.23) \qquad (3.3.10)$$

in which

$$\delta(x,y) = \cos\left[\left(\frac{2\pi}{2.46}\right)\left(x + \frac{y}{\sqrt{3}}\right)\right] + \cos\left[\left(\frac{2\pi}{2.46}\right)\left(x - \frac{y}{\sqrt{3}}\right)\right] + \cos\left[\left(\frac{4\pi}{2.46}\right)\left(\frac{y}{\sqrt{3}}\right)\right], \qquad (3.3.11)$$

the first component in eq. (3.3.10) describes the α sites while the second component describes the β sites. In this way, the physical significance of α or β sites can be individually adjusted so that the simulated image matches the usual STM image of graphite surfaces. Readers are referred to [91] for details of the Feddes model. Feddes *et al*. simulated a superlattice with its rotation angle, thus its periodicity [by eq. (3.1.1)], varies around the screw dislocation [Fig. 3.3.10(b). As such, it was shown that the anomalous phenomenon of the superlattice around a

screw dislocation is likely to be due to the varying rotation angle of the graphite layer around the screw dislocation. Bernhardt *et al*. [94] and Sawamura *et al*. [103] also observed superlattice structures with varying periodicities. However, the variations were along one direction rather than circulated around a screw dislocation.

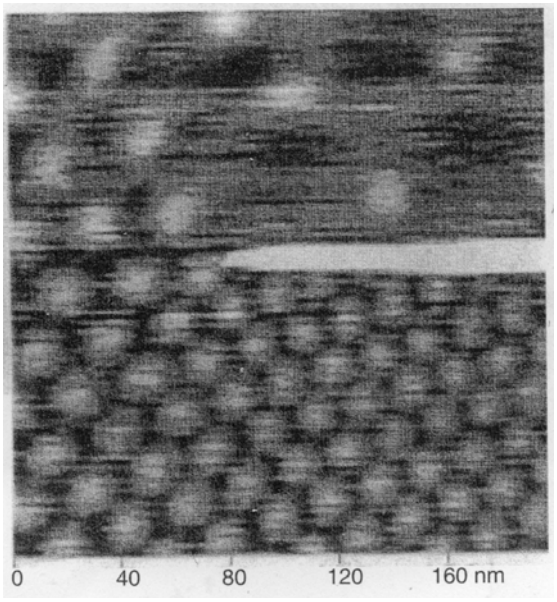

Fig. 3.3.10(a). The STM image (200 nm x 200 nm) of Feddes *et al*. showing a graphite superlattice around a screw dislocation. Image reprinted from [91].

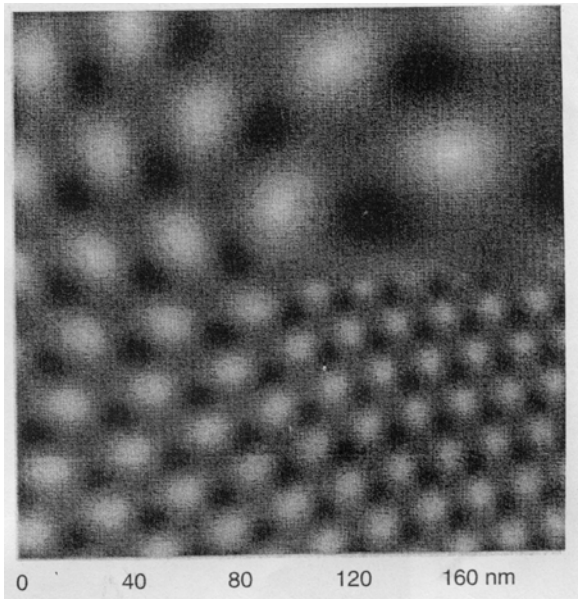

Fig. 3.3.10(b). The simulation result of the superlattice around a screw dislocation by Feddes *et al*. The superlattice constant changes from 18 nm to 72 nm as it circles around the dislocation. Image reprinted from [91].

The model described in this chapter is also used for simulating a superlattice with a screw dislocation. The moiré rotation angle θ varies from 4° to 8° as it goes around the dislocation anticlockwise with the angle ϕ as shown in the Fig. 3.3.11(a). The normal weightings of W_2 = 0.5 and W_3 = 0.125 are used. Fig. 3.3.11(b) shows the simulated superlattice around a screw dislocation with its moiré rotation angle θ of the first graphite layer with respect to the second layer varies as indicated in the graph of Fig. 3.3.11(a). The superlattice periodicity changes from 3.52 nm to 1.76 nm as ϕ changes from 0° to 360°. This result shows that the model described in this chapter can simulate a screw dislocation like the Feddes' model does. We simulated a superlattice with a smaller range of periodicity because of the computation power, but it will not have an effect on the physical meaning of the result. Fig. 3.3.11(c) is the Fast Fourier Transform (FFT) of Fig. 3.3.11(b). There are two sets of hexagonal patterns, with one inside the other. The outer hexagonal pattern consists of six dots and six spirals: the six dots correspond to the atomic lattices of the second layer whereas the

six spirals correspond to the atomic lattices of the first layer; the spiral shape is due to the fact that the atomic lattices of the first layer are stretched because of the varying moiré rotation angle around the screw dislocation. The inner hexagonal pattern is composed of six spirals which are related to the superlattice pattern. The spiral shape is due to the varying moiré rotation angle which causes the varying superlattice periodicity around the screw dislocation.

Our simulation work on superlattices around screw dislocations shows that the model introduced in this chapter can be applied in simulating superlattices with screw dislocations like Feddes' model does. Moreover, the simulation results of our model can be analyzed with the Fast Fourier Transform.

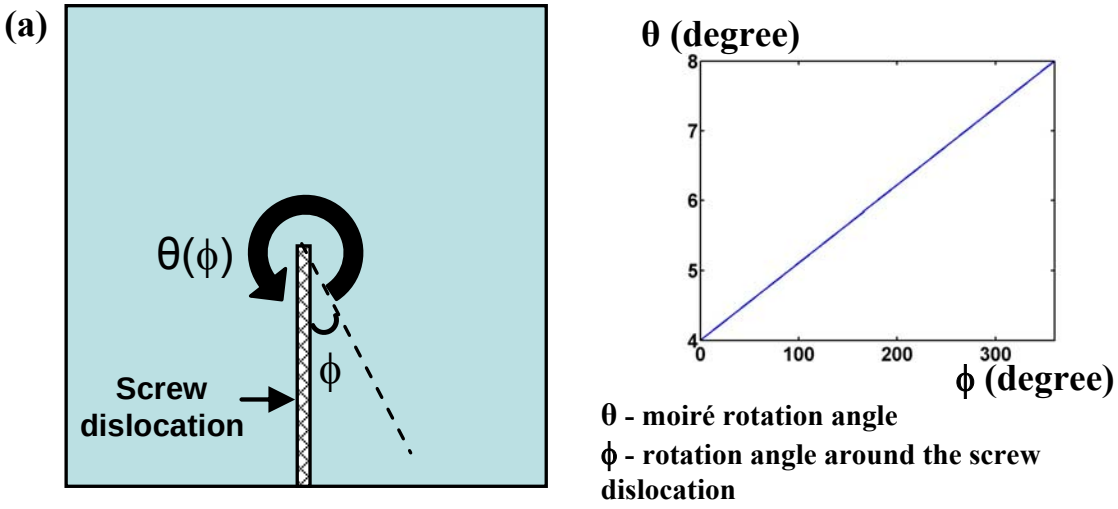

Fig. 3.3.11(a). The schematic model showing the superlattice with a screw dislocation which is simulated by the model described in section 3.3.2 with the graph on the right showing the variation of the graphite layer rotation angle θ as the angle ϕ around the screw dislocation increases from 0° to 360°.

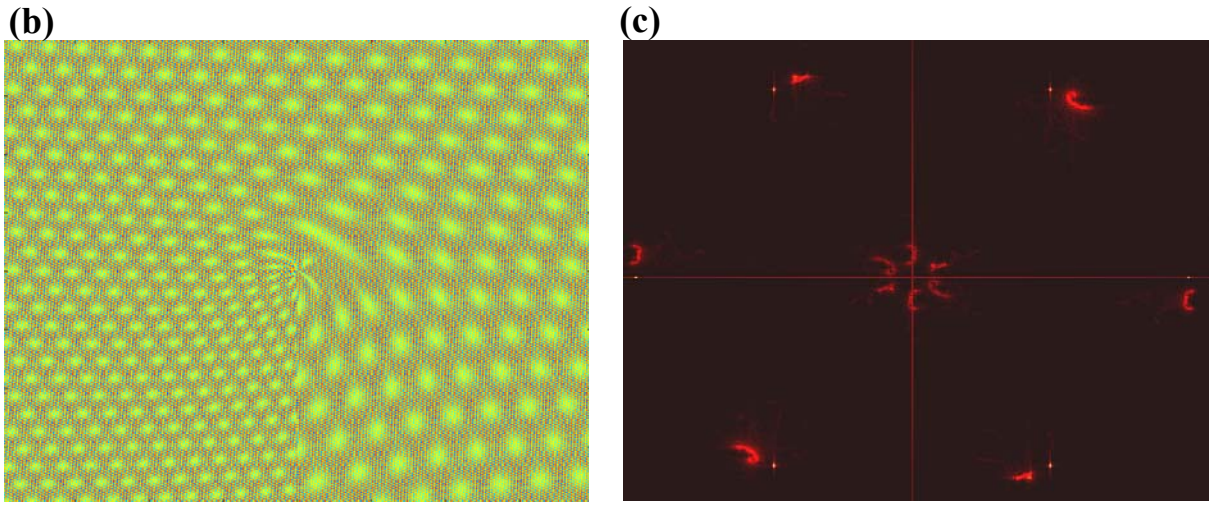

Fig. 3.3.11(b) – The simulation result of the superlattice with screw dislocation by using our model with the normal weightings. It is very similar to the result of Feddes *et al*. The simulation area is 40 nm x 40 nm with data points of 700 x 700.

Fig. 3.3.11(c) – The Fast Fourier Transform (FFT) spectrum of the simulation result in Fig. 3.3.11(b).

3.3.3.7 Other reported simulation works on superlattices

3.3.3.7.(i) Twist and glide boundaries by Sun *et al.* [90]

Sun *et al*. [90] used the simulation model to investigate the twist boundary between two different regions of superlattices. They constructed a Moiré pattern using three layers, and along one close-packed direction, the image is divided into two halves with different stacking faults. In this way, the simulated image is in agreement with the observed STM image, indicating that the boundary is indeed a twist boundary. The boundary with two parallel rows of bright protrusions between two different superlattice regions was studied by dividing the image along one close-packed direction into two halves with the other half glided along the 30°/60° direction with different gliding distances, which are an integer number of times the superlattice periodicity and fractional periodicity (1/3 for 30°, 1/2 for 60°). The simulation result exhibited that the boundary is a glide boundary, and by comparing the simulation results of the twist and glide boundaries, Sun *et al*. concluded that it is insufficient to identify twisting from gliding only based on a symmetry consideration. Their results show that the application of the simulation model is not only limited to superperiodic patterns of superlattices but also useful for studying superlattice boundaries, which initiated us to investigate superlattice boundaries with the aid of the simulation model as discussed in the next chapter.

3.3.3.7.(ii) Integrating tip shape and tip-sample distance by Sawamura *et al.* [103]

It is possible to take the tip shape and the tip-sample distance into consideration, and integrate them with the simulation model. First applied by Sawamura *et al*. [103] in the three-dimensional simulation for the experimental STM image on the superlattice based on the rotation angle of the crystal axis of the tip with respect to the substrate crystal axis, eq. (3.3.12) defines the tunnelling current as the summation of currents due to tunnelling from each atom on the tip to every atom of the sample surface. The current intensity between an atom on the surface and an atom on the tip is described by the Tersoff and Hamann relation in the low bias limit [11]. The net tunnelling current from an STM tip located at the position (l,k) to the surface can be defined as:

$$I_{total} = \sum_i \sum_j I_{ij}(l,k), \qquad (3.3.12)$$

in which

$$I_{ij}(l,k) = A\exp[-\alpha\{(x_{ij}-x_{lk})^2+(y_{ij}-y_{lk})^2+(z_{ij}-z_{lk})^2\}^{1/2}] \qquad (3.3.13)$$

where $I_{ij}(l,k)$ is the tunnelling current between an atom at (x_{ij},y_{ij},z_{ij}) on the surface and an atom at (x_{lk},y_{lk},z_{lk}) on the STM tip, and α is dependent upon the characteristics of the materials of both the tip and surface.

By integrating this formulation into the simulation model of this chapter, we can first simulate the graphite lattice with eq. (3.3.1), and then the shape of the tip and the tip-sample distance can be considered by eq. (3.3.12) and eq. (3.3.13). The final simulated STM image will be the image of the net tunnelling current which is the summation of all tunnelling occurrences between the tip and the sample. This combined model is useful for studying the influence of tip shape and tip-sample distance on the resulting superlattice structures on STM images. This will be further discussed in section 3.5.2.2 in chapter 3.5.

3.3.4 Conclusion

Here we describe a model for graphite layers and its applications in investigating superlattice structures that have been observed in numerous STM experiments. This model is shown to be a powerful tool for analyzing various kinds of superlattice phenomena, which is important for the research of superlattices whose origin is not yet totally understood. Our simulations show different results from those of [128], however they are consistent with the Moiré rotation pattern assumption. The "odd-even" transition phenomenon and the theory by Osing *et al.* are shown and proven in this work. Coexisting superlattice phenomenon is simulated by this model which shows that two superlattices can coexist in the same area by Moiré rotation.

The simulation programs written in Matlab language for each application in this chapter are included in the Appendix C, and the files are named as follows: "*superlattice3*" for section 3.3.3.1; "*rippling*" for section 3.3.3.2; "*Cee*" for section 3.3.3.3; "*oddeven3*" for section 3.3.3.4; *"coexist_sup"* for section 3.3.3.5; *"screw"* for section 3.3.3.6.

Here we have looked at how to use a simulation model to study graphite superlattices. In the next chapter, we shall investigate the origins of different kinds of superlattice boundaries with the aid of modelling.

Chapter 3.4 Observation and investigation of graphite superlattice boundaries by scanning tunnelling microscopy

Summary

In this chapter, we report on scanning tunnelling microscopy (STM) observations of several different kinds of superlattice boundaries on highly-oriented pyrolytic graphite (HOPG) including an array of bead-like structures, a thin wall-like boundary, a monolayer deep trench, a zig-zag shaped termination, and a plain boundary without features. Results of a simulation model show that a top rotated graphite layer with a straight boundary does not necessarily lead to the zig-zag shaped boundary of the resulting superlattice as has been previously claimed. The formation of the bead-like, thin wall-like, trench, and zig-zag shaped boundaries is explained from the energetic point of view. Our study also shows evidence for the superlattice-mediated observation of a low-angle grain boundary with a varying tilt angle. A relationship between the periodicity of the boundary dislocations and the periodicity of the superlattice across the boundary is derived. The result of this work is important for the understanding of the superlattice phenomenon on graphite whose origin is not yet completely understood. The analysis in this chapter is submitted to the Physical Review B for publication [132].

3.4.1. Introduction

Although superlattices on graphite have been observed many times by scanning tunnelling microscopy (STM) [60, 62, 63, 65-67, 80, 88, 89, 91, 94, 95, 128], a complete understanding has yet to be achieved over their physical origin. Several theories and hypotheses ranging from Moiré interference patterns due to a mis-orientation of two layers of graphite, to sub-surface arrays of nanoscale defects have been proposed to explain the origin of superlattices [66, 67, 90, 116]. To date however, not much discussion has been focussed on superlattice boundaries, which is an intriguing subject on its own due to the fact that the boundary is the region where the transition from normal graphite to a superlattice occurs. Having a deeper understanding of the nature of these boundaries will help us to understand the origin of the superlattices. In this chapter, we report our observation of several different types of superlattice boundaries by STM.

3.4.2. Experiment

The highly oriented pyrolytic graphite (HOPG) was freshly cleaved a number of times before being imaged with either the home-built STM (construction details in chapter 2) or a Nanosurf STM [32] in constant current mode under ambient conditions. Mechanically cut Pt/Ir tips were used.

3.4.3. Observations of superlattice boundaries

In this section we will briefly describe each of the different types of superlattice boundary we have observed. An in-depth discussion and analysis follows in later sections.

I. Array of bead-like structures (Fig. 3.4.1)

At the intersection between the normal graphite (i.e. a superlattice-free region) and a superlattice (which, in this case has a periodicity of 6.5 nm) there is an uneven boundary along which there is an array of bead-like structures whose corrugation is 0.26 nm, larger than the superlattice corrugation of 0.17 nm. Observations on similar boundary structures

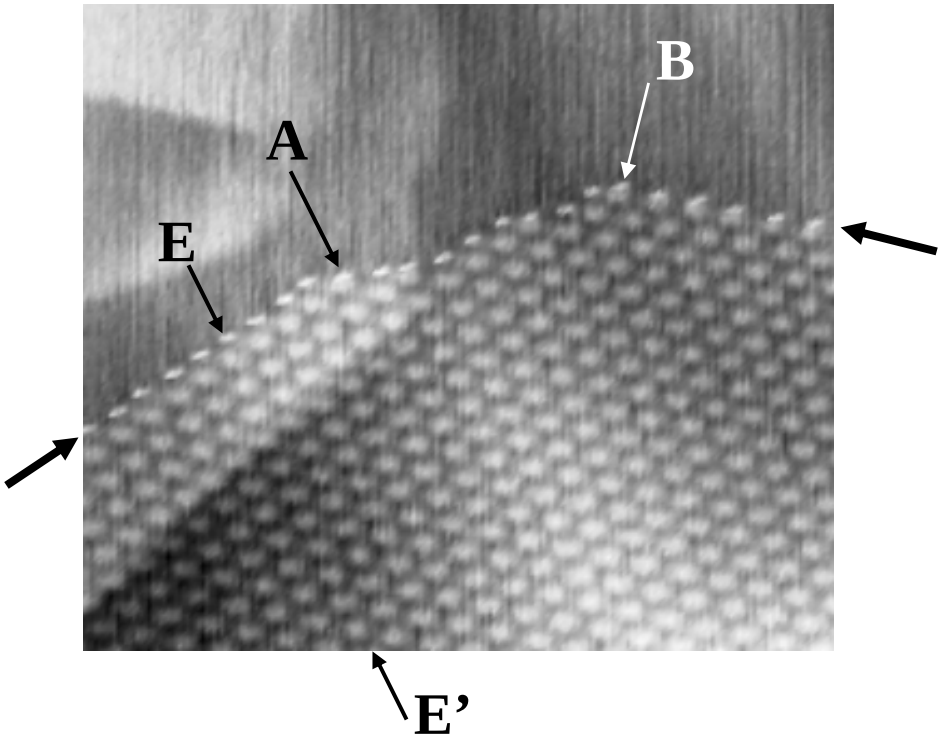

Fig. 3.4.1. 106 nm x 123 nm image, I_t = 0.5 nA, V_t = 230 mV, periodicity of the superlattice = 6.5 nm. The array of bead-like structure, which is the boundary for the superlattice, is indicated by the thicker arrows. At locations A and B, the bead-like boundary cuts through the bright spots of the superlattice which are of higher energy. If we look at the superlattice row by row each along the direction EE', each bead on the boundary corresponds to each row of the superlattice.

have previously been reported in the literature [66, 67, 87, 90]. Traversing the boundary indicated by the thick arrows in Fig. 3.4.1, the position of each bead on the boundary corresponds to each row of the superlattice (along the direction EE'). The boundary intersects localised regions of increased electron density (which appear as bright spots in the image) at locations A and B. According to the tight-binding density calculation of the electronic states on graphite by Charlier *et al*. [133], these bright spots are of AAB stacking [80] with higher energy of 0.0085 states/eV than the surrounding regions. It appears that the exact location and orientation of the superlattice boundary determines the boundary's appearance. These phenomena will be discussed in the next section.

II. Thin wall-like structure with corrugation (Fig. 3.4.2)

This thin wall-like structure acts as the termination of the superlattice whose periodicity is 6.4 nm. The boundary has a height of approximately 0.25 nm which is larger than the superlattice corrugation of 0.14 nm. Measurement of the height along the boundary reveals that the topography of the wall is modulated with a corrugation of 0.1 nm at the same periodicity as the superlattice next to the boundary. This observation is similar to the case of the bead-like boundary where each bead corresponds to each row of the superlattice. Buckley *et al*. has observed a similar boundary and ascribed it to the breakage of the carbon-carbon

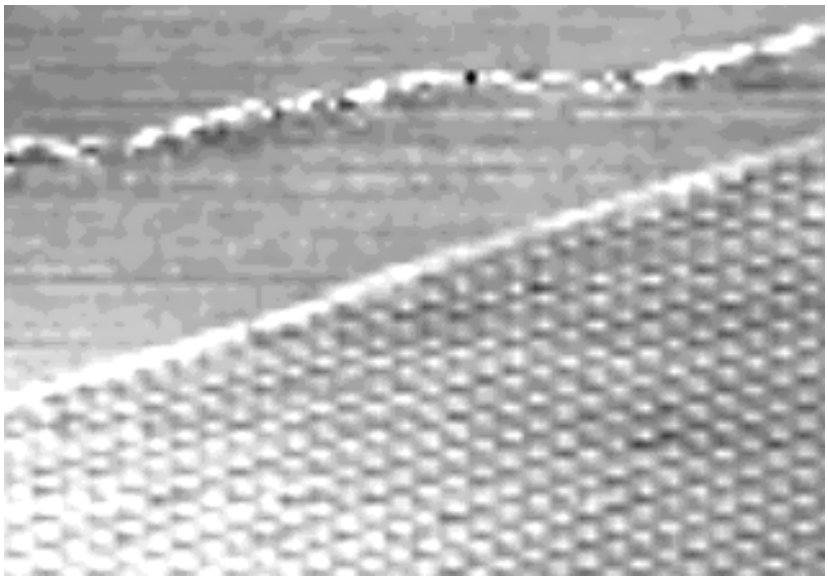

Fig. 3.4.2. 123 nm x 176 nm image, I_t = 0.36 nA, V_s = 450 mV, periodicity of the superlattice = 6.4 nm. The height of the thin wall-like boundary is approximately 0.25 nm, and the topography along the "thin wall" is a modulation with corrugation of around 0.1 nm and periodicity of 6.4 nm. The corrugation of the superlattice below the boundary is about 0.14 nm.

covalent bonds at atomic steps [87]. However in their images, the large height of the superlattice features makes it difficult to discern the existence of any steps.

III. One monolayer deep trench (Fig. 3.4.3)

The superlattice is terminated by a trench which is around one monolayer deep. The superlattices on each side of the trench are at equal heights. The trench is oriented parallel to the superlattice and stretches through the lower points of the superlattice without dissecting the bright spots. According to the calculation of Charlier *et al*. [133], the lower valleys of superlattices are of ABC stacking with lower energy of 0.0021 states/eV [80], thus such a boundary should be energetically stable as it does not involve the disruption of the high energy superlattice peaks.

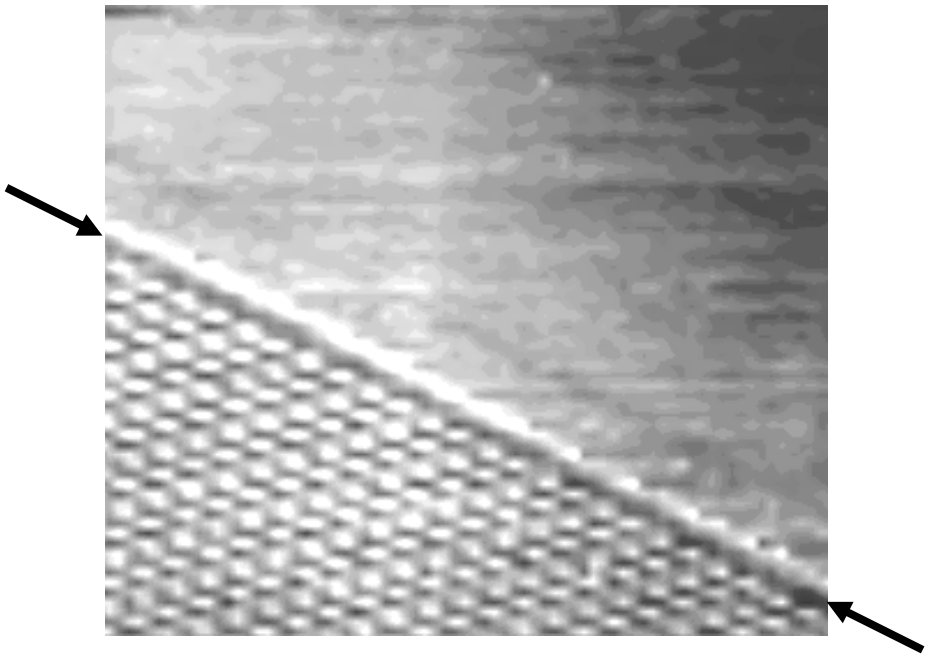

Fig. 3.4.3. 127 nm x 145 nm, I_t = 0.5 nA, V_s = 206 mV, periodicity of the superlattice = 5.0 nm. The trench, indicated by the arrows, has depth of approximately 0.33 nm.

IV. Zig-zag shaped boundary (Fig. 3.4.4)

The superlattice is terminated by a monoatomic step with a zig-zag shape. This kind of zig-zag shaped boundary has been observed previously [63, 95]. In all of these results, the zig-zag shaped boundaries appear to go around the superlattice bright spots rather than dissect them. This point will be further discussed later.

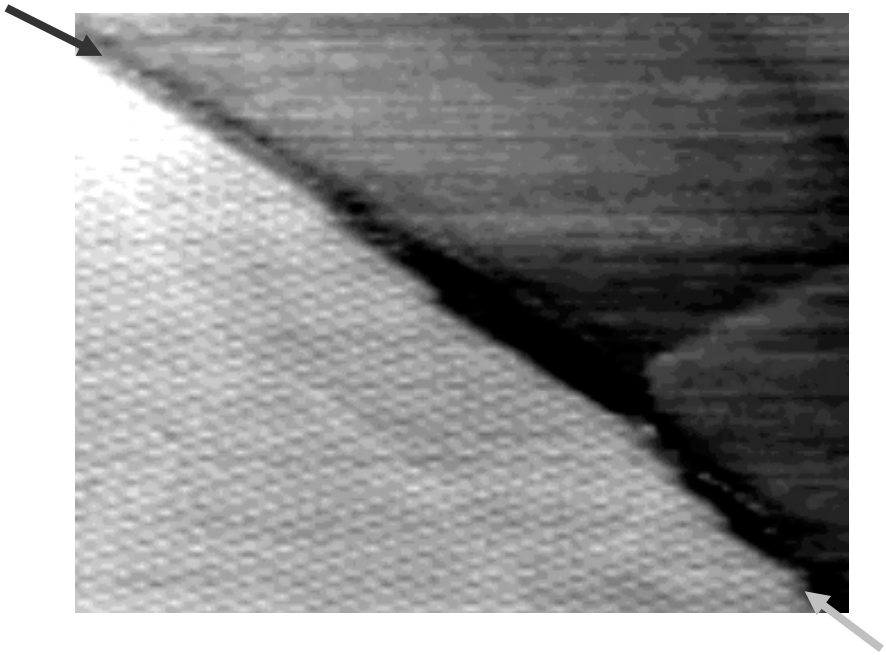

Fig. 3.4.4. 200 nm x 254 nm, I_t = 0.5 nA, V_s = 206 mV, periodicity of the superlattice = 5.3 nm. The zig-zag shaped termination is pointed by the arrows.

V. Plain boundary without features [Fig. 3.4.5(b)]

The intersection is a plain boundary without features [Fig. 3.4.5(b)]. Unlike the trench or the zig-zag shaped boundaries, it dissects some of the superlattice bright spots. On the left of the superlattice lies a double-stranded ribbon-like structure (G_2B_2) with a width of approximately 3.5 nm and height of 0.3 nm [Fig. 3.4.5(c)]. It has a corrugation of 0.2 nm and periodicity of 1.3 nm. Apparently the ribbon-like structures G_2B_2 and G_1B_1 [see Fig. 3.4.5(a)] were originally the same ribbon, but due to some reason, for instance the cleaving of the surface, they were shifted away from each other with the offset, coincidently, being the space between the plain boundary and the G_2B_2. This point will be further discussed in the next section. Similar graphite strands have been observed before with width from 10 to 16 nm, height from 1 to 3 nm, and more than six micron in length, which are about 10 times larger than the one reported here [85]. It was proposed that this kind of graphite strand is representative of a disrupted graphite surface and may be associated with flaking of the surface [85]. Other groups have observed similar strand-like structures with ordered features [84, 88, 94]. Gan *et al.* regarded this kind of double-stranded ribbon-like structure as a grain boundary [61]. Comparing the ribbon-like structure G_2B_2 in Fig. 3.4.5(c) with GB in Fig. 1(d) in [61], both of them have periodic features and their periodicities and corrugations are of similar order of magnitude, therefore it is likely G_1B_1 and G_2B_2 in Figures. 3.4.5(a) and 3.4.5(c) are also grain boundaries as the GB in [61].

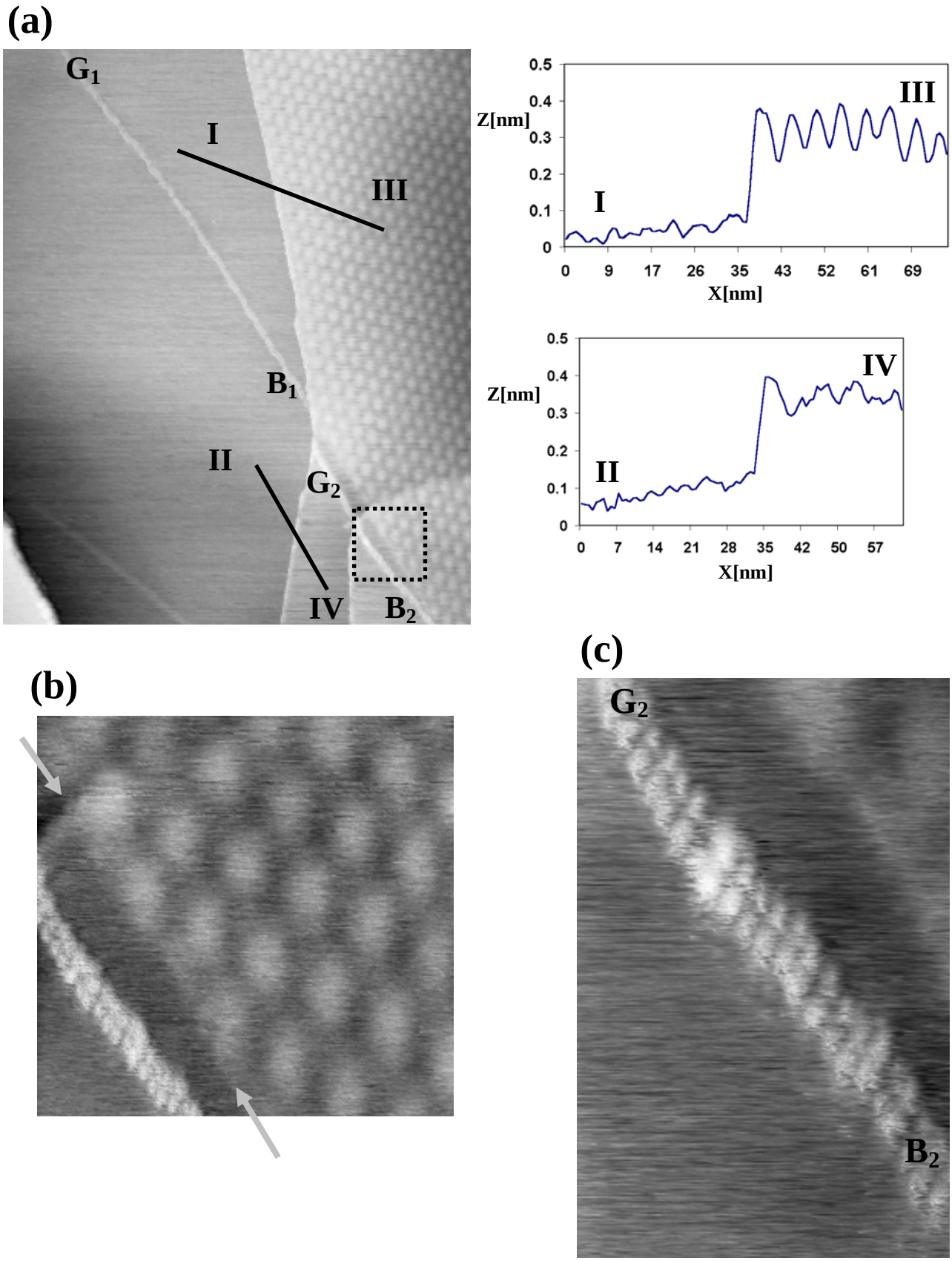

Fig. 3.4.5(a) – (c)

(Fig. 3.4.5(d) follows on next page)

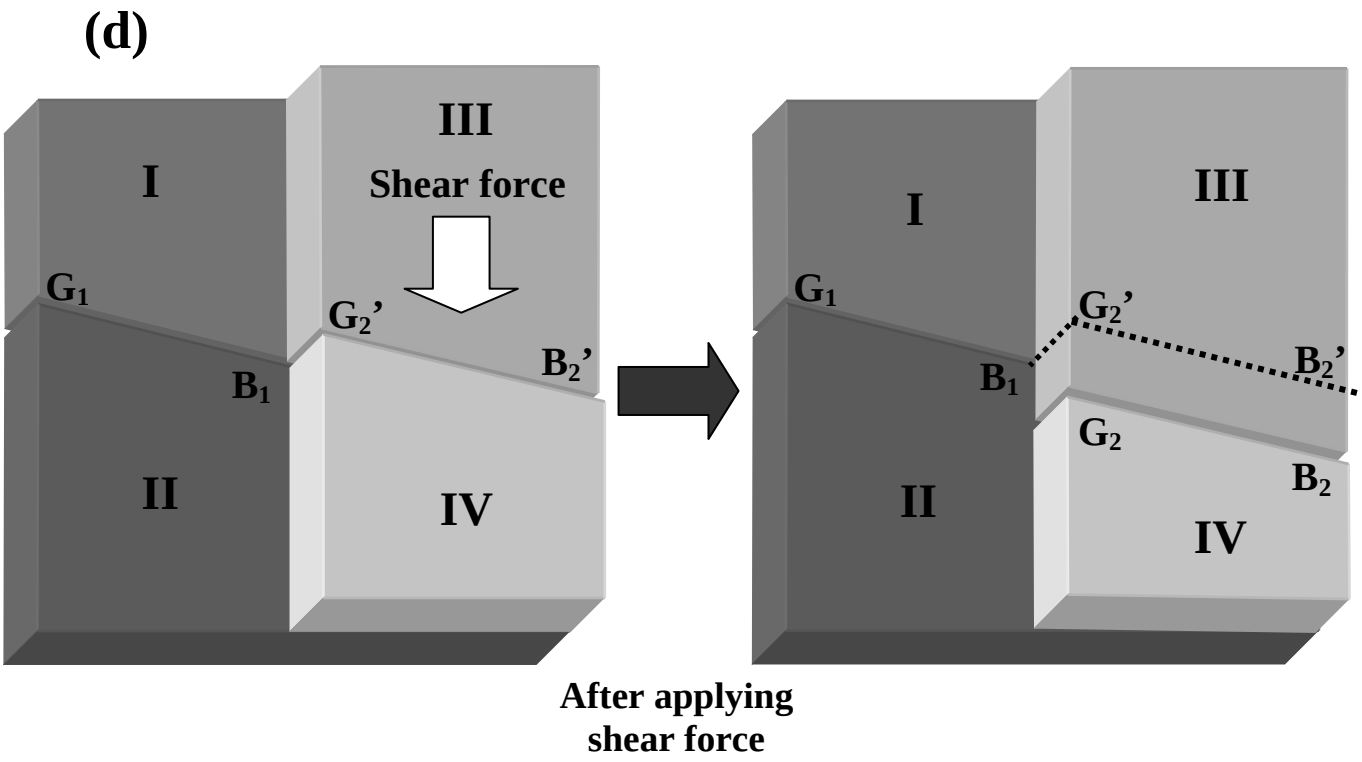

Fig. 3.4.5. (a) 157 nm x 194 nm, I_t = 0.5 nA, V_t = 230 mV. This image shows the location of the plain boundary and the grain boundaries associated with it. The cross-sections show that regions III and IV are one monolayer higher than regions I and II. (b) The zoom-in of the framed area in Fig. 3.4.5(a). 39 nm x 39 nm, I_t = 0.5 nA, V_t = 230 mV, periodicity of the superlattice = 7.1 nm. The plain boundary (pointed by the arrows), unlike the other kinds of boundaries, does not have any particular features. (c) 17.6 nm x 27.6 nm, I_t = 0.5 nA, V_t = 230 mV. A zoom-in of the double-stranded ribbon-like structure on the left of the plain boundary. It shows the periodic feature on the ribbon. (d) A model explaining the relative movement of the graphene sheets next to the grain boundary.

VI. Array of protrusions with uneven spacing (Fig. 3.4.6)

Here we observe a superlattice region with varying periodicity (from 7.1 nm to 9.6 nm) between the two conventional superlattice regions, and the intersection which marks the boundary is an array of protrusions with uneven spacing of tens of nanometres. Those protrusions have a range of heights from 0.34 nm at the lower side to 0.52 nm at the upper side. A superlattice region with varying periodicity was observed by Bernhardt *et al*. [94], but in that case, the superlattice was in a pit and so the boundary is a step edge.

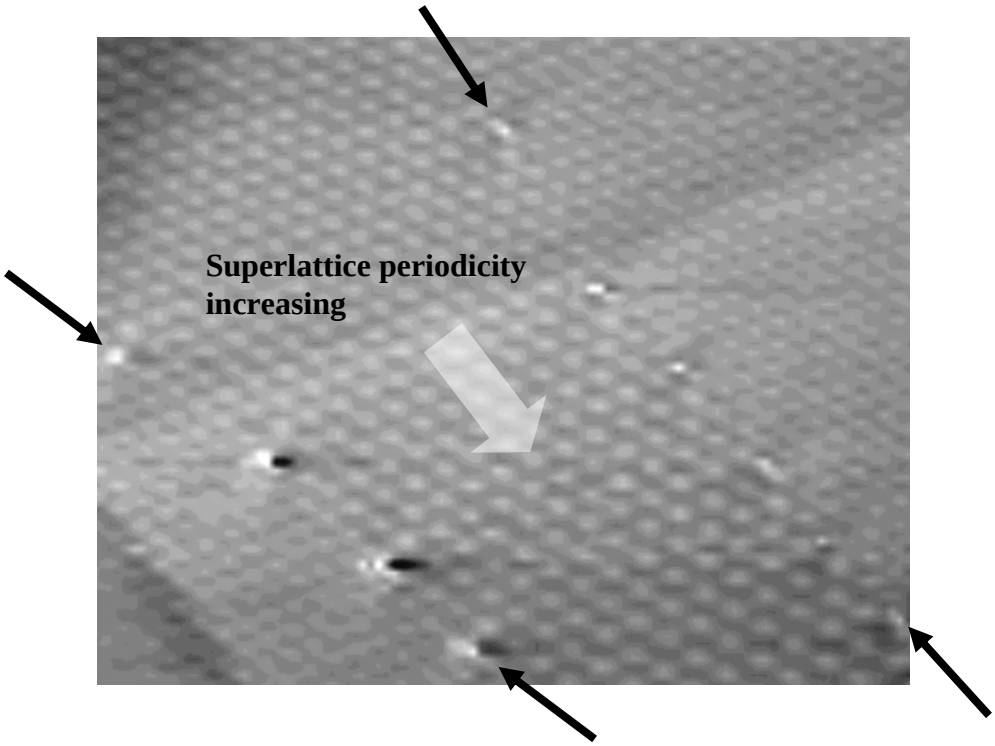

Fig. 3.4.6. 162 nm x 204 nm, I_t = 0.5 nA, V_s = 206 mV, the superlattice periodicity varies from around 9.6 nm to 7.1 nm within the boundaries which are in the form of the arrays of protrusions. The boundaries with arrays of protrusions are indicated by the black arrows.

3.4.4 Discussion

3.4.4.1 Origins of zigzag shaped boundary, bead-like boundary, and trench boundary

We have performed investigations into these superlattice boundaries from the energetic point of view. First, we will study the zig-zag shaped boundary. The zig-zag shaped boundary was discussed before and it was speculatively proposed that when the top graphite layer has a straight boundary, the observed superstructure induced by the Moiré pattern must have a zig-zag shape at the boundary [95, 99]. We have analyzed the zig-zag shaped boundary with the simulation model described in chapter 3.3. A top layer with a straight boundary is modelled and the result is shown in Fig. 3.4.7. According to the description in [95, 99], when the top rotated layer has a straight boundary which intersects the superlattice bright spots, we should observe a zig-zag shaped boundary with STM. In fact, we find experimentally that depending on its direction, the superlattice boundary does not necessarily have to intersect the bright spots. It can extend through the lower points (dark spots, or regions of reduced electron density) of the superlattice, and therefore does not result

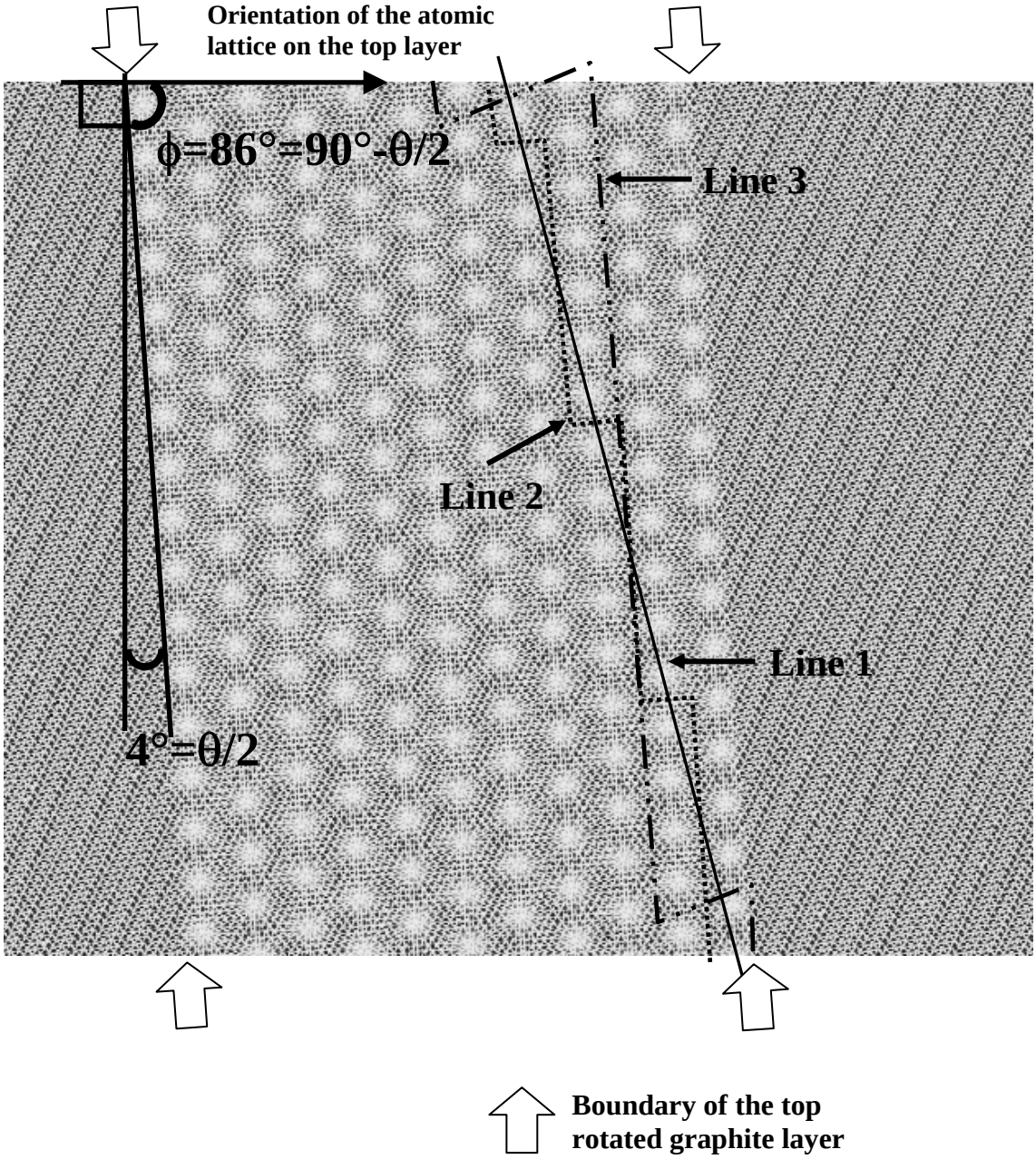

Fig. 3.4.7. 30 nm x 30 nm simulated graphite area with the top layer as a stripe in the shape of a parallelogram with the length of 30 nm and width of 16.5 nm, giving an area of 495 nm^2, whose atomic lattice is rotated 8˚ (θ) with respect to the second layer with the size of 30 nm x 30 nm. The top rotated layer has straight boundaries which are the same boundaries as the resulting superlattice. The simulation is performed with normal weightings of 0.5 for the first layer and 0.125 for the second layer. The configuration of the weightings of each layer for simulation of graphite is described and explained in chapter 3.3.

in a zig-zag shape as suggested. This argument is supported by our simulation results. We have simulated the superlattice which arises when the top graphite layer in the form of a

parallelogram stripe (length = 30 nm, width = 16.5 nm, area = length x width = 495 nm^2) has its atomic lattice rotated by eight degrees (θ) with respect to the second layer (length = 30 nm, width = 30 nm), and where the boundary of the top layer is straight with an angle of four degrees (θ/2) with respect to the perpendicular direction (see Fig. 3.4.7). Although it has a straight termination for its top layer, the simulation result shows that the resulting superlattice boundary does not intersect the bright spots, and thus would not form the zig-zag shape boundary according to the mechanism in [95, 99]. Moreover, as the boundary just cuts through the lower valleys which are of ABC stacking with lower energy (0.0021 states/eV) [80], it is energetically more stable. Hence a top rotated graphite layer with a straight termination can still form a superlattice with a straight boundary.

We would like to propose a physical reason for the origin of the zig-zag shaped boundary which was not reported before. From chapter 3.1, we know that the orientation angle of a Moiré superlattice pattern with respect to the top graphite layer is given by

$\phi=30°-\theta/2$ [eq. 3.1.2 from chapter 3.1]

where θ is the rotation between the graphite layers which causes the superlattice, as is schematically shown in Fig. 3.4.8. As we can see from the model, there are certain distinct

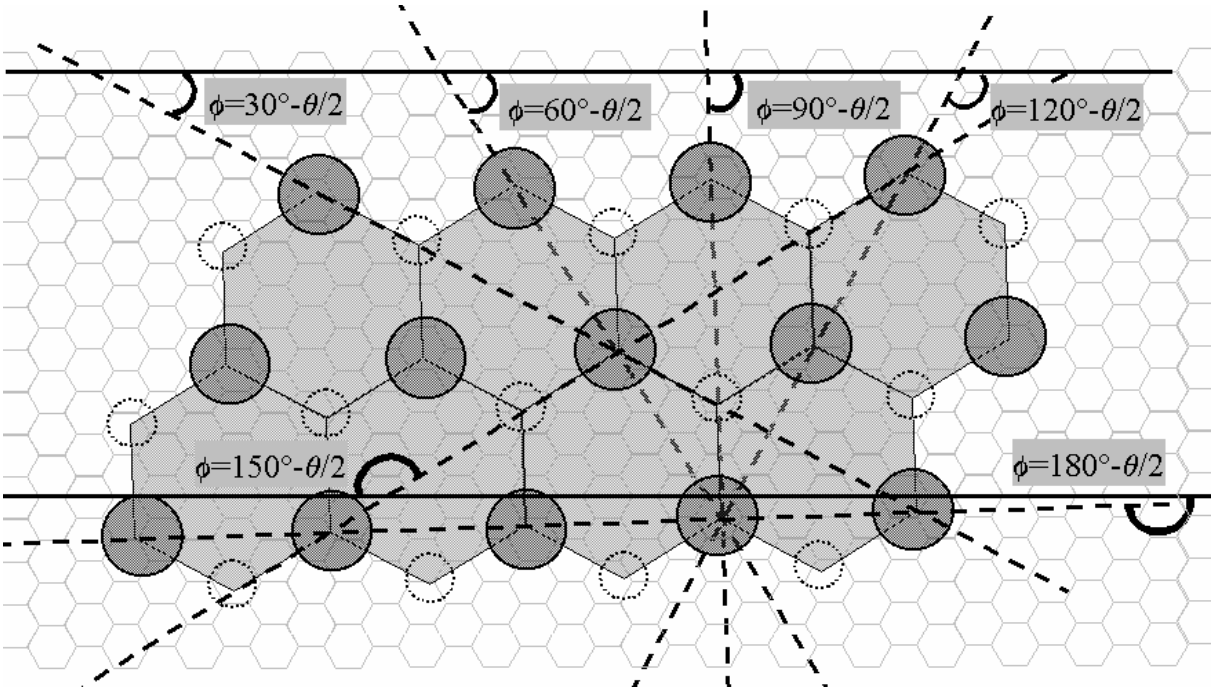

Fig. 3.4.8. This model illustrates the orientation angle of the superlattice with respect to the top graphite layer. The smaller hexagonal lattices underneath are the top graphite layer while the big closed circles are the brightest spots of the superlattice; the small open circles outlined with dashed lines are the medium bright spots of the superlattice. The orientation of the Moiré superlattice pattern is $\phi=30°-\theta/2$ relative to the top graphite layer with θ being the rotation angle between the top two graphite layers which causes the superlattice. We can see that in order to go in parallel with a superlattice, the boundary has to be with one of the angles ϕ indicated in the figure.

angles where the boundary is parallel to an axis of the superlattice: $\phi=30°-\theta/2$, $\phi=60°-\theta/2$, $\phi=90°-\theta/2$, $\phi=120°-\theta/2$, $\phi=150°-\theta/2$, $\phi=180°-\theta/2$ (the superlattice simulated in Fig. 3.4.7 has an angle of $\phi=90°-\theta/2$). The probability of having the top rotated layer boundary exactly along one of these directions is rather small and the more likely situation is that the boundary intersects the bright spots as shown by line 1 in Fig. 3.4.7. However, the bright spots are of AAB stacking whose energy is higher (0.0085 states/eV), and thus the boundary along line 1 is not energetically favourable. Instead of line 1, the boundary has a tendency to select line 2 because this line only cuts through energetically low points and is thus more stable. Line 2 is preferred to line 3 because it takes less effort to change from line 1 to line 2 as line 2 is the most similar to line 1. A superlattice simulation similar to the one in Fig. 3.4.7 where the top layer is in the form of a parallelogram and the second layer is in the form of a rectangle is carried out and shown in Fig. 3.4.9. However, in this simulation, the right-hand edge of the top layer which is originally straight as in Fig. 3.4.7 is replaced by line 2 which is zig-zag in shape. The simulation result in Fig. 3.4.9 shows a superlattice with the zig-zag shaped boundary as line 2 which indicates that a superlattice with a zig-zag shaped boundary is possible if the boundary of the rotated layer itself is zig-zag in shape. The zig-zag shaped boundary of the simulated superlattice in Fig. 3.4.9 is similar to the zig-zag shaped boundary in Fig. 3.4.4, except their periodicities of the transition edges are different. We conclude that a possible reason why a zig-zag shaped boundary occurs, for instance in Fig. 3.4.4, is as it is a way to lower the boundary energy.

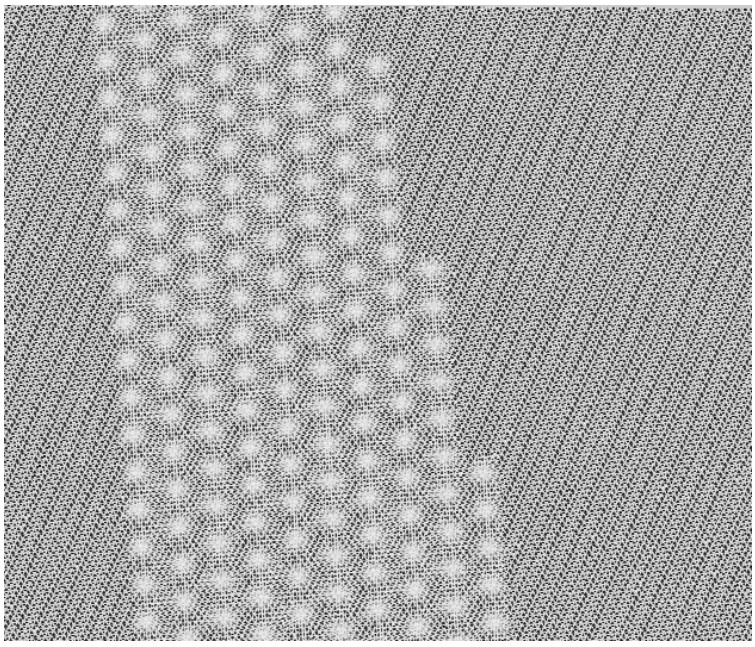

Fig. 3.4.9. The same simulation model as in Fig. 3.4.7 with the same rotation angle of 8°, weightings and size of area, but the right boundary for the top rotated layer is along line 2 in Fig. 3.4.7. As we can see here, the boundary of the superlattice is the same as that of the top layer, which is zig-zag in shape.

Now consider the case where our line labelled "1" happens to be the boundary. Since the superlattice bright spots are of high energy, when the boundary intersects them, the high energy points are terminated sharply and form some sites of concentrated electronic density. As the STM is probing the density of states at the Fermi level, these points consequently appear brighter than the other high points of the superlattice. This explains the bead-like boundary in Fig. 3.4.1 and the correspondence between each bead and each superlattice row.

A similar situation is shown in Fig. 3.4.2 although the "beads" are too close to be discernible. From the image, we can observe that there is a modulation along the thin wall-like boundary which is actually an array of beads but since the resolution of the STM tip was rather low in this case, it appears as a continuous line.

Using similar arguments, the trench boundary in Fig. 3.4.3 is oriented parallel to an axis of the superlattice and does not cut through those high energy bright peaks, therefore the boundary is straight without an array of bead-like structures, as discussed earlier. The appearance of a monolayer deep trench between the superlattice and the boundary is simply due to the position of the boundary, and is not in fact an actual physical trench. From the image, it is found that the peak-peak amplitude of the superlattice is around 0.4 nm, and the boundary happens to lie along the row of dips of the superlattice, thus it appears as a trench in the STM image.

3.4.4.2 Origin of plain boundary

The situation of the plain boundary in Fig. 3.4.5(b) is more complicated as it does intersect the superlattice bright peaks, yet no bead-like structures are apparent. The coincidence of the matching of the offset between G_1B_1 and G_2B_2 with the spacing between the plain boundary and G_2B_2 is related to the origin of the plain boundary. As mentioned before, G_1B_1 and $G_2'B_2'$ ($G_2'B_2'$ is the original position of G_2B_2 before the shear force is applied) were originally the same grain boundary, but possibly due to some shear force, there was a slip between the two graphite layers which caused the offset between G_1B_1 and G_2B_2 [see Fig. 3.4.5(d)]. The situation in Fig. 3.4.5(a) is schematically shown in the model of Fig. 3.4.5(d) where regions III and IV are one monolayer higher than regions I and II as displayed in the cross-sections of Fig. 3.4.5(a) of I-III and II-IV. The misorientation between region I and region III induces the Moiré rotation pattern, resulting in the superlattice structure. Region III extends into a part of region II and it happens that there is no misorientation between region II and region III, therefore no superlattice appears in the region between G_2B_2 and $G_2'B_2'$. Since the boundary of region I is along $G_2'B_2'$, the transition from the superlattice

to the normal graphite occurs along the direction of $G_2'B_2'$ on the second layer, rather than on the topmost layer. As the bisection of the bright peaks occurs underneath the surface, it is no surprise that no sites of concentrated electronic density (bead-like structures) are observed on the topmost layer under the STM. Ouseph *et al*. [89] used a similar model with a slip of a section of the graphite layer on one side of the dislocation ribbon with respect to the section of the layer on the other side to explain the formation of the superlattice successfully.

3.4.4.3 Origin of boundary as an array of protrusions with uneven spacing

The boundary in Fig. 3.4.6 consists of a line of protrusions with a spacing of tens of nanometres, where the spacing of these protrusions increases from the bottom to top while the superlattice periodicity within the boundaries increases from the top to bottom. We believe that each "protrusion" is in fact a dislocation, and the array of dislocations is consistent with the dislocation network for a low-angle grain boundary [134]. The difference in the superlattice periodicities across the boundary is related to the tilting between the graphite lattices on the two sides of the boundary. The difference in superlattice periodicities can be interpreted as the difference in the rotation angles of the graphite layers across the boundary since the rotation angle θ is related to the superlattice periodicity P_S (in nm) by:

$$\theta = 2\sin^{-1}\left(\frac{0.246}{2P_S}\right). \qquad (3.4.1)$$

The tilt angle at the low-angle grain boundary can be a possible explanation for the difference in the graphite rotation angles. A low-angle grain boundary is composed of an array of dislocations and the tilt angle over the boundary α (in radians) is associated with the spacing of the dislocations by

$P_D = b/\alpha$, (3.4.2)

where b is the Burgers vector and P_D is the dislocation spacing [134]. Based on the assumption that the boundary for the superlattice region with varying periodicities is a low-angle grain boundary, we have worked out the misorientation angle α from eq. (3.4.2) along both boundaries (on the left and on the right); the misorientation angle was also found by the difference in the rotation angles of the superlattices on the two sides of the boundary (Fig. 3.4.10) assuming that the superlattices are due to a Moiré rotation. The results are listed in Table. 3.4.I(a) and Table. 3.4.I(b), and they are plotted in Fig. 3.4.11(a) and Fig. 3.4.11(b). The value of the Burgers vector b is chosen to be one lattice constant of graphite (0.246 nm) as the results match most closely with this value. It is shown that the misorientation angles calculated by the two different means are rather close to each other and they follow the same

trend: the angle decreases as we go along from the bottom part of the superlattice with varying periodicity to the upper part. Such agreement strongly suggests that the boundaries for this superlattice with varying periodicity are low-angle grain boundaries, and the Burgers vector for the boundaries is one lattice constant. The tilt induced by each dislocation is of the order 0.1 degree, making this an extremely low-angle grain boundary.

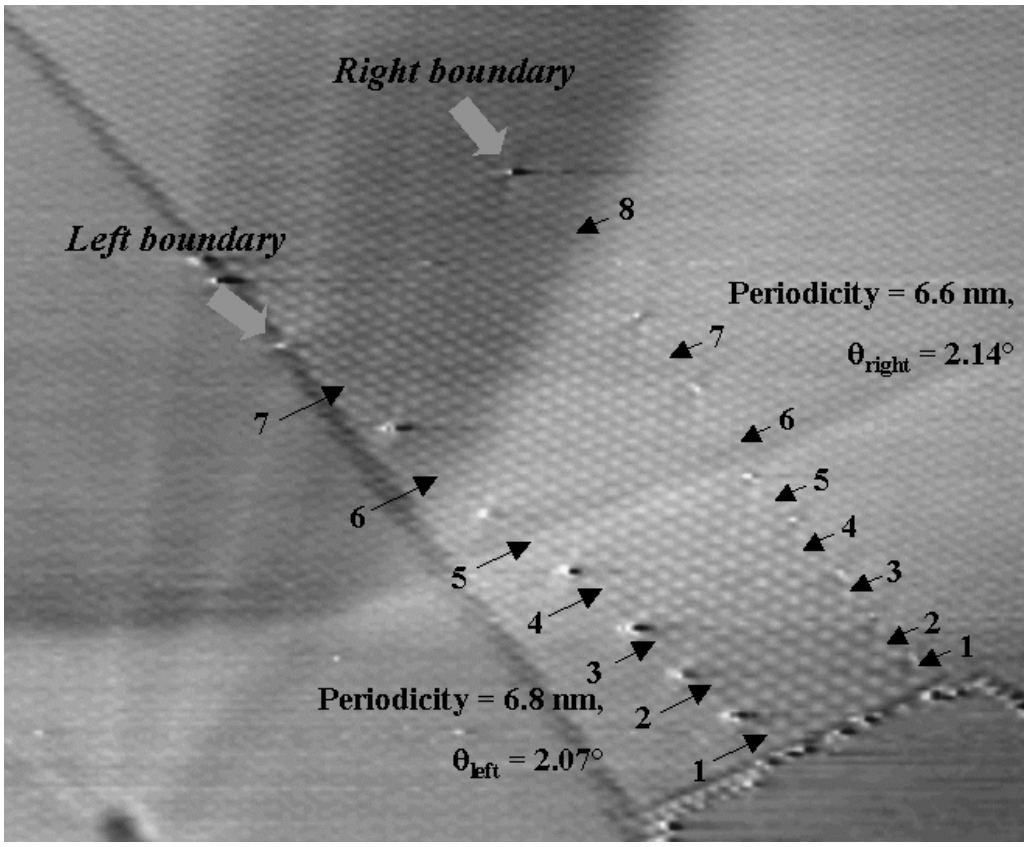

Fig. 3.4.10. 380 nm x 462 nm, I_t = 0.5 nA, V_s = 206 mV, about the same area as Fig. 3.4.6. Measurements of misorientation angle α are taken along the left and right boundaries. The misorientation angle α is worked out by two ways: firstly from the spacing of the protrusions along the boundary. The spacing of the protrusions P_D can be found from the STM image, and the magnitude of the Burgers vector b is chosen to be the lattice constant of the graphite which is 0.246 nm as this value gives the most closely matched results, thus the misorientation angle can be found by eq. (3.4.2); secondly from the periodicities of the superlattices. The rotation angle of a graphite sheet can be found from the superlattice periodicity by eq. (3.4.1). The superlattice regions outside the boundaries are of constant periodicities, and the one on the left is of 6.8 nm (rotation angle θ_{left} = 2.07º) while the one on the right is of 6.6 nm (rotation angle θ_{right} = 2.14º). The misorientation angle therefore can be found by the difference between the rotation angles of the superlattices on the two sides of the boundary. The results of the measurements along the left boundary and the right boundary are shown in Table. 3.4.I(a) and Table. 3.4.I(b) respectively. The positions where the measurements are taken are marked by the arrows and numbered; they are all midway between the protrusions.

Table. 3.4.I(a)

n	P_D (nm)	$\alpha_1 = b/P_D$ (express in degree below)	P_S (nm)	θn (degree)	$\alpha_2 = \theta_{right} - \theta n$ (degree)
1	20.8	0.678	9.613	1.466	0.669
2	23.0	0.613	9.314	1.513	0.622
3	27.8	0.507	8.856	1.592	0.544
4	31.9	0.442	8.388	1.681	0.455
5	28.6	0.493	8.138	1.732	0.404
6	45.6	0.309	7.936	1.776	0.360
7	43.1	0.327	7.517	1.875	0.261
8	86.0	0.164	7.125	1.978	0.157

Table. 3.4.I(a). The measurement results of the misorientation angle α along the right boundary of the region with non-constant superlattice periodicity by two different means [using eq. (3.4.1) and eq. (3.4.2)]. The notation n denotes the location of the measurement which is marked in Fig. 3.4.10, P_D is the spacing of the dislocations at the position n, b is the Burgers vector with the value of 0.246 nm, P_S is the periodicity of the superlattice, and θ_n is the rotation angle corresponding to the superlattice periodicity. The value of the constant periodicity of the superlattice on the right of the boundary θ_{right} is indicated in Fig. 3.4.10.

Table. 3.4.I(b)

n	P_D (nm)	$\alpha_1 = b/P_D$ (express in degree below)	P_S (nm)	θn (degree)	$\alpha_2 = \theta_{left} - \theta n$ (degree)
1	25.1	0.562	9.613	1.466	0.607
2	29.4	0.479	9.200	1.532	0.541
3	33.3	0.423	8.650	1.630	0.443
4	38.7	0.364	8.133	1.733	0.340
5	45.1	0.313	7.855	1.795	0.278
6	56.9	0.248	7.571	1.862	0.211
7	64.2	0.220	7.375	1.911	0.162

Table. 3.4.I(b). The measurement results of the misorientation angle α along the left boundary. The value of the constant periodicity of the superlattice on the left of the boundary θ_{left} is indicated in Fig. 3.4.10.

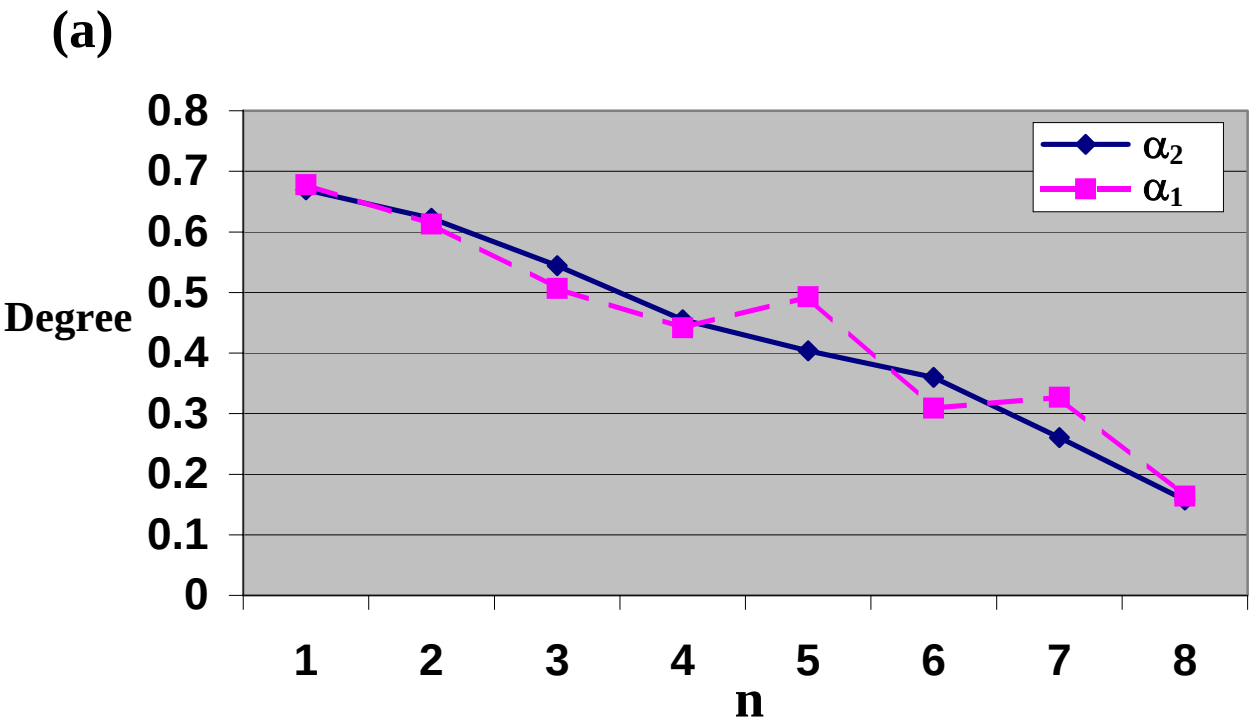

Fig. 3.4.11(a). Plotting of the results in Table. 3.4.I(a) for comparing the misorientation angles α found by the two different ways along the right boundary of the superlattice with varying periodicity.

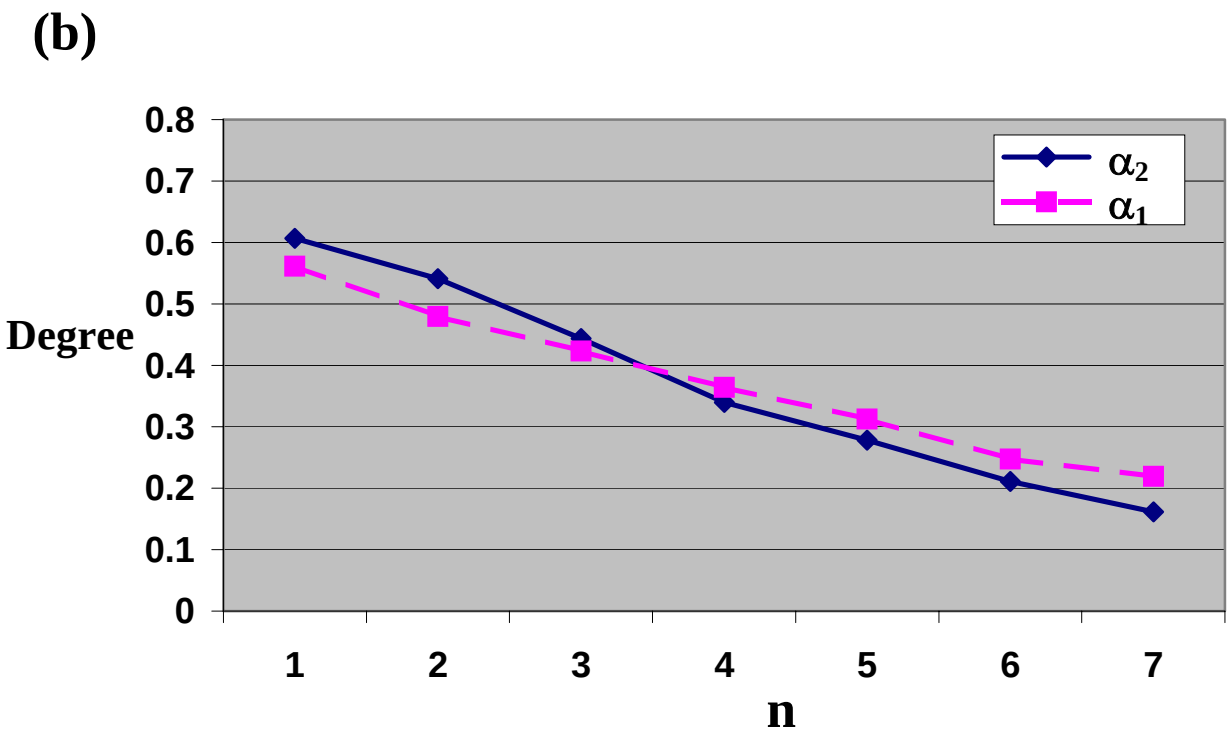

Fig. 3.4.11(b). Plotting of the results in Table. 3.4.I(b) for comparing the misorientation angles α found by the two different ways along the left boundary of the superlattice with varying periodicity.

The tilt boundary on graphite was described briefly before [135] and studied from the theoretical point of view [136, 137]. Daulan *et al*. [138] and Simonis *et al*. [139] reported their STM observation of grain boundaries in graphite with the constant tilt angles of 13° and 39° respectively. Tilt boundaries with angles of 19°, 8°, 6.5° were observed under the STM before as well [59]. However low-angle grain boundaries in graphite observed under STM were not well studied before. The protrusions on the boundaries (i.e. the dislocation points) have corrugations which are larger than that of the superlattice. In order to study this phenomenon, a model, based on the original structure proposed by Kittel for low-angle grain boundary with square lattices [134], is constructed with hexagonal lattices to replicate the surface structure along the low-angle grain boundary on a graphite layer. Since the above result shows that the value of the lattice constant gives the best matched results, the magnitude of the Burgers vector in the model is assigned to be 0.246 nm. This value of a lattice constant (0.246 nm) was also used by Garbarz *et al*. for the Burgers vector in constructing their model of honeycomb twist subboundaries on graphite [62]. Soto [140] found that a vacancy in graphite will create a charge enhancement in the atoms directly surrounding it. We therefore kept the number of vacancies as small as possible and minimized the number of bonds affected in the model. In Fig. 3.4.12, there are two hexagonal

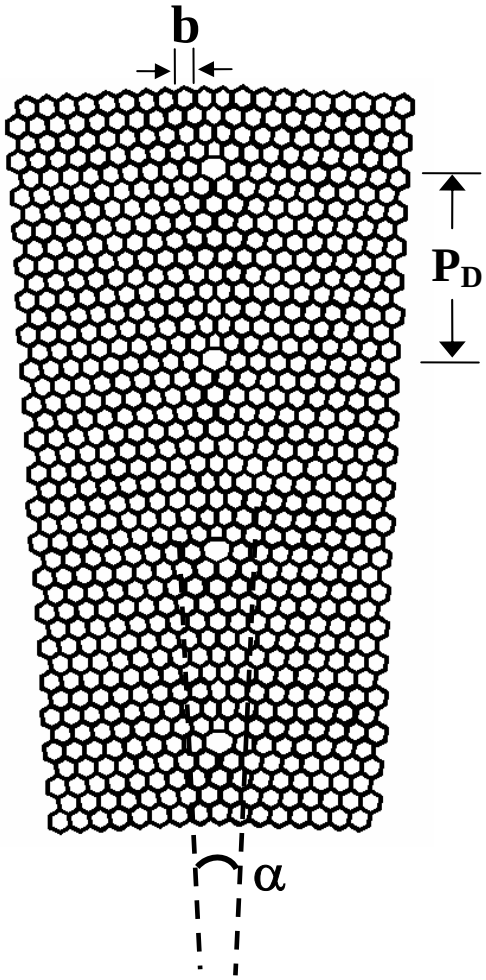

Fig. 3.4.12. A simplistic model of a low-angle grain boundary consisting of the hexagonal lattices of graphite. There is a misorientation angle α between the left lattice and the right lattice, which are separated by an array of dislocations (in the form of pentagon-heptagon pairs) in the middle. The spacing of the dislocation P_D and the magnitude of the Burgers vector b are related to the misorientation angle by eq. (3.4.5). This model is just to crudely illustrate the idea of a low-angle grain boundary on a graphite surface, and it is not meant to truly represent the boundaries of the superlattice with non-constant periodicity in Fig. 3.4.6 because this model does not take into account the varying misorientation angle along the boundary.

lattices with a misorientation angle α between them along the array of dislocation in the middle. This is obviously a rather naïve qualitative model which by no means can truly represent the low-angle grain boundary with varying dislocation spacings as we observed by STM, as the misorientation angle α is constant in this model. We exhibit this model simply for the purpose of roughly illustrating a low-angle grain boundary in a hexagonal lattice. This model is similar to the atomic model of the grain boundary of Simonis *et al*. (Fig. 3 in [139]) which they built for the grain boundary with a tilt angle of 39° in that both models have an array of dislocations at the boundary. In our model, the dislocations are in the form of an array of pentagon-heptagon pairs, similar to the pentagon-heptagon dislocation sites in the model of Simonis *et al*. but with opposite direction; the separation between the dislocations is just one row of hexagons whereas there are ten rows in our model. We believe the pentagon-heptagon dislocation sites enhance the local density of states which lead to the increased charge density at the dislocations, consequently the dislocation network along the low-angle grain boundary appears as an array of protrusions.

Based on the idea that the tilt angle of the low-angle grain boundary is the origin of the difference in the superlattice periodicities across the boundary, a further study is performed on the relationship between the periodicities of the boundary dislocations and the superlattices. Eq. (3.4.1) can be rewritten in this form:

$$P_S = d/\left[2\times\sin(\theta/2)\right] \approx d/\theta$$

where the rotation angle of the superlattice θ is small (e.g. less than 5 degree), and thus

$$\theta \approx d/P_S \qquad (3.4.3)$$

where d is the lattice constant and P_S is the superlattice periodicity. It is our assumption that the tilt angle of the boundary α is equal to the difference between the rotation angles of the superlattices on the two sides of the boundary (θ_1, θ_2 are the rotation angles and P_1, P_2 are the periodicities of the superlattices on the two sides of the boundary), therefore

$$\alpha = \theta_1 - \theta_2 \approx d/P_1 - d/P_2 \qquad (3.4.4)$$

while eq. (3.4.2) also gives the tilt angle

$$\alpha = b/P_D \qquad (3.4.5)$$

Hence eq. (3.4.4) can be related to eq. (3.4.5) and this gives

$$b/P_D \approx d/P_1 - d/P_2$$

and since b and d have the same numerical value, we arrive at this equation

$$1/P_D \approx 1/P_1 - 1/P_2 \qquad (3.4.6)$$

which means the reciprocal of the boundary dislocation periodicity is approximately equal to the difference between the reciprocals of the periodicities of the superlattice on each side of the low-angle grain boundary. In order to justify this equation, the data in Table. 3.4.I(a) and Table. 3.4.I(b) are used to find the reciprocal periodicities which are presented in Table. 3.4.II(a) and Table. 3.4.II(b). The results are plotted in Fig. 3.4.13(a) and Fig. 3.4.13(b), and it is shown that the $1/P_D$ values are very close to the $1/P_1$-$1/P_2$ values and they follow the same trend. This suggests that eq. (3.4.6) can be interpreted as the boundary dislocations being the cause of the difference in the superlattice periodicities across the boundary, which is not surprising as the dislocations induce the shift of the graphite lattice structure which in turn brings along the change of the superlattice rotation angle. Introducing terms for dislocation frequency F_D and superlattice frequency F_P, which are reciprocal to their corresponding periodicities, then eq. (3.4.6) becomes

$$\boldsymbol{F_D \approx F_{P_1} - F_{P_2}} \qquad (3.4.7)$$

This equation describes the situation that the superlattice, which is two dimensional, has its frequency adjusted by the frequency of the dislocation array which is one dimensional.

Table. 3.4.II(a)

n	P_D (nm)	P_1 (nm)	P_2 (nm)	$1/P_D$	$1/P_1$	$1/P_2$	$1/P_1$-$1/P_2$
1	20.8	6.6	9.613	0.04808	0.1515	0.1040	0.04749
2	23	6.6	9.314	0.04348	0.1515	0.1074	0.04415
3	27.8	6.6	8.856	0.03597	0.1515	0.1129	0.03860
4	31.9	6.6	8.388	0.03135	0.1515	0.1192	0.03230
5	28.6	6.6	8.138	0.03497	0.1515	0.1229	0.02864
6	45.6	6.6	7.936	0.02193	0.1515	0.1260	0.02551
7	43.1	6.6	7.517	0.02320	0.1515	0.1330	0.01848
8	86	6.6	7.125	0.01163	0.1515	0.1404	0.01116

Table. 3.4.II(a). The periodicities of the dislocations P_D and the superlattices on the two sides of the right boundary (P_1 for the superlattice periodicity on the right of the boundary while P_2 for the superlattice periodicity on the left of it) in Fig. 3.4.10 and their corresponding reciprocals.

Table. 3.4.II(b)

n	P_D (nm)	P_1 (nm)	P_2 (nm)	$1/P_D$	$1/P_1$	$1/P_2$	$1/P_1$-$1/P_2$
1	25.1	6.8	9.613	0.03984	0.14706	0.1040	0.04303
2	29.4	6.8	9.2	0.03401	0.14706	0.1087	0.03836
3	33.3	6.8	8.65	0.03003	0.14706	0.1156	0.03145
4	38.7	6.8	8.133	0.02584	0.14706	0.1230	0.02410
5	45.1	6.8	7.855	0.02217	0.14706	0.1273	0.01975
6	56.9	6.8	7.571	0.01758	0.14706	0.1321	0.01498
7	64.2	6.8	7.375	0.01558	0.14706	0.1356	0.01147

Table. 3.4.II(b). The periodicities of the dislocations and the superlattices on the two sides of the left boundary (P_1 for the superlattice periodicity on the left of the boundary while P_2 for the superlattice periodicity on the right of it) in Fig. 3.4.10 and their corresponding reciprocals.

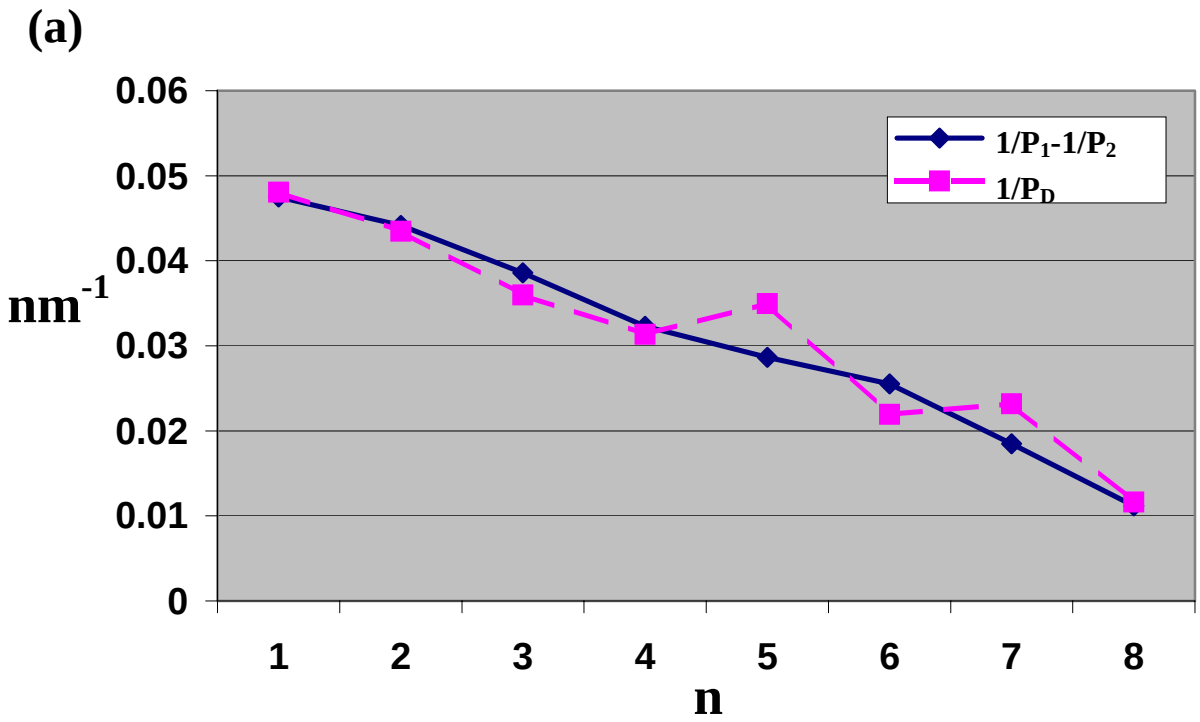

Fig. 3.4.13(a). Plotting of the results in Table. 3.4.II(a) for comparing $1/P_D$ and $1/P_1$-$1/P_2$ along the right boundary of the superlattice with varying periodicity to verify the relationship in eq. (3.4.6).

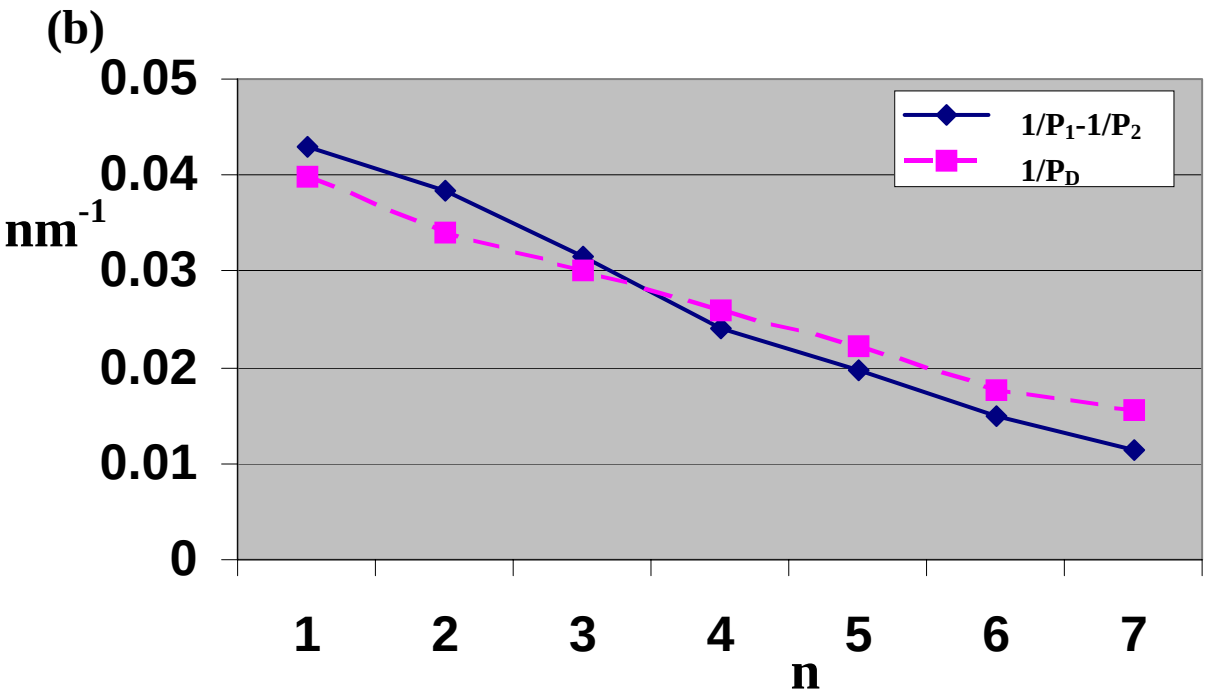

Fig. 3.4.13(b). Plotting of the results in Table. 3.4.II(b) for comparing $1/P_D$ and $1/P_1$-$1/P_2$ along the left boundary of the superlattice with varying periodicity.

3.4.5. Conclusion

In this chapter, we have reported our observation on six types of superlattice boundary. Analysis is given from an energetic point of view and an explanation for the formation of the boundaries is provided. The relationship between the low-angle grain boundary and the superlattice with varying periodicity is investigated and an equation relating the periodicity of the boundary dislocations to the periodicities of the superlattices across the boundary is derived.

As such, we have finished reporting our observation and simulation works on graphite superlattice in chapters 3.2 to 3.4. The next chapter will be the outlook on graphite superlattices. We will talk about the experimental and theoretical research possibilities on the superlattice phenomenon, and propose applications of it.

Chapter 3.5 Outlook on graphite superlattices and proposal of its applications

Summary

We have gained a comprehensive understanding on graphite superlattices in chapter 3.1, and reported our observation and simulation efforts on the superlattice phenomenon in chapters 3.2 to 3.4. Although the superlattice phenomenon was discovered nearly two decades ago, there are still unanswered questions for us to explore. Also, such an interesting phenomenon originated from Moiré pattern can have its applications in various aspects. Here we would like to conclude the field of graphite superlattice research by explaining the importance of findings on graphite superlattices, suggesting experimental and theoretical research possibilities, and proposing its applications. Finally, it ends with a conclusion for the whole chapter 3.

3.5.1 Significance of findings on graphite superlattices

An understanding of superlattice phenomena on graphite is of paramount importance for a better understanding of the STM imaging process at the atomic scale. STM is generally believed to be sensitive to the local density of states near the Fermi level on the topmost layer of a surface. However, the observation of Moiré rotation induced superlattices displays the fact that the interlayer electronic interaction with the subsurface layers can lead to periodic modulation of the density of states on the topmost layer. This carries a profound implication to STM images because STM images do not just reflect the topmost surface condition, but those of the subsurface layers as well. In addition, the apparent corrugation in STM images is often not the original true corrugation of the sample surface, but is due to the tip-sample surface deformation effect. Since the early days of the STM, graphite has been a surface of extensive study. Graphite is also commonly used as a substrate for the study of various kinds of adsorbates including organic molecules and biological species. However, in certain cases, it can be difficult to distinguish between specific adsorbate structures (especially periodic) and a superlattice on a graphite surface.

The works on superlattices provide a basis for understanding surface electronic structures with different subsurface layer configuration, which constitutes an important part of the principle of the STM technique. The graphite superlattice systems are useful for the comparative study of the three stacking structures: AAB, CAB, and BAB [66]. This may be

useful, as we have mentioned earlier on in section 3.1.3 in chapter 3.1, for the manipulation of material properties by reconfiguring stacking sequence of layered structures of graphite.

3.5.2 Future direction

3.5.2.1 Possible experiments to do

(1) Develop experimental protocol for producing superlattices

As discussed in section 3.1.4.6.(VI) in chapter 3.1, there exist methods to artificially produce graphite Moiré superlattices. In addition to cleaving a graphite with shear force, it is possible to fold back a graphite sheet with a slight rotation to artificially produce a superlattice structure on graphite by scanning with a STM tip. A systematic way which can routinely construct a superlattice would be of tremendous help for understanding the mechanism of superlattice structures as it will enable us to establish a superlattice in the desired pattern for experiments. As such, an established experimental procedure, entailing the configuration of the tunnelling conditions, feedback control parameters, scanning speed, and appropriate choice of area, to engineer a superlattice on a graphite surface would be an useful research subject to explore. The approach of exposing graphite to chloroform is also a practical route to generate Moiré superlattices. More research effort is needed to identify the mechanism for the introduction of defects by chloroform including superlattices. Also it would be of interest to investigate if there is any correlation between superlattice properties like corrugation amplitudes and periodicities and the exposure duration to chloroform.

(2) Experimentally verify coexisting superlattices

By using Gan's method, it is possible to tear off one layer first, and then another layer to be placed on top of the first one with a different rotation angle. In this way, the rotation angle between the first and second layer is different from the rotation angle between the second layer and the substrate. According to the Moiré rotation pattern assumption, we should be able to see two coexisting superlattices resulting from the coupling of the 1st layer with the substrate and the 2nd layer with the substrate respectively. It would be interesting to verify it experimentally as this will show the origin of coexisting superlattices in a same area and the influence of the electronic effect from the 3rd layer to the topmost layer under the STM. A simulation model with 2nd and 3rd layer rotated with respective angles to check if coexisting Moiré pattern is theoretically possible will be supplementary to the experimental work.

(3) Interrelation among superlattices, bias voltage, tunnelling current, and tip-sample distance

From the results of Rong *et al*. and Osing *et al*. [see section 3.1.4.6.(IV) in chapter 3.1], we know that the configuration of bias voltage and tunnelling current has a role to play in STM images of superlattices. This relationship depends upon the variation of the electron density of states of a superlattice with the bias voltage and tunnelling current. Research work on this topic will enable us to understand the influence of the tunnelling conditions on the interlayer electronic interaction of graphite which gives rise to the variation of the resulting Moiré superlattice pattern. However, no systematic study has been conducted so far.

To investigate this subject, when a superlattice is being imaged with a STM, the tunnelling condition can be varied with tunnelling current from 0.01 nA to 3 nA, bias voltage from –2 V to +2 V, and the corresponding superlattice periodicity, orientation, corrugation amplitude, and the atomic corrugation should be recorded. In this way we can see how the superlattice changes with the tunnelling condition, and compare the rates of decay of the electron density of states associated with the superlattice and the atomic lattice in the direction from the surface to the vacuum. We can then analyse the correlations between superlattices and these different parameters.

3.5.2.2 Possible theoretical calculations to do

(1) Continuation of the Kobayashi theoretical work

As discussed earlier on in chapter 3.1, Kobayashi [116] pointed out that nanoscale waves propagating through many layers without decay can be the cause of superlattices. His theory provides an alternative route to explain superlattices observed in STM, nevertheless, further theoretical work is needed to delineate the theoretical correlation between the superlattice structures observed in STM images and the nanoscale structures buried deep in the bulk, for instance, what kind of nanoscale structures does it have to be in order to form Moiré superlattices on the surface, do the nanoscale structures have to be an array of structures, and what is the relationship between the periodicity and corrugation of a superlattice and nanoscale structures. Should the correlation be elucidated, the aspects of the relationship between superlattice corrugations and number of overlayers and the dependence of the Moiré pattern on the tip-sample distance are worth further investigation because in this respect, experimental results contrary to Kobayashi's theory have been shown as mentioned in section 3.1.4.6.(IV) in chapter 3.1.

(2) Superlattice corrugation

The large superlattice corrugation is speculated to be related to tip-surface mechanical deformation similar to the mechanism for giant atomic corrugation for graphite. However, there is no theoretical work to support such speculation. In this regard, a simulation should be performed which considers a rotated top graphite layer misoriented with respect to the bulk, with the commonly used tunnelling conditions to observe superlattices (Table 3.1.I), and in the framework of Moiré rotation pattern assumption to study tip-surface interaction and its effect on the resulting superlattice corrugation.

(3) Influence of tip shape and tip-sample distance

The simulation model combined with the integration of the tip shape and tip-sample distance enables us to investigate their influence on the resulting STM images of superlattice structures. Rong *et al*. [80] reported two kinds of patterns for superlattice bright spots: triangular and circular shapes. Distorted hexagonal arrangements of superlattices were sometimes observed [67, 87]. Both of these phenomena may be attributable to the shape of the STM tip. The knowledge on the influence of tip shape on superlattices will help us to interpret the STM images properly with more insight. Since there is experimentally no way to prepare a tip with a specific shape, theoretical calculation with the simulation model described in chapter 3.3 grants a possible route for the relevant investigation. Moreover, this model enables us to simulate the relationship between the tip-sample distance and the resulting STM images which would be complementary to the above-mentioned theoretical study on the correlation between the tip-surface interaction and the superlattice corrugation upon various tunnelling conditions [section 3.5.2.2.(2)], together they will deliver the whole picture of the tip-imaging mechanism on superlattices.

(4) Electron density of states with different stacking faults

Xhie *et al*. [67] and Rong *et al*. [66] used different models to explain the correlation of the local stackings with the local density of states, and they lead to different conclusion as discussed in section 3.1.4.7.(III): Xhie's model, AB stacking (brightest), CAB (medium), AAB (darkest), slip-AB (ignored); Rong's model, AAB stacking (brightest), slip-AB (second brightest), AB (second darkest), CAB (darkest). It is experimentally difficult to verify their models because the STM cannot check the stacking of the topmost three layers of a superlattice. In order to clarify the controversy, we need a first-principles calculation of local

density of states on these kinds of stackings with a normal AB stacked graphite bulk: ABABAB…, CABAB…, AABAB…, slip-ABAB… This result will tell us the order of intensity with different kinds of stacking and thus different surface-atom sites, and it would be of tremendous aid to the understanding of the formation of superlattices.

3.5.2.3 Possible applications of superlattice structure

Moiré phenomenon, the origin of a superlattice on graphite, has long been applied in various aspects, and it was first put into practical application by Lord Rayleigh in 1874 [141] for scrutinizing the fidelity of a replica of a diffraction grating. It is also a means for the metrologist and precision engineer for accurate measurement of tiny displacements. Moreover, Moiré pattern renders a convenient method for the representation and solution of a variety of mathematical problems, as well as in the study of fields and flows in physics [114]. The works by H. M. Guo *et al*. [142] and Z. W. Liu *et al*. [143] on nanometre Moiré fringes in STM show that by using the sample atomic lattice as the specimen grating and the STM scan lines as the reference grating, the Moiré pattern can offer a high sensitivity for surface deformation and defect measurement with nanometre spatial resolution. In view of these, it is conceivable that Moiré induced superlattice structures contain the potentiality in precision measurement at the atomic scale. With the atomic lattices of the rotated graphene layers as the gratings, the resulting graphite superlattice consequently projects the small rotation angle between the two graphene layers onto the topmost layer in the form of a superperiodic hexagonal structure (superlattice) on a much larger scale. Given a scan range of a couple of micrometres for a STM, a rotation angle between two graphene layers can be detected with sensitivity down to a hundredth of a degree by imaging a superlattice with periodicity of a few hundred nanometres.

Xhie *et al*. [67] reported that the peaks (high electron density of states) of a superlattice are the preferential adsorption sites for both atoms and clusters. Together with the technique of manually creating superlattices by using STM tips discussed in section 3.1.4.6.(VI) in chapter 3.1, this may present a way to prepare a template with any predetermined periodicity for adsorbing external atoms or molecules in the form of an array as illustrated in Fig. 3.5.1. It is potentially a more efficient way to manipulate atoms and molecules as it is a parallel process, instead of being in series by manipulating with scanning probe techniques.

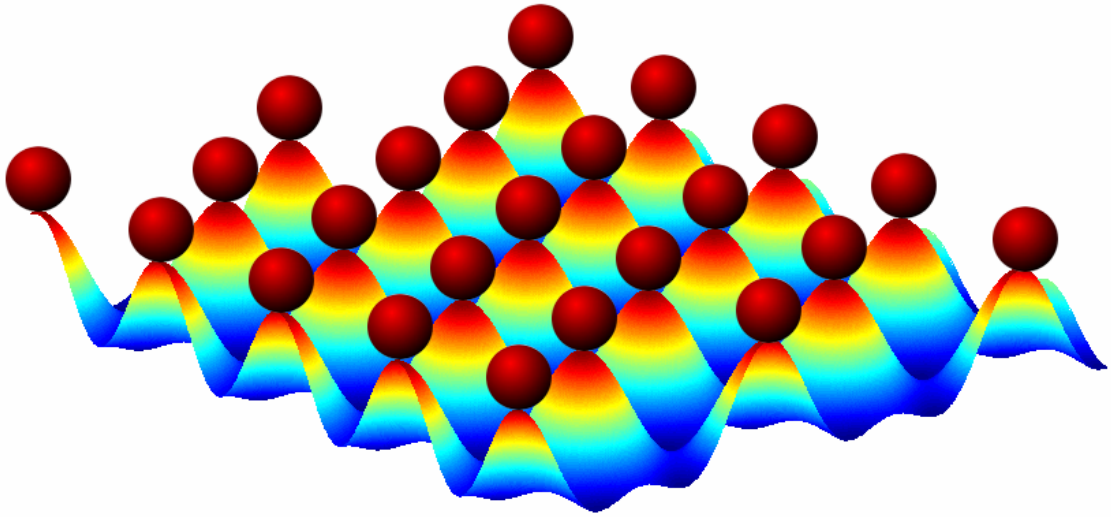

Fig. 3.5.1. Possible application of superlattice in manipulating molecules or atoms in the form of an array by offering a template of adsorption sites where the periodicity can be predetermined. The balls represent adsorbed molecules or atoms, the underlying template is the graphite superlattice.

Recently atomically thin carbon films from a single layer to a few atomic layers were demonstrated to exhibit electric field effect by applying a gate voltage, which may suggest graphite to be a suitable material for transistor applications, a potential candidate to get over the limits of performance improvement for the current electronics technology dominated by silicon [144, 145]. A Moiré rotation induced superlattice encompasses the electronic interaction between a few graphite layers, and a STM tip scanning over a superlattice essentially resembles a transport measurement on every point of the superlattice which is like the atomically thin carbon films that Novoselov *et al*. [144] suggests to be few-layer graphene (FLG) devices. The findings on the electronic interaction among graphene layers in superlattices observed with the STM will be relevant to the development of the FLG devices.

3.5.3 Conclusion

Graphite is one of the most often studied substrates in scanning tunnelling microscopy for its atomic flatness, chemical inertness, ease of preparation, and applicability as a weakly interacting substrate for experiments involving deposited species, be they chemical or biological objects. Graphite contains various kinds of defects, in particular, superlattices, which are superperiodic structures with hexagonal symmetry, that cause ambiguity with the absorbed species.

A graphite superlattice, in its own right, is an intriguing phenomenon as its existence in STM images is contrary to the general perception that a STM is only probing the information at the topmost layer. There is constant research in the field concerning the origin and various properties of graphite superlattices. Despite the controversies, the Moiré rotation pattern assumption is generally accepted to be the major cause of the formation of a superlattice. Nevertheless, our understanding on superlattices is still rather limited, for instance, we are not totally clear about the reason for the anomalously large superlattice corrugation, and its dependence on the tunnelling condition.

The occurrence of a graphite superlattice is related to the dislocations caused by cleavage or crystal growth and we do not have much control over this process. As such it is impossible to prepare a specific superlattice for experiments, contributing part of the reason why research on this topic is restricted. Having said that, the situation is now changing. It is demonstrated that by using a STM tip, we can apply the tip-sample interaction to fold over a graphite layer to form a superlattice with a certain degree of control on the rotation angle and thus the resulting superlattice periodicity. By exposing graphite to chloroform, a high concentration of graphite superlattices is formed, which makes it easier to find a superlattice on a graphite surface to study.

As mentioned in section 3.5.2.1 and 3.5.2.2, there are several research possibilities in the subject both experimentally and theoretically, alongside with the potential application of graphite superlattice in making a template for an array of adsorption sites and its relevance in developing the new generation electronics devices, which render this subject a topic that deserves more research effort.

Chapter 4

Characterization of overlayers on single crystal surfaces at the atomic-level

In this chapter, our efforts towards STM characterization of overlayers on single crystal surfaces at the atomic-level are described. These overlayers are interesting samples for future single electron spin detection and spin-polarized STM (SPSTM) experiments. Free radical organic molecules contain unpaired electrons which provide electron spin signal. An organic free radical molecule called BDPA (α,γ-bisdiphenylene-β-phenylallyl), which is a stable free radical, is chosen as the species for deposition. Thermal evaporation, microcontact printing, and solvent deposition were used for depositing the BDPA molecules onto graphite and gold. The experimental details, deposition results, advantages and disadvantages of each method are discussed in chapter 4.1. Iron, which is ferromagnetic, is deposited on the substrate of silicon which is non-magnetic. The combination of iron with silicon forms a binary magnetic system. Reactive deposition epitaxy (RDE) and solid phase epitaxy (SPE) without heating were used for depositing iron onto silicon. Iron silicide formed by RDE is useful for future single electron spin detection experiments. The deposition and characterization results are discussed in chapter 4.2.

The work in chapter 4.1 is submitted to the Journal of Applied Physics for publication.

Chapter 4.1 Deposition and characterization of free radical organic molecules

Summary

The experiments by Manassen *et al*. [36] and Durkan *et al*. [146] demonstrated that it may be possible to detect single electronic spins by scanning tunnelling microscopy (STM). Sample preparation is key to the success of this technique. In this work we explore varieties of deposition methods to deposit free radical organic molecules reliably for STM experiments. Free radical organic molecules BDPA (α,γ-bisdiphenylene-β-phenylallyl) were deposited by thermal evaporation, microcontact printing, and solvent deposition. The thermal evaporation method can deposit a monolayer of BDPA without destroying their spin signals. Microcontact printing has also successfully deposited BDPA patterns onto a substrate. Solvent deposition of a monolayer of BDPA onto graphite is also demonstrated. The results of this chapter are a significant first step towards single electron spin detection with STM experiments.

4.1.1 Introduction

A technique which brings the resolution of a STM on magnetic systems down to the ultimate limit of single electron spin was developed by Manassen in 1989, in which the electron spin signal is extracted from the STM tunnelling current [36]. Free radical organic molecules are suitable candidates for this kind of experiment as they contain unpaired electrons and thus provide electron spins [147]. We have explored three different methods (thermal evaporation, microcontact printing, solvent deposition) of depositing free radical organic molecules onto a substrate. Each deposition method has its own limitations which will be discussed later. Also a deposition method applicable to some kinds of molecules may not be applicable to others. Therefore, it is of tremendous help to widen up more deposition means so that an experiment would not be constrained by the restriction of a certain deposition method.

We have chosen BDPA (α,γ-bisdiphenylene-β-phenylallyl)[1] as the material to deposit as it is a well-known spin label used in electron spin resonance (ESR) measurements. Also BDPA molecules are suitable for demonstrating all the three deposition methods that we explore in this work. The chemical formula of BDPA is $C_{39}H_{28}$, and its structure is shown in Fig. 4.1.1(a) and Fig. 4.1.1(b). The nominal size of a BDPA molecule is approximately 1.2

nm x 0.88 nm x 0.87 nm. In this work we will describe the deposition experiments and their characterization results for comparison and discussion.

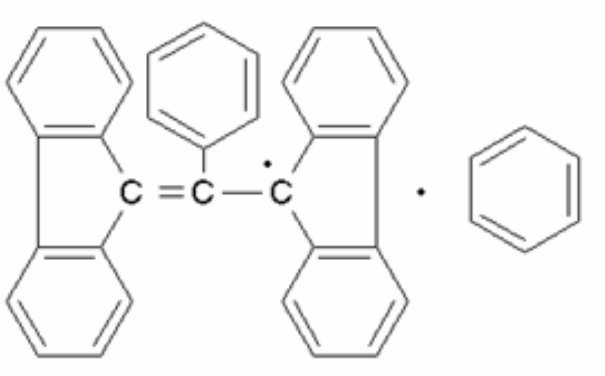

Fig. 4.1.1(a). The structure of BDPA molecule

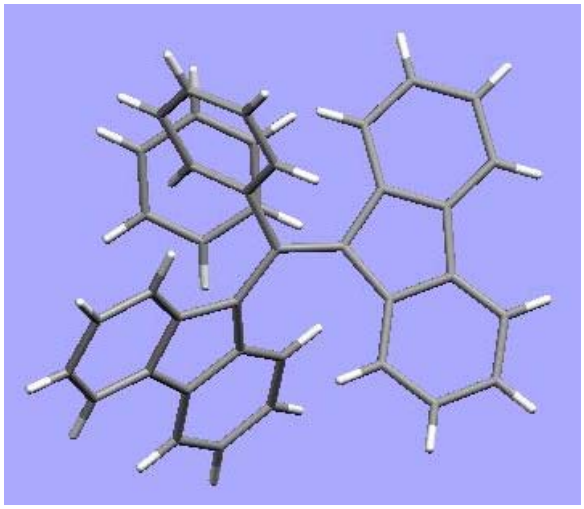

Fig. 4.1.1(b). The 3D structure of BDPA molecule

[1]Molecular weight 496.6, CAS number 35585-94-5, purchased from Sigma-Aldrich.

4.1.2 Deposition experiments and results

4.1.2.1 Thermal evaporation

Our evaporator operates in high vacuum (base pressure ~ 10^{-8} mbar) and is equipped with a quartz crystal microbalance to monitor the thickness of deposition. Graphite was used as the substrate as it is easy to cleave to provide a fresh clean surface and it contains atomically flat terraces. The graphite was freshly cleaved by adhesive tape a few times immediately before it was loaded into the vacuum chamber via a load lock. We have deposited a 70 nm thick film onto a 5 mm x 5 mm graphite surface, at a deposition rate of ~ 0.05 nm/sec, by heating the BDPA to approximately 210 ^{o}C. The sample surface was then imaged by AFM operating in tapping mode. In Fig. 4.1.2(a), we can observe the bare graphite surface on the right which was masked during the evaporation process and the part deposited with 70 nm of BDPA on the left. The morphology of the BDPA in the AFM image is consistent with that observed by scanning electron microscopy (SEM) in Fig. 4.1.2(b). This sample was then taken to perform electron spin resonance (ESR) measurement in order to examine whether or not the heat of the evaporation process has damaged the spin property of the BDPA. The electron spin resonance measurement was taken by Dr. Wolfgang Harneit in Physics Department, Free University, Arnimallee 14, D-14195 Berlin, Germany. Fig. 4.1.3(a) shows a typical X-band ESR spectrum of the BDPA film on graphite. The surface normal was oriented at an angle of $\vartheta = 135° \pm 5°$ with respect to the external magnetic field B. The spectrum exhibits two lines, an asymmetric one crossing zero at B = 3345.5 G and a symmetric one at B = 3380 G. It is well known [148] that the conduction electrons of graphite

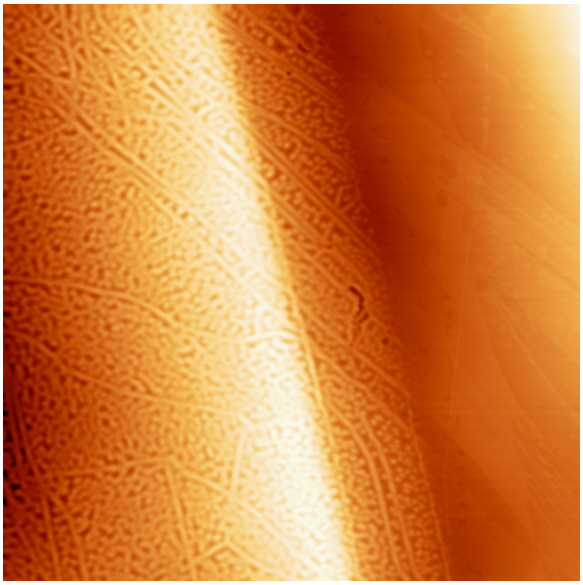

Fig. 4.1.2(a). AFM tapping mode image, 20 μm x 20 μm. The right hand side of this area was masked during evaporation, leaving the left side deposited with BDPA molecules. There is a transition region in the middle which carries out the gradual change from the BDPA molecules to the bare graphite surface due to the diffusion of the BDPA molecules into the underneath of the mask.

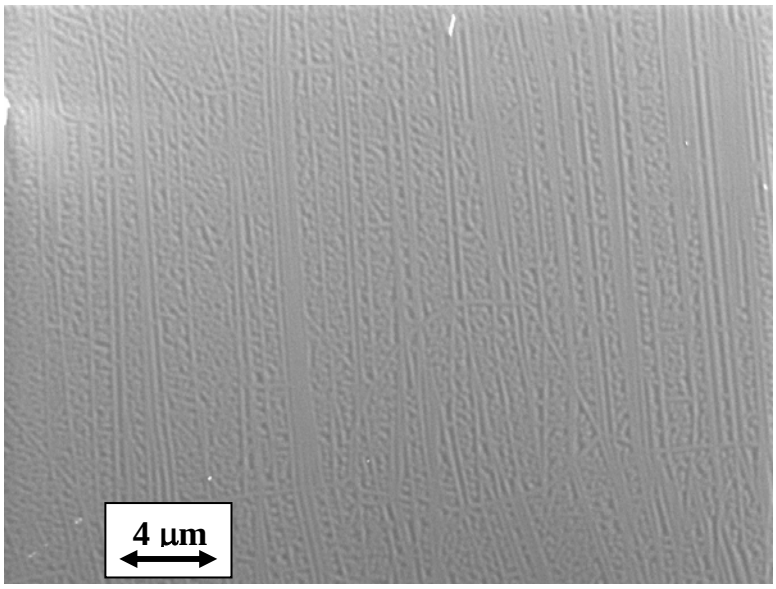

Fig. 4.1.2(b). SEM image of the BDPA molecules on the graphite surface.

give rise to an asymmetric peak in ESR measurements that can be described by Dyson's formula [149]. Due to the electronic anisotropy of graphite, the position of this peak has a characteristic angular dependence, as shown in Fig. 4.1.3(b). We thus assign the symmetric, angle-independent peak to the BDPA molecules. Taking the HOPG peak positions as an internal standard and assuming $g^{HOPG} = 2.0026$ [148], we find a g-factor for BDPA $g^{BDPA} = 2.0020$ (±0.0005), which is a little smaller than the literature value of $g^{BDPA} = 2.00359$ [150]. In summary, the ESR measurements show that the spin signal of the BDPA molecules is preserved after the evaporation process, and therefore thermal evaporation provides a feasible way to deposit the free radical organic molecules.

Having determined that evaporation does not destroy the BDPA molecules, we then prepared a number of samples with sub-monolayer thicknesses of BDPA. From the AFM images in Fig. 4.1.4(a) and Fig. 4.1.4(b) we can observe that the BDPA molecules tend to aggregate together, forming islands ranging in size from around a few hundred nanometres to a micrometre with a tendency to decorate the step edges. The molecules appear to be rather mobile on the graphite surface and diffuse around until they either settle down along the step edges or attach to other molecules. The height cross-section in Fig. 4.1.4(b) shows that the thickness of the islands is relatively even at around 0.486 nm, given that the nominal height of BDPA molecules is approximately 0.88 nm, those islands are likely to be a monolayer high. The thickness of the islands is smaller than the nominal height of a BDPA molecule, such a discrepancy can be attributed to the fact that one of the atomic planes of a BDPA molecule is rotatable, and thus the actual height of the molecule on a surface depends on the interaction between the substrate and the molecule, and can be smaller than its nominal

height. These molecular islands are relatively flat as opposed to the crystalline surface of the 70 nm thick BDPA film in Fig. 4.1.2(a). This sample was imaged under AFM again after two months and the surface condition did not change noticeably over this period. This indicates that the molecular islands are stable and have stopped diffusing on the graphite surface.

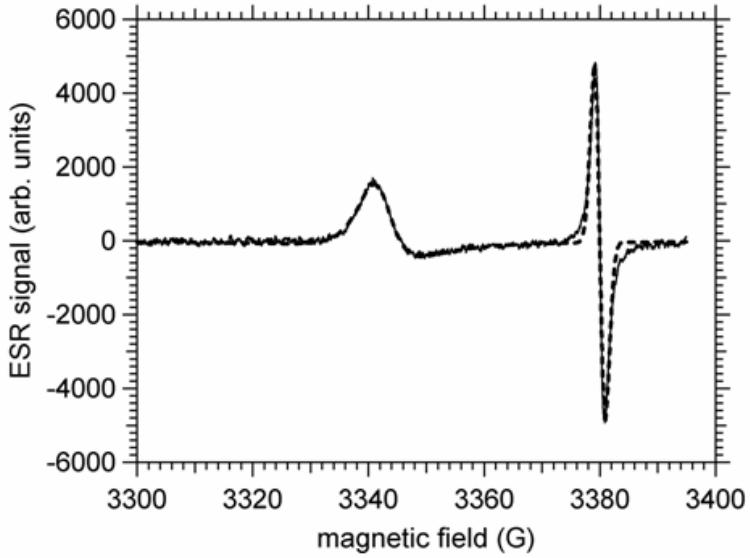

Fig. 4.1.3(a). Solid curve: room temperature cw-ESR spectrum (X-band, 9.5 GHz) of a 70 nm thick BDPA film on HOPG. The surface normal was oriented at $\vartheta = 135°$ with respect to the magnetic field. Dotted line: fit with Dysonian profile [149] for the left peak which is due to HOPG conduction electrons, and with a Gaussian profile for the right peak due to BDPA.

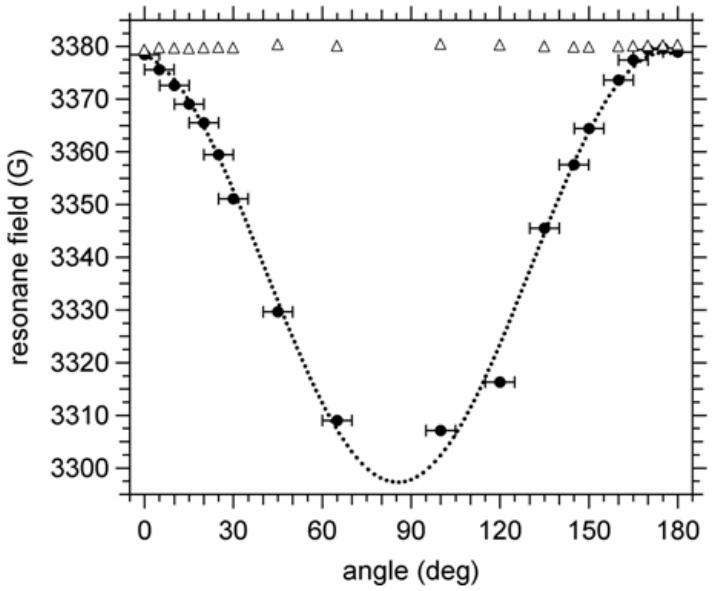

Fig. 4.1.3(b). Angular dependence of peak positions as obtained from fits similar to those shown in fig. 4.1.3(a). Open triangles: BDPA, no significant angular dependence. Solid circles: HOPG, the angular dependence can be described [148] by $B_0 - A\cos^2(\vartheta - \vartheta_0)$ with B_0 = 3297.3(±1.5) G, δB = 81.6(±1.9) G (dotted curve).

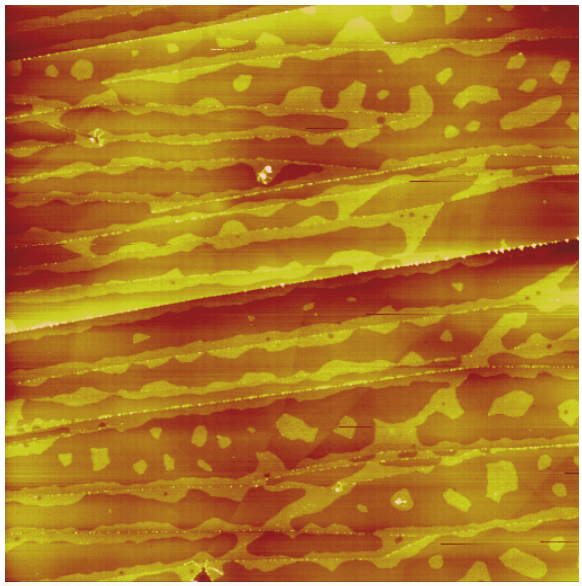

Fig. 4.1.4(a). AFM tapping mode image, 11 μm x 11 μm, on the BDPA molecules evaporated onto the graphite.

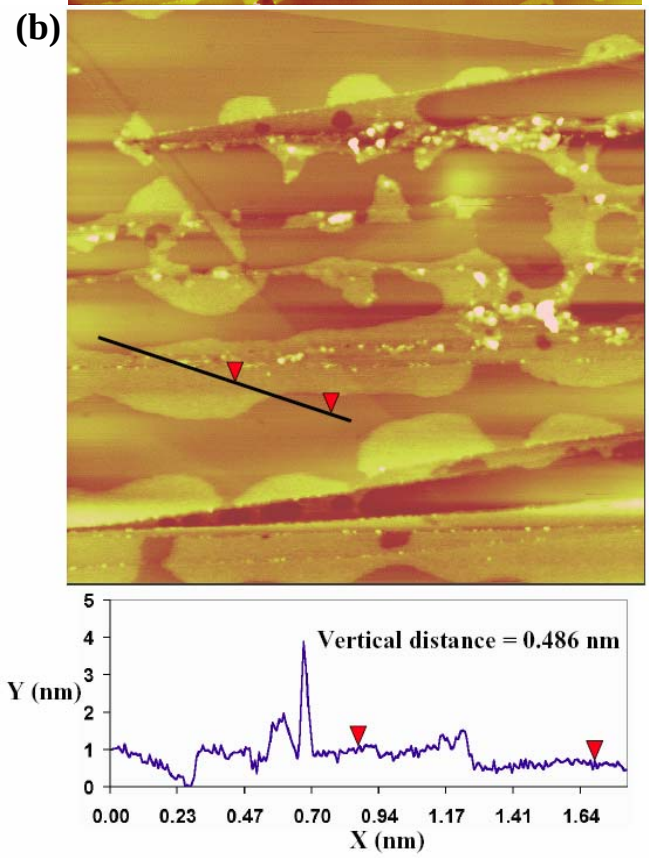

Fig. 4.1.4(b). AFM tapping mode image, 3.8 μm x 3.8 μm, on the BDPA molecules evaporated onto the graphite. The cross-section along the island shows its thickness to be approximately 0.486 nm which is a monolayer.

Repeated attempts at STM imaging of these evaporated samples however proved unsuccessful, even with tunnelling conditions of 5 pA and 850 mV. Fig. 4.1.4(c) shows the STM image obtained on the same sample as in Fig. 4.1.4(a) and Fig. 4.1.4(b). Apart from graphite steps and terraces, BDPA islands are not observed in the STM image, on the contrary to Fig. 4.1.4(a) and Fig. 4.1.4(b) where BDPA islands hundreds of nanometres are visible. We concluded that this is due to the low conductivity of both the HOPG and the molecules, as the STM tip is rather closer to that surface than for a metal. As the molecular islands are extremely large, the tip has to penetrate the molecular layer in order for a measurable current to flow.

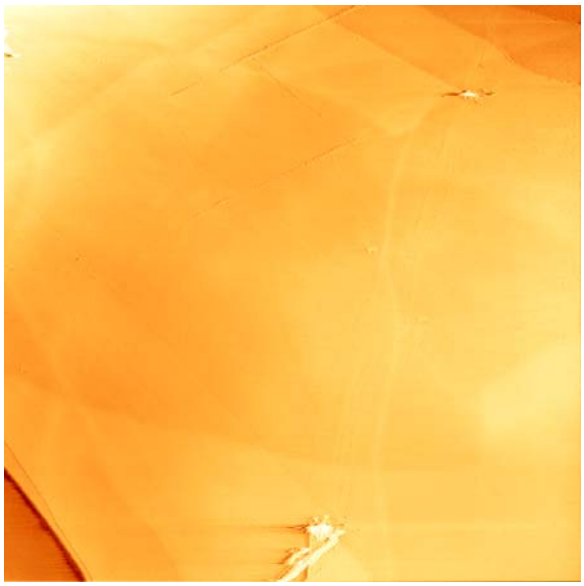

Fig. 4.1.4(c). STM image on the graphite deposited with BDPA by evaporation, the same sample as in Fig. 4.1.4(a) and Fig. 4.1.4(b). 2500 nm x 2500 nm, I_t = 5 pA, V_s = -850 mV. BDPA islands are not observed in the STM image whereas they are visible in the AFM images in Fig. 4.1.4(a) and Fig. 4.1.4(b).

For STM imaging, small scattered islands of molecules are preferred as the scan range of STM is usually limited within a few micrometres. As the distribution of the molecules is closely related to the nature of the molecule-substrate and molecule-molecule interactions, we also investigated the use of the gold (111) surface as a substrate [151]. We used gold on mica which was annealed in-situ (in the UHV chamber containing the STM) at 380°C for an hour to clean the surface. The gold was left to cool down for 30 minutes. Using a K-Cell operating at 210 ^{o}C, we then deposited a submonolayer of BDPA onto the Au(111) surface and transferred it into the STM. This sample was then imaged with a tunnel current of 20 pA. From Fig. 4.1.5(a) and Fig. 4.1.5(b), we can see that the molecules scatter around very well on the surface, and they form small, monolayer-high islands of tens of nanometres in size, ten times smaller than those on the graphite [cf Fig. 4.1.4(a) and Fig. 4.1.4(b)]. The BDPA molecules tend not to diffuse very far, and stay on the Au(111) surface without decorating the terrace edges. We can observe that there are many small pits on the Au(111) surface [Fig. 4.1.5(b)] which anchor the molecules onto the surface and prevent them from diffusing far. The diffusion length of BDPA on Au(111) is therefore around 10 nm, as compared to around 500 nm for HOPG. The thickness of the islands observed by STM is 0.4 nm, which is a monolayer. STM does not give accurate topographic information for adsorbed species; however, the correspondence between the measured thickness by the STM (0.4 nm) and by the AFM (0.486 nm) suggests that the BDPA molecules are physically deformed on the substrate surfaces. The molecules on the surface are rather stable, as the sample was imaged by STM again after two months and it showed no obvious changes. From this experiment we learn that the substrate plays an important role in the deposition result as we have seen that

the behaviour of BDPA on the Au(111) surface is very different from that on graphite. Au(111) surfaces are relatively more suitable substrates for depositing BDPA free radicals. Thermal evaporation of BDPA molecules onto Au(111) surfaces is a promising way to deposit isolated islands of free radical BDPA molecules.

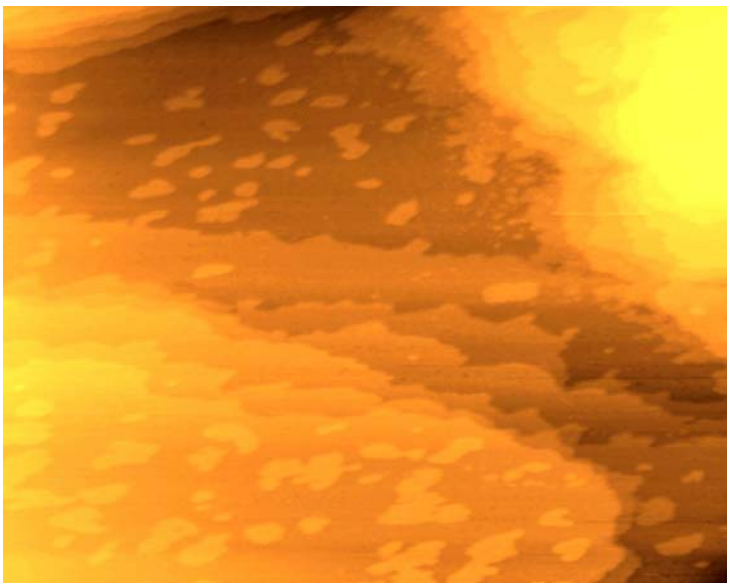

Fig. 4.1.5(a). STM image on the BDPA islands on Au(111). 300 nm x 260 nm, I_t = 20 pA, V_s = -850 mV.

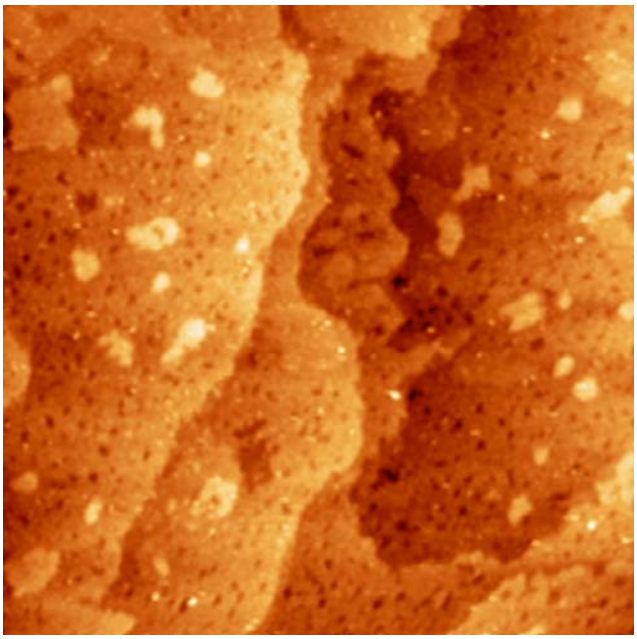

Fig. 4.1.5(b). STM image on the BDPA islands on Au(111). 200 nm x 200 nm, I_t = 20 pA, V_s = -800 mV.

There is one point worth mentioning concerning surface features of the Au(111) surface. In our experiment, we have observed gold stripes (gold fingers) along the terrace step edges [Figures 4.1.6(a) and 4.1.6(b)]. These gold stripe structures, not as well-known as the herringbone reconstruction, have been reported previously [151-154]. It was proposed that these stripe structures are due to atomic diffusion induced by the STM tip operating with a

strong local electric field [152, 153]. The electric field enhances the atomic mobility on the Au(111) surface. The diffusion rate R is governed by the Arrhenius equation,

$$R = v \exp(-E/kT) \qquad (4.1.1)$$

where v is the vibrational frequency of a surface atom, E is the activation energy, k is the Boltzmann constant, and T is the temperature [153]. Previous works produced the striped structures by applying a high electric field with the STM tip. However, in our case, we did not apply a high electric field to deliberately induce the gold stripes. In fact, the tunnelling conditions we used were 10-20 pA and 500 mV, which would produce a much weaker electric field than the electric field by the tunnelling condition of 30 nA and 1.5 V used by Guo *et al.* [152]. Such a low electric field is unlikely to lower the activation E enough to accentuate the diffusion process. We believe that the activation energy has in fact been reduced by the molecules, as the molecules alter the surface energy. Similar effects have been reported before for Lander molecules on the Cu(110) surface [155].

(a)

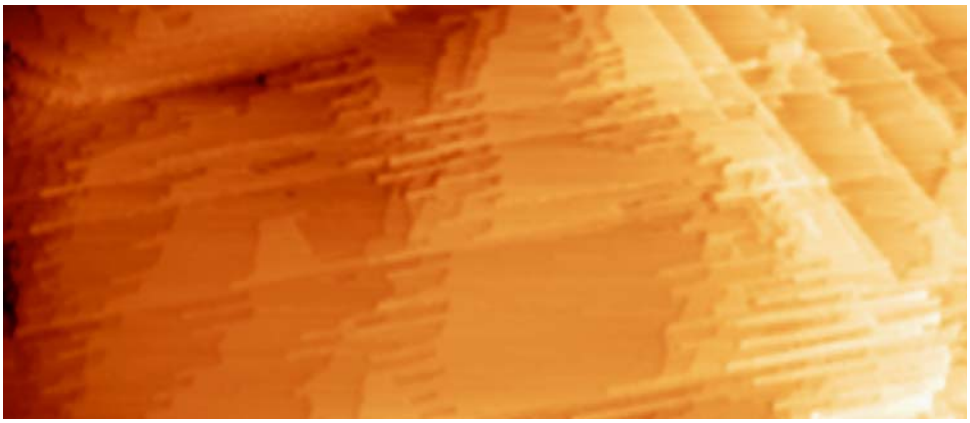

(b)

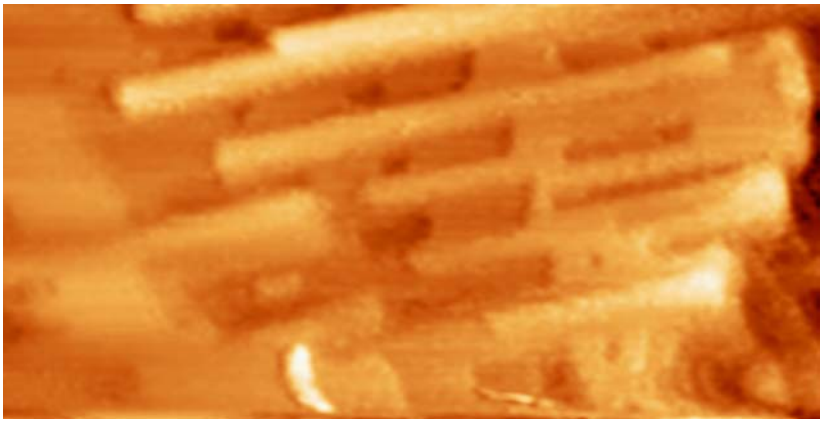

Fig. 4.1.6(a). Gold stripe structures along the terrace step edges. 900 nm x 450 nm, I_t = 10 pA, V_s = 800 mV. Fig. 4.1.6(b) A zoom-in of the gold stripe structure. 200 nm x 100 nm, I_t = 50 pA, V_s = 800 mV.

4.1.2.2. Microcontact printing (μCP)

Microcontact printing is a powerful technique for printing structures in the nanoscale to microscale [156]. It uses a poly(dimethylsiloxane) (PDMS) stamp to deposit molecules with patterns onto a surface. The stamp is made by replicating the master structures on a solid master by molding with liquid prepolymer. The stamp is then inked with a solution of molecules such as proteins or alkanethiols which are to be coated onto the surface of a substrate. The stamp is dried, pressed into conformal contact with the substrate and the molecules are printed onto the surface. Complex surface patterns of more than one kind of molecules are possible by repeated printing with different stamps. In addition to molecules, colloidal particles can also be printed by microcontact printing. Microcontact printing has many applications such as protein patterning [157], polymer growth [158], microelectrodes arrays [159, 160], organic light-emitting diodes [161], and organic thin-film transistors [162]. However, microcontact printing may have the problem of surface diffusion which leads to edge disorders of the resulting patterns.

The procedure of microcontact printing consists of a number of steps (Fig. 4.1.7). First of all, a silicon master is fabricated by photolithography. Then PDMS prepolymer is cast onto the solid master to make an elastomeric stamp. After the crosslink of the PDMS, the elastomeric stamp is peeled off with the inverse structures of the master. The stamp is then immersed into the molecular solution. The stamp is then rinsed and dried, and a conformal contact is formed between the substrate and the stamp in order to transfer the pattern of the molecules onto the substrate surface.

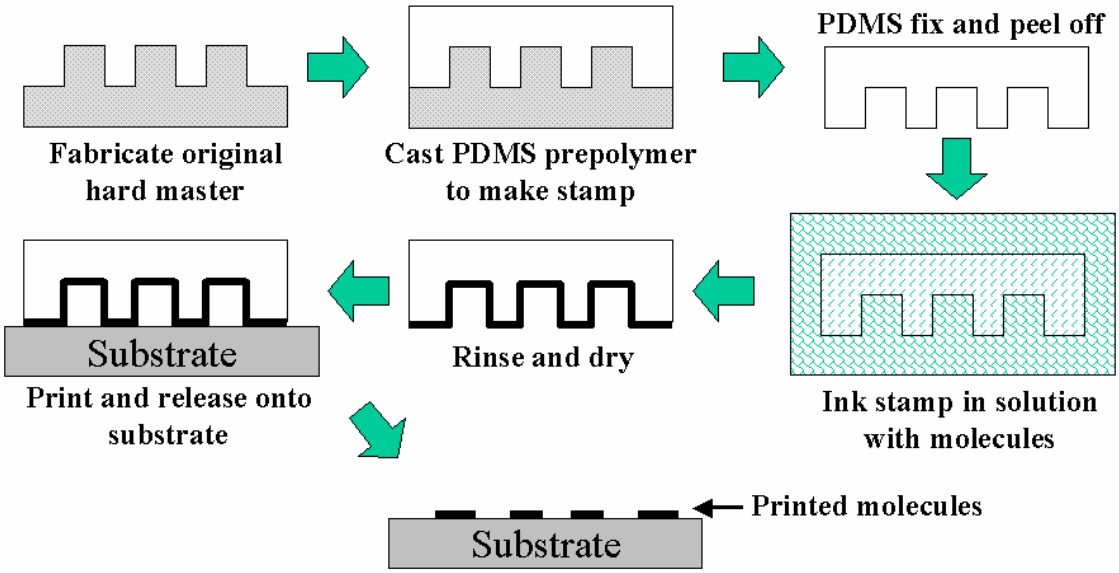

Fig. 4.1.7. The procedure of microcontact printing.

In our experiment, the BDPA molecules were dissolved in ethanol (99.99% Fisher Scientific) with concentration of 0.04% by weight. The PDMS stamp has a pattern of an array of circles with diameter of around 1 μm and spacing of 4 μm, and the size of the stamp is around 10 mm x 10 mm. The stamp was first immersed into the BDPA solution for a minute to ink its surface. Then the stamp was briefly rinsed with deionised water and dried in a stream of nitrogen gas. After that the stamp was pressed to form a conformal contact with the freshly cleaved graphite surface for 5 seconds to print the molecules onto the surface.

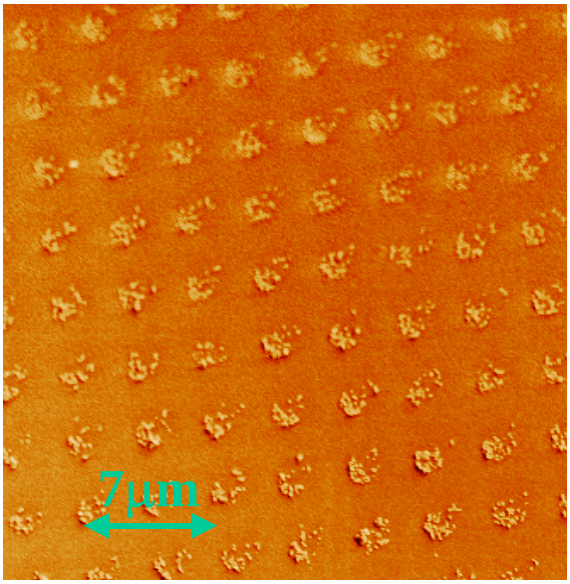

Fig. 4.1.8(a). The SEM image of the microcontact printed graphite surface with an array of circles of BDPA molecules.

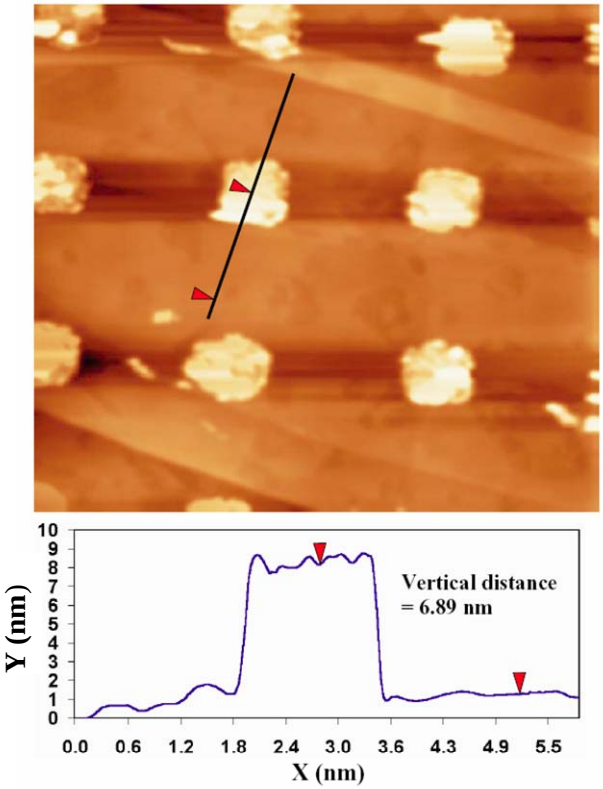

Fig. 4.1.8(b). The AFM tapping mode image of the microcontact printed graphite surface, 12 μm x 12 μm.

From the SEM image in Fig. 4.1.8(a), we can see that a large area of the graphite surface is covered with the array of circles of BDPA. In fact, more than 4 mm x 4 mm area is printed with this kind of pattern with BDPA. The size and the spacing of the circles conform to the patterns on the stamp. If we look closer as in Fig. 4.1.8(b), the BDPA molecules form an array of circles, though their shapes are not very regular and their morphologies are uneven. The BDPA molecules aggregate to form clusters. The line profile across one of these circles shows the thickness of the circle is around 6.89 nm [Fig. 4.1.8(b)], which is significantly thicker than a monolayer. We have attempted to make the circles thinner by using a solution with a lower concentration (0.025% in weight); however, the molecules incline to diffuse and aggregate together to form clusters rather than wetting the surface to form a monolayer [Fig. 4.1.8(c)], probably due to the hydrophobicity of graphite. This behaviour is similar to the case of evaporation on the graphite where the molecules move around and aggregate together to form the big islands. The problem of aggregation exacerbates in the case of microcontact printing because solvent is involved which enhances the molecule mobility, whereas for evaporation the BDPA molecules are in powder form without involving any solvents.

Our experimental result shows microcontact printing can transfer the free radical organic molecules BDPA onto the substrate with patterns. This provides a possible route towards the experiment of chemical analysis by spin detection with the STM, which will be described in detail in chapter 5.

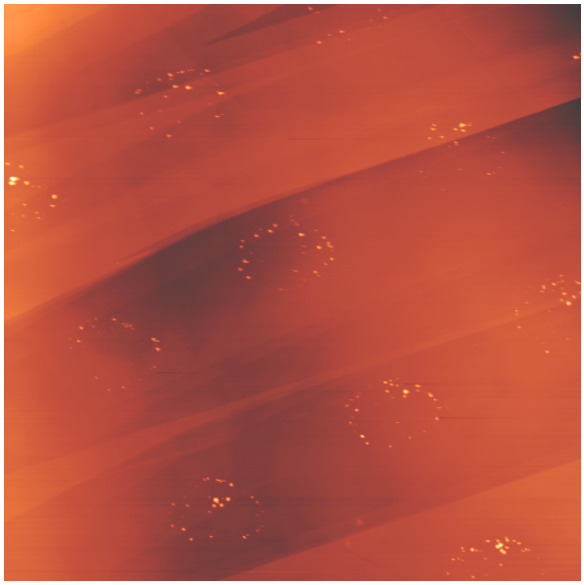

Fig. 4.1.8(c). Microcontact printing of BDPA with a lower concentration solution onto graphite surface, 12 μm x 12 μm. AFM tapping mode image.

4.1.2.3. Solvent deposition

Solvent deposition is one of the most commonly used deposition method in SPM experiments, especially for biological species like DNA, protein, and organic molecules. Organic solvents such as methanol, ethanol, toluene, are suitable for dissolving organic molecules, and some biological samples can be dispersed in pure water. In order to make the deposition as uniform as possible, spin coating is sometimes applied to disperse the material in a more even manner after drop casting. This deposition method delivers the advantage of convenience and wide applicability as it is easy to use, does not require a complicated experimental set-up, and is applicable to a variety of samples. In our experiments, ethanol (99.99% Fisher Scientific, according to the specification, the 0.01% impurity is mostly other solvents, and no residue is detected after evaporation) was used as the solvent for BDPA molecules and the solution concentration is 0.0033% by weight. Drop casting with a micropipette and spin coating were applied to deposit the BDPA molecules onto a freshly cleaved graphite surface. We subsequently imaged the sample surface with the AFM in tapping mode.

Similar to the case of evaporation, the BDPA molecules tend to diffuse on the graphite surface, forming islands ranging in size from around a few hundred nanometres to a micrometre and decorating the step edges [Fig. 4.1.9(a) and Fig. 4.1.9(b)]. The molecules, similar to their behaviour on the graphite deposited by evaporation, incline to move around until they either attach to other molecules or obtain stability at the step edges. However, in addition to the islands, there are several clusters with the size of around 100 nm x 100 nm scattered on the surface. If we look at the line profile [Fig. 4.1.9(b)], the thickness of the island is around 0.52 nm which is a monolayer, and it shows that the method of solvent deposition can deposit the BDPA free radicals with monolayer thickness onto the substrate. Nevertheless, the dot has a height of 8 – 9 nm which is relatively large. The conjugated bonding structures in the hexagonal and pentagonal rings of BDPA form relatively large electron clouds which will induce strong intermolecular interaction between the molecules, and thus the BDPA will have the tendency to move close together and aggregate in the solvent. We believe that these dots are due to the aggregation of the BDPA within the solution. The aggregation problem here is more pronounced than with microcontact printing because of the direct participation of the solvent in the deposition process. It is difficult to filter out these aggregated clusters due to their small sizes.

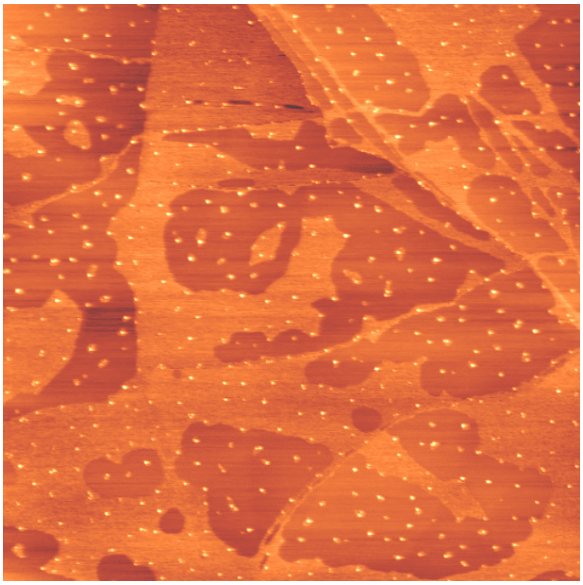

Fig. 4.1.9(a). AFM tapping mode image on the BDPA islands deposited onto the graphite by solvent deposition, 6 μm x 6 μm.

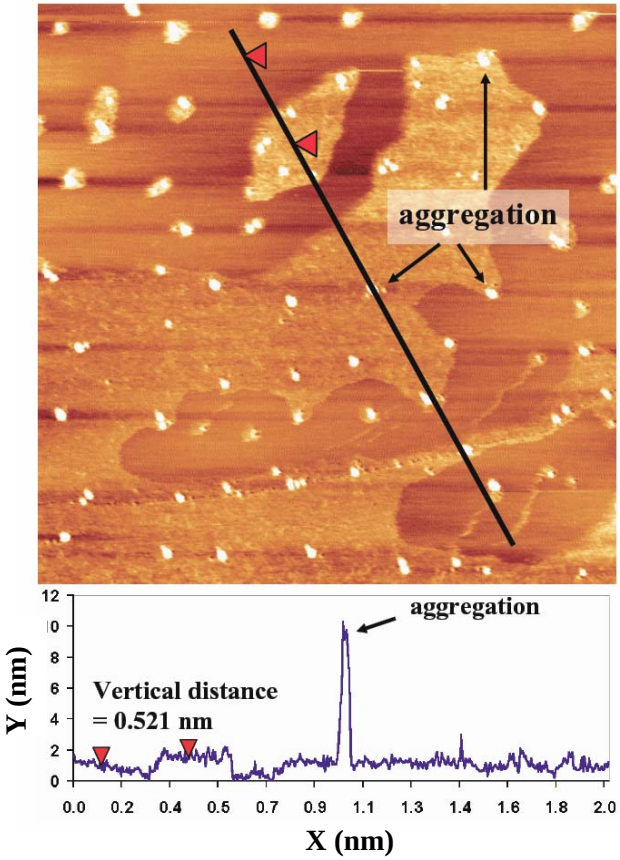

Fig. 4.1.9(b). AFM tapping mode image on the same surface as in Fig. 4.1.9(a), 2 μm x 2 μm. The line profile shows the thickness of the islands and the clusters.

Previous experiments [146] have involved the use of significantly less concentrated solutions of BDPA in isopropanol, which resulted in small clusters of molecules a few nm across, which are small enough for STM imaging on HOPG. Clearly the polarity of the solvent also plays a role in determining the morphology of the deposited islands.

We have carried out additional experiments to investigate the influence of the impurity in a solvent with a lower purity on the deposition result. In this experiment, we deposited the ethanol solvent of a lower purity[2] (96% Hayman) onto the graphite surface

[2]According to the manufacturer, the remaining 4% is water and some impurities. However, the elements of the impurities are not specified.

without the involvement of the BDPA molecules. In the SEM image [Fig. 4.1.10(a)], we can observe equilateral triangular structures with the size of a few hundred nanometres, which we name “nanotriangles”. This kind of structure occupies about 150 μm x 150 μm out of 5 mm x 5 mm substrate surface area. The lines align along three axes with triangular symmetry with a distribution of lengths from around 100 nm to 2 μm while the line widths range from around 50 nm to 80nm. These triangular structures were observed with the AFM in tapping mode as well [Fig. 4.1.10(b)]. The Fast Fourier Transform (FFT) spectrum in Fig. 4.1.10(b) is a six-point star with equivalent angles of sixty degrees between each point which has a tapered

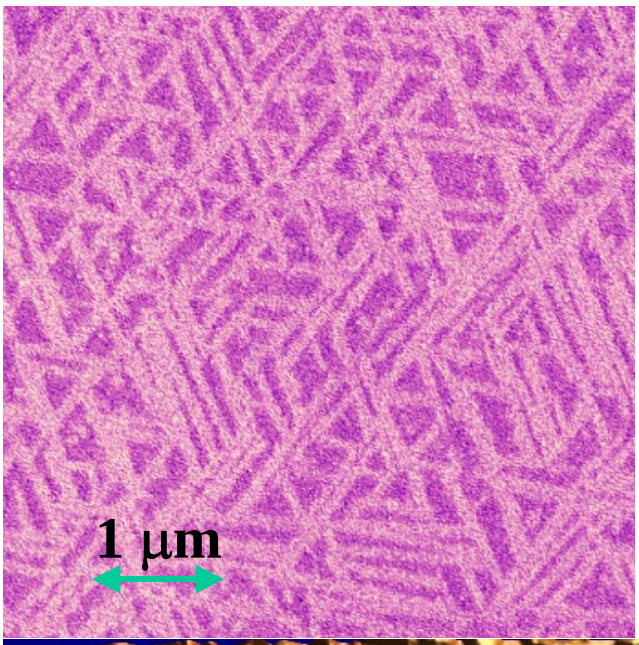

Fig. 4.1.10(a). SEM image of the “nanotriangles” on the graphite surface which are due to the residue of the low purity solvent.

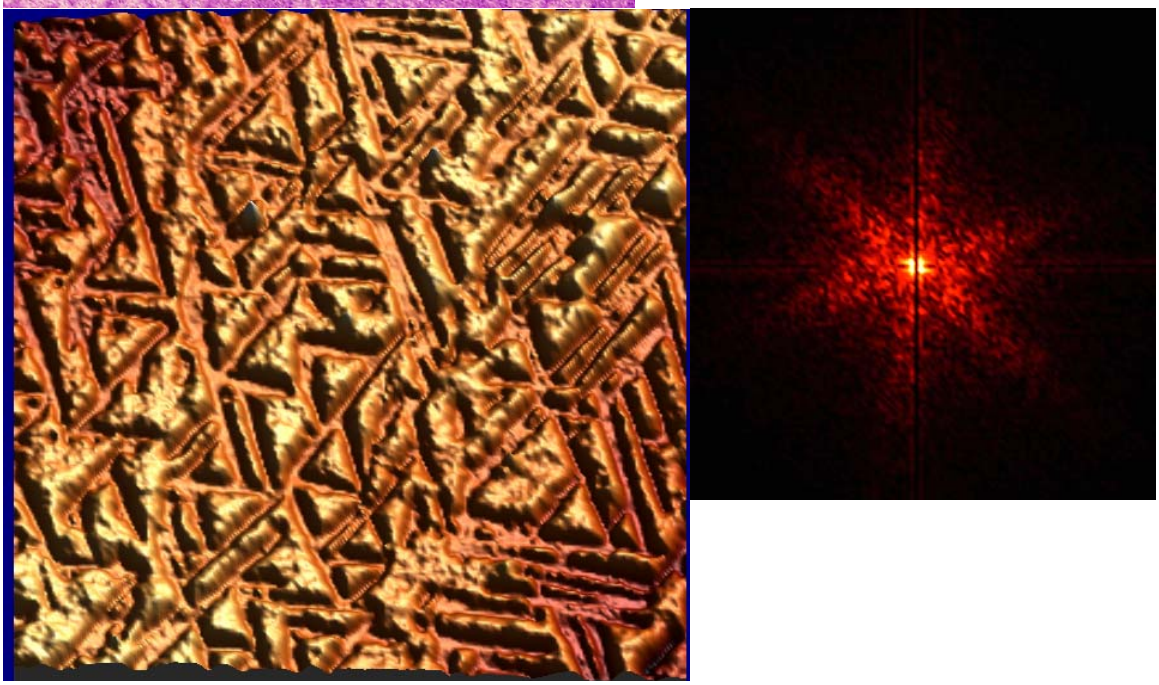

Fig. 4.1.10(b). 3.5 μm x 3.5 μm AFM tapping mode image of the “nanotriangles” in 3D format and its corresponding Fast Fourier Transform spectrum.

shape, and it matches with our observation in the actual image in the way that its sixty degree angle correlates with the triangular symmetry, and its tapered shape implies the ranges of the width and length for those aligned lines in the SEM image. The hexagonal symmetry highlighted in the FFT spectrum is related to the underlying hexagonal graphite lattice. Even after heating this sample to 175°C for an hour, the "nanotriangles" were observed again in the SEM suggesting that these structures are quite stable and robust. The result of this experiment shows that even impurities in a solvent can form highly ordered structures on a surface, indicating that ultra-high purity solvents should be used, particularly when handling low-concentration solutions.

4.1.3 Discussion on deposition methods

In this work, we have used thermal evaporation, microcontact printing, and solvent deposition methods to deposit free radical organic molecules (BDPA) onto a substrate with controlled thickness. Thermal evaporation, which is an in–situ sample preparation method for ultrahigh vacuum experiments, can deposit a submonolayer of BDPA without destroying their spin property. This method is an ideal way to do the deposition as it eliminates the problem of aggregation or residue. However, for some free radical organic molecules like TEMPO[3] whose melting points are relatively low (37°C for TEMPO), it would be difficult to control their evaporation rates for depositing a submonolayer. In these cases, the solvent deposition method is more suitable. From the deposition results on graphite and on gold by evaporation, it is clear that the substrate plays an important role in determining the deposition result. It is interesting to notice that the behaviour of the BDPA on graphite surfaces is essentially independent of the deposition method used. However we can control the influence of such behaviour on the deposition result by avoiding the involvement of the solvent, as shown by the deposition results of evaporation and solvent deposition. The microcontact printing technique has successfully printed the BDPA free radicals with the pattern of an array of circles onto a graphite surface over a large area.

The solvent deposition method can deposit a monolayer of BDPA onto the substrate. This method is particularly useful for free radical organic molecules whose low melting points (e.g. TEMPO) make them unsuitable for thermal evaporation since it would be difficult to control their evaporation rates. The aggregation of organic molecules may present a problem to solvent deposition, but the deposition results can be optimised by trying different kinds of solvents, for instance methanol, isopropanol, toluene, and chloroform. It is also possible to perform solvent deposition in–situ. A high-speed solenoid pulse valve[4] can

[3]Molecular weight 156.2, CAS number 2564-83-2, purchased from Sigma-Aldrich.

inject the solution towards the substrate under the UHV environment when the valve is opened for a millisecond [163, 164]. However, the uniformity of the deposition on a substrate is not guaranteed. For free radical organic molecules with poor solubilities, we can use thermal evaporation for deposition.

4.1.4. Conclusion

The possibilities of a variety of deposition methods for free radical organic molecules were explored, which is a significant first step towards single electron spin detection with the STM. Thermal evaporation, microcontact printing, and solvent deposition can controllably deposit the free radical organic molecules BDPA onto the substrate. Each deposition method has its own pros and cons, and the physical properties like melting point and solubility of the free radical organic molecules will determine which method to use. The results of this work provide information for the sample preparations with free radical organic molecules. In the next chapter, we will talk about the deposition of iron on silicon. As iron is normally not soluble, thermal evaporation is used for the deposition.

The work in this chapter is submitted for publication and is currently under review [165].

[4]General Valve Co., Series 9

Chapter 4.2 Deposition and characterization of iron on silicon

Summary

This section describes our work on deposition of iron onto silicon which can be useful for future spin-polarized scanning tunnelling microscopy (SPSTM) and single electron spin detection experiments. Iron was deposited onto silicon by reactive deposition epitaxy (RDE) at 873 K and by solid phase epitaxy (SPE) without heating. Surfaces with different electrical and magnetic properties were formed depending on the type of deposition. The iron silicide on silicon crystal surfaces formed by RDE will be useful for single electron spin detection experiments. However, neither of these methods produced satisfactory binary magnetic systems for SPSTM investigation. Future work will involve designing improved means of deposition to provide well-ordered iron species deposited on silicon, with the ferromagnetism of iron being preserved.

4.2.1 Introduction

The Curie temperature of iron is 1043 K and thus remains ferromagnetic at room temperature, and iron is electrically conducting for STM tunnelling. Silicon is nonmagnetic, and preparation of a clean, well-ordered silicon surface is known. In this light, iron deposited on silicon will be a binary magnetic system suitable for STM experiments.

In this experiment, silicon was used as the substrate because it is compatible with conventional lithography technology and can be widely applied in the forthcoming era of spintronic devices. Single-crystal tungsten(110) is one of the most common substrates for SPSTM studies; however, it is not as useful as silicon in terms of practical application [166].

It is reported that iron deposited onto silicon by RDE will form iron silicide ($FeSi_2$) which can provide spin centres for single electron spin detection experiments [167]. RDE deposition at 873 K will result in β-$FeSi_2$ which is a semiconductor material with a direct band gap of 0.85 eV [168]. The structure of β-$FeSi_2$ is orthorhombic (a = 9.86 Å, b = 7.79 Å, c = 7.83 Å), which is similar to the CaF_2 structure as shown in Fig. 4.2.1. The advantage of making samples for single electron spin detection experiments by RDE is that the whole process can be performed in-situ, thus a sample will be intrinsically clean. Moreover, instead of a random distribution in the bulk of the silicon crystal by doping iron atoms on a silicon wafer, iron atoms deposited by RDE will be distributed near the sample surface, and provide a spin signal at g = 2.07 [167]. The Mössbauer spectroscopy measurement shows that the iron silicide prepared by RDE is paramagnetic.

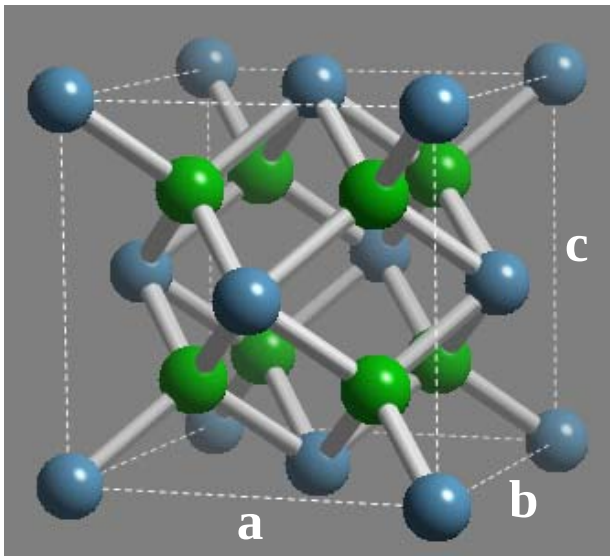

Fig. 4.2.1. Atomistic model of β-$FeSi_2$. β-$FeSi_2$ has an orthorhombic (a = 9.86 Å, b = 7.79 Å, c = 7.83 Å) structure. Blue balls are iron atoms, green balls are silicon atoms.

4.2.2 Experiment

4.2.2.1 Preparation of silicon substrates

Our silicon wafers [Si(111)] were purchased from Virginia Semiconductor, USA. Before deposition, a silicon substrate with the size of 4 mm x 7 mm was cleaned with organic solvents (acetone and isopropyl alcohol) and deionised water, then blown dry with nitrogen gas. The silicon was loaded into the chamber and degassed at around 600°C by resistive heating for 2 hours. The silicon was left to cool down slowly before direct heating. A dc current of 0.4 A at 8.5 V was passed through the silicon. The current level was set at the threshold of visible light emission (observed in low-light conditions) otherwise the SiO_2 layer would evaporate. The sample was degassed for 10 hours. After degassing, flashing (procedure shown in Fig. 4.2.2) was performed on the sample to eliminate the oxide layer and induce the 7 x 7 reconstruction. (a) First we flashed at 3 A for a few seconds and observed the pressure increase. After repetitions of around three times, the pressure stayed in the 10^{-10} mbar range. (b) We then flashed at 5 A and repeated the same procedure. (c) The temperature of the sample at 8 A is approximately 1200°C as measured with a pyrometer (Minolta, Japan). Flashing at 8 A several times until the pressure remained below 2 x 10^{-9} mbar over the subsequent 10 second 8 A pulse. (d) Once the 10 sec 8 A pulse finished, the current was quickly decreased to 5 A which corresponds to a temperature around 900°C. The current was then decreased at a rate of 0.01 As^{-1} until zero, to allow the high-temperature 1 x 1 surface structure to transform into the energetically favourable 7 x 7 surface structure caused by the reduction in dangling bond density. Finally, the sample was cooled for 30 minutes.

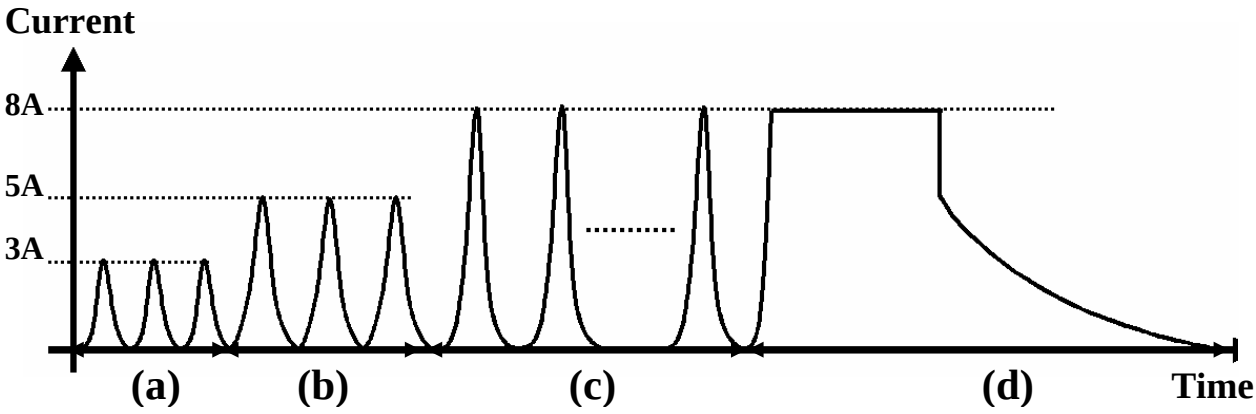

Fig. 4.2.2. The flashing procedure for Si(111) surface. This procedure was found to produce 7 x 7 reconstruction on Si(111) surface.

4.2.2.2 Reactive deposition epitaxy (RDE) and solid phase epitaxy (SPE) depositions

The experiments were performed in a UHVSTM system with pressure in the range of 10^{-10} mbar. A lock-in amplifier was equipped to measure the dI/dV signal which is proportional to the density of states of the sample as shown in chapter 1 by eq. (1.10). The flashed silicon surface was imaged to observe the general morphology and the 7 x 7 reconstruction. Deposition was conducted by an e-beam evaporator with a flux corresponding to an iron deposition rate of 1 monolayer per minute. RDE mode was used in which iron was deposited onto a silicon substrate resistively heated up to around 873 K by a filament. Upon reaching the heated silicon surface, the iron reacts with it and forms iron silicide.

The RDE deposition method was used with the silicon substrate heated to 873 K by resistive heating. According to the work of Minami *et al*. [169], the deposited iron will form triangular domains of the size of tens of nanometres, which are easily distinguishable from the silicon substrate. The topography and local density of states images were acquired simultaneously so as to obtain structural and electrical information.

After that, the SPE without heating method was used to deposit iron onto silicon to avoid the formation of iron silicide so that the ferromagnetism of the iron can be preserved.

4.2.2.3 STM imaging

STM imaging was performed with the Omicron STM/AFM system described in section 1.2.1. Mechanically cut Pt/Ir tips were used.

4.2.3 Results

4.2.3.1 RDE deposition results

After flashing, the silicon was imaged to check if the 7 x 7 reconstruction occurred on the surface. Fig. 4.2.3 shows a 1500 nm x 1500 nm area of the flashed silicon surface. There are many terraces and steps on the surface. Fig. 4.2.4 is another image with smaller range giving a magnified view of the terraces. The terraces are clean and flat, thus suitable for the iron deposition afterwards. The atomic resolution revealed by Fig. 4.2.5 shows the 7 x 7 reconstruction, indicating that the flashing procedure can properly prepare the silicon surface.

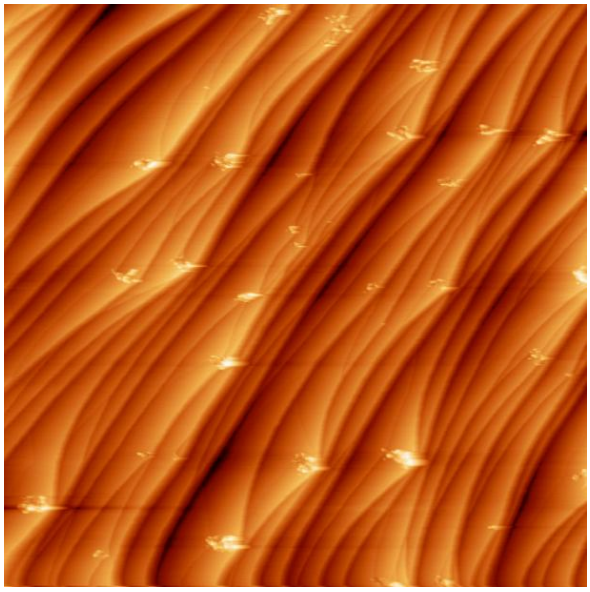

Fig. 4.2.3. 1500 nm x 1500 nm image of the flashed silicon. I_t = 0.4 nA, V_s = 2000 mV. Steps with flat terraces are visible. There is still some debris (the bright structures of irregular shape occurring at the edges of the terraces in the image) on the surface, but this comprises less than 10% of the surface area.

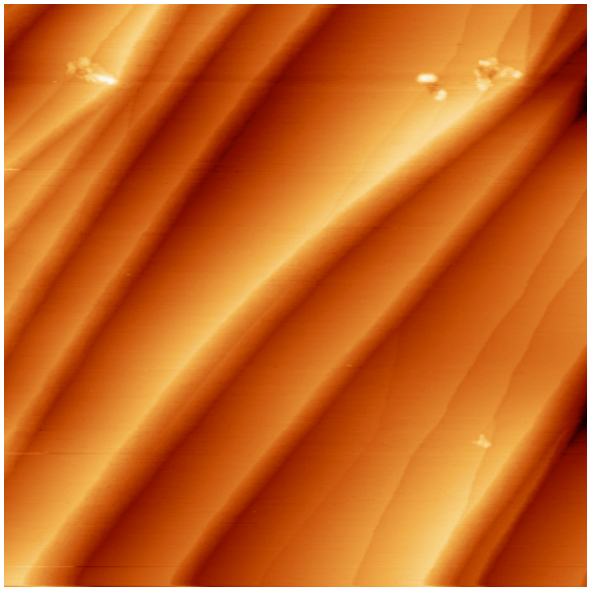

Fig. 4.2.4. 552 nm x 552 nm image of the flashed silicon. I_t = 0.4 nA, V_s = 2000 mV. This image shows that the terraces are clean and flat, and thus suitable for subsequent iron deposition.

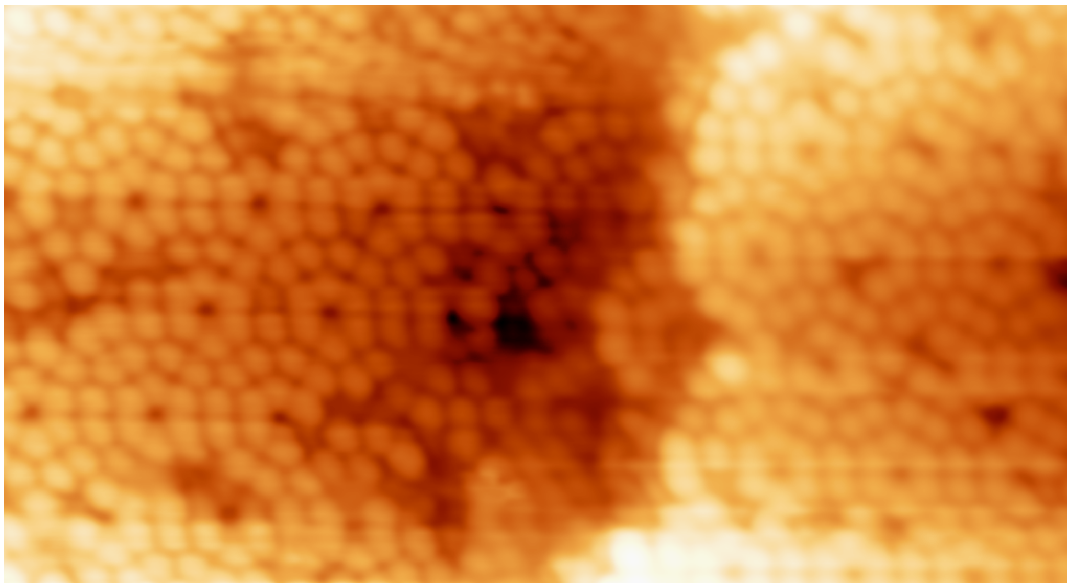

Fig. 4.2.5. 20.3 nm x 11 nm image of the flashed silicon. I_t = 1 nA, V_s = 1250 mV. This shows a closer view of the terraces. Atomic resolution 7 x 7 reconstruction can be seen on the terraces. This image indicates that the silicon preparation procedure can successfully produce 7 x 7 reconstruction on a silicon surface.

After checking the surface reconstruction, deposition of iron was carried out on the silicon substrates. To confirm the iron deposition, the first sample was deposited by RDE (at 873 K, resistive heating with a filament) with a relatively thick layer of iron of around 2 monolayers (ML). Instead of forming triangular islands, the iron tended to form islands of irregular shapes around 20 nm to 30 nm in size, as shown in Fig. 4.2.6(a). This is probably because the amount of iron deposited is too much; previously, 0.2 to 0.4 ML were deposited

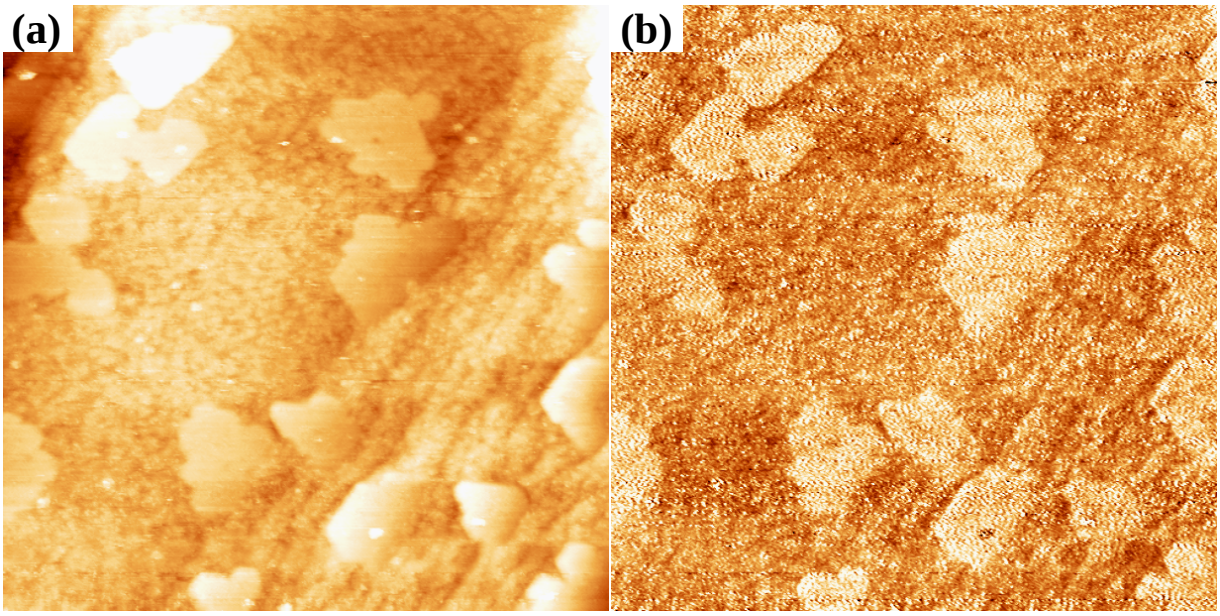

Fig. 4.2.6. (a) 140 nm x 140 nm, I_t = 0.4 nA, V_s = +2000 mV. Topography image of the iron silicide with 2 ML thick of iron deposited by RDE at 873 K. (b) The density of state image taken simultaneously with the topography image at V_s = +2000 mV.

in [170] which then formed triangular domains. The thickness of the iron clusters is distributed from 0.5 nm to 0.9 nm. The density of states image [Fig. 4.2.6(b)] shows the contrast between the background and the iron clusters, which indicates the difference in density of states at V_s = +2000 mV between the iron clusters and the background substrate. At this energy level, the local densities of states of the iron clusters are higher than the background substrate. This difference shows the disparity between the electronic structures of the background substrate and the iron clusters at +2000 mV.

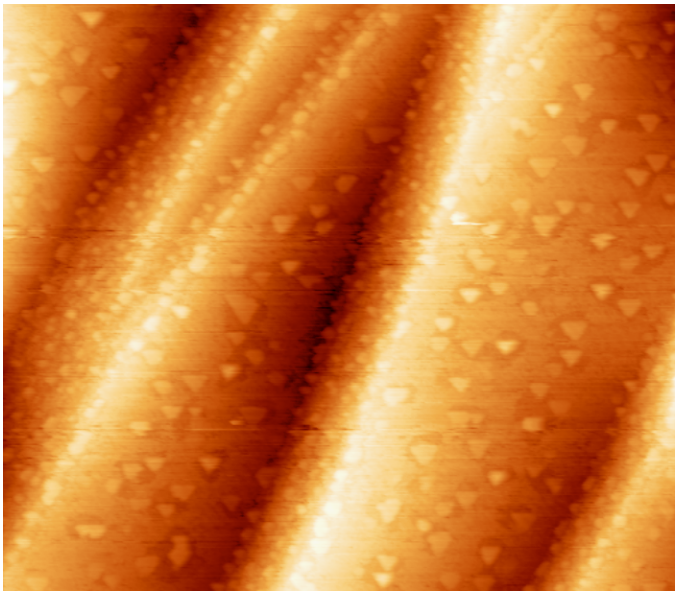

Fig. 4.2.7. 238 nm x 208 nm, I_t = 0.4 nA, V_s = +2000 mV. 0.5 ML of iron deposited onto the Si(111) surface by reactive deposition epitaxy at 873 K. The iron silicide formed triangular islands of size tens of nanometre.

Once iron deposition was confirmed, the next sample was prepared by RDE (at 873 K, resistive heating with a filament); a thinner iron layer of approximately 0.5 ML was deposited. Fig. 4.2.7 shows a 238 nm x 208 nm area of the sample surface, some triangular islands are formed on the terraces and step edges. From Fig. 4.2.8(a), the iron silicide islands form triangular shapes with a range in size around 5 nm to 15 nm, similar to the results in [170] where iron was deposited onto the silicon by RDE at 870 K and the resulting iron silicide formed into triangular shapes with sizes under 100 nm. The height of these iron silicide islands is around 0.5 nm and the islands are quite flat as seen in Fig. 4.2.9. The density of states image [Fig. 4.2.8(b)] does not show the difference between the background substrate and the triangular iron islands at V_s = +2000 mV. This means there is no disparity between the electronic structures of the substrate silicon and the triangular iron silicide domains at +2000 mV, and both the silicon substrate and the triangular iron silicide domains have similar local density of states at this energy level. This is in contrast to the density of states measurement of the above-mentioned RDE deposition of 2 ML of iron. It may be possible that for the 2 ML deposition of iron, the amount of the deposited iron is enough to

form a layer of the iron silicide, and on top of it are some iron clusters that do not react with silicon to form iron silicide, whereas for the 0.5 ML deposition, all the iron reacts with the substrate to form iron silicide and there is not enough iron to form another layer of iron on top of the triangular iron silicide domains. The difference in local density of states at +2000 mV is probably due to the difference in electronic structure between the iron and the iron silicide and not the iron silicide and the silicon substrate.

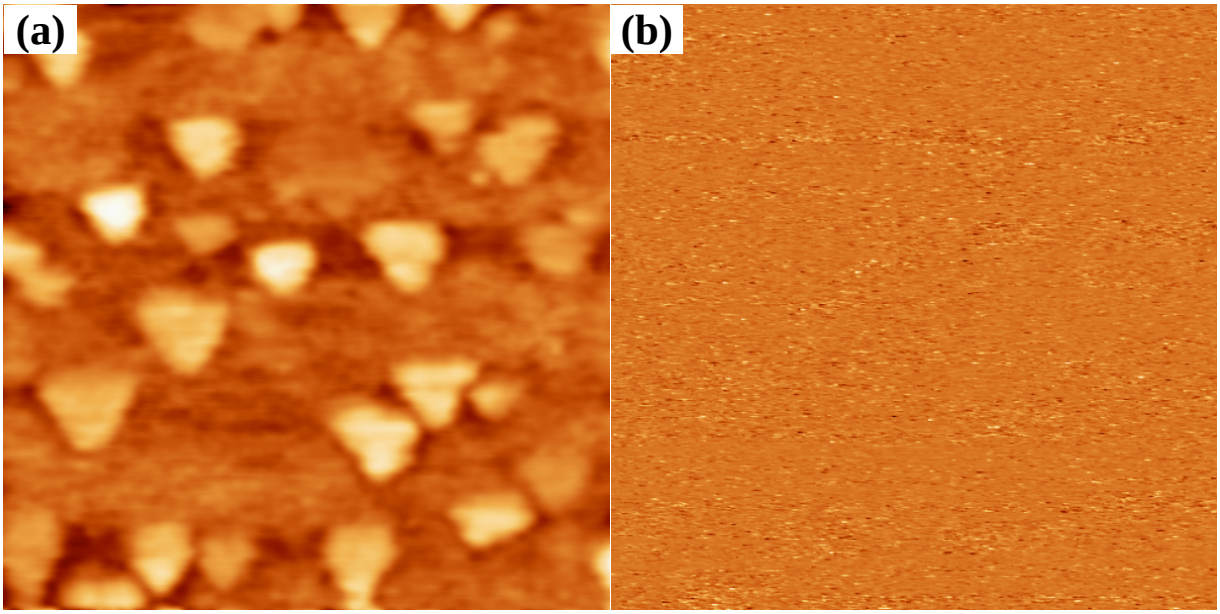

Fig. 4.2.8. (a) 75 nm x 75 nm, I_t = 0.4 nA, V_s = +2000 mV. Topography image of the iron silicide with 0.5 ML thick of iron deposited with RDE at 873 K. (b) The density of state image taken simultaneously with the topography image at V_s = +2000 mV. There is no difference between the density of states of the iron silicide and the substrate silicon at +2000 mV.

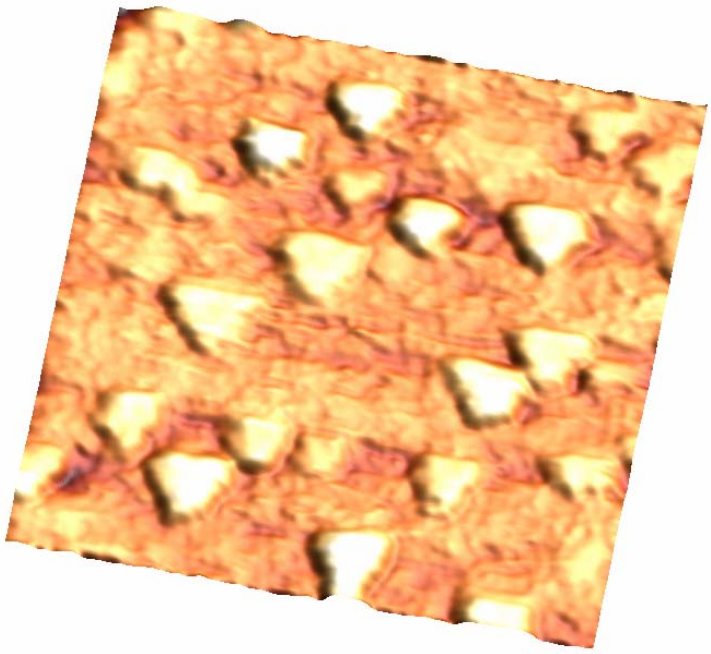

Fig. 4.2.9. 74.8 nm x 74.8 nm, I_t = 0.4 nA, V_s = +2000 mV. The height of the iron silicide triangular islands is around 0.5 nm. The sizes of the islands range from 5 nm to 15 nm. The triangular shapes of the islands make them easy to locate against the background substrate.

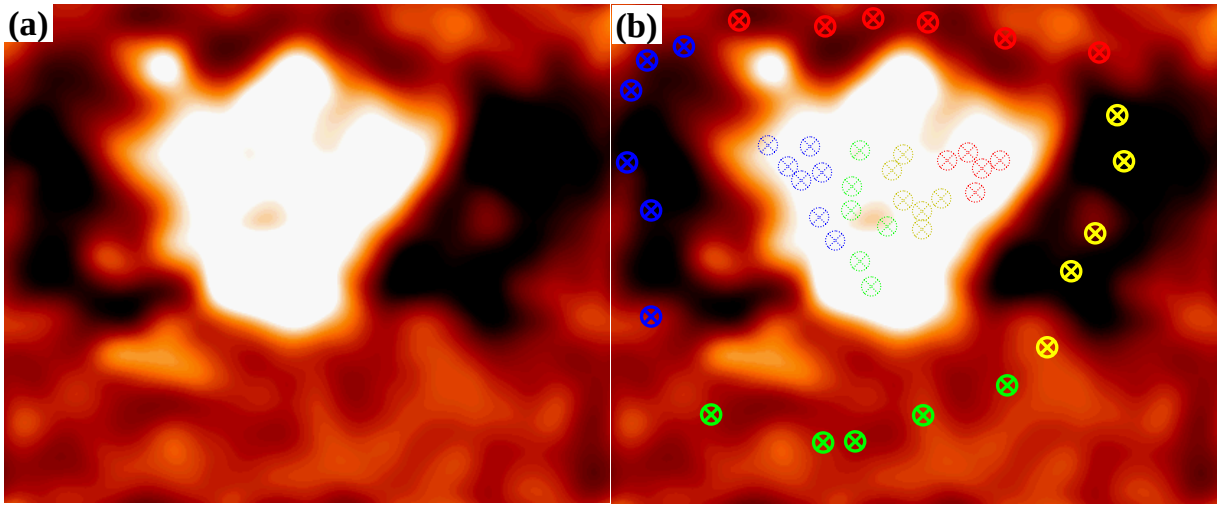

Fig. 4.2.10(a). 11.5 nm x 9.5 nm, I_t = 1 nA, V_s = 2000 mV. An isolated triangular iron silicide island with thickness of 0.46 nm and size of 6.2 nm. Fig. 4.2.10(b). Positions of I/V spectra taken on the silicon substrate and the iron silicide island. They are divided into eight groups: four on the silicon substrate (red, yellow, green, and blue markers in solid line), and four on the iron silicide island (red, yellow, green, and blue markers in dashed line). Image low pass filtered.

Iron was successfully deposited onto silicon and formed triangular iron silicide islands which are distinguishable against the substrate. This kind of sample would be suitable for single electron spin detection experiments. Another sample was prepared by RDE deposition of iron (at 873 K, resistive heating with a filament) with a thinner iron layer of around 0.25 ML. Fig. 4.2.10(a) shows a single triangular iron silicide island on the sample surface. Its thickness is measured as approximately 0.46 nm with size of around 6.2 nm. The electronic structure of the island was investigated by local tunnelling spectroscopy. The positions where the I/V spectra were obtained are indicated in Fig. 4.2.10(b). There are 46 spectra in total, 24 taken on the iron silicide island and the rest on the silicon substrate. Each of the spectra is one measurement of I/V signal against bias voltage without averaging. For easier representation and comparison, the spectra are categorized into eight groups; four on the silicon substrate [I/V spectra in Fig. 4.2.10(c)] and four on the iron silicide island [I/V spectra in Fig. 4.2.10(d)]. The representative spectrum of each group is the average result of all the spectra of the group. Due to the instability of the tip, the spectra were not reproducible and varied from each other as can be seen in Fig. 4.2.10(c) and Fig. 4.2.10(d). The I/V spectra in Fig. 4.2.10(e) were obtained by averaging all the I/V spectra taken on the silicon substrate and on the iron silicide island respectively. A dI/dV signal image was taken at 2 V in the same area and it is shown in Fig. 4.2.10(f), and there is no difference between the dI/dV signals from the silicon substrate and the iron silicide island in the image. However, this result is inconclusive because of the tip instability.

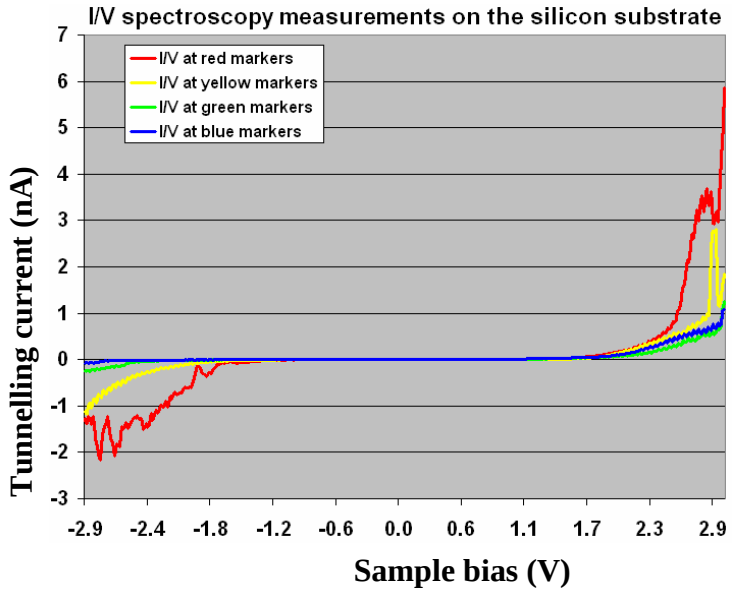

Fig. 4.2.10(c). Representative I/V spectra averaged from the spectra in each group obtained on the silicon substrate as marked in Fig. 4.2.10(b). The colours of the curves correspond to the colours of the markers (in solid line) for different groups in Fig. 4.2.10(b).

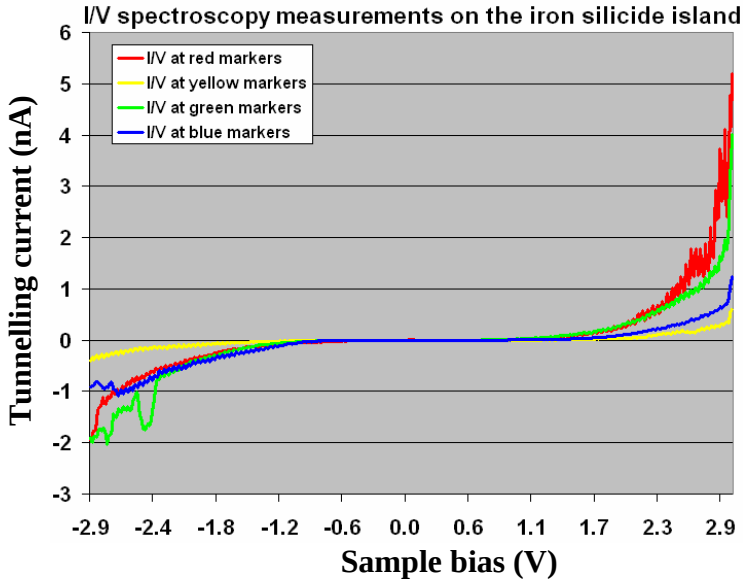

Fig. 4.2.10(d). Representative I/V spectra averaged from the spectra in each group obtained on the iron silicide island as marked in Fig. 4.2.10(b). The colours of the curves correspond to the colours of the markers (in dashed line) for different groups in Fig. 4.2.10(b).

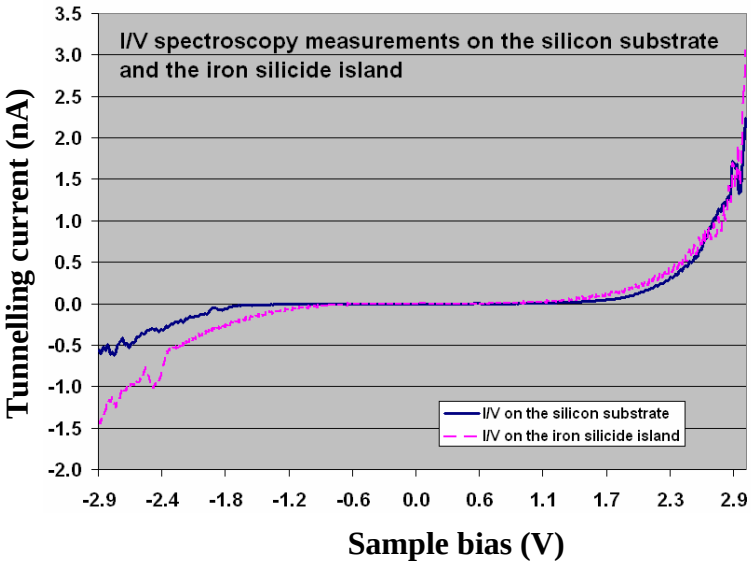

Fig. 4.2.10(e). I/V spectra obtained by averaging all the spectra on the silicon substrate (solid line) and the iron silicide island (dashed line) respectively.

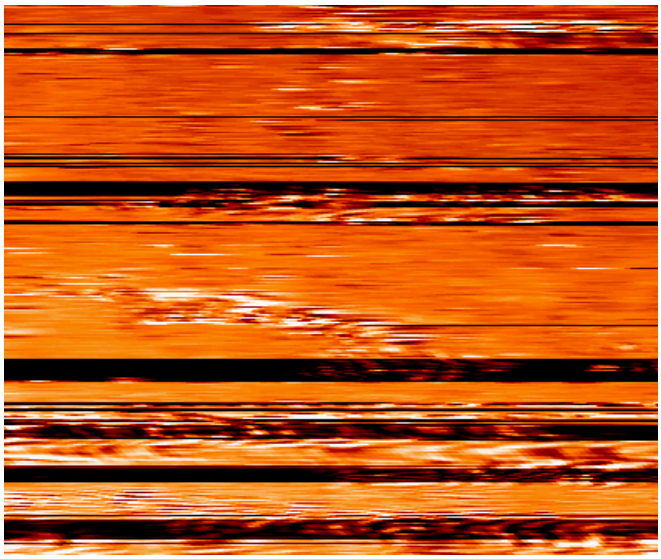

Fig. 4.2.10(f). The density of states image (dI/dV) taken simultaneously with the topography image (Fig. 4.2.10(a)) at V_s = +2000 mV. There is no clear difference between the dI/dV signals from the iron silicide and the substrate silicon at +2000 mV; however, it may be due to the tip instability.

The causes of the instability of the tip are twofold: first, the tip was made by mechanical cutting so its shape was not uniform and thus it was not structurally rigid; second, the tip was not cleaned by any tip cleaning procedures such as annealing and ion sputtering, and so there might be dirt at the tip end. As such, the conclusion is that chemically etched tungsten tips would appear to be preferable for this kind of experiment because they are more uniformly shaped and thus sturdier, and tip cleaning processes are necessary. More works with better tips are needed to characterize the electrical properties of iron silicide.

4.2.3.2 SPE deposition results

Although the triangular iron silicide domains can be well distinguished from the silicon substrate, the work by Matsumoto *et al*. [170] provides the result of Mössbauer spectroscopy on the iron in the silicide film prepared by the RDE at 870 K, showing that the iron, after forming iron silicide, lost its ferromagnetism and becomes paramagnetic. This makes the iron silicide unsuitable for SPSTM experiments. As such, it was attempted to deposit iron onto silicon without heating up the silicon substrate so as to avoid forming iron silicide.

SPE without heating was used to carry out the iron deposition. Approximately 0.3 ML of iron was deposited onto silicon by thermal evaporation without heating up the silicon substrate. The STM image of the sample shows that the resulting surface after deposition is quite granular and rough as shown in Fig. 4.2.11. Roughness analysis was conducted on the image data:

$$\text{RMS roughness: } R_{rms} = \sqrt{\frac{1}{N}\sum_{i=1}^{N}(Z_i - \overline{Z})^2} \qquad (4.2.1)$$

$$\text{Arithmetic mean: } R_a = \frac{1}{N}\sum_{i=1}^{N}\left|Z_i - \overline{Z}\right| \qquad (4.2.2)$$

where N is the number of data points involved and $\overline{Z} = \frac{1}{N}\sum_{i=1}^{N} Z_i$ is the mean Z-value. The roughness analysis states that the RMS roughness R_{rms} is 0.191 nm and the arithmetic mean height R_a is 0.136 nm, which is four times as rough, comparing with a silicon 7 x 7 reconstructed atomically flat surface generally having R_{rms} of around 0.05 nm and R_a around 0.05nm. This result is very similar to the work of Matsumoto *et al*. [170] where they deposited around 0.4 ML of iron onto silicon by evaporation without heating, and the surface obtained was also rough as observed in Fig. 4.2.11. It is difficult to discern the deposited iron particles from the silicon substrate. As the iron particles are not distinct enough, this system is not ideal for SPSTM experiments because it would be difficult to assign the contrast in the spin-polarized spectroscopic image to the corresponding magnetic species on the sample surface.

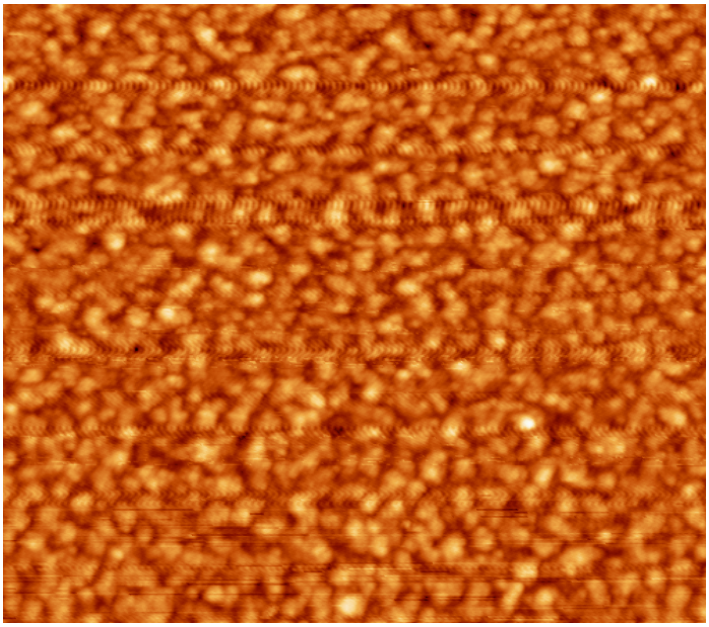

Fig. 4.2.11. 44 nm x 50 nm, I = 0.5 nA, V = +2000 mV. Approximately 0.3 ML of iron is deposited onto the silicon surface by SPE without heating. As shown in the image, the surface is rough and granular, confirmed by the roughness analysis, and it is difficult to discern the difference between the iron particles and the silicon substrate.

4.2.4 Conclusion

Iron was deposited onto silicon in order to prepare samples for future SPSTM and single electron spin detection experiments. Iron was deposited by RDE and formed triangular iron silicide islands which are distinguishable against the silicon substrate are suitable samples for single electron spin detection experiments. However, the instability of the tip made the I/V spectroscopy measurements irreproducible. As such, it is important to use chemically etched tungsten tips for characterization experiments since they are structurally rigid, and furthermore tip cleaning procedures must be employed in order to obtain reproducible spectroscopy measurements.

Since the work by Matsumura *et al*. [170] shows that the iron silicide is no longer ferromagnetic, it was attempted to avoid forming iron silicide by depositing the iron onto silicon by SPE without heating so as to preserve the ferromagnetism of the iron. However, the result shows that the sample surface becomes very rough and it is difficult to distinguish the deposited iron from the silicon substrate. In this light, a more appropriate deposition method is needed to make the binary system distinguishable without losing the ferromagnetism of the deposited iron. An alternative binary magnetic system, for example iron on tungsten, may be a more suitable sample for realizing SPSTM experiments.

Although the iron islands deposited by RDE have lost ferromagnetism and are not suitable for SPSTM experiments, they may have applications in silicon-based optoelectronic devices. Recently semiconducting silicides have been attracting much attention as one of the candidates for silicon-based light emitting diodes (LEDs), semiconducting iron silicide ($FeSi_x$) in particular, has attracted much interest because it can be grown epitaxially on silicon substrates, and has a direct band gap of about 0.85 eV at room temperature. While the other implantation methods of iron can damage silicon crystals which will require long-time annealing at high temperature to recover, RDE is supposed to create less damage to silicon because it only involves the deposition of iron on heated silicon substrates [171]. Our results are very similar to that of Matsumura *et al*. [170] in the sense that the deposited iron by RDE forms the iron silicide in triangular shapes. However, Matsumura *et al*. used direct heating i.e. passing a current through the silicon for heating up the silicon in RDE deposition whereas we used resistive heating i.e. using heating filament for the RDE deposition of iron. This opens an alternative route to achieve RDE deposition for iron on silicon surface without involving passing an electric current directly into the silicon substrate, which can simplify the RDE process as one heating filament can heat up many silicon substrates at the same time while for direct heating electric current is needed to pass through each piece of silicon.

Chapter 5

Conclusions

In this thesis, we described our work on the development of a scanning tunnelling microscope for the atomic-level characterization of overlayers on single crystal surfaces and our investigation of the anomaly of STM – superlattices on graphite. The primary aim of this dissertation was to design and construct a STM specifically for characterising overlayers on single crystal surfaces with the future intention of conducting single electron spin detection and spin-polarized STM experiments. In the course of achieving this end, we observed graphite superlattices which remain a phenomenon not yet understood. In view of its profound implication for STM imaging and its importance for advancing scientific knowledge, we have performed a literature review and summarized the current understanding of this subject. Furthermore we have reported our observations on the peculiarities of the graphite superlattices that we have imaged with the STM and proposed a theory from the energetic point of view, which explains the formation of all these different types of superlattice boundaries.

At the beginning of this thesis, we provided a brief introduction to STM, STM spin detection capability, and the application of STM to surface science. The basic principles of STM and the electron spin detection with STM techniques were described. The STM scanning on graphite, gold, and silicon allows us to demonstrate the application of STM measurements on a layered material, a metal, and a semiconductor.

The design and construction of a UHVSTM for characterizing overlayers on single crystal surfaces at the atomic scale, with the potentiality of conducting single electron spin detection, was then described together with some preliminary imaging results. The essence of the design is the use of a high-frequency coaxial cable to carry the tunnelling current and the novel design of the slip-stick walker on which a magnet and a sample are mounted that provides extra freedom of motion for the sample and thus extends the scanning range of the system. In order to incorporate the relatively stiff high-frequency coaxial cable into a STM which is extremely sensitive to vibration, three levels of vibration isolation were employed: first, a separate foundation; second, air legs; third, spring suspension with magnetic damping.

Moreover, the high-frequency coaxial cable is regularly anchored to break down the vibration mode and relieve the stress applied to the inner stage of the STM. All the other connecting wires from the inner stage to the outer stage were made of 30-μm-thick wires to minimize the coupling to the external vibration. The wiring of the walker is designed in such a way that the walker can move back, forth, sideways, and rotate without breaking the feedback control. The main chamber is compact in size and it can be evacuated relatively quickly. In addition to the fundamental components for a conventional STM, a bias tee, a RF amplifier, and a spectrum analyzer are integrated into our system for future single electron spin detection experiments. The bias tee splits the tunnelling current into its low frequency and high frequency components; while the low frequency component is passed to a IV amplifier, the high frequency component is amplified by a RF amplifier and processed by the spectrum analyzer to look at the frequency spectrum of the tunnelling current for the inherited high frequency modulation signal. Atomic resolution on graphite and gold surfaces were achieved which exhibit the imaging capability of the STM under ambient and UHV conditions.

With the UHVSTM successfully built, we commenced our work on characterization of overlayers on single crystal surfaces; our first observation was of graphite superlattices. In chapter 3, we first reviewed the literature concerned with graphite superlattices observed with STM. Upon the first discovery in the late 1980s, many groups reported the observation of graphite superlattices. It is widely accepted that the origin of most superlattices is due to the misorientation between graphite layers resulting in a Moiré rotation pattern. There are some unexplained and controversial observations concerning graphite superlattices, nevertheless, generally speaking, the Moiré rotation pattern assumption is capable of providing an explanation of most of the observed aspects of graphite superlattices. The established simulation model together with the proposed protocol of manually producing graphite superlattices are promising routes towards further understanding of this anomaly of STM.

In our STM measurement of the graphite superlattices, we observed some peculiar characteristics in addition to the usual superperiodic hexagonal structure. First of all, the corrugation conservation phenomenon observed on one of the graphite superlattices does not agree with the previously reported attenuation of superlattice corrugation by an overlayer above the superlattice. This phenomenon was not observed before, and its origin is unknown. Further investigation is needed in order to gain a better understanding of it. Second, some rippling fringes with periodicities of 20 nm and 30 nm were observed on the superlattice and the region nearby, which indicate the graphite surface is highly strained and being buckled. On another superlattice, we observed the corrugation attenuation by an overlayer which is in

stark contrast to the corrugation conservation phenomenon on the first superlattice, and we proposed an equation which relates the attenuation factor to the number of overlayers. Our research effort in this subject contributes to unveiling the previously unobserved aspects of graphite superlattices and provide more data for other scientists to analyze.

The simulation model provides a useful tool to analyze graphite superlattices. It enables the simulation of a superlattice with predefined rotation angle and periodicity. In chapter 3.3, we have applied this model to investigate the rippling fringes which we observed on the superlattice, and the simulation result confirmed that the rippling fringes are not related to the superlattice itself. By making use of this model, we have shown results which refute the criticism of the Moiré rotation pattern assumption. The simulation model is also applicable in investigating some proposed theories concerning graphite superlattices, for instance the odd-even transition theory.

In chapter 3.4, we reported our observation of some types of superlattice boundaries which have not been observed before. Some research groups have suggested explanations of the origin of the superlattice boundaries previously; however, their explanations are not consistent with each other nor can they explain all the anomalous phenomena that occur on the graphite superlattices whose physical origin is still not completely understood. We have proposed a theory from the energetic point of view, which explains the formation of all these different types of superlattice boundaries. Furthermore, in our experiment, we have observed a very uncommon type of superlattice, a superlattice with varying periodicity, and this superlattice has a special type of boundary in the form of a linear chain of protrusions. This phenomenon was not reported nor explained before. We have discovered that the variation of the superlattice periodicity is due to a low-angle grain boundary which has its tilt angle varies along one direction. This finding is supported convincingly by our experimental STM data. A simple equation which relates the variation of the superlattice periodicity to the periodicity of the dislocations at the boundary is derived, it also brings out a theoretical view that a chain of dislocations that is one-dimensional in nature can bring along changes to two-dimensional features on a surface. A theory of the zig-zag shape boundary was proposed by previous groups but they did not give physical reasons to explain the theory. However, we have found their theory to be non-comprehensive and cannot be true for all situations. In view of this, we have suggested another hypothesis to explain the zig-zag boundary shape, and simulation results were provided to support our theory.

Although graphite superlattices have been observed with STM many times, there are still plenty of research opportunities, both theoretically and experimentally, to broaden our

knowledge on this phenomenon. Graphite superlattices potentially have some important applications including acting as a template for absorbing particles and measuring surface deformation and defects in the nanometre range.

After the studies on graphite superlattices, we demonstrated that solvent deposition, microcontact printing (μCP), and thermal evaporation are feasible ways to deposit free radical organic molecules, which provide spin signals with their unpaired electrons for realization of single electron spin detection with STM. Each method has its advantages and disadvantages, and depending on the physical properties of the organic molecules such as melting point and solubility, either means can be used for deposition which is an important step for sample preparation. The highly-ordered triangular structures formed on graphite surfaces remind us of the importance of using highly-pure solvent for the deposition of organic molecules with low concentration. Due to the timescale of this PhD, we could not complete the single electron spin detection experiments. Future work will involve, firstly, accomplishing the single electron spin detection experiments on BDPA molecules, then repeating with TEMPO molecules. The ultimate goal will be to perform chemical analysis by spin detection with STM.

Our experimental result shows microcontact printing can transfer the free radical organic molecules BDPA onto the substrate with patterns, and this provides a possible route towards the experiment of chemical analysis by spin detection with the STM. This experiment is a novel idea, and its aim is to develop a technique which can carry out chemical analysis on a single molecule by using the STM to detect its spin signal.

The proposed experimental procedure is shown in Fig. 5.1(a). We will use Au(111) as the substrate. BDPA free radicals are printed with a pattern of an array of circles with a diameter of 500 nm by microcontact printing. TEMPO free radicals (2,2,6,6-tetramethyl-1-piperidinyloxy) are then printed with another stamp with a pattern of an array of triangles with a size of 500 nm across. These two arrays are printed in such a way that they align with each other without overlapping. Since they are of different shapes, we can recognize their identities under the STM. Triangular and square patterns on the stamps can be made by e-beam lithography. According to the previous work, we know that the tunnelling current spectrum when the tip is tunnelling through BDPA is different from that of TEMPO. The spectrum of BDPA only has one peak (Fig. 5.1(b), image from [146]) whereas the spectrum of TEMPO has three peaks due to hyperfine splitting (Fig. 5.1(c), image from [147]). Therefore from their tunnelling current spectra we will be able to identify these chemical species. The difficulty of this experiment lies mainly in the alignment of the two sets of

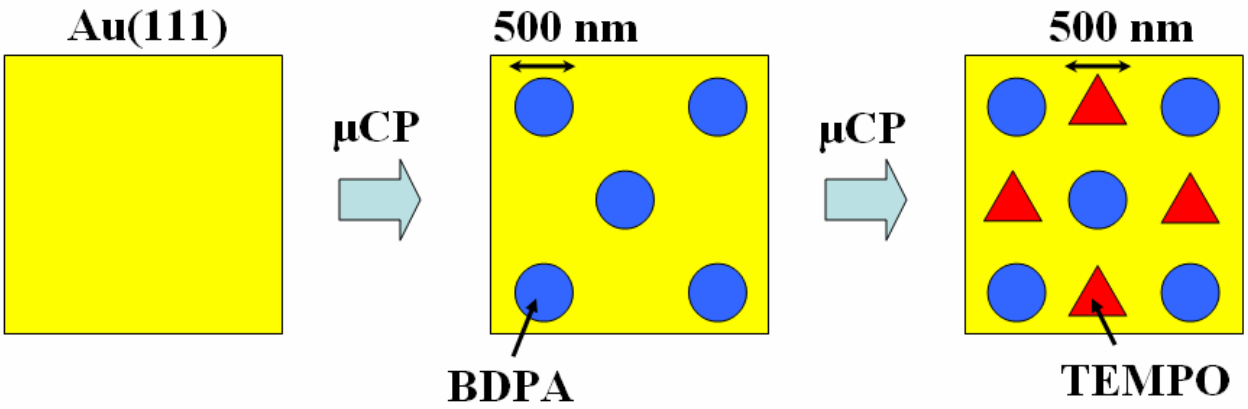

Fig. 5.1(a). The proposed experimental procedure for chemical analysis by spin detection with the STM. Au(111) is used as the substrate. The BDPA molecules are microcontact printed with an array of square patterns. Then the TEMPO molecules are printed with another stamp in the form of an array of triangles aligning with the arrays of BDPA.

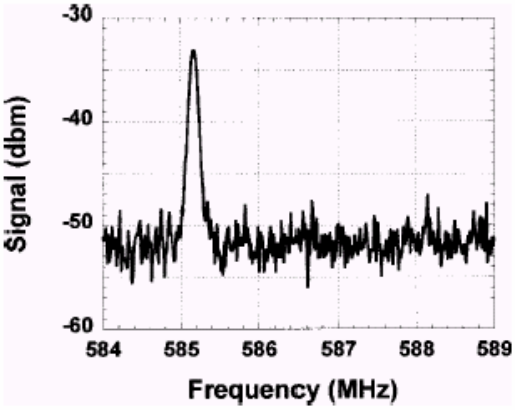

Fig. 5.1(b). The spectrum of the tunnelling current when the STM tip is tunnelling through BDPA molecules.

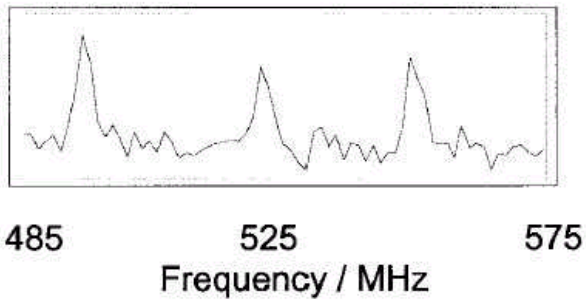

Fig. 5.1(c). The spectrum of the tunnelling current when the STM tip is tunnelling through TEMPO molecules.

arrays of molecules. It can be imagined that it will take many attempts to have two separate sets of patterns aligned with each other without overlapping. This problem may be solved by using a different periodicity pattern for printing each kind of molecule. This experiment is not limited to BDPA and TEMPO, it is applicable to other free radical organic molecules as well, provided their tunnelling current spectra are different. We can also extend this experiment to include more than two free radical species. The sizes of the patterns can be varied within the limit of e-beam lithography or photolithography which we use to make the master. The combination of single electron spin detection with the STM and microcontact printing provides a possibility to realize the technique of chemical analysis with resolution down to single molecular level.

Finally, we have worked towards deposition of iron onto silicon for future SPSTM and single electron spin detection experiments. The deposition of iron onto silicon was performed by reactive deposition epitaxy at 873 K (RDE) and solid phase epitaxy without heating (SPE). The RDE deposition of 0.5 ML and 0.25 ML resulted in the formation of iron silicide islands of triangular shape on the silicon surfaces which are suitable for imminent single electron spin detection experiments. I/V spectroscopy measurements were attempted on such systems; however, the instability of the mechanically cut Pt/Ir tips failed to reproduce the spectroscopy measurements which made it difficult to obtain any conclusive results. Therefore chemically etched tungsten tips are recommended for future characterization experiments for their structural stability, and tip cleaning procedures are necessary. Although the resulting triangular iron silicide domains on silicon by RDE were later found to lose their ferromagnetism and thus were not suitable for realizing SPSTM experiments, the experimental results are useful for fabricating silicon-based optoelectronic devices. We have deposited 0.3 ML of iron onto the silicon substrate by SPE without heating; however, the resulting surface was very rough and granular. It was difficult to distinguish the deposited iron from the silicon surface. In order to realize SPSTM experiments on iron on silicon, a more appropriate deposition method is needed to make the binary system more distinct and easier to discern, otherwise, it would be difficult to attribute properly the contrast in the spin-polarized spectroscopic image to the corresponding magnetic species. As such, the future work on this respect is to find out a better means to deposit iron onto silicon to form obvious well-ordered structures such as islands or domains with certain kinds of shapes for distinction without losing ferromagnetism. An alternative binary magnetic system, such as iron on tungsten, may also be an appropriate sample.

Appendix A

Simulation programs for chapter 2

A MATLAB simulation program was created to simulate the single-stage vibration isolation system. The details of the simulation results are described in section 2.2.2.2. This Appendix is a brief overview of the simulation program with the codes provided.

This Appendix contains one MATLAB m-file which is named *"vibration2"*.

Program codes

A. Single-stage vibration isolation system simulation program

MATLAB m-file: vibration2

```
%%%%%%%%%%%% Simulation: Single-stage vibration isolation system of STM


%%%%%%%%% A. Optimisation via adjusting system parameters

%%%% 1. The influence of mass on system performance

%% 1.1 mass m = 1kg

k=100;          %spring stiffness
m=1;            %STM stage mass
b=10;           %damping coefficient
y=b/(2*m);
wo=sqrt(k/m);    %natural angular frequency

counter=0;
amp=[];
while counter<=(wo*10)
   w=counter;
   temp=((sqrt(4*y*y*(w^6)+((wo^2)-(wo^2)*(w^2)+4*y*y*(w^2))^2))/((((wo^2)-
(w^2))^2+4*y*y*(w^2))));
   amp=[amp; temp];
   counter=counter+1;
end
w=0:(wo*10);
amp;
axes('fontsize',14,'linewidth',3,'fontweight','bold')
plot(w/wo, amp, 'c-','linewidth',3);
xlabel('w/wo')
ylabel('Amplitude ratio')
hold

%% 1.2 mass m = 2kg

k=100;          %spring stiffness
m=2;            %STM stage mass
b=10;           %damping coefficient
y=b/(2*m);
wo=sqrt(k/m);    %natural angular frequency

counter=0;
amp=[];
while counter<=(wo*10)
   w=counter;
```

```
   temp=((sqrt(4*y*y*(w^6)+((wo^2)-(wo^2)*(w^2)+4*y*y*(w^2))^2))/((((wo^2)-
(w^2))^2+4*y*y*(w^2))));
   amp=[amp; temp];
   counter=counter+1;
end
w=0:(wo*10);
amp;
plot(w/wo, amp, 'g-','linewidth',3);

%% 1.3 mass m = 3kg

k=100;          %spring stiffness
m=3;            %STM stage mass
b=10;           %damping coefficient
y=b/(2*m);
wo=sqrt(k/m);    %natural angular frequency

counter=0;
amp=[];
while counter<=(wo*10)
   w=counter;
   temp=((sqrt(4*y*y*(w^6)+((wo^2)-(wo^2)*(w^2)+4*y*y*(w^2))^2))/((((wo^2)-
(w^2))^2+4*y*y*(w^2))));
   amp=[amp; temp];
   counter=counter+1;
end
w=0:(wo*10);
amp;
plot(w/wo, amp, 'r-','linewidth',3);

%% 1.4 mass m = 4kg

k=100;          %spring stiffness
m=4;            %STM stage mass
b=10;           %damping coefficient
y=b/(2*m);
wo=sqrt(k/m);    %natural angular frequency

counter=0;
amp=[];
while counter<=(wo*10)
   w=counter;
   temp=((sqrt(4*y*y*(w^6)+((wo^2)-(wo^2)*(w^2)+4*y*y*(w^2))^2))/((((wo^2)-
(w^2))^2+4*y*y*(w^2))));
   amp=[amp; temp];
   counter=counter+1;
end
w=0:(wo*10);
amp;
plot(w/wo, amp, 'k-','linewidth',3);
legend('mass 1kg', 'mass 2kg', 'mass 3kg', 'mass 4kg');
```

```
figure


%%%% 2. The influence of spring constant on system performance

%% 2.1 spring constant k = 200Nm(^-1)

k=200;          %spring stiffness
m=1;            %STM stage mass
b=10;           %damping coefficient
y=b/(2*m);
wo=sqrt(k/m);    %natural angular frequency

counter=0;
amp=[];
while counter<=(wo*10)
   w=counter;
   temp=((sqrt(4*y*y*(w^6)+((wo^2)-(wo^2)*(w^2)+4*y*y*(w^2))^2))/((((wo^2)-
(w^2))^2+4*y*y*(w^2))));
   amp=[amp; temp];
   counter=counter+1;
end
w=0:(wo*10);
amp;
axes('fontsize',14,'linewidth',3,'fontweight','bold')
plot(w/wo, amp, 'c-','linewidth',3);
xlabel('w/wo')
ylabel('Amplitude ratio')
hold

%% 2.2 spring constant k = 300Nm(^-1)

k=300;          %spring stiffness
m=1;            %STM stage mass
b=10;           %damping coefficient
y=b/(2*m);
wo=sqrt(k/m);    %natural angular frequency

counter=0;
amp=[];
while counter<=(wo*10)
   w=counter;
   temp=((sqrt(4*y*y*(w^6)+((wo^2)-(wo^2)*(w^2)+4*y*y*(w^2))^2))/((((wo^2)-
(w^2))^2+4*y*y*(w^2))));
   amp=[amp; temp];
   counter=counter+1;
end
w=0:(wo*10);
amp;
plot(w/wo, amp, 'g-','linewidth',3);
```

```
%% 2.3 spring constant k = 400Nm(^-1)

k=400;          %spring stiffness
m=1;            %STM stage mass
b=10;           %damping coefficient
y=b/(2*m);
wo=sqrt(k/m);    %natural angular frequency

counter=0;
amp=[];
while counter<=(wo*10)
   w=counter;
   temp=((sqrt(4*y*y*(w^6)+((wo^2)-(wo^2)*(w^2)+4*y*y*(w^2))^2))/((((wo^2)-
(w^2))^2+4*y*y*(w^2))));
   amp=[amp; temp];
   counter=counter+1;
end
w=0:(wo*10);
amp;
plot(w/wo, amp, 'r-','linewidth',3);

%% 2.4 spring constant k = 500Nm(^-1)

k=500;          %spring stiffness
m=1;            %STM stage mass
b=10;           %damping coefficient
y=b/(2*m);
wo=sqrt(k/m);     %natural angular frequency

counter=0;
amp=[];
while counter<=(wo*10)
   w=counter;
   temp=((sqrt(4*y*y*(w^6)+((wo^2)-(wo^2)*(w^2)+4*y*y*(w^2))^2))/((((wo^2)-
(w^2))^2+4*y*y*(w^2))));
   amp=[amp; temp];
   counter=counter+1;
end
w=0:(wo*10);
amp;
plot(w/wo, amp, 'k-','linewidth',3);
legend('spring constant k = 200Nm^-1', 'spring constant k = 300Nm^-1', 'spring constant k =
400Nm^-1', 'spring constant k = 500Nm^-1');
figure


%%%% 3. The influence of damping on system performance

%% 3.1 damping coefficient b = 0kgs^(-1)

k=100;          %spring stiffness
```

```
m=1;            %STM stage mass
b=0;            %damping coefficient
y=b/(2*m);
wo=sqrt(k/m);    %natural angular frequency

counter=0;
amp=[];
while counter<=(wo*10)
   w=counter;
   temp=((sqrt(4*y*y*(w^6)+((wo^2)-(wo^2)*(w^2)+4*y*y*(w^2))^2))/((((wo^2)-
(w^2))^2+4*y*y*(w^2))));
   amp=[amp; temp];
   counter=counter+1;
end
w=0:(wo*10);
amp;
axes('fontsize',14,'linewidth',3,'fontweight','bold')
plot(w/wo, amp, 'c-','linewidth',3);
xlabel('w/wo')
ylabel('Amplitude ratio')
hold

%% 3.2 damping coefficient b = 4kgs^(-1)

k=100;          %spring stiffness
m=1;            %STM stage mass
b=4;            %damping coefficient
y=b/(2*m);
wo=sqrt(k/m);    %natural angular frequency

counter=0;
amp=[];
while counter<=(wo*10)
   w=counter;
   temp=((sqrt(4*y*y*(w^6)+((wo^2)-(wo^2)*(w^2)+4*y*y*(w^2))^2))/((((wo^2)-
(w^2))^2+4*y*y*(w^2))));
   amp=[amp; temp];
   counter=counter+1;
end
w=0:(wo*10);
amp;
plot(w/wo, amp, 'g-','linewidth',3);

%% 3.3 damping coefficient b = 20kgs^(-1)

k=100;          %spring stiffness
m=1;            %STM stage mass
b=20;           %damping coefficient
y=b/(2*m);
wo=sqrt(k/m);    %natural angular frequency
```

```
counter=0;
amp=[];
while counter<=(wo*10)
   w=counter;
   temp=((sqrt(4*y*y*(w^6)+((wo^2)-(wo^2)*(w^2)+4*y*y*(w^2))^2))/((((wo^2)-
(w^2))^2+4*y*y*(w^2))));
   amp=[amp; temp];
   counter=counter+1;
end
w=0:(wo*10);
amp;
plot(w/wo, amp, 'r-','linewidth',3);

%% 3.4 damping coefficient b = 40kgs^(-1)

k=100;          %spring stiffness
m=1;            %STM stage mass
b=40;           %damping coefficient
y=b/(2*m);
wo=sqrt(k/m);     %natural frequency

counter=0;
amp=[];
while counter<=(wo*10)
   w=counter;
   temp=((sqrt(4*y*y*(w^6)+((wo^2)-(wo^2)*(w^2)+4*y*y*(w^2))^2))/((((wo^2)-
(w^2))^2+4*y*y*(w^2))));
   amp=[amp; temp];
   counter=counter+1;
end
w=0:(wo*10);
amp;
plot(w/wo, amp, 'k-','linewidth',3);
legend('damping coefficient b = 0kgs^-1', 'damping coefficient b = 4kgs^-1', 'damping
coefficient b = 20kgs^-1', 'damping coefficient b = 40kgs^-1');
figure



%%%%%%%% B. Vibration response of the System
%%%% The parameters used in this section are roughly estimated from our STM system

%% 1. Frequency response of the system
k=200;          %spring stiffness
m=0.8;          %STM stage mass
b=8;           %damping coefficient
y=b/(2*m);
wo=sqrt(k/m)     %natural angular frequency

counter=0;
amp=[];
```

```
while counter<=(wo*10)
   w=counter;
   temp=((sqrt(4*y*y*(w^6)+((wo^2)-(wo^2)*(w^2)+4*y*y*(w^2))^2))/((((wo^2)-
(w^2))^2+4*y*y*(w^2))));
   amp=[amp; temp];
   counter=counter+1;
end
w=0:(wo*10);
amp;
axes('fontsize',14,'linewidth',3,'fontweight','bold')
plot(w/wo, amp, 'b-','linewidth',3);
xlabel('w/wo')
ylabel('Amplitude ratio')
figure

%% 2. Time response of the system
k=200;          %spring stiffness
m=0.8;          %STM stage mass
b=8;           %damping coefficient
y=b/(2*m);
wo=sqrt(k/m)     %natural frequency

w_dash=(k/m-(b*b)/(4*m*m))^(1/2);
displ=[];
t=0;
while t<=100
   time=t/25;
   displ=[displ; exp((-b*time)/(2*m))*sin(w_dash*time)];
   t=t+1;
end
t=0:0.04:4;
axes('fontsize',14,'linewidth',3,'fontweight','bold')
plot(t, displ, 'b-','linewidth',3);
xlabel('time (second)')
ylabel('Displacement (x(t)/x(0))')
```

Appendix B

Design drawings for chapter 2

This appendix contains the detailed design drawings with dimensions for some components of the STM system discussed in chapter 2. Section B.1 consists of the design drawings for the inner and outer stages and the magnetic damping system, which show the positions and orientations of the copper plates and the magnets on the inner stages and the outer ring respectively. Additionally, the designs of the magnet mountings and the copper plates are displayed. In section B.2, the designs for the outer stage with the supporting rods are shown, and the internal structure design of the supporting rods is illustrated. The structures and dimensions of the scanning head are included in section B.3.

B.1 Design drawings for the inner and outer stages, and magnetic damping

Design 1.1 - The positions and orientations of the "U" shaped copper plates on the inner stage for the magnetic damping. The inner stage is a circular disc made of aluminium. M3 tapped holes are the locations where the copper plates are screwed onto the inner stage. The hooks on the inner stage are for suspending the springs from the outer stage.

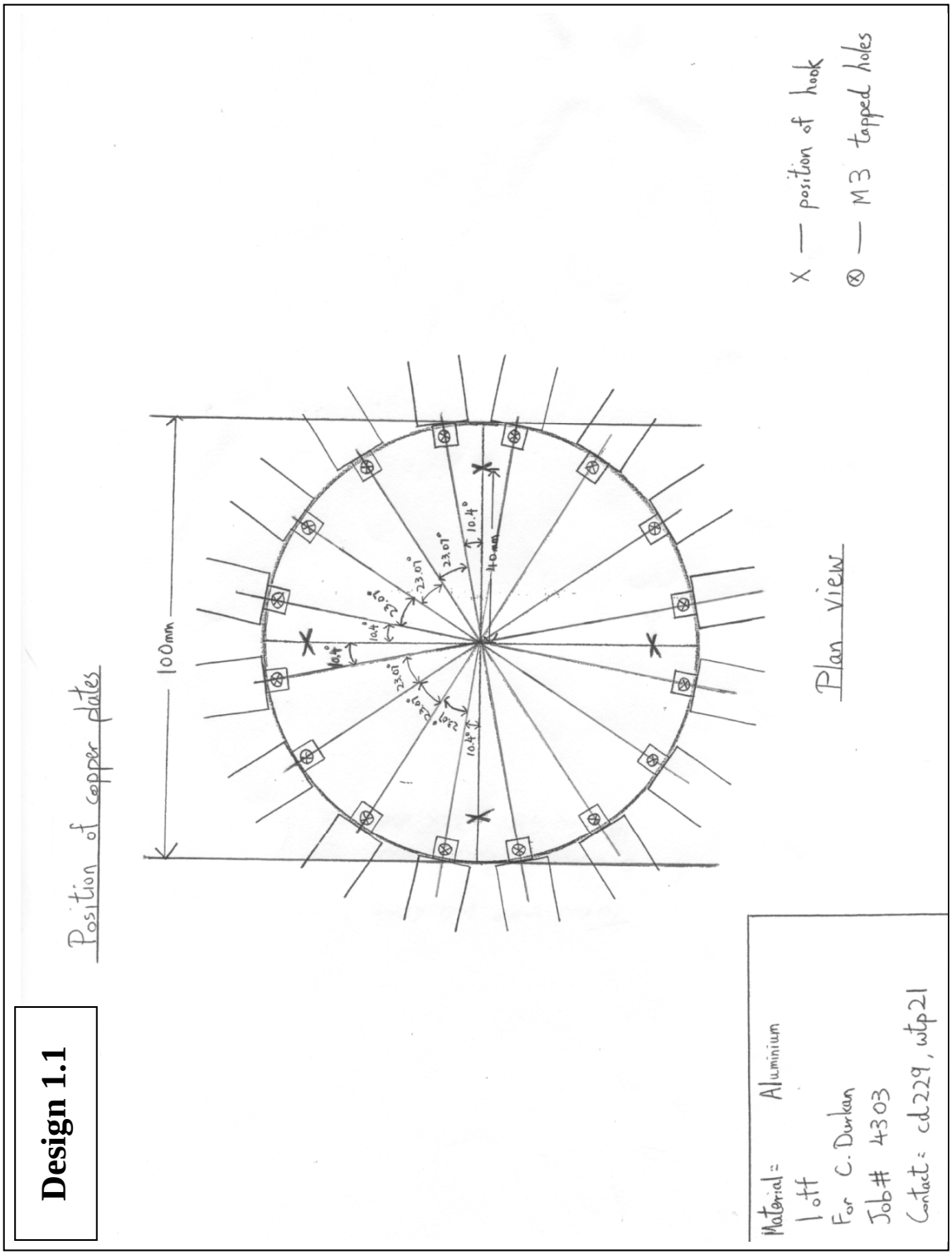

Design 1.2 - The positions (M3 clearance holes) and orientations of the magnets on the outer stage relative to the copper plates (M3 tapped holes) on the inner stage for the magnetic damping. The outer stage is a circular ring made of aluminium, on which the M4 clearance holes are for the stainless steel supporting rods. The design drawings for the outer stage and the supporting rods are shown in section B.2.

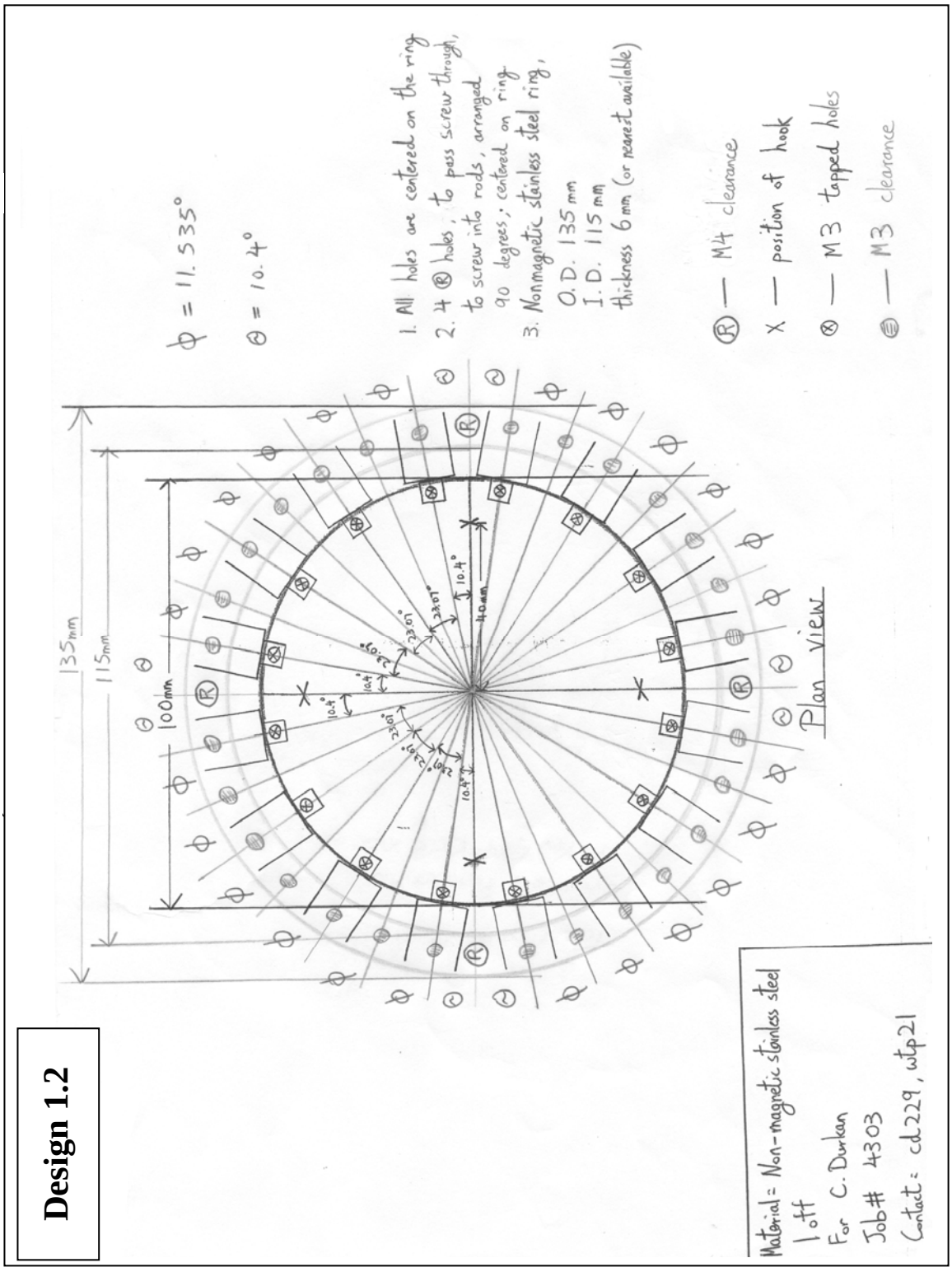

Design 1.3 –3D schematic view of the inner stage with the copper plates and the hooks.

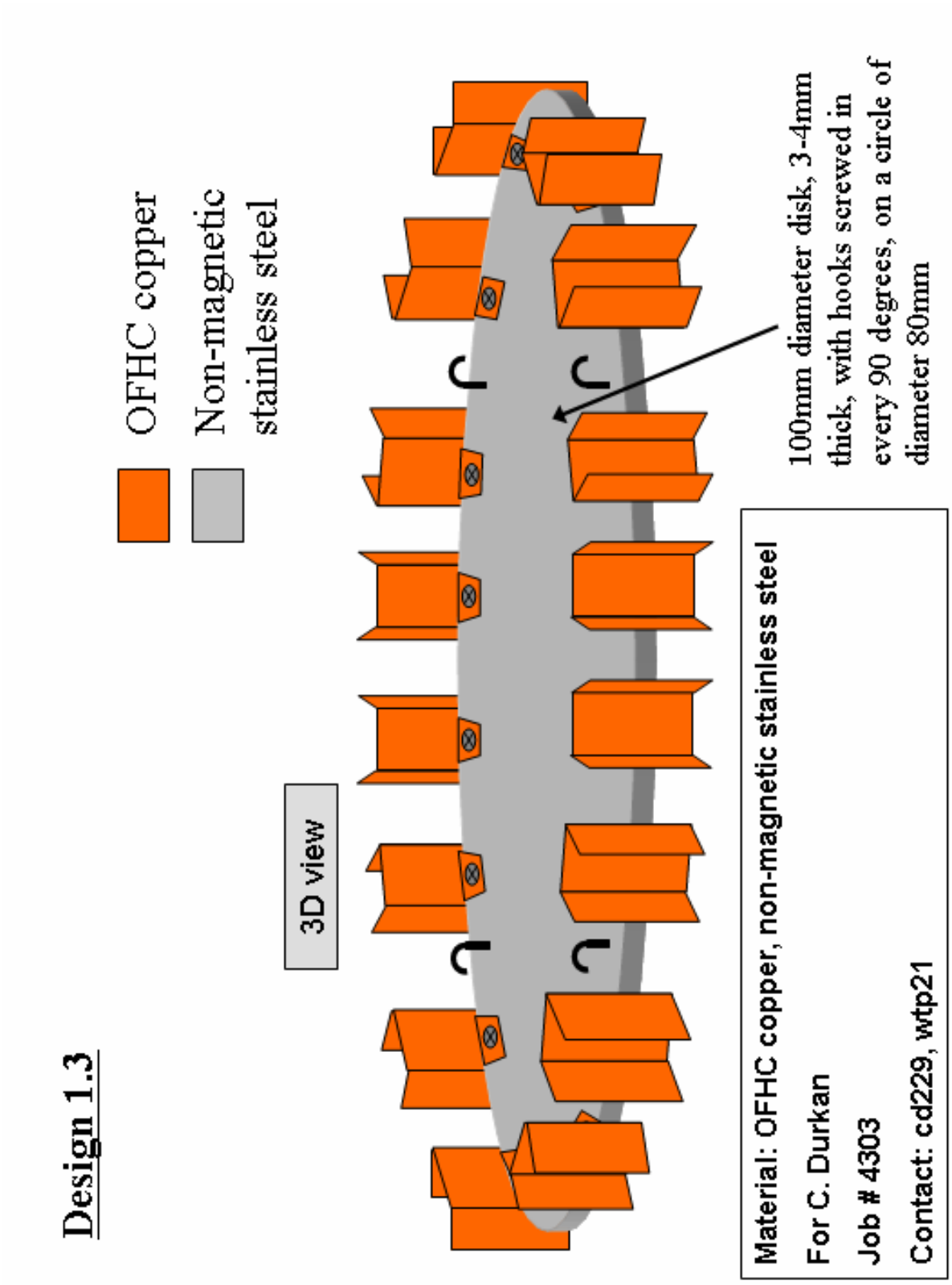

Design 1.4 – The plan view of the inner stage with the copper plates. The positions of the hooks and the scanning head are indicated.

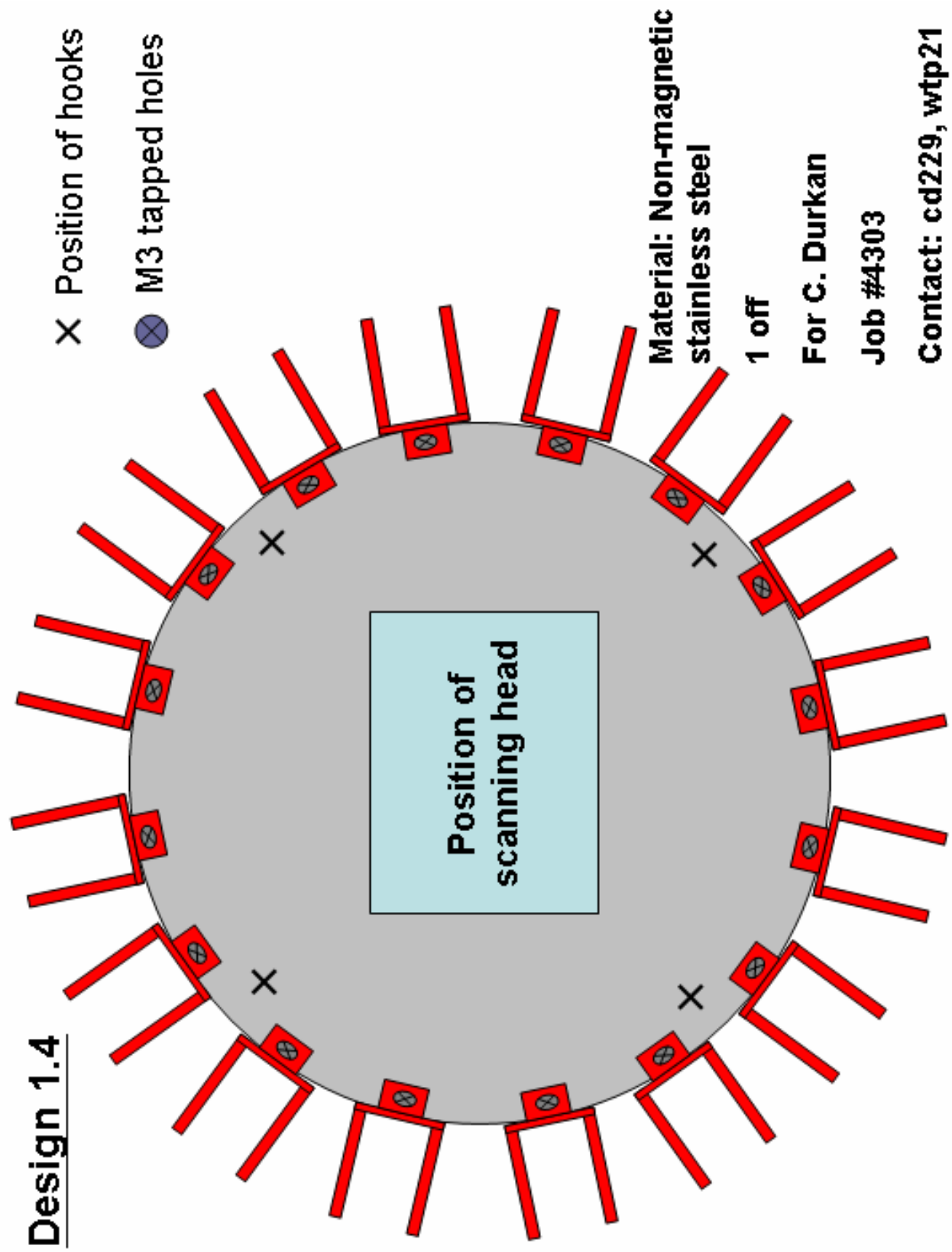

Design 1.5 – The design drawing of the magnet mountings. These mountings have to be able to hold the magnets in place tightly, otherwise the magnetic forces between the magnets will give rise to strong interaction and move the magnets out of place.

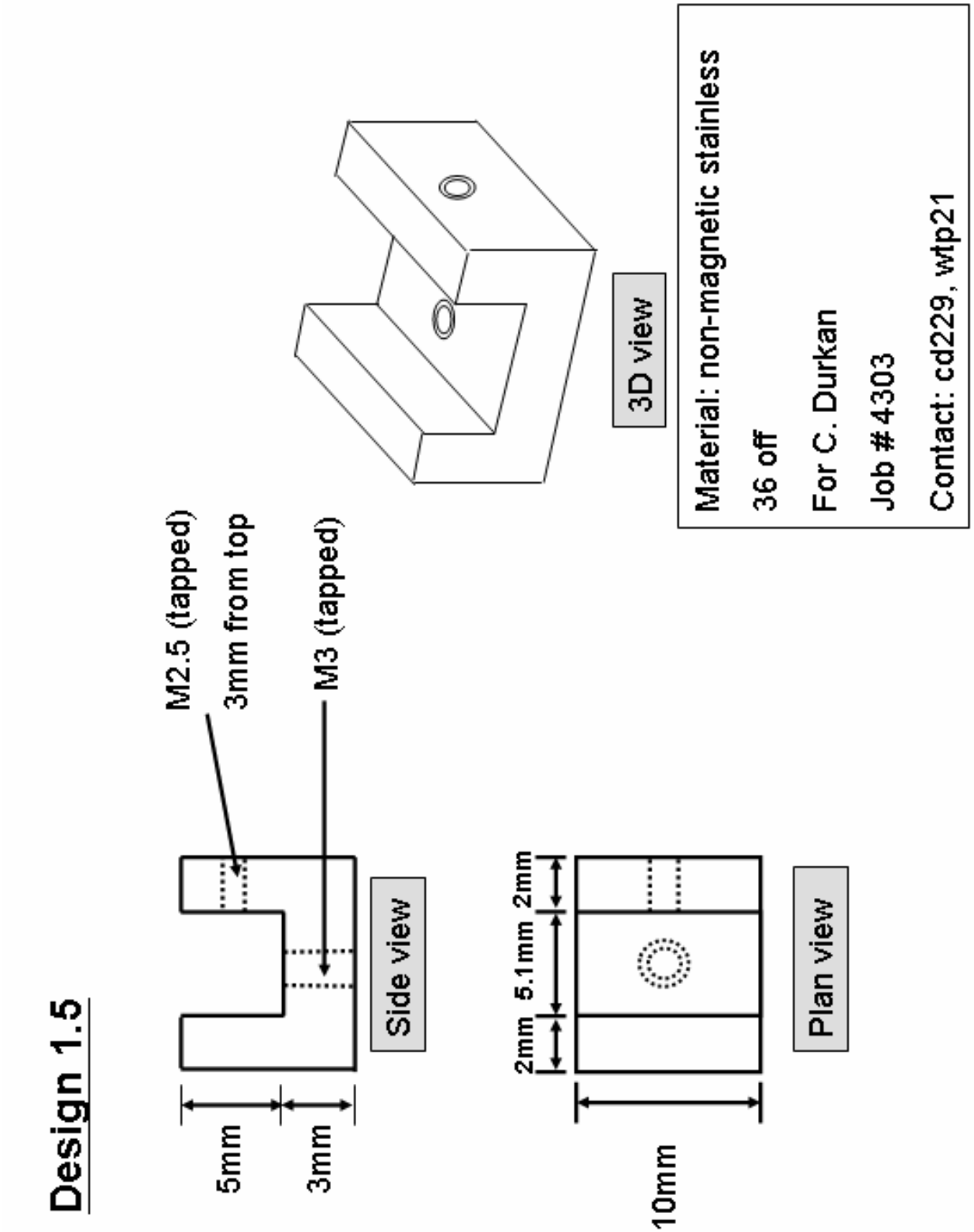

Design 1.6 – The design drawing of the "U" shaped copper plates for the magnetic damping.

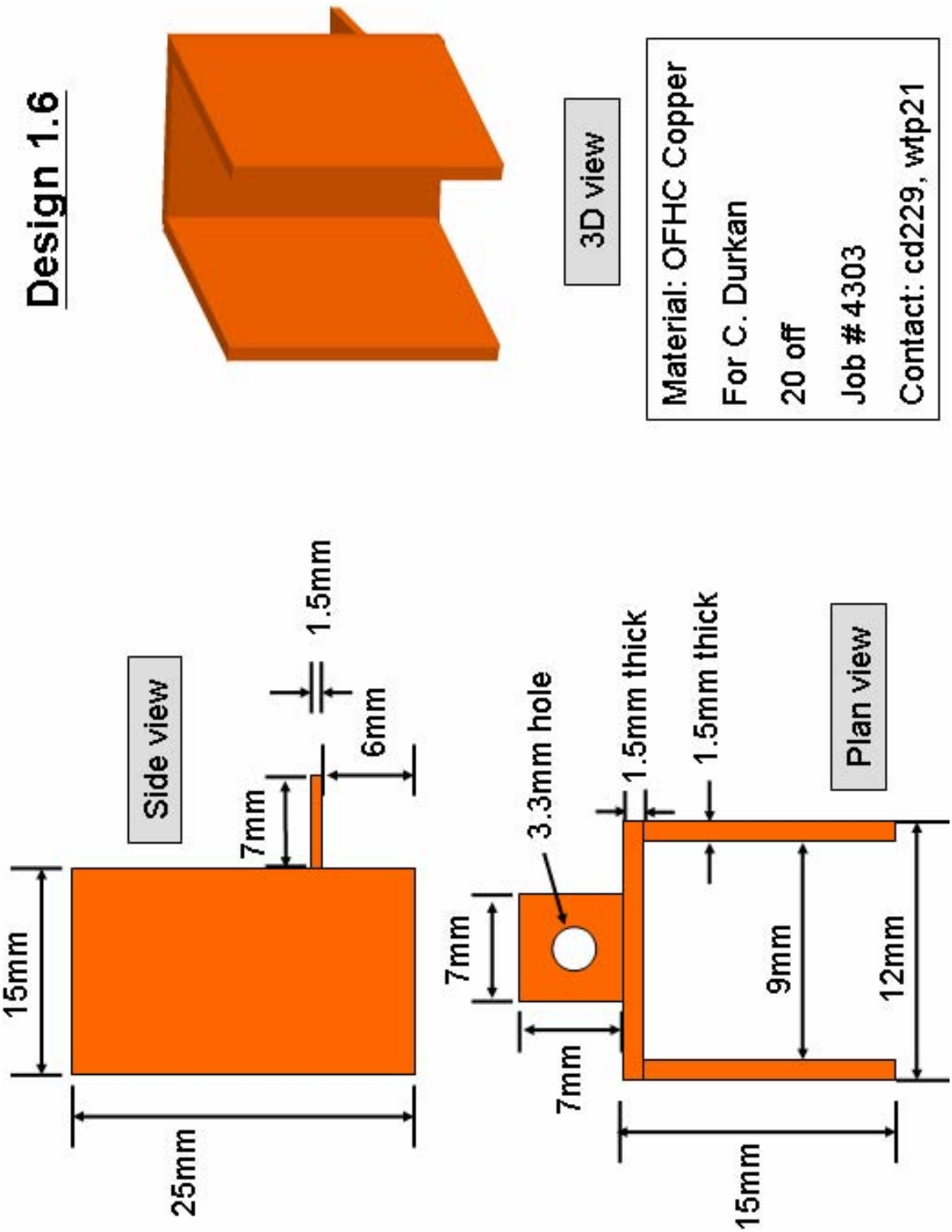

B.2 Design drawings for the outer stage and the supporting rods

Design 2.1 – The design drawing of the outer stage with the supporting rods.

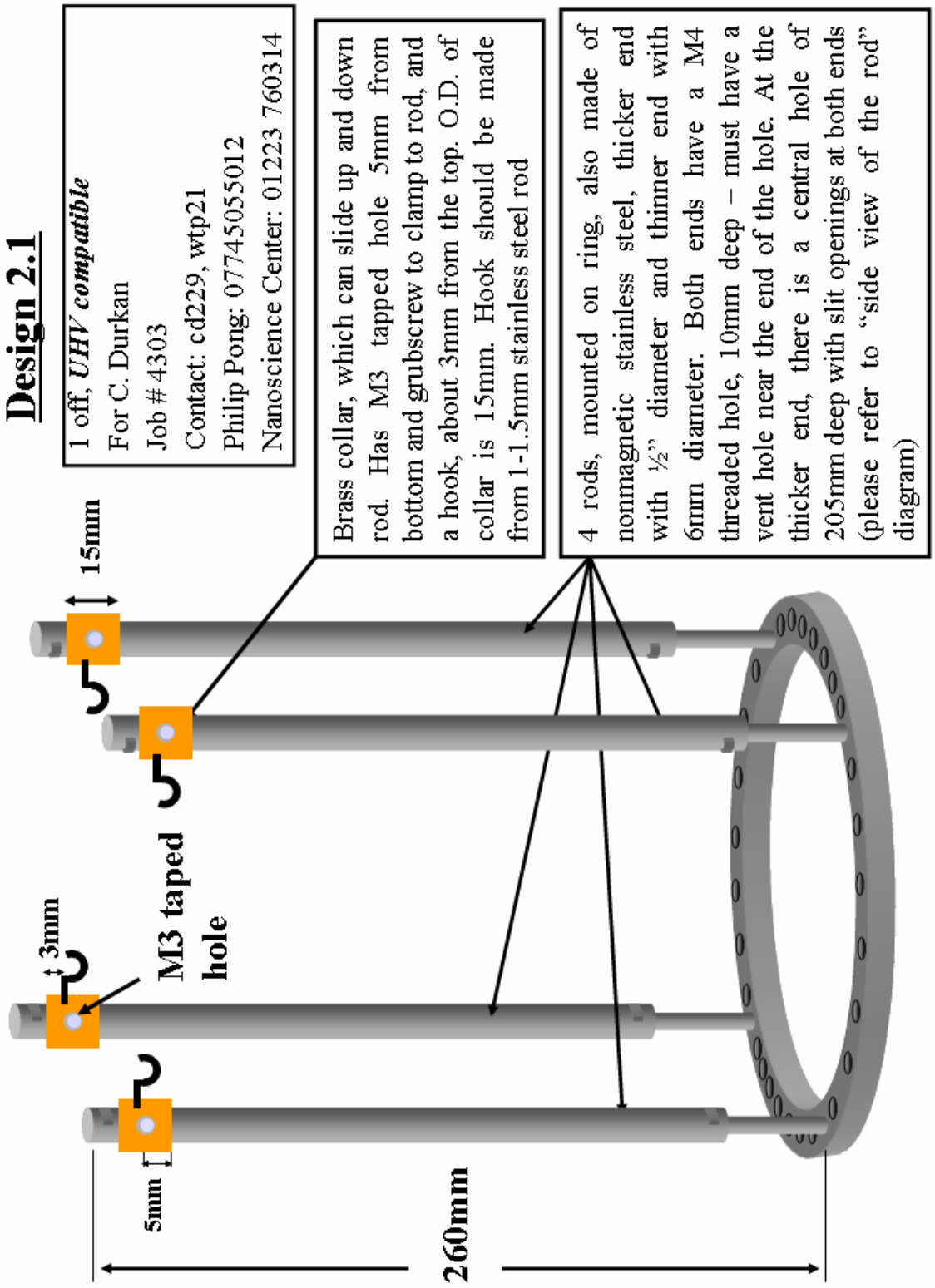

Design 2.2a – The internal structure of the supporting rods of the inner stage. The supporting rods are hollow to allow passage of connecting wires to the scanning head and thus provide electrical and mechanical protection.

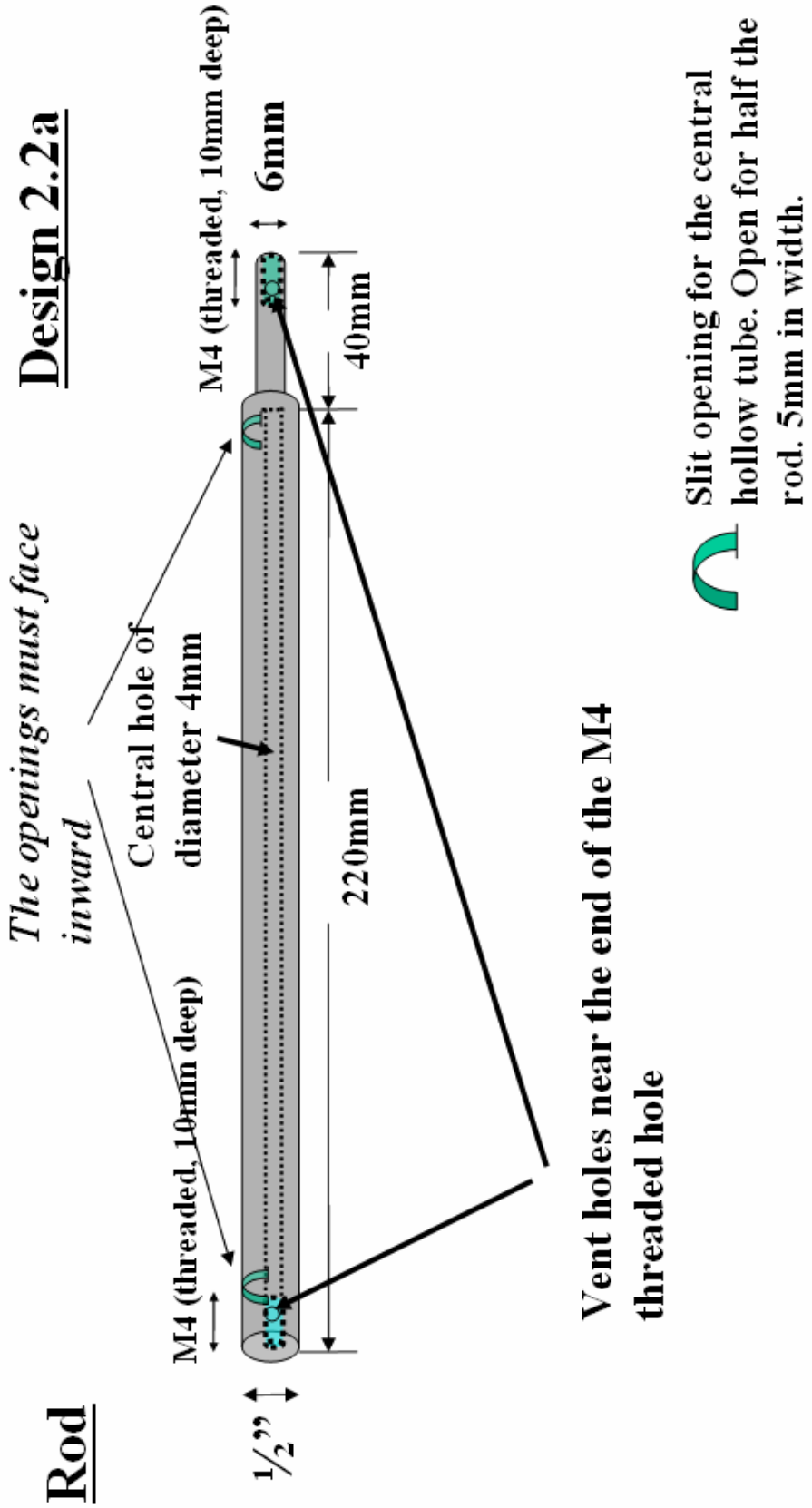

Design 2.2b – The internal structure of the supporting rods (side view).

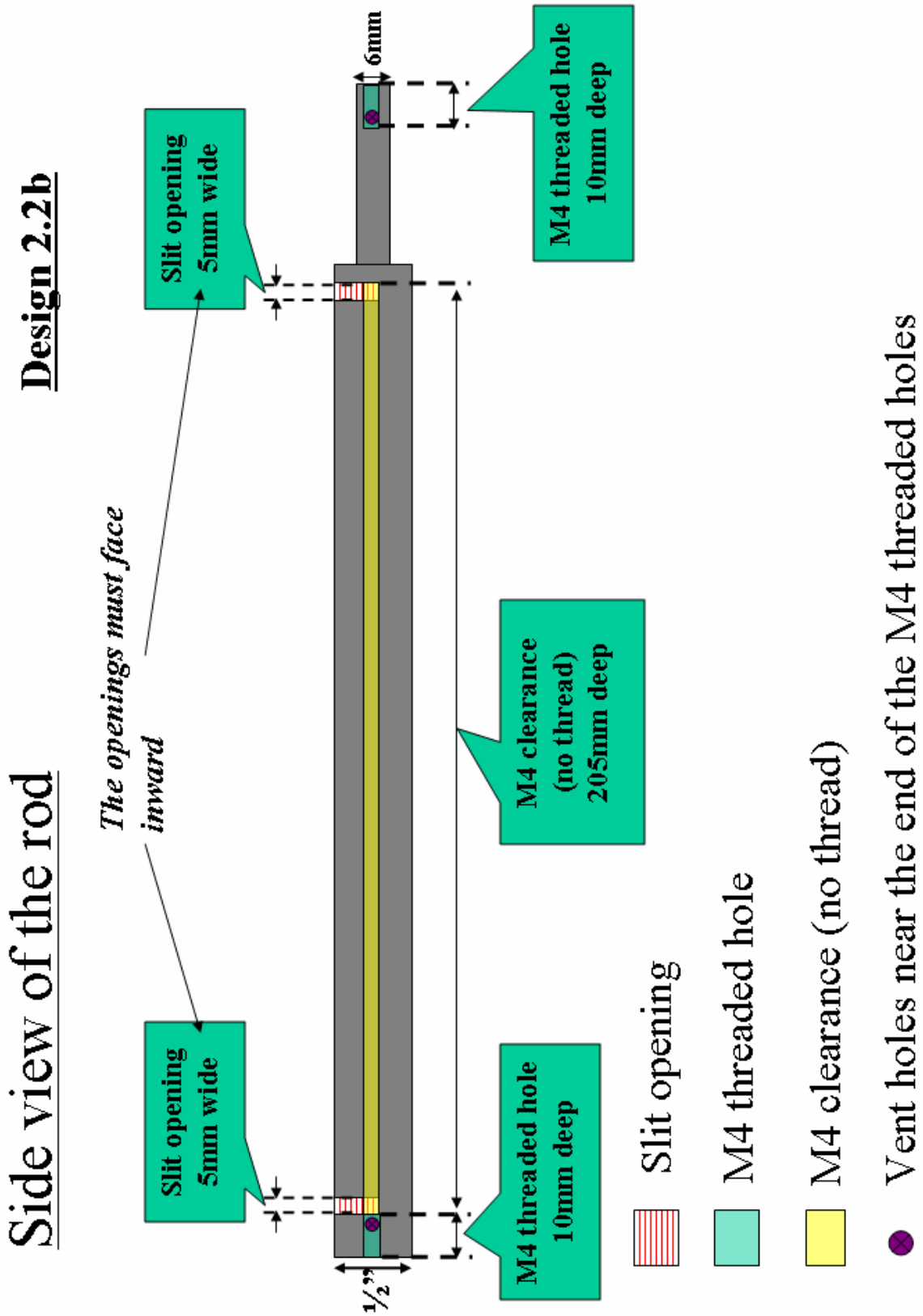

Design 2.3 – The design drawing for the brass collars with the extension arms

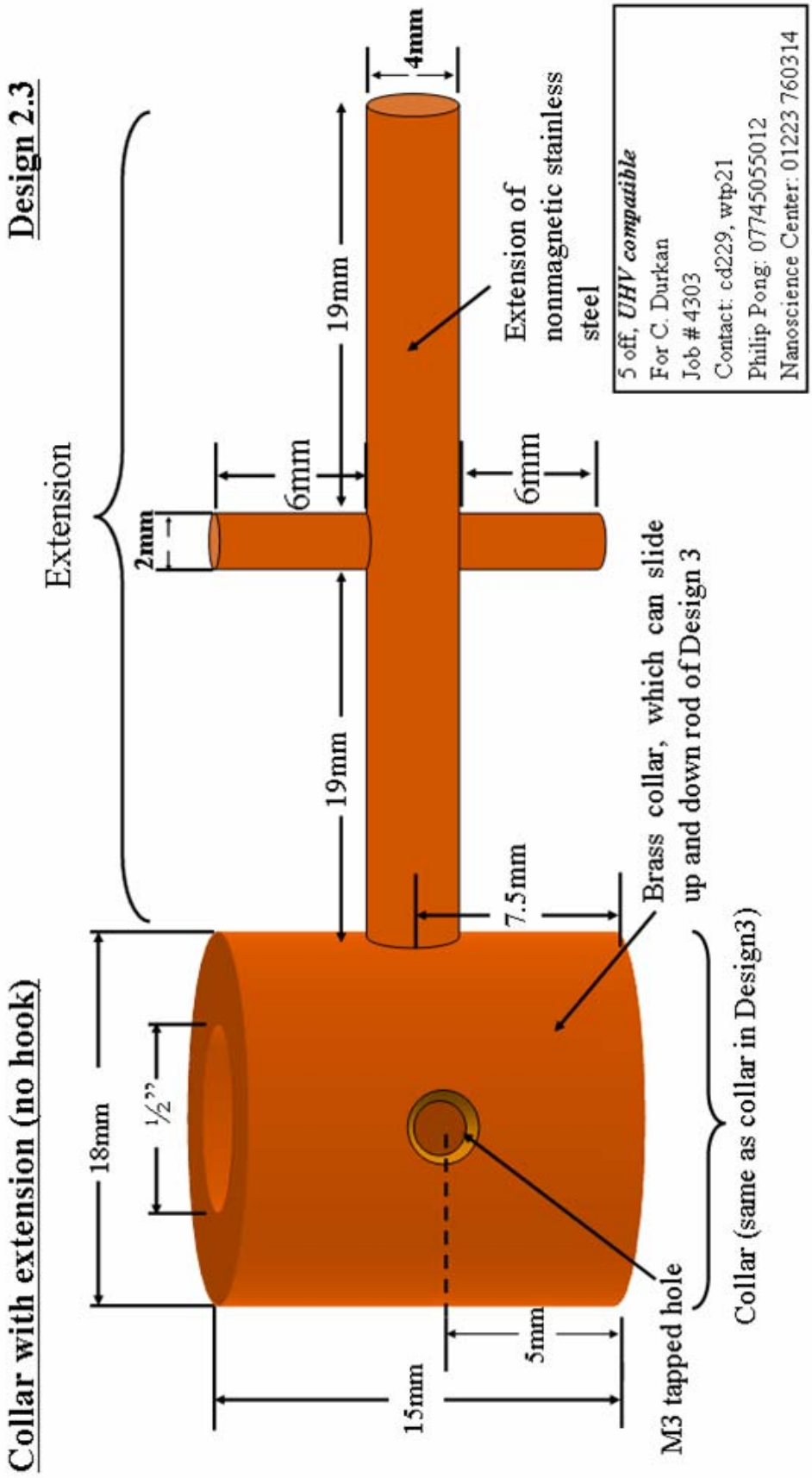

B.3 Design drawings for the scanning head

Design 3.1a – The design drawing for the scanning head. Piece 2 is the walker carrying a magnet and a sample, while piece 1 is the stage on which the walker moves.

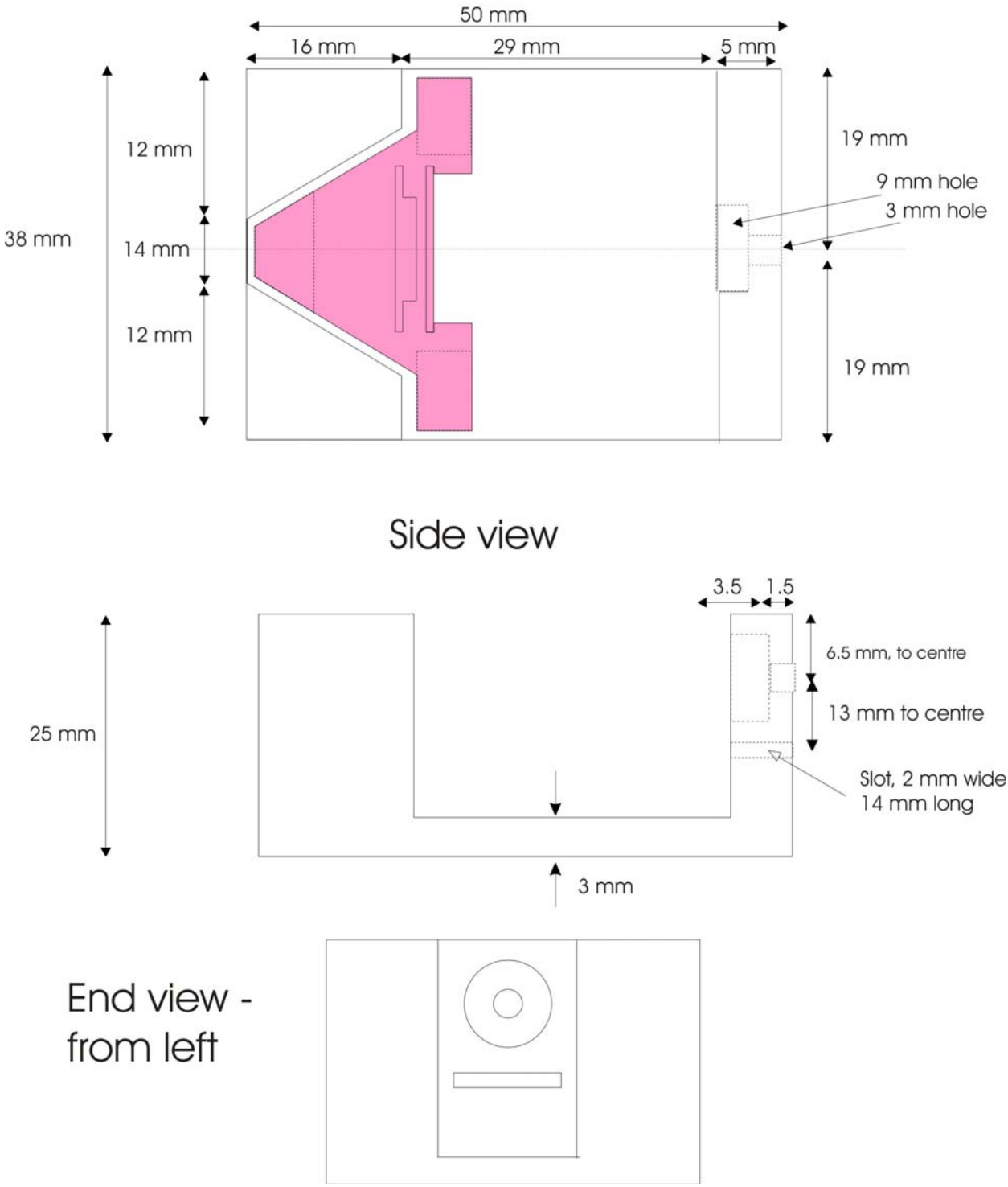

Overall Schematic – Top view. White = piece 1, lilac = piece 2

Design 3.1b – The design drawing for the walker (piece 2) of the scanning head

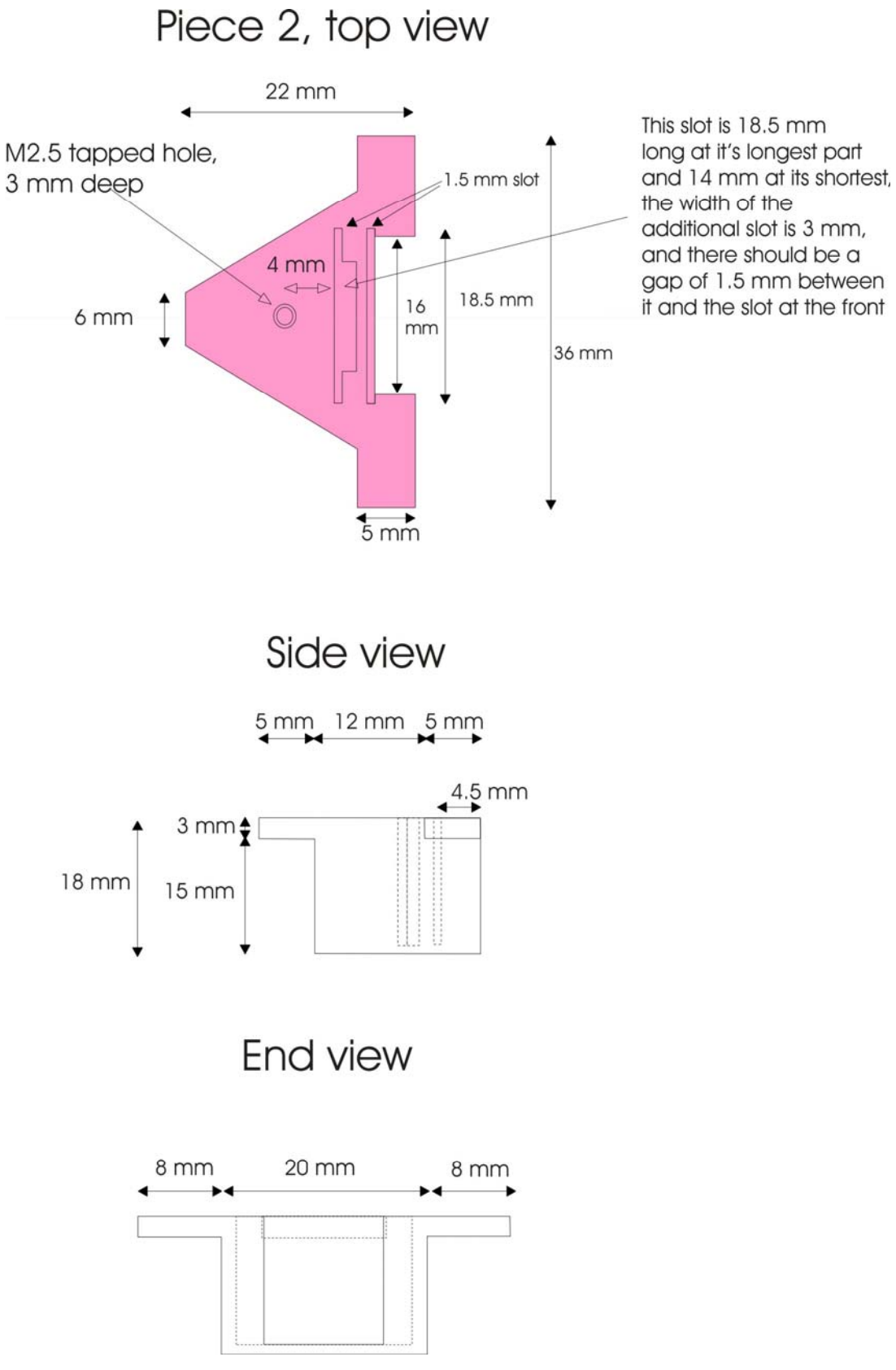

Appendix C

Simulation programs for chapter 3

Simulation programs were written in MATLAB for the modelling of the electronic density of states of graphite and the investigation of superlattices. A MATLAB simulation program is written for each application in chapter 3.3. The details of the simulation results are described in the chapter.

The program files are named and arranged as follows: 1. "*superlattice3*" for section 3.3.3.1 – modelling of superlattice structure; 2. "*rippling*" for section 3.3.3.2 – rippling fringes on superlattice; 3. "*Cee*" for section 3.3.3.3 – study on the unusual aspect of superlattice proposed by Cee *et al.*; 4. "*oddeven3*" for section 3.3.3.4 – "odd-even" transition along atomic rows; 5. *"coexist_sup"* for section 3.3.3.5 – coexisting superlattices; 6. *"screw"* for section 3.3.3.6 – superlattice with screw dislocation.

Program codes

C.1 Modelling of superlattice structure – for section 3.3.3.1

MATLAB m-file: superlattice3

```
%%%%%%%%%%% Simulation – Modelling of superlattice structure

image_size=130;     %% specify size of image to simulate
pixel=500;          %% specify the number of data points for the simulated image

%% input the rotation angle for each graphite layer

rotation1=8*(pi/180);
rotation2=0*(pi/180);
rotation3=0*(pi/180);

layer1=[];
layer2=[];
layer3=[];

x_axis=image_size/pixel:image_size/pixel:image_size;
y_axis=x_axis;

%% Simulate the first (topmost) layer

for x=1:1:pixel
   x
   for y=1:1:pixel

        x1_pos=(x*(image_size/pixel))*(cos(rotation1))-
(y*(image_size/pixel))*(sin(rotation1));

y1_pos=(x*(image_size/pixel))*(sin(rotation1))+(y*(image_size/pixel))*(cos(rotation1));
        layer1(x,y)=1-
(2/9)*(cos((2*pi/2.46)*(x1_pos+y1_pos/sqrt(3)))+cos((2*pi/2.46)*(x1_pos-
y1_pos/sqrt(3)))+cos((4*pi/2.46)*(y1_pos/sqrt(3)))+3/2);
   end
end
pack

%% Simulate the second layer

for x=1:1:pixel
   x
   for y=1:1:pixel
         x2_pos=(x*(image_size/pixel))*(cos(rotation2))-
(y*(image_size/pixel))*(sin(rotation2))+1.23;
         y2_pos=(x*(image_size/pixel))*(sin(rotation2))+
(y*(image_size/pixel))*(cos(rotation2))+0.71;
```

```
        layer2(x,y)=1-
(2/9)*(cos((2*pi/2.46)*(x2_pos+y2_pos/sqrt(3)))+cos((2*pi/2.46)*(x2_pos-
y2_pos/sqrt(3)))+cos((4*pi/2.46)*(y2_pos/sqrt(3)))+3/2);
    end
end
pack

%% Simulate the third layer

for x=1:1:pixel
   x
   for y=1:1:pixel

        x3_pos=(x*(image_size/pixel))*(cos(rotation3))-
(y*(image_size/pixel))*(sin(rotation3));

y3_pos=(x*(image_size/pixel))*(sin(rotation3))+(y*(image_size/pixel))*(cos(rotation3));

         layer3(x,y)=1-
(2/9)*(cos((2*pi/2.46)*(x3_pos+y3_pos/sqrt(3)))+cos((2*pi/2.46)*(x3_pos-
y3_pos/sqrt(3)))+cos((4*pi/2.46)*(y3_pos/sqrt(3)))+3/2);
    end
end
pack

%% Integrating the three layers together and outputting the simulated superlattice image

surface_nor=[];
surface_nor=layer1-0.5*layer2+0.125*layer3;
imagesc(x_axis,y_axis,surface_nor)
colormap (gray)
figure
colormap;
mesh(x_axis,y_axis,surface_nor)
colorbar
```

C.2 Rippling fringes on superlattice – for section 3.3.3.2

MATLAB m-file: rippling

```
%%%%%%%%%% Simulation – Rippling fringes on superlattice

image_size=4000;  %% specify size of image to simulate
pixel=1000;       %% specify the number of data points for the simulated image

%% input the rotation angle for each graphite layer

rotation1=2.56*(pi/180);
rotation2=0*(pi/180);
rotation3=0*(pi/180);

layer1=[];
layer2=[];
layer3=[];

x_axis=image_size/pixel:image_size/pixel:image_size;
y_axis=x_axis;

%% Simulate the first (topmost) layer

for x=1:1:pixel
   x
   for y=1:1:pixel

        x1_pos=(x*(image_size/pixel))*(cos(rotation1))-
(y*(image_size/pixel))*(sin(rotation1));

y1_pos=(x*(image_size/pixel))*(sin(rotation1))+(y*(image_size/pixel))*(cos(rotation1));
        layer1(x,y)=1-
(2/9)*(cos((2*pi/2.46)*(x1_pos+y1_pos/sqrt(3)))+cos((2*pi/2.46)*(x1_pos-
y1_pos/sqrt(3)))+cos((4*pi/2.46)*(y1_pos/sqrt(3)))+3/2);
   end
end
pack

%% Simulate the second layer

for x=1:1:pixel
   x
   for y=1:1:pixel

        x2_pos=(x*(image_size/pixel))*(cos(rotation2))-
(y*(image_size/pixel))*(sin(rotation2))+1.23;

y2_pos=(x*(image_size/pixel))*(sin(rotation2))+(y*(image_size/pixel))*(cos(rotation2))+0.7
1;
```

```
        layer2(x,y)=1-
(2/9)*(cos((2*pi/2.46)*(x2_pos+y2_pos/sqrt(3)))+cos((2*pi/2.46)*(x2_pos-
y2_pos/sqrt(3)))+cos((4*pi/2.46)*(y2_pos/sqrt(3)))+3/2);

  end
end
pack

%% Simulate the third layer

for x=1:1:pixel
   x
   for y=1:1:pixel

        x3_pos=(x*(image_size/pixel))*(cos(rotation3))-
(y*(image_size/pixel))*(sin(rotation3));

y3_pos=(x*(image_size/pixel))*(sin(rotation3))+(y*(image_size/pixel))*(cos(rotation3));

         layer3(x,y)=1-
(2/9)*(cos((2*pi/2.46)*(x3_pos+y3_pos/sqrt(3)))+cos((2*pi/2.46)*(x3_pos-
y3_pos/sqrt(3)))+cos((4*pi/2.46)*(y3_pos/sqrt(3)))+3/2);
    end
end
pack

%% Integrating the three layers together and outputting the simulated superlattice image

surface_nor=[];
surface_nor=layer1-0.5*layer2+0.125*layer3;
imagesc(x_axis,y_axis,surface_nor)
colormap (gray)
figure
colormap;
mesh(x_axis,y_axis,surface_nor)
colorbar
```

C.3 Study on the unusual aspect of superlattice proposed by Cee *et al.* – for section 3.3.3.3

MATLAB m-file: Cee

```
%%%%%%%%%%% Simulation – Study on the unusual aspect of superlattice proposed
%%%%%%%%%%% by Cee et al.

image_size=100;   %% specify size of image to simulate
pixel=500;        %% specify the number of data points for the simulated image

%% input the rotation angle for each graphite layer, here we use the same rotation angle as
Cee

rotation1=5*(pi/180);
rotation2=0*(pi/180);
rotation3=0*(pi/180);

layer1=[];
layer2=[];
layer3=[];

x_axis=image_size/pixel:image_size/pixel:image_size;
y_axis=x_axis;

%% Simulate the first (topmost) layer

for x=1:1:pixel
   x
   for y=1:1:pixel

        x1_pos=(x*(image_size/pixel))*(cos(rotation1))-
(y*(image_size/pixel))*(sin(rotation1));

y1_pos=(x*(image_size/pixel))*(sin(rotation1))+(y*(image_size/pixel))*(cos(rotation1));
        layer1(x,y)=1-
(2/9)*(cos((2*pi/2.46)*(x1_pos+y1_pos/sqrt(3)))+cos((2*pi/2.46)*(x1_pos-
y1_pos/sqrt(3)))+cos((4*pi/2.46)*(y1_pos/sqrt(3)))+3/2);
   end
end
pack

%% Simulate the second layer

for x=1:1:pixel
   x
   for y=1:1:pixel

        x2_pos=(x*(image_size/pixel))*(cos(rotation2))-
(y*(image_size/pixel))*(sin(rotation2))+1.23;
```

```
y2_pos=(x*(image_size/pixel))*(sin(rotation2))+(y*(image_size/pixel))*(cos(rotation2))+0.7
1;
        layer2(x,y)=1-
(2/9)*(cos((2*pi/2.46)*(x2_pos+y2_pos/sqrt(3)))+cos((2*pi/2.46)*(x2_pos-
y2_pos/sqrt(3)))+cos((4*pi/2.46)*(y2_pos/sqrt(3)))+3/2);

  end
end

%% Simulate the third layer

for x=1:1:pixel
   x
   for y=1:1:pixel

        x3_pos=(x*(image_size/pixel))*(cos(rotation3))-
(y*(image_size/pixel))*(sin(rotation3));

y3_pos=(x*(image_size/pixel))*(sin(rotation3))+(y*(image_size/pixel))*(cos(rotation3));

         layer3(x,y)=1-
(2/9)*(cos((2*pi/2.46)*(x3_pos+y3_pos/sqrt(3)))+cos((2*pi/2.46)*(x3_pos-
y3_pos/sqrt(3)))+cos((4*pi/2.46)*(y3_pos/sqrt(3)))+3/2);

  end
end
pack

%% Integrating the three layers together with exaggerated weightings as Cee and outputting
the %% simulated superlattice image

surface_nor=[];
surface_nor=layer1-0.125*layer2+0.25*layer3;
imagesc(x_axis,y_axis,surface_nor)
colormap (gray)
figure
colormap;
mesh(x_axis,y_axis,surface_nor)
colorbar
```

C.4 "Odd-even" transition along atomic rows – for section 3.3.3.4

MATLAB m-file: oddeven3

```
%%%%%%%%%% Simulation – "Odd-even" transition along atomic rows

image_size=50;   %% specify size of image to simulate
pixel=500;       %% specify the number of data points for the simulated image

%% input the rotation angle for each graphite layer

rotation1=10*(pi/180);
rotation2=10*(pi/180);
rotation3=0*(pi/180);

layer1=[];
layer2=[];
layer3=[];

x_axis=image_size/pixel:image_size/pixel:image_size;
y_axis=x_axis;

%% Simulate the first (topmost) layer

for x=1:1:pixel
   x
   for y=1:1:pixel

        x1_pos=(x*(image_size/pixel))*(cos(rotation1))-
(y*(image_size/pixel))*(sin(rotation1));

y1_pos=(x*(image_size/pixel))*(sin(rotation1))+(y*(image_size/pixel))*(cos(rotation1));
        layer1(x,y)=1-
(2/9)*(cos((2*pi/2.46)*(x1_pos+y1_pos/sqrt(3)))+cos((2*pi/2.46)*(x1_pos-
y1_pos/sqrt(3)))+cos((4*pi/2.46)*(y1_pos/sqrt(3)))+3/2);
   end
end
pack

%% Simulate the second layer

for x=1:1:pixel
   x
   for y=1:1:pixel
            x2_pos=(x*(image_size/pixel))*(cos(rotation2))-
(y*(image_size/pixel))*(sin(rotation2))+1.23;

y2_pos=(x*(image_size/pixel))*(sin(rotation2))+(y*(image_size/pixel))*(cos(rotation2))+0.7
1;
```

```
        layer2(x,y)=1-
(2/9)*(cos((2*pi/2.46)*(x2_pos+y2_pos/sqrt(3)))+cos((2*pi/2.46)*(x2_pos-
y2_pos/sqrt(3)))+cos((4*pi/2.46)*(y2_pos/sqrt(3)))+3/2);

  end
end

%% Simulate the third layer

for x=1:1:pixel
   x
   for y=1:1:pixel

        x3_pos=(x*(image_size/pixel))*(cos(rotation3))-
(y*(image_size/pixel))*(sin(rotation3));

y3_pos=(x*(image_size/pixel))*(sin(rotation3))+(y*(image_size/pixel))*(cos(rotation3));

         layer3(x,y)=1-
(2/9)*(cos((2*pi/2.46)*(x3_pos+y3_pos/sqrt(3)))+cos((2*pi/2.46)*(x3_pos-
y3_pos/sqrt(3)))+cos((4*pi/2.46)*(y3_pos/sqrt(3)))+3/2);

  end
end
pack

%% Integrating the three layers together and outputting the simulated superlattice image

surface_nor=[];
surface_nor=layer1-0.5*layer2+0.125*layer3;
imagesc(x_axis,y_axis,surface_nor)
colormap (gray)
figure
colormap;
mesh(x_axis,y_axis,surface_nor)
colorbar
```

C.5 Coexisting superlattices – for section 3.3.3.5

MATLAB m-file: coexist_sup

```
%%%%%%%%%% Simulation – Coexisting superlattices

image_size=700;     %% specify size of image to simulate
pixel=4000;         %% specify the number of data points for the simulated image

%% input the rotation angle for each graphite layer

rotation1=4.34*(pi/180);
rotation2=0.734*(pi/180);
rotation3=0*(pi/180);

x_axis=image_size/pixel:image_size/pixel:image_size;
y_axis=x_axis;

%% Simulate the first (topmost) layer

layer1=ones(pixel,pixel);
for x=1:1:pixel
   x
   for y=1:1:pixel

        x1_pos=(x*(image_size/pixel))*(cos(rotation1))-
(y*(image_size/pixel))*(sin(rotation1));

y1_pos=(x*(image_size/pixel))*(sin(rotation1))+(y*(image_size/pixel))*(cos(rotation1));
        layer1(x,y)=1-
(2/9)*(cos((2*pi/2.46)*(x1_pos+y1_pos/sqrt(3)))+cos((2*pi/2.46)*(x1_pos-
y1_pos/sqrt(3)))+cos((4*pi/2.46)*(y1_pos/sqrt(3)))+3/2);
   end
end
pack

%% Simulate the second layer

layer2=ones(pixel,pixel);
for x=1:1:pixel
   x
   for y=1:1:pixel

        x2_pos=(x*(image_size/pixel))*(cos(rotation2))-
(y*(image_size/pixel))*(sin(rotation2))+1.23;

y2_pos=(x*(image_size/pixel))*(sin(rotation2))+(y*(image_size/pixel))*(cos(rotation2))+0.7
1;
        layer2(x,y)=1-
(2/9)*(cos((2*pi/2.46)*(x2_pos+y2_pos/sqrt(3)))+cos((2*pi/2.46)*(x2_pos-
y2_pos/sqrt(3)))+cos((4*pi/2.46)*(y2_pos/sqrt(3)))+3/2);
```

```
  end
end
pack

%% Simulate the third layer

layer3=ones(pixel,pixel);
for x=1:1:pixel
   x
   for y=1:1:pixel

        x3_pos=(x*(image_size/pixel))*(cos(rotation3))-
(y*(image_size/pixel))*(sin(rotation3));

y3_pos=(x*(image_size/pixel))*(sin(rotation3))+(y*(image_size/pixel))*(cos(rotation3));

         layer3(x,y)=1-
(2/9)*(cos((2*pi/2.46)*(x3_pos+y3_pos/sqrt(3)))+cos((2*pi/2.46)*(x3_pos-
y3_pos/sqrt(3)))+cos((4*pi/2.46)*(y3_pos/sqrt(3)))+3/2);

  end
end
pack

%% Integrating the three layers together and outputting the simulated superlattice image

surface_nor=[];
surface_nor=1*layer1-0.5*layer2+0.125*layer3;
clear layer1;
clear layer2;
clear layer3;
imagesc(x_axis,y_axis,surface_nor)
colormap (gray)
```

C.6 Superlattice with screw dislocation – for section 3.3.3.6

MATLAB m-file: screw

```
%%%%%%%%%% Simulation – Superlattice with screw dislocation

start_angle=4*(pi/180);    %% setting the initial degree for the moiré rotation angle θ
end_angle=8*(pi/180);      %% setting the final degree for the moiré rotation angle θ


image_size=400;            %% specify size of image to simulate
pixel=700;                 %% specify the number of data points for the simulated image

origin_x=pixel/2;
origin_y=pixel/2;

rotation1=0*(pi/180);
rotation2=0*(pi/180);
rotation3=0*(pi/180);

rotation=[];

layer1=[];
layer2=[];
layer3=[];

x_axis=image_size/pixel:image_size/pixel:image_size;
y_axis=x_axis;

%% This section is for calculating the moiré rotation angle θ at each point as the angle ϕ
increases from 0° to 360° around the screw dislocation, and simulates the first layer.

for x=1:1:pixel
   x
   for y=1:1:pixel
        if (x-origin_x)>0 & (y-origin_y)==0
           rotation1=start_angle;
        end
        if (x-origin_x)>0 & (y-origin_y)>0
           rotation1=atan(abs(y-origin_y)/abs(x-origin_x))/(pi*2)*(end_angle-
start_angle)+start_angle;
        end
        if (x-origin_x)==0 & (y-origin_y)>0
           rotation1=(end_angle-start_angle)*0.25+start_angle;
        end
        if (x-origin_x)<0 & (y-origin_y)>0
           rotation1=(pi/2-atan(abs(y-origin_y)/abs(x-origin_x)))/(pi*2)*(end_angle-
start_angle)+(end_angle-start_angle)*0.25+start_angle;
        end
        if (x-origin_x)<0 & (y-origin_y)==0
           rotation1=(end_angle-start_angle)*0.5+start_angle;
```

```
        end
        if (x-origin_x)<0 & (y-origin_y)<0
           rotation1=atan(abs(y-origin_y)/abs(x-origin_x))/(pi*2)*(end_angle-
start_angle)+(end_angle-start_angle)*0.5+start_angle;
        end
        if (x-origin_x)==0 & (y-origin_y)<0
           rotation1=(end_angle-start_angle)*0.75+start_angle;
        end
        if (x-origin_x)>0 & (y-origin_y)<0
           rotation1=(pi/2-atan(abs(y-origin_y)/abs(x-origin_x)))/(pi*2)*(end_angle-
start_angle)+(end_angle-start_angle)*0.75+start_angle;
        end

        x1_pos=(x*(image_size/pixel))*(cos(rotation1))-
(y*(image_size/pixel))*(sin(rotation1));

y1_pos=(x*(image_size/pixel))*(sin(rotation1))+(y*(image_size/pixel))*(cos(rotation1));
        layer1(x,y)=1-
(2/9)*(cos((2*pi/2.46)*(x1_pos+y1_pos/sqrt(3)))+cos((2*pi/2.46)*(x1_pos-
y1_pos/sqrt(3)))+cos((4*pi/2.46)*(y1_pos/sqrt(3)))+3/2);
   end
end
pack

%% Simulate the second layer

for x=1:1:pixel
   x
   for y=1:1:pixel

        x2_pos=(x*(image_size/pixel))*(cos(rotation2))-
(y*(image_size/pixel))*(sin(rotation2))+1.23;

y2_pos=(x*(image_size/pixel))*(sin(rotation2))+(y*(image_size/pixel))*(cos(rotation2))+0.7
1;
        layer2(x,y)=1-
(2/9)*(cos((2*pi/2.46)*(x2_pos+y2_pos/sqrt(3)))+cos((2*pi/2.46)*(x2_pos-
y2_pos/sqrt(3)))+cos((4*pi/2.46)*(y2_pos/sqrt(3)))+3/2);

  end
end
pack

%% Simulate the third layer

for x=1:1:pixel
   x
   for y=1:1:pixel

        x3_pos=(x*(image_size/pixel))*(cos(rotation3))-
(y*(image_size/pixel))*(sin(rotation3));
```

```
y3_pos=(x*(image_size/pixel))*(sin(rotation3))+(y*(image_size/pixel))*(cos(rotation3));

        layer3(x,y)=1-
(2/9)*(cos((2*pi/2.46)*(x3_pos+y3_pos/sqrt(3)))+cos((2*pi/2.46)*(x3_pos-
y3_pos/sqrt(3)))+cos((4*pi/2.46)*(y3_pos/sqrt(3)))+3/2);

   end
end
pack

surface_nor=[];
surface_nor=layer1-0.5*layer2+0.125*layer3;
imagesc(x_axis,y_axis,surface_nor)
colormap (gray)
figure
colormap;
mesh(x_axis,y_axis,surface_nor)
colorbar

%% This section is for analyzing the simulated superlattice by Fast Fourier Transform

fft_spec=fft2(surface_nor);
fft_spec =fftshift(abs(fft_spec));
fft_spec (1001,1001)=0;
figure
imagesc(fft_spec)
colormap (hot)
```

References

[1] R. Young, J. Ward, and F. Scire, Phys. Rev. Lett. 27 (1971) 922.

[2] R. Young, J. Ward, and F. Scire, Rev. Sci. Instrum. 43 (1972) 999.

[3] G. Binnig, H. Rohrer, Ch. Gerber, and E. Weibel, Phys. Rev. Lett. 49 (1982) 57.

[4] G. Binnig, H. Rohrer, Ch. Gerber, and E. Weibel, Phys. Rev. Lett. 50 (1983) 120.

[5] A. Baratoff, G. Binnig, H. Fuchs, F. Salvan, and E. Stoll, Surf. Sci. 168 (1986) 734.

[6] R. S. Becker, J. A. Golovchenko, D. R. Hamann, and B. S. Swartzentruber, Phys. Rev. Lett. 55 (1985) 2032.

[7] G. Binnig, N. Garcia, and H. Rohrer, Phys. Rev. B 32 (1985) 1336.

[8] J. G. Simmons, J. Appl. Phys. 34 (1963) 1793.

[9] J. Bardeen, Phys. Rev. Lett. 6 (1961) 57.

[10] C. J. Chen, Chap. 2 in Introduction to Scanning Tunneling Microscopy, Oxford University Press (1993)

[11] J. Tersoff and D. R. Hamann, Phys. Rev. Lett. 50 (1983) 1998.

[12] J. P. Ibe, P. P. Bey, S. L. Brandon, R. A. Brizzolara, N. A. Burnham, D. P. DiLella, K. P. Lee, C. R. K. Marrian, and R. J. Colton, J. Vac. Sci. Technol. A 8 (1990) 3570.

[13] R. L. Nicolaides, W. E. Yong, W. F. Packard, and H. A. Zhou, J. Vac. Sci. Technol. A 6 (1988) 445.

[14] A. H. Sørensen, U. Hvid, M. W. Mortensen, and K. A. Mørch, Rev. Sci. Instrum. 70 (1999) 3059.

[15] Homepage of Scanning Probe Methods Group, at the Institute of Applied Physics, University of Hamburg, headed by Prof. Roland Wiesendanger, http://www.nanoscience.de/group_r/stm-spstm/stm/

[16] G. Binnig and H. Rohrer, Phys. Rev. Lett. 59 (1987) 615.

[17] P. K. Hansma and J. Tersoff, J. Appl. Phys. 61 (1987) R1.

[18] A. Blank, C. R. Dunnam, P. P. Borbat, and J. H. Freed, J. Magn. Reson. 165 (2003) 116.

[19] L. Ciobanu, D. A. Seeber, and C. H. Pennington, J. Magn. Reson. 158 (2002) 178.

[20] M. Xiao, I. Martin, E. Yablonovitch, and H. W. Jiang, Nature 430 (2004) 435.

[21] J. M. Elzerman, R. Hanson, L. H. Willems van Beveren, B. Witkamp, L. M. K. Vandersypen, and L. P. Kouwenhoven, Nature 430 (2004) 431.

[22] F. Jelezko, I. Popa, A. Gruber, C. Tietz, J. Wrachtrup, A. Nizovtsev, and S. Kilin, Appl. Phys. Lett. 81 (2002) 2160.

[23] J. Kohler, J. A. J. M. Disselhorst, M. C. J. M. Donckers, E. J. J. Groenen, J. Schmidt, and W. E. Moerner, Nature 363 (1993) 242.

[24] J. Wrachtrup, C. von Borczyskowski, J. Bernard, M. Orritt, and R. Brown, Nature 363 (1993) 244.

[25] D. Rugar, R. Budakian, H. J. Mamin, and B. W. Chui, Nature 430 (2004) 329.

[26] S. Heinze, M. Bode, A. Kubetzka, O. Pietzsch, X. Nie, S. Blügel, and R. Wiesendanger, Science 288 (2000) 1805.

[27] M. Kleiber, M. Bode, R. Ravlic, and R. Wiesendanger, Phys. Rev. Lett. 85 (2000) 4606.

[28] R. Wiesendanger, H. –J. Güntherodt, G. Güntherodt, R. J. Gambino, and R. Ruf, Phys. Rev. Lett. 65 (1990) 247.

[29] A. Kubetzka, O. Pietzsch, M. Bode, and R. Wiesendanger, Phys. Rev. B (2001) 140407.

[30] M. Pratzer, H. J. Elmers, M. Bode, O. Pietzsch, A. Kubetzka, and R. Wiesendanger, Phys. Rev. Lett. 87 (2001) 127201

[31] M. Bode, M. Getzlaff, and R. Wiesendanger, Phys. Rev. Lett. 81 (1998) 4256.

[32] Nanosurf AG, Grammetstrasse 14, CH-4410 Liestal, www.nanosurf.com

[33] SPI Supplies West Chester, PA 19380, USA

[34] Agar Scientific Limited, Essex CM24 8DA, England, United Kingdom

[35] R. Wiesendanger, Section 4.1.2.1 in *Scanning Probe Microscopy and Spectroscopy: Methods and applications* Cambridge University Press, Cambridge, England, United Kingdom (1994)

[36] Y. Manassen, R. J. Hamers, J. E. Demuth, and A. J. Castellano Jr., Phys. Rev. Lett. 62 (1989) 2531.

[37] M. Okano, K. Kajimura, S. Wakiyama, F. Sakai, W. Mizutani, and M. Ono, J. Vac. Sci. Technol A. 5 (1987) 3313.

[38] K. Nagaya, J. Dynam. Syst. Meas. Control. 106 (1984) 52.

[39] K. Nagaya and H. Kojima, J. Dynam. Syst. Meas. Control. 106 (1984) 46.

[40] Control electronics of the STM provided by East Coast Scientitic (ECS) Ltd, United Kingdom

[41] G. Binnig and D. P. E. Smith, Rev. Sci. Instrum. 57 (1986) 1688.

[42] Y. Kuk and P. J. Silverman, Rev. Sci. Instrum. 60 (1989) 165.

[43] W. T. Pong and C. Durkan, *Proceedings of the 5th International Conference 7th Annual General Meeting of the European Society for Precision Engineering and Nanotechnology*, Montpellier, France, vol. 1, p. 241 (2005)

[44] F. A. Cotton and G. Wilkinson, Part 2, *Advanced Inorganic Chemistry*, fifth edition (John Wiley and Sons, New York, 1988)

[45] T. R. Albrecht, M. M. Dovek, C. A. Lang, P. Grutter, C. F. Quate, S. W. Kuan, C. W. Frank, and R. F. W. Pease, J. Appl. Phys. 64 (1988) 1178.

[46] P. G. Arscott, G. Lee, V. A. Bloomfield, and D. F. Evans, Nature 339 (1989) 484.

[47] R. Coratger, A. Claverie, F. Ajustron, and J. Beauvillain, Surf. Sci. 227 (1990) 7.

[48] D. D. Dunlap and C. Bustamante, Nature 342 (1989) 204.

[49] L. Feng, C. Z. Hu, and J. D. Andrade, J. Colloid Interface Sci. 126 (1988) 650.

[50] M. Hara, Y. Iwakabe, K. Tochiji, H. Sasabe, A. F. Garito, and A. Yamada, Nature 344 (1990) 228.

[51] J. K. H. Horber, C. A. Lang, T. W. Hansch, W. M. Heckl, and H. Mohwald, Chem. Phys. Lett. 145 (1988) 151.

[52] C. A. Lang, J. K. H. Horber, T. W. Hansch, W. M. Heckl, and H. Mohwald, J. Vac. Sci. Technol. A 6 (1988) 368.

[53] B. H. Loo, Z. F. Liu, and A. Fujishima, Surf. Sci. 227 (1990) 1.

[54] W. Mizutan, M. Shigeno, K. Saito, K. Watanabe, M. Sugi, M. Ono, and K. Kajimura, Jpn. J. Appl. Phys. 27 (1988) 1803.

[55] D. P. E. Smith, A. Bryant, C. F. Quate, J. P. Rabe, C. Gerber, and J. D. Swalen, Proc. Natl. Acad. Sci. USA. 84 (1987) 969.

[56] D. P. E. Smith, H. Horber, C. Gerber, and G. Binning, Science 245 (1989) 43.

[57] D. P. E. Smith, M. D. Kirk, and C. F. Quate, J. Chem. Phys. 86 (1987) 6034.

[58] X. L. Wu and C. M. Lieber, J. Phys. Chem. 92 (1988) 5556.

[59] T. R. Albrecht, H. A. Mizes, J. Nogami, S. Park, and C. F. Quate, Appl. Phys. Lett. 52 (1988) 362.

[60] H. Beyer, M. Muller, and Th. Schimmel, Appl. Phys. A 68 (1999) 163.

[61] Y. Gan, W. Chu, and L. Qiao, Surf. Sci. 539 (2003) 120.

[62] J. Garbarz, E. Lacaze, G. Faivre, S. Gauthier, and M. Schott, Phil. Mag. A 65 (1992) 853.

[63] M. Kuwabara, D. R. Clarke, and D. A. Smith, Appl. Phys. Lett. 56 (1990) 2396.

[64] C. Y. Liu, H. Chang, and A. J. Bard, Langmuir 7 (1991) 1138.

[65] J. Osing and I. V. Shvets, Surf. Sci. 417 (1998) 145.

[66] Z. Y. Rong and P. Kuiper, Phys. Rev. B 48 (1993) 17427.

[67] J. Xhie, K. Sattler, M. Ge, and N. Venkateswaran, Phys. Rev. B 47 (1993) 15835.

[68] J. R. Hahn and H. Kang, Phys. Rev. B 60 (1999) 6007.

[69] K. F. Kelly, D. Sarkar, G. D. Hale, S. J. Oldenburg, and N. J. Halas, Science 273 (1996) 1371.

[70] S. Kondo, M. Lutwyche, and Y. Wada, Jpn. J. Appl. Phys. 33 (1994) L1342.

[71] H. A. Mizes and J. S. Foster, Science 244 (1989) 559.

[72] P. W. de Bont, P. M. L. O. Scholte, M. H. J. Hottenhuis, G. M. P. van Kempen, J. W. Kerssemakers, and F. Tuinstra, Appl. Surf. Sci. 74 (1994) 73.

[73] L. Porte, C. H. de Villeneuve, and M. Phaner, J. Vac. Sci. Technol. B 9 (1991) 1064.

[74] J. P. Rabe, M. Sano, D. Batchelder, and A. A. Kalatchev, J. Microscopy 152 (1988) 573.

[75] G. M. Shedd and P. E. Russell, J. Vac. Sci. Technol. A 9 (1991) 1261.

[76] J. Xhie, K. Sattler, U. Muller, N. Venkateswaran, and G. Raina, J. Vac. Sci. Technol. B 9 (1991) 833.

[77] D. E. Moncton, J. D. Axe, and F. J. Disalvo, J. Phys. Rev. B: Condens. Matter 16 (1977) 801.

[78] C. G. Slough, W. W. McNairy, R. V. Coleman, J. Garnaes, C. B. Prater, and P. K. Hansma, Phys. Rev. B 42 (1990) 9255.

[79] X. L. Wu and C. M. Lieber, Science 243 (1989) 1703.

[80] Z. Y. Rong, Phys. Rev. B 50 (1994) 1839.

[81] D. Keller, C. Bustamante, and R. W. Keller, Proc. Natl. Acad. Sci. U.S.A. 86 (1989) 5356.

[82] G. Lee, P. G. Arscott, V. A. Bloomfield, and D. F. Evans, Science 244 (1989) 475.

[83] T.P. Beebe Jr., T. E. Wilson, D. F. Ogletree, J. E. Katz, R. Balhorn, M. D. Salmeron, and W. J. Siekhaus, Science 243 (1989) 370.

[84] C. R. Clemmer and T. P. Beebe Jr., Science 251 (1991) 640.

[85] H. Chang and A. J. Bard, Langmuir 7 (1991) 1143.

[86] X. Yang, Ch. Bromm, U. Geyer, and G. von Minnigerode, Ann. Phys. 1 (1992) 3.

[87] J. E. Buckley, J. L. Wragg, and H. W. White, J. Vac. Sci. Technol. B 9 (1991) 1079

[88] P. J. Ouseph, Phys. Rev. B 53 (1996) 9610.

[89] P. J. Ouseph, Appl. Surf. Sci. 165 (2000) 38.

[90] H. Sun, Q. Shen, J. Jia, Q. Zhang, and Q. Xue, Surf. Sci. 542 (2003) 94.

[91] B. Feddes, I. I. Kravchenko, and L. E. Seiberling, Scanning 20 (1998) 376.

[92] P. I. Oden, T. Thundat, L. A. Nagahara, S. M. Lindsay, G. B. Adams, and O. F. Sankey, Surf. Sci. Lett. 254 (1991) L454.

[93] I. K. Song, J. R. Kitchin, and M. A. Barteau, Proc. Natl. Acad. Sci. USA. 99 (suppl. 2) (2002) 6471.

[94] T. M. Bernhardt, B. Kaiser, and K. Rademann, Surf. Sci. 408 (1998) 86.

[95] K. Miyake, K. Akutsu, T. Yamada, K. Hata, R. Morita, M. Yamashita, and H. Shigekawa, Ultramicroscopy 73 (1998) 185.

[96] J. W. Lyding, J. S. Hubacek, G. Gammie, S. Skala, and R. Brockenbrough, J. Vac. Sci. Technol. A 6 (1988) 363.

[97] V. Elings and F. Wudl, J. Vac. Sci. Technol. A 6 (1988) 412.

[98] W. T. Pong and C. Durkan, Jpn. J. Appl. Phys. 44 (No. 7B) (2005) 5443.

[99] G. Dai, T. Xie, H. Cheng, and H. Ye, J. Mater. Sci. Technol. 19 (2003) 246.

[100] F. I. Dalidchik, M. V. Grishin, and S. A. Kovalevskii, Phys. Low-Dim. Struct. 3/4 (2003) 45.

[101] D. L. Patrick and T. P. Beebe Jr., Surf. Sci. Lett. 297 (1993) L119.

[102] B. Nysten, J. -C. Roux, S. Flandrois, C. Daulan, and H. Saadaoui, Phys. Rev. B 48 (1993) 12527.

[103] M. Sawamura, J. F. Womelsdorf, and W. C. Ermler, J. Phys. Chem. 95 (1991) 8823.

[104] J. F. Womelsdorf and W. C. Ermler, J. Phys. Chem. 95 (1991) 503.

[105] T. Hashizume, I. Kamiya, Y. Hasegawa, N. Sano, T. Sakurai, and H. W. Pickering, J. Microscopy 152 (1988) 347.

[106] Phys. Today, 41 (5) (1988) 129

[107] S. J. Ball, J. M. MacLeod, and A. B. McLean, in preparation (2005)

[108] L. Markey, D. Stievenard, A. Devos, M. Lannoo, F. Demol, and M. de Backer, Supramolecular Science 4 (1997) 375.

[109] S. J. Ball, G. E. Contant, and A. B. McLean, Rev. Sci. Instrum. 75 (2004) 5293.

[110] T. Tanii, K. Hara, K. Ishibashi, K. Ohta, and I. Ohdomari, Appl. Surf. Sci. 162-163 (2000) 662.

[111] J. –C. Charlier, J. –P. Michenaud, and X. Gonze, Phys. Rev. B 46 (1992) 4531

[112] H. Lipson and A. R. Stokes, Proc. R. Soc. London, Ser. A 181 (1942) 101

[113] T. A. Green and J. Weigle, Helv. Phys. Acta 21 (1948) 217.

[114] G. Oster, Endeavour 27 (1968) 60.

[115] I. Amidror, *The Theory of the Moiré Phenomenon* (Kluwer Academic Publishers, Netherlands, 1999)

[116] K. Kobayashi, Phys. Rev. B 53 (1996) 11091.

[117] J. –C. Charlier and J. –P. Michenaud, Phys. Rev. B 46 (1992) 4540

[118] Z. Wei, C. Xu, X. Chen, and K. Xu, Appl. Surf. Sci. 228 (2004) 158.

[119] S. R. Snyder, W. W. Gerberich, and H. S. White, Phys. Rev. B 47 (1993) 10823.

[120] J. J. Gilman, *Micromechanics of Flow in Solids* (McGraw – Hill, New York, 1969), Chap. 5

[121] D. E. Soule and C. W. Nezbeda, J. Appl. Phys. 39 (1968) 5122.

[122] S. Gwo and C. K. Shih, Phys. Rev. B 47 (1993) 13059.

[123] H. J. Mamin, E. Ganz, D. W. Abraham, R. E. Thomson, and J. Clarke, Phys. Rev. B 34 (1986) 9015.

[124] J. M. Soler, A. M. Baro, N. Garcia, and H. Rohrer, Phys. Rev. Lett. 57 (1986) 444.

[125] H. Saadaoui, J. -C. Roux, S. Flandrois, and B. Nysten, Carbon 31 (1993) 481.

[126] E. Ganz, K. Sattler, and J. Clarke, Phys. Rev. Lett. 60 (1988) 1856.

[127] U. Muller, K. Sattler, J. Xhie, N. Venkateswaran, and G. Raina, J. Vac. Sci. Technol. B 9 (1991) 829.

[128] V. J. Cee, D. L. Patrick, and T. P. Beebe Jr., Surf. Sci. 329 (1995) 141.

[129] W. T. Pong and C. Durkan, to be published in J. Phys. D: Appl. Phys. as a review article (2005)

[130] W. T. Pong and C. Durkan, Jpn. J. Appl. Phys. 44 (No. 7B) (2005) 5365.

[131] R. Hentschke, B. Schurmann, and J. Rabe, J. Chem. Phys. 96 (1992) 6213.

[132] W. T. Pong, J. Bendall, and C. Durkan, submitted to Phys. Rev. B. (2005)

[133] J. C. Charlier, J. P. Michenaud, and P. Lambin, Phys. Rev. B 46 (1992) 4540.

[134] C. Kittel, *Introduction to Solid State Physics* (John Wiley & Sons, New York, sixth edition, 1986), Chap.2, p. 567 - 570

[135] S. Amelinckx, P. Delavignette, and M. Heerschap, in “Chemistry and Physics of Carbon”, edited by P. L. Walker, Jr. (M. Dekker inc., New York 1965), Vol. 1, p. 41

[136] G. L. Bleris, G. Nouet, S. Hagege, and P. Delavignette, Acta Cryst. A 38 (1982) 550.

[137] H. Grimmer and D. H. Warrington, Acta Cryst. A 43 (1987) 232.

[138] C. Daulan, A. Derré, S. Flandrois, J. C. Roux, and H. Saadaoui, J. Phys. I France 5 (1995) 1111.

[139] P. Simonis, C. Goffaux, P. A. Thiry, L. P. Biro, P. Lambin, and V. Meunier, Surf. Sci. 511 (2002) 319.

[140] M. R. Soto, J. Microscopy 152 (1988) 779.

[141] Lord Rayleigh, Phil. Mag. 47 (1874) 81.

[142] H. M. Guo, H. W. Liu, Y. L. Wang, H. J. Gao, H. X. Shang, Z. W. Liu, H. M. Xie, and F. L. Dai, Nanotechnology 15 (2004) 991.

[143] Z. W. Liu, H. M. Xie, D. N. Fang, H. X. Shang, and F. L. Dai, J Mater. Process Tech. 148 (2004) 77.

[144] K. S. Novoselov, A. K. Geim, S. V. Morozov, D. Jiang, Y. Zhang, S. V. Dubonos, I. V. Grigorieva, and A. A. Firsov, Science 306 (2004) 666.

[145] Y. Zhang, J. P. Small, M. E. S. Amori, and P. Kim, Phys. Rev. Lett. 94 (2005) 176803.

[146] C. Durkan and M. E. Welland, Appl. Phys. Lett. 80 (2002) 458.

[147] C. Durkan, Contemporary Physics 45 (2004) 1.

[148] G. Wagoner, Phys. Rev. 118 (1960) 647.

[149] F. J. Dyson, Phys. Rev. 98 (1955) 349.

[150] A. Jánossy, F. Simon, T. Fehér, A. Rockenbauer, L. Korecz, C. Chen, A. J. S. Chowdhury, and J. W. Hodby, Phys. Rev. B 59 (1999) 1176.

[151] R. Emch, J. Nogami, M. M. Dovek, C. A. Lang, and C. F. Quate, J. Appl. Phys. 65 (1989) 79.

[152] Q. Guo, F. Yin, and R. Palmer, Small 1 (2005) 76.

[153] J. Kim, H. Uchida, K. Yoshida, H. Kim, K. Nishimura, and M. Inoue, Jpn. J. Appl. Phys. 42 (2003) 3616.

[154] Z. H. Wang and M. Moskovits, J. Appl. Phys. 71 (1992) 5401.

[155] M. Schunack, F. Rosei, Y. Naitoh, P. Jiang, A. Gourdon, E. Lægsgaard, I. Stensgaard, C. Joachim, and F.Besenbacher, J. Chem. Phys. 117 (2002) 6259.

[156] H. Li, D. J. Kang, M. G. Blamire, and W. T. S. Huck, Nano Letters 2 (2002) 347.

[157] A. Bernard, E. Delamarche, H. Schmid, B. Michel, H. R. Bosshard, and H. Biebuyck, Langmuir 14 (1998) 2225.

[158] N. L. Jeon, I. S. Choi, G. M. Whitesides, N. Y. Kim, P. E. Laibinis, Y. Harada, K. R. Finnie, G. S. Girolami, and R. G. Nuzzo, Appl. Phys. Lett. 75 (1999) 4201.

[159] T. L. Breen, P. M. Fryer, R. W. Nunes, and M. E. Rothwell, Langmuir 18 (2002) 194.

[160] H. X. He, Q. G. Li, Z. Y. Zhou, H. Zhang, S. F. Y. Li, and Z. F. Liu, Langmuir 16 (2000) 9683.

[161] Y. Koide, Q. Wang, J. Cui, D. D. Benson, and T. J. Marks, J. Am. Chem. Soc. 122 (2000) 11266.

[162] C. R. Kagan, T. L. Breen, and L. L. Kosbar, Appl. Phys. Lett. 79 (2001) 3536.

[163] C. Hamai, H. Tanaka, and T. Kawai, J. Vac. Sci. Technol. B 17 (1999) 1313.

[164] H. Tanaka and T. Kawai, J. Vac. Sci. Technol. B 15 (1997) 602.

[165] W. T. Pong, H. Li, W. Harneit, and C. Durkan, submitted to J. Appl. Phys.

[166] T. Kawagoe, Y. Suzuki, M. Bode, and K. Koike, J. Appl. Phys. 93 (2003) 6575.

[167] Y. Manassen, I. Mukhopadhyay, and N. Ramesh Rao, Phys. Rev. B 61 (2000) 16223

[168] J. Alvarez, J. J. Hinarejos, E. G. Michel, G. R. Castro, and R. Miranda, Phys. Rev. B 45 (1992) 14042.

[169] N. Minami, D. Makino, T. Matsumura, C. Egawa, T. Sato, K. Ota, and S. Ino, Surf. Sci. 514 (2002) 211.

[170] M. Matsumoto, K. Sugie, T. Kawauchi, K. Fukutani, and T. Okano, 12th International Colloquium on Scanning Probe Microscopy (Dec 2004) in Izu-Atagawa, Japan

[171] T. Suemasu, T. Fujii, Y. Iikura, K. i. Takakura, and F. Hasegawa, Jpn. J. Appl. Phys. 37 (1998) L1513.